



universität
wien

DISSERTATION

Titel der Dissertation

Mountain-wave-induced rotors and low-level turbulence:
new insights from remote-sensing observations and
numerical simulations

verfasst von

Dipl.-Ing. Lukas Strauss

angestrebter akademischer Grad

Doktor der Naturwissenschaften (Dr. rer. nat.)

Wien, 2015

Studienkennzahl lt. Studienblatt:	A 791 415
Dissertationsgebiet lt. Studienblatt:	Meteorologie
Betreuerin:	Univ.-Prof. Dr. Vanda Grubišić

Abstract

Atmospheric rotors are among the most vigorous phenomena related to the airflow over mountains. Rotors are traditionally described as turbulent low-level circulations, forming downwind of a mountain range in association with large-amplitude mountain waves. Today, the physical mechanisms of rotor formation are relatively well understood, owing to several observational programmes devoted to their study and high-resolution numerical simulations. The traditional, time-averaged description of the rotor circulation is, however, overly simplistic. It disregards the possibility of time-varying meteorological conditions upwind of the mountain range and the dynamic and thermal characteristics of the downwind environment. Also, quantitative measurements of turbulence intensity and its temporal evolution in the rotor interior are quite rare.

The objectives of this work are, first, to develop an observational technique allowing a quantitative estimation of the spatial distribution and intensity of rotor turbulence, and second, to elucidate the origin of unsteadiness of the rotor flow and to understand better its spatial structure in complex topography. To this end, observations of mountain waves and rotors are analysed and reproduced with real-case numerical simulations. The observational data was collected during two field campaigns that were carried out in 2006, one over the Medicine Bow Mountains in southeastern Wyoming, the other over the southern Sierra Nevada and Owens Valley in California.

Airborne in situ and Doppler radar measurements made over the Medicine Bow Mountains provide insight into the turbulent rotor flow in unprecedented detail. A method to derive turbulence intensity from the radar data is devised and it is shown that quantitative estimates of low-level turbulence can be obtained within reasonably small uncertainty bounds. The results of this analysis offer a quasi-instantaneous, two-dimensional depiction of turbulence intensity in the rotor interior.

Numerical simulations of two cases of rotor formation in the lee of the Medicine Bow Mountains reveal that the observed rapid evolution of rotors is caused by the transient breaking of large-amplitude hydrostatic mountain waves. The onset and cessation of wave breaking are tightly linked to the passage of short-wave synoptic disturbances, modulating the vertical profiles of wind and stability upwind of the obstacle and causing a change in lee-side flow regimes.

In order to broaden our understanding of atmospheric rotors in different topographic environments, several cases of enhanced mountain-wave activity and associated low-level turbulence over the Sierra Nevada and in Owens Valley are examined. Their analysis sheds new light on the complex interactions between cross-mountain and along-valley flows and points to substantial modifications of the rotor flow by atmospheric processes in the valley. Four typical scenarios of turbulence generation are distilled from the observations, representing extensions to the traditional rotor concept that are appropriate for a deep elongated valley.

This work contributes to a more realistic description of the rotor flow by the new airborne observation approach and the design of refined conceptual models. It also points to the big challenges in the accurate forecasting of mountain-wave-induced low-level turbulence, which is of great relevance for aircraft navigating over mountainous terrain.

Zusammenfassung

Atmosphärische Rotoren zählen zu den turbulentesten Strömungsphänomenen im Gebirge. Rotoren werden im Allgemeinen als turbulente, bodennahe Wirbelwalzen an der windabgewandten Seite eines Gebirgsrückens beschrieben, welche zusammen mit Gebirgswellen großer Amplitude entstehen können. Durch mehrere große Messkampagnen und hochauflösende numerische Simulationen ist die Physik der Rotorbildung heute relativ gut geklärt. Die traditionelle, zeitlich gemittelte Beschreibung der Rotorströmung ist jedoch eine stark vereinfachende. In ihr unberücksichtigt sind die zeitliche Variabilität der Anströmbedingungen an der Luvseite eines Gebirges und die dynamischen und thermischen Eigenschaften der Atmosphäre an seiner Leeseite. Zudem sind quantitative Messungen der Turbulenzintensität und ihrer zeitlichen Veränderlichkeit im Rotorinneren rar.

Das Ziel der vorliegenden Arbeit ist es zum einen, eine Beobachtungsmethode zu entwickeln, die die quantitative Messung der räumlichen Verteilung und Intensität der Rotorturbulenz erlaubt, zum anderen, die zeitliche Veränderlichkeit der Rotorströmung und deren räumliche Struktur im komplexen Gelände besser zu verstehen. Zu diesem Zwecke werden Beobachtungen von Gebirgswellen und Rotoren analysiert und mittels numerischer Simulationen nachgestellt. Die Beobachtungsdaten stammen von zwei Feldkampagnen über den Medicine Bow Mountains in Wyoming und über der Sierra Nevada und dem Owens Valley in Kalifornien aus dem Jahr 2006.

Flugzeuggetragene in situ- und Dopplerradar-Messungen über den Medicine Bow Mountains erlauben einen detaillierten Einblick in die turbulente Rotorströmung. Eine Methode zur Bestimmung der Turbulenzintensität aus den Radardaten wird entwickelt und es wird gezeigt, dass quantitative Aussagen über die bodennahe Turbulenz innerhalb akzeptabler Unsicherheitsgrenzen möglich sind. Die Ergebnisse ermöglichen eine unmittelbare, zweidimensionale Darstellung der Turbulenzintensität im Rotorinneren.

Numerische Simulationen zweier Fälle von Rotorbildung im Lee der Medicine Bow Mountains zeigen, dass die beobachtete rasche zeitliche Entwicklung der Rotoren durch das kurzzeitige Brechen von hydrostatischen Gebirgswellen großer Amplitude verursacht wird. Das Einsetzen und Abklingen des Wellenbrechens ist eng verbunden mit dem Vorbeiziehen einer kurzwelligen synoptischen Störung, welche das luvseitige vertikale Wind- und Stabilitätsprofil verändert und zu einem Wechsel der leeseitigen Strömungsregime führt.

Um atmosphärische Rotoren in verschiedenartiger Topografie besser zu verstehen, werden mehrere Fälle erhöhter Gebirgswellenaktivität und damit einhergehender bodennaher Turbulenz über der Sierra Nevada und im Owens Valley untersucht. Die Fallstudien werfen neues Licht auf die komplexen Wechselwirkungen zwischen den Strömungen über den Gebirgsrücken und jenen entlang des Tales und zeigen damit den wesentlichen Einfluss der atmosphärischen Prozesse im Tal auf die Rotorströmung auf. Vier typische Szenarien der Turbulenzbildung werden aus den Beobachtungen gewonnen. Diese ermöglichen Erweiterungen des traditionellen Rotorbegriffs, welche für ein tiefes, langgezogenes Tal Gültigkeit besitzen.

Die Arbeit trägt durch die neue flugzeuggetragene Beobachtungsmethode und die Entwicklung verfeinerter konzeptueller Modelle zur realistischeren Beschreibung der Rotorströmung bei. Sie zeigt auch die großen Herausforderungen bei der genauen Vorhersage von gebirgswelleninduzierter bodennaher Turbulenz auf, welche insbesondere für den Flugverkehr in Gebirgsnähe von großer Relevanz ist.

“Like Cerberus at the gate of Hades, the rotor guards the gates to the smooth wave and a flying intruder venturing unsuspectingly into his range is first clubbed by an unbelievable turbulence, then dumped in a severe downdraft and eventually will be happy to beat a hasty retreat.”

Joachim Kuettner (1959)

Contents

Abstract	i
Zusammenfassung	iii
Introduction	1
1 Mountain-wave and rotor research	5
1.1 Past research on mountain waves and rotors	5
1.1.1 Early observations of wave and rotor clouds	5
1.1.2 Field experiments and theoretical advancements	7
1.1.3 Idealized conceptual models	9
1.1.4 Progress in the understanding of non-linear mountain flows . .	11
1.1.5 Impact of the atmospheric boundary layer on mountain waves .	14
1.1.6 Use of instrumented aircraft for the study of mountain flows . .	14
1.1.7 Reviving interest in rotors	16
1.2 Recent advances in mountain-wave and rotor research	17
1.2.1 Theory and high-resolution numerical simulation of wave-induced boundary-layer separation and rotors	20
1.2.2 The Terrain-induced Rotor Experiment (T-REX)	22
1.3 Scope of this work	27
1.3.1 Open questions	27
2 Wave-induced boundary-layer separation in the lee of the Medicine Bow Mountains: numerical modelling	31
2.1 Introduction	35
2.2 Numerical simulations	38
2.3 Analysis of model results: 26 January	44
2.4 Analysis of model results: 5 February	53
2.5 Summary and conclusions	56
2.6 References	58
2.7 Figures	65

3	Turbulence in breaking mountain waves and atmospheric rotors estimated from airborne in situ and Doppler radar measurements	81
3.1	Introduction	83
3.2	Field campaign and airborne instruments	84
3.3	Quantitative turbulence estimates from airborne in situ and Doppler radar measurements	85
3.4	Case studies	87
3.5	Turbulence intensities in mountain-induced turbulent processes	89
3.6	Summary and conclusions	90
3.7	Appendices	91
3.8	References	92
3.9	Tables	94
3.10	Figures	95
4	Atmospheric rotors and severe turbulence in a deep valley	109
4.1	Introduction	113
4.2	The Terrain-induced Rotor Experiment	115
4.3	Observations	118
4.4	Discussion	129
4.5	Summary and conclusions	136
4.6	References	138
4.7	Tables	148
4.8	Figures	154
5	Conclusions	173
5.1	Summary and discussion	173
5.1.1	Quantitative estimation of turbulence intensity in complex mountain flows	173
5.1.2	Transient mountain waves, wave breaking, and rotors	175
5.1.3	Predictability of mountain-wave-induced turbulence	179
5.1.4	Atmospheric rotors in a deep valley	180
5.2	Concluding remarks	182
5.3	Outlook	183
	Bibliography	185
	Acronyms and abbreviations	199
	Acknowledgements	201
	Curriculum vitae	203

Introduction

Mountains exert a great influence on the atmosphere. Their presence enhances the amount of rainfall on their windward slopes, accelerates the flow at their flanks, promotes the genesis of weather systems, or produces severe winds in their lee. People living in the vicinity of mountains are familiar with their impact on the local weather and the associated implications for their lives. Hikers depend on good mountain weather for their tours, tourism entrepreneurs rely on sufficient snowfall in the winter season, air-traffic controllers know how to cope with periods of foehn windstorm at Alpine airports, and energy suppliers benefit from enhanced wind speeds at the flanks of the Alps for wind power production.

The impact of mountain-induced atmospheric phenomena on social and economic matters is one of the greatest motivations for their scientific description. The field of mountain meteorology today represents a very active branch of the atmospheric sciences. This is evidenced by a large number of textbooks overviewing the subject and scholarly books reviewing recent advances in the field¹, as well as regular specialized scientific conferences. Through scientific progress, mountain weather forecasts have improved significantly over the past decades. The accurate prediction of precipitation, severe winds, or lightning in mountainous terrain, however, remains a great challenge due to the multitude of physical processes and the wide range of spatial and temporal scales that need to be faithfully represented in numerical weather prediction models.

One of the most intriguing atmospheric phenomena related to the airflow over mountains is the generation of atmospheric gravity waves. When the air flows over a mountain ridge, internal waves can be excited owing to the vertical layering of air density. Unlike waves travelling along the free surface of a body of water, these waves can propagate both in the horizontal and vertical directions. For high mountains and suitable environmental conditions, in terms of the vertical profile of wind speed and air density, vertical wave deflections of the initially undisturbed air parcels of one kilometre or more can occur. Mountain waves of such amplitude are often associated with impressive formations of lenticular clouds – a popular object among nature photographers.²

Large-amplitude mountain waves may also cause more vigorous perturbations in the atmosphere. As mountain waves propagate upward they can steepen, overturn, and break – in

¹ See, for example, *Mountain Meteorology. Fundamentals and Applications* by Whiteman (2000) and *Mountain Weather Research and Forecasting* by Chow et al. (2013).

² A collection of photographs of mountain-wave clouds can be found on the [website](#) of the *Cloud Appreciation Society*.

a similar manner to water waves running up a beach – thereby causing turbulent mixing of the atmospheric flow. The breaking of mountain waves also favours the generation of downslope windstorms. These shooting flows form over the lee of a mountain ridge and underneath a wave-breaking region and can lead to severe lee-side winds, sometimes reaching speeds of 150 kilometres per hour or more. Downslope windstorms are known in various regions around the world. Prominent examples include the severe occurrences of *foehn* in the Alps, *bora* over the Dinaric Alps at the eastern coast of the Adriatic Sea, *chinook* in the lee of the Rocky Mountains, or *Santa Ana winds* in southern California.

Among the most energetic atmospheric disturbances associated with mountain waves are *atmospheric rotors*. The formation of rotors is tightly linked to the pressure forcings that mountain waves exert on the low-level flow in the lee of a mountain. These act to accelerate the flow under the downwelling wave branches but decelerate it under the upwelling ones. If the wave amplitude and the resulting pressure perturbations are sufficiently large, the lee-side flow may be brought to a standstill and may be forced to detach from the surface (Figure 1a). Once the near-surface flow has separated, a turbulent rotor circulation downwind of the mountain ridge forms, rotating around a horizontal axis parallel to the ridge line. The rotor turbulent zones can reach a vertical extent well beyond the mountaintop height (Figure 1b).

Rotors and intense small-scale perturbations embedded in them pose a significant aeronautical hazard. Sailplane pilots seeking the upwelling branches of mountain waves to reach spectacular altitudes are aware of the violent low-level turbulence they need to overcome before entering the smooth wave updraught. Vertical gusts on the order of $\pm 10 \text{ m s}^{-1}$ or accelerations of 5 g on aircraft penetrating into the rotor zone are not uncommon. Numerous aviation incidents and accidents have been related to encounters of commercial and general aviation aircraft with rotors. Due to their potential threats, special attention is paid to mountain waves and rotors in aviation guidelines and handbooks for pilots³. The popular literature and features on TV and on the web⁴ convey their impacts to a broader audience.

Fascination with the coupled system of the smooth mountain wave and the turbulent rotor and its threat for aviation have been among the primary drivers of scientific research on the subject. Since the 1930s, a number of meteorological field campaigns have been devoted to their study. The most recent of these investigations was the Terrain-Induced Rotor Experiment (T-REX), organized in 2006 in the southern Sierra Nevada and Owens Valley, California. The main objective of T-REX was to further our understanding of the interaction between mountain waves, the atmospheric boundary layer and rotors. Among other aspects, the experiment aimed at new observational insights into the small-scale turbulent structure of rotors and improvements in the high-resolution numerical modelling of the rotor flow. A vast set of meteorological instruments was deployed in the field, including ground-based scanning lidars and research aircraft equipped with modern on-board instrumentation and radars.

³ See, for example, *Hazardous Mountain Winds and Their Visual Indicators* by Carney et al. (1997), or *Turbulence: A New Perspective for Pilots* by Lester (1993).

⁴ See, for example, *Exploring the Monster. Mountain Lee Waves: The Aerial Elevator* by Whelan (2000), or the OSTIV Mountain Wave Project [website](#).



Photograph by R. Symons



Photograph by T. Henderson

Figure 1: Photographs over Owens Valley in the lee of the southern Sierra Nevada, California, taken during the Sierra Wave Project in the 1950s. The view in both photographs is from the north with the cross-mountain flow coming from the right. (a) Near-surface blowing dust and crest-level cumulus clouds, indicative of flow separation and rotor formation. (b) A severe rotor with an almost vertical wall of clouds topped by lenticular wave clouds, extending considerably beyond the mountaintop height. Reproduced from Doyle and Durran (2004).

Through the scientific studies excited by T-REX, significant progress in the understanding of mountain waves and associated low-level turbulence has been made in the past fifteen years. Nevertheless, a few open questions remain. For example, until recently, the measurement of turbulence intensity in rotors relied on research aircraft penetrating into the rotor zones – a hazardous undertaking. Also, conceptual models of the coupled mountain-wave and rotor flow in the lee of an isolated mountain range exist today, but they largely lack information on the rotor temporal evolution and they do not account for the possible influence of the downstream atmospheric environment or secondary topography.

The present work contributes to a more realistic description of the rotor flow, its spatial structure and temporal behaviour in different topographic environments. A new approach is proposed to deriving quantitative estimates of atmospheric turbulence in mountainous terrain from airborne remote-sensing measurements. The rapid temporal evolution of observed cases of mountain-wave breaking and rotors is studied using high-resolution numerical simulation. Finally, the onset and evolution of rotors and similar turbulent flow patterns in a deep valley are investigated.

The remainder of this work is organized as follows. In Chapter 1, a review of past and present research on mountain waves and rotors is given and open research questions are presented. In Chapters 2–4, the open questions are addressed in three journal contributions, including the numerical simulation of two transient rotor events, the analysis of mountain-induced turbulence from airborne Doppler radar, and the systematic comparison of rotor-like turbulent structures in Owens Valley. Results are summarized and discussed and final conclusions are drawn in Chapter 5.

Chapter 1

Mountain-wave and rotor research

The purpose of this chapter is to provide a review of the rich literature on mountain waves, mountain-wave-induced turbulent phenomena, and the airborne measurement of atmospheric turbulence. In Sections 1.1 and 1.2, the scientific findings on which this work relies are presented in a chronological manner, starting with the early descriptions of wave and rotor clouds and ending with recent progress in the understanding of the fine-scale rotor structure. Open research questions are formulated in Section 1.3.

1.1 Past research on mountain waves and rotors

1.1.1 Early observations of wave and rotor clouds

For a long time preceding the first scientific studies of mountain waves, people living in the vicinity of mountains must have been struck at the view of impressive cloud formations, sometimes lingering in the lee of hills or mountain ridges for hours without notable motion, amidst periods of strong and gusty winds at the surface. Short notes on sightings of these standing clouds started to appear in the scientific literature during the second half of the 19th century, at the time of the foundation of the first meteorological journals.¹ Mohorovičić (1889) and Marriott (1886, 1889) seem to have been the first to conduct systematic studies of such clouds in southeastern Europe and on the British Isles (Grubišić and Orlić 2007). Andrija Mohorovičić, a professor at the Royal Nautical School in Bakar, made observations of a special type of stationary cumulus clouds in Bakar Bay on the northern Adriatic coast of Croatia during bora wind events. William Marriott had been requested by the Royal Meteorological Society to enquire the origin of the *Helm Bar*, a horizontal, slim cloud bar occasionally appearing downwind of Cross Fell (the highest mountain of the Pennines, northern England) during episodes of the *Helm Wind*. The sketches of the flow in and around these clouds that emerged from Mohorovičić's and Marriott's work (Fig. 1.1) were influenced by the visual appearance of rotation at the stationary cloud tops, which seemed to imply the presence

¹ The *Meteorologische Zeitschrift* of the Austrian Meteorological Society and the *Quarterly Journal* of the British Royal Meteorological Society were first issued in 1866 and 1873, respectively.

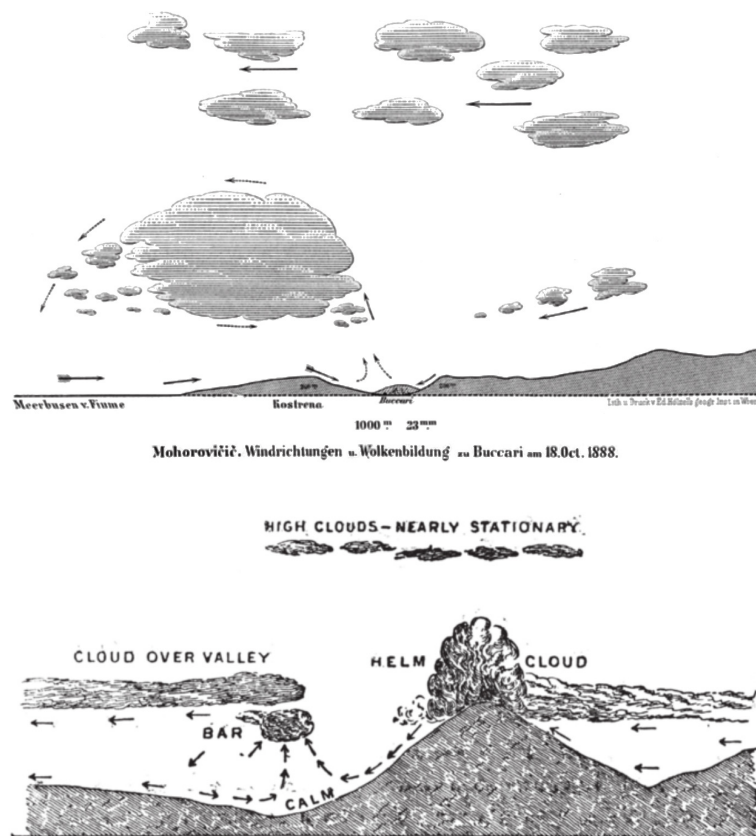


Figure 1.1: Historic depictions of the rotor flow. Upper panel: wind directions and cloud formation over the Bakar Bay during bora wind episode on 18 October 1888 (reproduced from Mohorovičić 1889). Lower panel, the Helm Cloud and Helm Bar and wind vectors during periods of the Helm Wind at Cross Fell, northern England (reproduced from Marriott 1889).

of a counter-current underneath them against the ambient wind. Even if marked by a few elements of speculative character, Mohorovičić’s and Marriott’s conceptual drawings are today regarded as the pioneering contributions to the scientific research on mountain-wave-induced rotors.

Numerous reports of stationary clouds, together with a variety of explanations of their origin, were given over the following decades (e.g. Koschmieder 1920; Koch and Wegener 1930). The increase in popularity of the sport of gliding in Central Europe after World War I offered new perspectives on the phenomenon. In 1933, sailplane pilot Wolf Hirth (1933) reported encounters with violently turbulent near-surface winds underneath unexpectedly smooth and sustained updraughts in the lee of the Riesengebirge, Sudetes Mountains², a mountain ridge well known for its stationary *Moazagotl* cloud. Hirth’s and other pilots’ reports sparked the interest of fellow glider pilot Joachim Kuettnner, then aspiring atmospheric scientist. In spring 1937, Kuettnner and Hirth coordinated measurements by 25 instrumented sailplanes with the aim of characterizing the three-dimensional structure of the *Moazagotl* wave. In his

² situated at today’s borders between Poland, Czech Republic, and Germany

seminal papers (Küttner 1938, 1939), Kuettner summarized previous observations of similar terrain-induced clouds in different regions of the world and detailed the characteristics of *foehn* episodes associated with their occurrence. His careful analysis of the 1937 sailplane measurements led him to the conclusion that the observed phenomenon corresponded indeed to a wave-like oscillation in the atmospheric flow (a question then yet to be answered) and that stationary wave clouds were simply the result of the lifting of moist air to its level of condensation in the upwelling branches of the waves. Kuettner finally commented on the origin of the lines of cumulus clouds, frequently occurring under the crests of strong waves. The fragmented character of these clouds and the apparent rotation at their tops suggested that they were part of a violent circulation extending from the surface to the cloud tops, inspiring Kuettner to give them the name *rotor clouds*.

1.1.2 Field experiments and theoretical advancements

In the following years, the interest in mountain waves and related phenomena grew in a broader scientific community (e.g., Queney 1936a,b; Hoinkes 1942; Manley 1945). From the 1950s to the 1970s, several field campaigns devoted to the study of mountain waves were organized in the U.S. and Europe. The Sierra Wave Project (SWP) and the Mountain Wave-Jet Stream Project (JSP, Holmboe and Klieforth 1957; Grubišić and Lewis 2004) were conducted in the early 1950s over the southern Sierra Nevada and Owens Valley, a region famous for its wave clouds (the *Bishop-Wave* phenomenon, Colson 1952). A large number of scientists, glider pilots, and U.S. military staff were involved in the experiment. Comprehensive measurements by upstream radiosondes, surface stations in Owens Valley and instrumented sailplanes and powered aircraft were made during several months of field activities, allowing to document a few dozen mountain-wave cases. The SWP and JSP are today considered as important predecessors of modern mesoscale field experiments (Grubišić and Lewis 2004).

Other experiments in Europe and the U.S. with a similar focus followed, the most noteworthy of which are the studies of lee waves over the French Alps in the late 1950s (Gerbiere and Berenger 1961) and the Colorado Lee Wave Program (CLWP) over the Rocky Mountains in the 1960s and 1970s (Kuettner and Lilly 1968; Lilly and Toutenhoofd 1969). In the latter programme, specially instrumented research aircraft by U.S. and Canadian agencies³ were used to obtain estimates of the wave length and amplitude of lee waves and the momentum fluxes and low-level turbulence associated with them at various levels across the mountains (e.g., Vergeiner and Lilly 1970; Lilly 1971; Lester and Fingerhut 1974).

Stimulated by the growing quantitative evidence of mountain waves, important steps ahead in their theoretical description were made from the 1940s to the 1960s. Queney et al. (1960) and Grubišić and Lewis (2004) deliver a comprehensive review of these, of which a brief account is given here.

Steady-state solutions for small-amplitude upward-propagating mountain waves in flow

³ The aircraft were deployed under the auspices of the recently established National Center for Atmospheric Research (NCAR), founded in 1960.

over two-dimensional obstacles had first been derived by Queney (1936a,b, 1947) and Lyra (1940, 1943). These solutions, obtained for highly idealized inflow profiles of constant wind speed and stratification, were soon extended to account for two-layer and multi-layer atmospheres (Scorer 1949; Palm 1955), permitting partial wave reflection on the interface between two layers and consequently the formation of horizontally propagating but vertically trapped lee waves.

Even though the above authors laid the foundations of mountain-wave theory, the commonality of their *perturbation theories*, describing only linear deviations from the mean state, called for further improvement. In fact, linear theories would not allow to model or even predict the large-amplitude mountain waves observed, for example, over the Sierra Nevada. Important contributions to the solution of this problem were made in a series of papers by Long (1953a,b, 1954, 1955). Long found that the steady-state non-linear mountain flow can be described by a simple linear equation of the same form as that analysed earlier by Lyra (1943) and Queney (1947) for a special class of vertically uniform upstream profiles. His approach, known today as *Long's model*, “stands as one of the cornerstones of the subject” (Smith 1979) for the remarkable agreement of his theoretical predictions of finite-amplitude waves with laboratory experiments of continuously stratified fluids (Long 1955). In the latter, Long observed turbulent stagnant regions underneath the lee-wave crests, which he attributed to the effect of lee-side flow separation. Scorer and Klieforth (1959) adopted Long's model to the atmosphere allowing for vertically varying stratification and linked their results to the newly available case studies from the Sierra Wave Project.

In the early theoretical works on mountain waves, rotors almost always received considerable attention (e.g., Lyra 1943; Scorer 1949; Scorer and Klieforth 1959). At that time, obtaining a better idea of the origin of rotors was not regarded merely as a beneficial side result, but became a major motivator for scientists seeking to develop realistic descriptions of large-amplitude mountain waves. In addition, a few studies focused explicitly on rotors (e.g., Queney 1955; Scorer 1955; Kuettner 1959). Towards the end of the 1950s, a number of possible explanations of rotors existed, of which Kuettner (1959) listed six prominent ones. Two of them deserve special attention.

Lyra (1943) had noted that pressure perturbations induced by lee waves and resultant adverse pressure gradient forces may decelerate the lee-side low-level flow sufficiently to bring it to a standstill. For reasons of continuity, the decelerated flow may be forced to detach from the ground, be lifted upwards and subsequently form a closed circulation at the location of surface pressure maxima below lee-wave crests. Lyra concluded that rotors were therefore “merely a concomitant phenomenon of the lee-wave flow”. Taking note of Lyra's description, Scorer (1949) referred to this process as *boundary-layer separation*, a process which he later described on a broader basis, going beyond purely wave-induced flow separation (Scorer 1955).

The second explanation of rotors was motivated by the similarity of observations of strong downslope winds in the lee of the Sierra Nevada and of foehn in the Central Alps (Knox 1952, 1954; Schweitzer 1952) with laboratory experiments of two-layer hydraulic flows (e.g., Long

1953a, 1954) . Under conditions in which the lower and mid-tropospheric layers are decoupled by a strong temperature inversion or by significant directional wind shear between them, the flow may be described in the framework of hydraulic theory. According to this concept, gravity accelerates the airflow over the lee slope of a mountain range to a supercritical *shooting* flow. At some point downstream of the obstacle, however, the flow switches back to subcritical in an internal hydraulic jump, in which streamlines shoot vertically up (equivalent to the separating flow in Lyra's explanation) and can extend considerably above the height of the mountain. A considerable portion of the kinetic energy acquired by the shooting flow is dissipated in the internal jump through turbulent mixing, a possible origin of the severe rotor turbulence.

1.1.3 Idealized conceptual models

With the completion of several field experiments and advancements in mountain-wave theory, a good level of understanding of the origin of severe turbulence beneath large-amplitude lee waves was reached by the mid-seventies. From this period, schematic depictions of the mountain wave-rotor system emerged which have since then shaped the ideas about rotors. Until today, they are featured in mountain meteorology textbooks as well as aviation handbooks (e.g., Whiteman 2000; Lester 1993; WMO 1993).

Two idealized cross-sections of the rotor flow, reproduced from Lester and Fingerhut (1974), are shown in Fig. 1.2. The *lee-wave-type* rotor is depicted in Fig. 1.2a. In the lee of the mountain range, a large-amplitude lee wave forms in the laminar mid-tropospheric flow. The lee-wave-induced pressure perturbations decelerate the boundary-layer flow and force it to separate from the mountain lee slope. A low-level rotor circulation forms, rotating around a horizontal axis parallel to the mountain range. Downwind of the separation point, the flow recirculates back toward the mountain. The top of the rotor is often capped by a roll or rotor cloud. Turbulence, as experienced by aircraft penetrating into the rotor region, is severe underneath the leading wave updraught (vertical gusts exceeding $10\text{--}15\text{ m s}^{-1}$), while it is somewhat weaker and more diffuse but still strong beneath the wave downdraught. The vertical extent of lee-wave rotors is usually that of the upstream mountain ridge. Their horizontal dimension depends on the lee wave's length (typically on the order of $10\text{--}30\text{ km}$). If a train of lee waves is present, several rotors can exist under successive lee-wave crests, evident as several parallel lines of cumulus clouds downwind of the mountain range (Kuettner 1959).

The *hydraulic-jump-type* rotor is shown in Fig. 1.2b. It is distinguished by its vertical extent, sometimes reaching twice the height of the mountain crest and more. To the visual observer, this rotor type is evident by an almost vertical wall of cloud located a significant distance downstream of the mountain range (cf. Fig. 1, right panel). Uttermost turbulence is expected in rotors of this type, however, quantitative aircraft measurements are almost non-existent – for good reason. During the JSP of 1955, Lawrence Edgar's sailplane was destroyed in the leading edge of a jump-type rotor, as his plane was exposed to accelerations in excess of 10 g .⁴ Decades later, Kuettner and Hertenstein (2002) still concluded that it seems

⁴ The pilot survived thanks to his parachute.

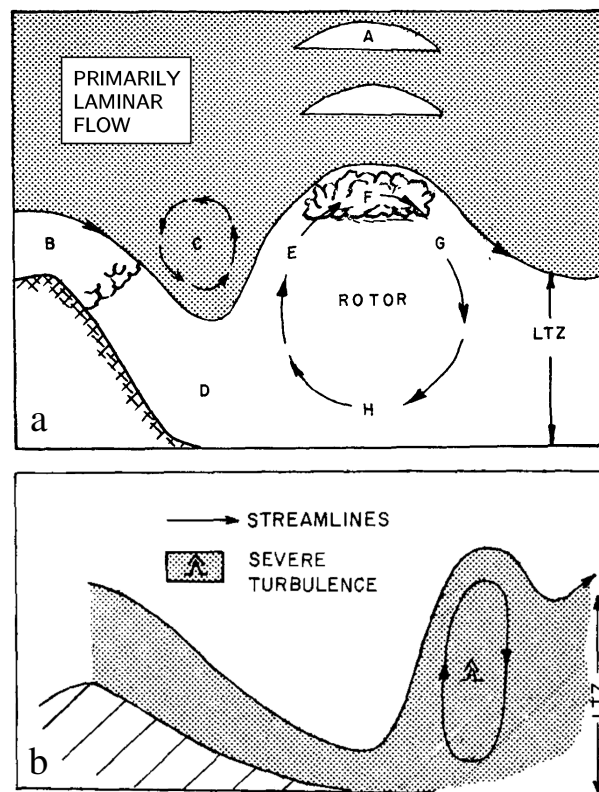


Figure 1.2: Schematic representations of (a) a lee-wave rotor and (b) a hydraulic-jump-type rotor. (a) The *low-level turbulence zone* (LTZ), reproduced from Lester and Fingerhut (1974, their Fig. 1): “Idealized cross section of the LTZ: A, lenticular clouds; B, cap cloud; C, reversed rotor; D, region of gusty surface winds; E, region of strong updraught and extreme turbulence; F, rotor or roll cloud; G, region of strong downdraught and severe turbulence; H, lower portion of rotor circulation and occasionally reversed surface winds.” (b) Hydraulic airflow over a mountain ridge: supercritical downslope flow over the lee slope and hydraulic jump-like adjustment to the subcritical regime further downwind, with a large rotor forming underneath the jump. Reproduced from Lester and Fingerhut (1974, their Fig. 10). (Copyright 1974 American Meteorological Society. Used with permission.)

“unlikely that aircraft can be designed strong enough to withstand the excessive loads of a fully developed [jump-type] rotor” and that “this rare rotor type should be avoided the same way boats avoid the Niagara Falls”.

Beyond the conceptual models of rotors, a multitude of other findings emerged from the observational and theoretical studies, not all of which are reflected in the idealized descriptions of the rotor flow. In the following, the most relevant results are summarized in loose order.

Vergeiner and Lilly (1970), among others, recognized that the two idealized types of lee flow patterns only rarely occurred in pure form, referring to a third type as “irregular three-dimensional flow structure”. Also, changes in the flow regime from jump-type to wave-type may happen within one hour or less due to the sensitivity of the flow patterns to small changes in the upstream conditions. Another contribution to the temporal variability of wave patterns was the diurnal heating cycle. Lee waves were frequently observed to reach their largest amplitude in the afternoon (Kuettner 1959).

Early on, the rotor clouds had been noted for their appearance of rotation (Section 1.1.1). However, several authors (e.g., Scorer 1955) remarked that the apparent rotation may be attributed to the large vertical wind shear, present during most of the cloud occurrences. They concluded that the presence of a counter-current, closing the (idealized) rotor circulation underneath these clouds may not be a strict requirement for rotor formation. Indeed, near-surface reversed flow underneath the rotor clouds was only observed for the largest-amplitude waves. Nevertheless, the existence of a low-level recirculation was adopted as a criterion in the mathematical description of rotors (e.g., Scorer and Klieforth 1959), giving additional weight to the concept of a closed rotor circulation.

Observations of moderate to severe turbulence were not restricted to low levels on the lee side of mountain ranges. Occasionally, strong clear-air turbulence was detected in the upper part of the troposphere. It was hypothesized that this secondary turbulence zone owes its origin to the interaction of upward-propagating mountain waves with the upper-level jet (Holmboe and Klieforth 1957).

1.1.4 Progress in the understanding of non-linear mountain flows

While the attention of the scientific community shifted away from rotors after the 1970s, progress in the research on topographically forced flows continued. A detailed review of this progress is beyond the scope of this introductory chapter and seems unnecessary in view of the large number of review articles (e.g., Smith 1979; Durran 1990, 2003a,b; Jackson et al. 2013) and book chapters (e.g., Baines 1995; Whiteman 2000; Nappo 2002; Lin 2007) on the subject. The aim of this and the following subsections is thus to provide the basics of *non-linear* mountain-wave phenomena, relevant for the understanding of wave-induced turbulence and rotors, and to highlight other relevant scientific findings and technical developments prior to the 2000s. Note that, we deliberately omit the discussion of air flow over and around isolated three-dimensional mountains (see Smith 1989, for a review), since three-dimensional effects are only of secondary importance in the studies presented in Chapters 2–4.

Control parameters governing the flow over mountains in two dimensions

The results by Long (1953b, 1955) serve as the starting point for the exploration of the full spectrum of non-linear mountain flow phenomena, such as upstream blocking, wave breaking, and high lee-side winds. Our discussion follows in part that by Lin (2007, Chapter 5).

For the case of continuously stratified flow over a two-dimensional bell-shaped mountain, three non-dimensional parameters controlling the flow emerged from Long's and subsequent works: the non-dimensional mountain height Nh/U , the mountain steepness h/a , and the non-dimensional mountain width Na/U , where N , U , h , and a denote, respectively, the upstream stability (buoyancy frequency), upstream wind speed, mountain height, and mountain half width. The three parameters can be reduced to two independent parameters, e.g., Nh/U and Na/U . For hydrostatic flow ($Na/U \gg 1$), the non-dimensional mountain height becomes the primary control parameter.

Nh/U is a measure of the degree of non-linearity of the flow. For a small non-dimensional mountain height ($Nh/U \lesssim 0.3$), flow perturbations remain small and can be approximately described using linear theory. Upon increase of the non-dimensional mountain height, streamlines in the vertically propagating mountain wave gradually steepen and become vertical at a critical limit. For the hydrostatic solution of Long's model with a two-dimensional bell-shaped mountain, this limit is reached at a critical value of $Nh/U = 0.85$ (Miles and Huppert 1969). Upon further increase of Nh/U , streamlines overturn, forming a region above the mountain where denser fluid is temporarily placed above lighter fluid. Such a configuration is statically unstable and cannot be maintained for long. *Wave breaking* – strong vertical mixing, turbulent dissipation, and flow stagnation – ensues.

Gravity-wave breaking and downslope windstorms

The turbulent breakdown of internal gravity waves has been the focus of numerous investigations. The process has been studied theoretically, with numerical simulation and laboratory experiments, and has been observed in the real atmosphere using remote sensors and research aircraft (e.g., Staquet and Sommeria 2002; Dörnbrack 1998; Eiff and Bonneton 2000; Ralph et al. 1997b; Jiang and Doyle 2004). Interest in gravity-wave breaking results mainly from two aspects. Even when the tropospheric flow is linear, mountain waves tend to amplify and break as they propagate upwards into the stratosphere due to the decrease of air density with height. The energy dissipation and flow stagnation in the upper-level breaking region acts as a net decelerative force on the mean atmospheric flow, which constitutes a sink of horizontal momentum in the large-scale atmospheric circulation that needs to be accounted for in global numerical weather prediction models (Fritts and Alexander 2003; Kim et al. 2003). Another important aspect of wave breaking is the threat that the clear-air turbulence associated with it poses to aviation (Sharman et al. 2012).

In the present work, the effect of tropospheric wave breaking on the low-level flow is of particular interest. Low-level non-linear phenomena concurring with wave breaking include upstream blocking, downslope windstorms and internal hydraulic jumps. If an upward-propagating mountain wave breaks in the troposphere, a stagnant region forms above the mountain which acts as a critical level to stationary gravity waves, impeding further upward propagation (Bretherton 1969). Underneath the stagnant region, the flow is accelerated down the lee slope and attains supercritical speed, sometimes reaching hurricane strength (32 m s^{-1} , or 115 km h^{-1}). Farther downstream, the transition to the ambient subcritical regime often takes the form of an internal hydraulic jump.

Downslope windstorms occur in various places around the world. Well-known examples are the severe occurrences of *chinook* in the lee of the Rocky Mountains, *foehn* in the Alps, *bora* in the Dinaric Alps, and *Santa Ana winds* in southern California. Research on downslope windstorms has been stimulated by the observation of a few exceptionally strong cases, some of which were documented using instrumented aircraft. The best-known of these cases is the near-legendary 11 January 1972 Boulder windstorm (Lilly and Zipser 1972; Lilly 1978). During

this event, surface wind gusts as high as 60 m s^{-1} were reported, producing severe damage in the Boulder area. The analysis of aircraft data by Lilly (1978) showed the presence of a wave system of exceptionally large amplitude during the windstorm, with significant turbulence at mid-tropospheric levels indicative of wave breaking. Other well-known downslope windstorm events include those documented by the first aircraft observations of bora over the Dinaric Alps during the Alpine Experiment in 1982 (ALPEX, Smith 1987).

A number of theoretical and numerical studies attempted to elucidate the dynamics of the observed windstorms (cf. Durran 1990; Lin 2007). Two main lines of thought on their formation emerged: *resonant amplification theory* and *hydraulic theory*. Clark and Peltier (1984) suggested that the critical level induced by wave breaking (a *wave-* or *self-induced* critical level) acts as an internal boundary in the mountain flow, (over-)reflecting upward propagating waves back toward the mountain. Such a configuration leads to the resonant amplification of wave perturbations and subsequently to a strongly accelerated lee-side flow. Smith (1985) proposed the concept of the *dividing streamline* encompassing the stagnant region of neutral stability, below which the low-level flow can be described with hydraulic theory using a Bernoulli equation. Some discrepancies exist between the two concepts, which have been discussed extensively in the literature (see, e.g., Durran 1990, and references therein). Both approaches, however, confirm the role of a stagnant layer above the mountain as a key element for the generation of severe lee-side winds. In total, three types of conditions were found to promote downslope windstorms: (i) the generation of a *self-induced critical level* through wave breaking, (ii) *non-uniform vertical layering* of upstream wind speed and stability, such as an elevated inversion at or near the mountaintop, and (iii) a *mean-state critical level*, provided by ambient flow reversal or directional wind shear, at which waves break and dissipate. The essence of the three types of conditions is that all of them lead to the transition from wave-like behaviour over the upstream mountain slope to a non-wave-like regime in the lee (Durran 2003a).

In the above investigations, Nh/U was used as the prime parameter allowing to assess the susceptibility of the atmosphere to non-linear phenomena. For layered atmospheric flows, however, a single value of Nh/U , representative of the whole tropospheric column, cannot normally be provided. Instead, the *local* non-linearity parameter (NLP) $N(z)h/U(z)$ can be computed from measured or numerically modelled soundings (Durran 2003b). For arbitrary background profiles of wind and stability, non-linear effects can become significant at rather small values of the NLP (Durran 1986) and no distinct critical value for which streamlines will start to overturn seems to exist. Nevertheless, a value of $N(z)h/U(z) \geq 1$ is almost always a reliable indicator of wave overturning. Recently, the local NLP has been used with remarkable success in the analysis of severe bora episodes along the Adriatic coast of Croatia, where it helped to explain periods with and without pulsations in near-surface bora winds (Belušić et al. 2004, 2007; Grisogono and Belušić 2009).

1.1.5 Impact of the atmospheric boundary layer on mountain waves

Another important aspect of topographically forced flows is the atmospheric boundary layer. Richard et al. (1989) were perhaps the first to recognize that mountain-wave amplitudes tend to be reduced in the presence of a boundary layer. Their work was extended to elongated mountain ridges in three dimensions by Ólafsson and Bougeault (1997), who accounted for the effects of both the boundary layer and the Coriolis force. Numerical simulations showed that, in the presence of surface friction, wave breaking was greatly suppressed well beyond the expected critical values of Nh/U .

A new observational perspective on mountain waves was gained from two field campaigns in Europe in the middle and late 1990s: the Pyrénées Experiment (PYREX, Bougeault et al. 1997) and the Mesoscale Alpine Experiment (MAP, Bougeault et al. 2001; Smith et al. 2007). During both experiments, extensive use was made of research aircraft and new remote-sensing instruments, such as ground-based radar wind profilers and sodars and airborne lidars. A surprising result of the campaigns was that observed wave amplitudes were often significantly smaller than expected and wave breaking was only rarely found (Smith et al. 2007). Also, observations of trapped waves in the lee of the mountain ridges, although predicted from a suitable layering of the Scorer parameter, were often lacking (Smith et al. 2002). The complex three-dimensional nature of the underlying topography of the Pyrenees and the Alps, leading to a more rapid dispersion of energy by three-dimensional waves, and the interaction of mountain waves with the atmospheric boundary layer were suspected to be at the origin of these observations.

The findings from PYREX and MAP inspired a series of studies on the impact of atmospheric boundary layers on mountain waves and lee waves. Smith et al. (2002) investigated the generation and propagation of waves excited by Mont Blanc on 2 November 1999. They found that a stagnant layer, encompassing a significant region around the Mont Blanc massif, acted as an absorber of downward reflected waves, preventing the formation of a resonant wave cavity required for trapped lee waves. Idealized numerical simulations by Jiang et al. (2006) showed that, indeed, among different types of boundary layers (stable, convective, and stagnant), the stagnant layer in the lee of a mountain is most efficient in absorbing waves. Two primary wave absorption mechanisms were proposed: turbulent dissipation and critical-level absorption. On the other hand, simulations of untrapped mountain waves by the same authors (Jiang et al. 2008) showed that the influence of the boundary layer tends to shift wave patterns upstream and weaken them aloft, and that the boundary-layer effect is generally more pronounced over a 2D ridge than over a 3D hill. The numerical results were consolidated theoretically by Smith et al. (2006) and Smith (2007).

1.1.6 Use of instrumented aircraft for the study of mountain flows

In many of the above investigations, instrumented research aircraft played an important role in the study of mountain-meteorological phenomena. Airborne observing systems have become an indispensable tool for the quantitative characterization of mountain flows across a

Table 1.1: Selection of peer-reviewed articles on mountain-wave-induced turbulence relying on airborne turbulence measurements.

Authors	Title	Field Programme
Lilly (1971)	Observations of mountain-induced turbulence	CLWP
Lilly and Lester (1974)	Waves and turbulence in the stratosphere	CLWP
Lester and Fingerhut (1974)	Lower turbulent zones associated with mountain lee waves	CLWP
Lilly (1978)	A severe downslope windstorm and aircraft turbulence event induced by a mountain wave	CLWP
Marwitz and Dawson (1984)	Low-level airflow in southern Wyoming during wintertime	–
Smith (1987)	Aerial observations of the Yugoslavian bora	ALPEX
Attié et al. (1999)	Turbulence on the lee side of a mountain range: Aircraft observations during PYREX	PYREX
Lothon et al. (2003)	Experimental study of five föhn events during the Mesoscale Alpine Programme: From synoptic scale to turbulence	MAP
Jiang and Doyle (2004)	Gravity wave breaking over the Central Alps: Role of complex terrain	MAP
Darby and Poulos (2006)	The evolution of lee-wave-rotor activity in the lee of Pike’s Peak under the influence of a cold frontal passage: Implications for aircraft safety	–
Jiang et al. (2010)	Turbulence characteristics in an elevated shear layer over Owens Valley	T-REX
Woods and Smith (2011)	Short-wave signatures of stratospheric mountain wave breaking	T-REX
Večenaj et al. (2012)	Along-coast features of bora-related turbulence	MAP

wide range of spatial and temporal scales. Accurate meteorological measurements on aircraft have been made possible through refined airborne measurement techniques. These consist of suitable airborne instrumentation, capable of sampling atmospheric parameters such as wind, temperature, and humidity at high rate (25 Hz and greater), as well as sophisticated data-processing algorithms, allowing to remove non-meteorological components of the measurement due to the motion of the airborne platform (e.g., MacCready Jr. 1964; Brown et al. 1983; Lenschow 1986). More recently, the advent of the Global Positioning System (GPS) has contributed further to improving the accuracy of airborne measurements. A review of the state of the art of airborne measurements and their applications to environmental research has been given by Wendisch and Brenguier (2013).

Research aircraft have been successfully used for the study of mountain-wave-induced turbulent phenomena in the past. Noteworthy deployments before the 2000s include the CLWP (Lilly and Toutenhoofd 1969), ALPEX (Kuettner 1986), PYREX (Bougeault et al. 1997), and MAP (Bougeault et al. 2001). A selection of relevant studies that have resulted

from these and other campaigns is provided in Table 1.1.

Early on, aircraft measurements were used to determine the vertical fluxes of horizontal momentum due to waves (e.g., Lilly 1971; Lilly and Lester 1974) and quantify the drag that mountains exert on the atmosphere through the wave generation. Airborne *high-rate* measurements allowed to estimate turbulence intensity, for example, in the mid-level gravity wave breaking zone during the 1972 Boulder windstorm. For that event, the first attempt was made to evaluate the individual terms of the TKE budget of mountain-wave-induced turbulence (Lilly 1978). The derivation of meaningful estimates of wave momentum fluxes or turbulence from aircraft data, however, is not straightforward and requires a thorough treatment of the data series. A number of investigators have addressed these issues (e.g., Lenschow 1970; Lenschow et al. 1994) and work is still ongoing (e.g., Lothon et al. 2003; Weigel and Rotach 2004; Večenaj et al. 2012).

Despite their obvious advantages, the risks involved in navigating research aircraft in the vicinity of mountainous terrain should not be underestimated. This is illustrated by numerous reports of aircraft encounters with severe mountain-induced turbulence (e.g., Carney et al. 1997; Sharman et al. 2012). In this context, the development of powerful remote sensors and the possibility of operating them aboard aircraft seems promising. Airborne remote sensors were first used for the observation of mountain flows during PYREX and MAP (e.g., Smith et al. 2002; Gohm and Mayr 2004). Since then, remote-sensing techniques have improved and have led to countless applications to the airborne study of, for instance, the atmospheric boundary layer, terrain-induced flows, or thunderstorms (Banta et al. 2013). The estimation of atmospheric turbulence with these sensors is non-trivial (e.g., Lothon et al. 2005; Geerts et al. 2011) and is the subject of work in progress.

1.1.7 Reviving interest in rotors

The above sections attest to the continued advances in the understanding of non-linear mountain-flow phenomena since the beginning of the 1970s. These relied on the refined theoretical description of mountain waves, airborne observations, and, perhaps most importantly, the development of non-linear numerical models, including the parametrization of sub-grid-scale physical processes. Despite the availability of these new powerful tools, rotors remained out of scientific limelight for at least two decades – for a few reasons.

Firstly, with the origins of severe low-level turbulence regarded as sufficiently understood after the experiments of the 1950s to 1970s, the interest of mountain meteorologists was directed towards wave phenomena in the middle and upper troposphere that had been illuminated to a lesser degree. Also, the risk involved in flying aircraft through regions of severe turbulence ever more closely to the mountain slopes to improve on past observations appeared unacceptably high. Secondly, numerical models were yet lacking a faithful representation of turbulent boundary-layer processes. Close inspection of a few modelling studies of downslope windstorms (e.g., Durran 1986, their Fig. 10, or Richard et al. 1989, their Fig. 5) reveals that their simulated flow patterns bear striking resemblance to those from more recent high-

resolution rotor simulations (e.g., Jiang et al. 2007). However, the specifics of the model setups frequently prevented rotors to be produced in simulation runs, owing to, for instance, the use of a free-slip lower boundary condition (Durran 1986), the exclusion of non-hydrostatic effects (Richard et al. 1989), or, generally, insufficient horizontal grid resolution or inappropriate numerical methods.

Only towards the end of the last century did the interest in rotors revive, perhaps due to the new evidence of their destructive power. Over the years, numerous aviation incidents and accidents had been related to the phenomenon (Lester 1993; Carney et al. 1997). For instance, on 31 March 1993, a severe turbulence encounter, likely associated with a rotor, resulted in the loss of an engine on a Japan Airlines Boeing 747-100 a few minutes after departing from Anchorage, Alaska (Kahn et al. 1997; Doyle and Durran 2007). At the surface, the devastating effects of small-scale vigorous perturbations embedded in severe downslope winds were observed and asked for further investigations (Bedard 1990).

Finally, new boundary-layer remote sensors (Banta et al. 2013), in particular scanning Doppler lidars, allowed insight into the low-level flow underneath lee waves and internal jumps at increasingly higher spatial and temporal resolution, and at a safe distance. Starting towards the end of the 1980s, measurements by ground-based lidars were made on several occasions in the lee of the Front Range of the Colorado Rockies, a region particularly well-known for its high frequency of severe winds. Rather fortuitously, jump-like flow reversals and lee-wave rotors were observed (Neiman et al. 1988; Clark et al. 1994; Ralph et al. 1997a; Darby and Poulos 2006). First attempts to simulate these using fully three-dimensional numerical model setups with realistic topography and time-dependent inflow boundary conditions were made (Clark et al. 1994; Ralph et al. 1997a). The hitherto most direct observational evidence of a coherent rotor circulation underneath a lee-wave crest was collected by Ralph et al. (1997a, their Fig. 7). Observations of hydraulic-jump-like flow separation were also made with an airborne backscatter lidar in the Inn Valley, Austria, during MAP (Gohm and Mayr 2004).

1.2 Recent advances in mountain-wave and rotor research

The past fifteen years have seen a veritable renaissance of research on rotors. This is most evident from Table 1.2, in which the attempt is made to provide a complete list of related studies that have emerged from this period.

Ideas for a new field project devoted to rotors had been excited by the new observational evidence as well as the increasing capacity of high-performance computers. The latter would allow to run mesoscale model simulations at increasingly higher resolution and explicitly resolve rotors and rotor sub-structures. The southern Sierra Nevada and Owens Valley, theatre of the Sierra Wave Project 50 years earlier, appeared a logical location for a new edition of a rotor experiment. After several years of planning, a two-phase field programme, consisting of the pilot Sierra Rotors Project (SRP) and the Terrain-induced Rotor Experiment (T-REX), was carried out in 2004 and 2006 (Grubišić et al. 2004; Grubišić et al. 2008).

1 Mountain-wave and rotor research

Table 1.2: Peer-reviewed literature on wave-induced boundary-layer separation, rotors and low-level turbulence from the past 15 years, in chronological order. Letters in the third column stand for theoretical analysis (T), idealized numerical simulation (I), real-case numerical simulation (R), observations (O), laboratory experiments (L), and historical review (H).

Authors	Title	Type
Doyle and Durran (2002)	The dynamics of mountain-wave-induced rotors	I, T
Doyle and Durran (2004)	Recent developments in the theory of atmospheric rotors	I, R
Grubišić and Lewis (2004)	Sierra Wave Project revisited – 50 years later	H
Vosper (2004)	Inversion effects on mountain lee waves	I, T
Gohm and Mayr (2005)	Numerical and observational case-study of a deep Adriatic bora	O, R
Ambaum and Marshall (2005)	The effects of stratification on flow separation	T
Mobbs et al. (2005)	Observations of downslope winds and rotors in the Falkland Islands	O
Hertenstein and Kuettner (2005)	Rotor types associated with steep lee topography: Influence of the wind profile	I, T
Darby and Poulos (2006)	The evolution of lee-wave-rotor activity in the lee of Pike’s Peak under the influence of a cold frontal passage: Implications for aircraft safety	O, R
Sheridan and Vosper (2006a)	Numerical simulations of rotors, hydraulic jumps and eddy shedding in the Falkland Islands	I
Sheridan and Vosper (2006b)	A flow regime diagram for forecasting lee waves, rotors and downslope winds	I
Vosper et al. (2006)	Flow separation and rotor formation beneath two-dimensional trapped lee waves	T, I
Belušić et al. (2007)	Numerical simulation of pulsations in the bora wind	R
Doyle and Durran (2007)	Rotor and subrotor dynamics in the lee of three-dimensional terrain	I, T
Grubišić and Billings (2007)	The intense lee-wave rotor event of Sierra Rotors IOP 8	O, R
Grubišić and Orlić (2007)	Early observations of rotor clouds by Andrija Mohorovičić	H
Jiang et al. (2007)	On boundary layer separation in the lee of mesoscale topography	I, T
Sheridan et al. (2007)	Influence of lee waves on the near-surface flow downwind of the Pennines	O, I, T
Gohm et al. (2008)	On the onset of bora and the formation of rotors and jumps near a mountain gap	O, R
Grubišić and Billings (2008a)	Climatology of the Sierra Nevada mountain-wave events	O
Grubišić and Billings (2008b)	Summary of the Sierra Rotors Project wave and rotor events	O, R
Grubišić et al. (2008)	The Terrain-Induced Rotor Experiment	O, R
Raab and Mayr (2008)	Hydraulic interpretation of the footprints of Sierra Nevada windstorms tracked with an automobile measurement system	O, T
Hertenstein (2009)	The influence of inversions on rotors	I

1.2 Recent advances in mountain-wave and rotor research

Table 1.2: (Continued.)

Authors	Title	Type
Doyle et al. (2009)	Observations and numerical simulations of subrotor vortices during T-REX	O, I
De Wekker and Mayor (2009)	Observations of atmospheric structure and dynamics in the Owens Valley of California with a ground-based, eye-safe, scanning aerosol lidar	O
Grubišić and Stiperski (2009)	Lee-wave resonances over double bell-shaped obstacles	I
Prtenjak and Belušić (2009)	Formation of reversed lee flow over the north-eastern Adriatic during bora	R
Reinecke and Durran (2009)	Initial-condition sensitivities and the predictability of downslope winds	R
Smith and Skillingstad (2009)	Investigation of upstream boundary layer influence on mountain wave breaking and lee wave rotors using a large-eddy simulation	I
Weissmann et al. (2009)	Vorticity from line-of-sight lidar velocity scans	O
Hill et al. (2010)	Coplanar Doppler lidar retrieval of rotors from T-REX	O
Jiang et al. (2010)	Turbulence characteristics in an elevated shear layer over Owens Valley	O, T
Knigge et al. (2010)	Laboratory experiments on mountain-induced rotors	L
Krishnamurthy et al. (2010)	Large-eddy simulation-based retrieval of dissipation from coherent Doppler lidar data	O
Armi and Mayr (2011)	The descending stratified flow and internal hydraulic jump in the lee of the Sierras	O, T
Cohn et al. (2011)	Wind profiler observations of mountain waves and rotors during T-REX	O
Stiperski and Grubišić (2011)	Trapped lee wave interference in the presence of surface friction	I
Večenaj et al. (2011)	Near-surface characteristics of the turbulence structure during a mountain-wave event	O
Parish and Oolman (2012)	Isobaric Height Perturbations Associated with Mountain Waves Measured by Aircraft during the Terrain-Induced Rotor Experiment	O
Sawada et al. (2012)	Transient downslope winds under the influence of stationary lee waves from the Zao mountain range	O, R
Sheridan and Vosper (2012)	High-resolution simulations of lee waves and downslope winds over the Sierra Nevada during T-REX IOP 6	O, R
Stiperski et al. (2012)	Complex bora flow in the lee of Southern Velebit	O, R
Belušić et al. (2013)	Wind regimes associated with a mountain gap at the north-eastern Adriatic coast	O, R
Kühnlein et al. (2013)	High-resolution Doppler lidar observations of transient downslope flows and rotors	O, I
Vosper et al. (2013)	A climatology of lee waves over the UK derived from model forecasts	R
Ágústsson and Ólafsson (2014)	Simulations of observed lee waves and rotor turbulence	R
Worthington (2014)	Boundary-layer effects on mountain waves: A new look at some historical studies	H

1.2.1 Theory and high-resolution numerical simulation of wave-induced boundary-layer separation and rotors

Ahead of SRP and T-REX, a better understanding of the physical mechanisms behind rotor formation was gained through a series of studies relying on high-resolution, idealized numerical simulation in two and three dimensions (Doyle and Durran 2002; Vosper 2004; Hertenstein and Kuettner 2005; Vosper et al. 2006; Jiang et al. 2007; Doyle and Durran 2007).

In their seminal work, Doyle and Durran (2002) confirmed the fundamental role of wave-induced boundary-layer separation (BLS) in the formation of rotors. Their results corroborated the original hypothesis by Lyra (1943), put forward almost 60 years earlier. Figure 1.3a shows a snapshot of one of their simulations. At the separation point, a sheet of shear-generated horizontal vorticity is lifted and carried up into the lee wave, where it disperses and contributes to the positive vorticity inside the rotor. At the surface, reversed flow occurs in the simulation, the strength of which was shown to be highly correlated with the lee-wave amplitude and the resultant magnitude of the surface pressure perturbations. Surface friction was found to be a crucial ingredient to the formation of realistic rotors, leading the authors to the conclusion that boundary-layer friction and wave-induced perturbations “interact synergistically to produce low-level rotors”. This result is consistent with the classical laboratory experiments by Long (1955) and his theoretical calculation using a free-slip lower boundary condition. In fact, for an experimental setup comparable to that by Doyle and Durran (2002), Long’s theory had not predicted stagnation or flow reversal at any point in the fluid, but lee-side BLS did occur in the physical experiment, pointing to the role of surface friction in promoting BLS and rotors (Doyle and Durran 2002).

While the essential mechanisms of rotor formation were well explained from simulations in two dimensions, only very high-resolution three-dimensional simulations could afford a realistic representation of the fine-scale structure of the flow in the rotor interior (Doyle and Durran 2007). In these simulations, the shear in the separated vorticity sheet could not be sustained and broke up into smaller-scale turbulent vortices – *subrotors* – as a result of Kelvin-Helmholtz instability. The comparison between 2D and 3D simulations revealed substantial differences in the strength and evolution of subrotors, the 3D subrotors being generally much more intense. Also, the 3D internal rotor flow seemed rather chaotic as opposed to a more coherent rotor circulation in two dimensions. In realistic 3D subrotors (Fig. 1.3b), vorticity was found to intensify by virtue of the stretching and tilting of the along-ridge horizontal vorticity. While intensifying, 3D vortices were advected along the interface between the rotor and the lee wave aloft and did not necessarily contribute to the main rotor circulation.

The work by Doyle and Durran (2002, 2007) also provided an explanation for previous aircraft measurements of the rotor turbulence in the 1970s (e.g., Lester and Fingerhut 1974). The overall spatial distribution and intensity of turbulence in simulations agreed well with the observational finding of the occurrence of severe turbulence in the updraught area just upstream of the rotor. The presence of subrotors and their distribution in the simulations are consistent with aircraft encounters with the most intense patches of turbulence in the leading

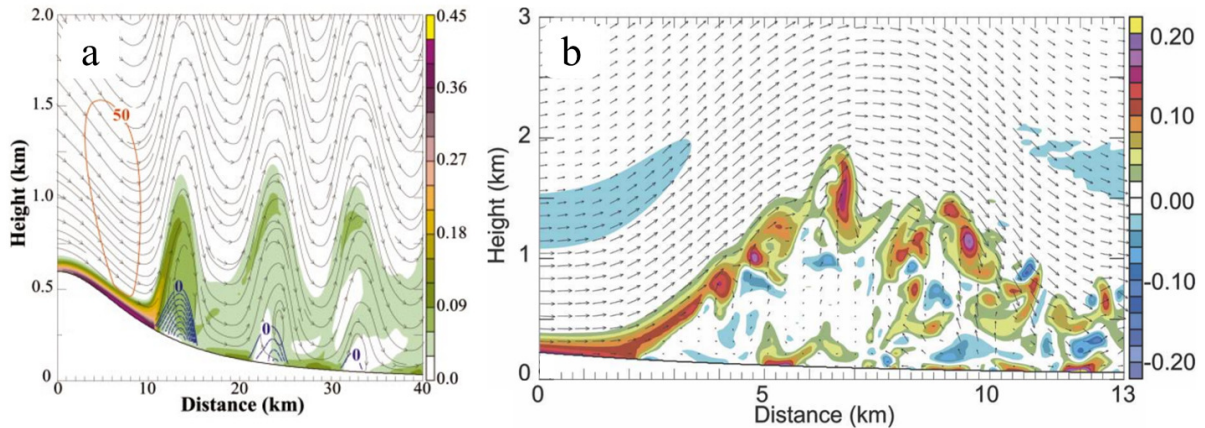


Figure 1.3: High-resolution numerical simulations of rotors and subrotors in two and three dimensions. (a) Streamlines and colour contours of horizontal vorticity (in units of s^{-1}) from a 2D simulation using a horizontal grid increment of 100 m. Blue contour lines are isotachs (drawn every 2 m s^{-1}). Reproduced from Doyle and Durran (2002, their Fig. 7). (b) Flow vectors and colour contours of horizontal vorticity (in units of s^{-1}) from a 3D simulation, using a horizontal grid increment of 60 m in the innermost nested domain. Reproduced from Doyle and Durran (2007, their Fig. 7). (Copyright 2002, 2007 American Meteorological Society.)

edge of the rotor. These patches have been believed to pose the greatest threat to aircraft.

Building on the results by Doyle and Durran (2002, 2007), a variety of upstream conditions under which rotors can form was examined by other authors (Vosper 2004; Hertenstein and Kuettner 2005; Vosper et al. 2006; Jiang et al. 2007). Vosper (2004) investigated the effect of a strong temperature inversion on lee waves, rotors, and low-level hydraulic jumps and wave breaking aloft. His regime diagram, constructed from a set of two-dimensional numerical simulations, is particularly appealing for its potential to predict the occurrence of such processes as a function of only two parameters, the shallow-water Froude number and the ratio of mountain height to inversion height. As the latter exceeds a critical threshold, lee waves grow sufficiently large to trigger flow separation.

Hertenstein and Kuettner (2005) demonstrated the sensitivity of rotor shape to relatively small variations in the upstream environmental profiles, in their case, the magnitude of the vertical wind shear in a crest-level inversion. Their simulations produced a lee-wave rotor and a hydraulic-jump-type rotor for forward shear and no shear, respectively.

The most comprehensive study is perhaps that by Jiang et al. (2007), who identified three types of BLS: (i) BLS induced by trapped waves, associated with the decrease of the Scorer parameter with height in the upstream flow, (ii) BLS induced by internal bores generated by the breaking of a hydrostatic mountain wave in a uniform upstream flow, and (iii) BLS induced by undular jumps or trapped waves behind a jump associated with an elevated inversion. The hydraulic jumps in the third type were found to be steady or propagating. The meteorological conditions conducive to BLS and the formation of rotors, in particular cases (ii) and (iii), are similar to those that favour the generation of downslope windstorms (Section 1.1.4).

The occurrence of BLS, however, is not limited to an atmosphere that supports internal

gravity waves. As a matter of fact, wave-induced BLS represents only a variant of flow separation from a solid boundary, a process that has long been known by fluid dynamicists (Batchelor 1967). The first to discuss its atmospheric analogs was probably Scorer (1955). In the neutrally stratified atmosphere, free of pressure forcings from waves, flow separation can occur downwind of steep mountain peaks (*salient-edge* or *bluff-body* separation, Baines 1995), as shown by both theoretical considerations and laboratory experiments (Baines and Hoinka 1985; Ambaum and Marshall 2005).

1.2.2 The Terrain-induced Rotor Experiment (T-REX)

In preparation for T-REX, the Sierra Rotors Project was conducted in Owens Valley as the exploratory phase of the experiment in March and April 2004. Topographic maps of the region are shown in Fig. 1.4. A more detailed description of the topography is provided in Section 4.2.

The SRP ground-based instrumentation was distributed around the town of Independence, located in the central part of Owens Valley. The set of instruments included 16 automated weather stations (the DRI Mesonet), GPS radiosondes launched upwind of the Sierra Nevada and in Owens Valley, two radar wind profilers, and mobile measurements by an instrumented car (Grubišić and Billings 2007; Raab and Mayr 2008). No research aircraft were deployed at this point of the programme. During the two-month field activities, 16 intensive observing periods were conducted, nine of which displayed wave activity and three rotor activity (Grubišić and Billings 2007).

T-REX took place in March and April 2006 as the major phase of the programme. Measurements were made throughout the two-month period and in particular during 15 intensive observing periods (IOPs) and 5 enhanced observing periods (EOPs). For T-REX, the set of instruments employed during SRP was extended by a large number of additional ground-based and airborne in situ and remote sensing instruments, some of which produced great excitement among T-REX participants. For instance, at the valley floor, the proper arrangement of two scanning Doppler lidars offered the opportunity for the first ever dual-Doppler lidar analyses of terrain-induced flows (Grubišić et al. 2008). Moreover, T-REX was the first operational field project deployment for the new NSF/NCAR GV High-Performance Instrumented Airborne Platform for Environmental Research aircraft (HIAPER, or GV; UCAR/NCAR cited 2015), capable of measuring wave perturbations and turbulence at altitudes up to 14 km. Finally, the University of Wyoming King Air (UWKA) research aircraft, equipped with high-rate in situ sensors, and the dual-Doppler Wyoming Cloud Radar (WCR, Damiani and Haimov 2006; Wang et al. 2012), carried aboard UWKA, were expected to provide insight into the turbulent flow within and over Owens Valley in high detail.

Beyond physical instrumentation, a suite of large-scale medium-range and mesoscale numerical weather prediction models represented the second major experimental component, with their forecasts aiding the successful short-term planning of activities on site. A comprehensive overview of the T-REX instrumentation, modelling efforts, and the IOPs and their observational highlights has been given by Grubišić et al. (2008). A description of the T-REX

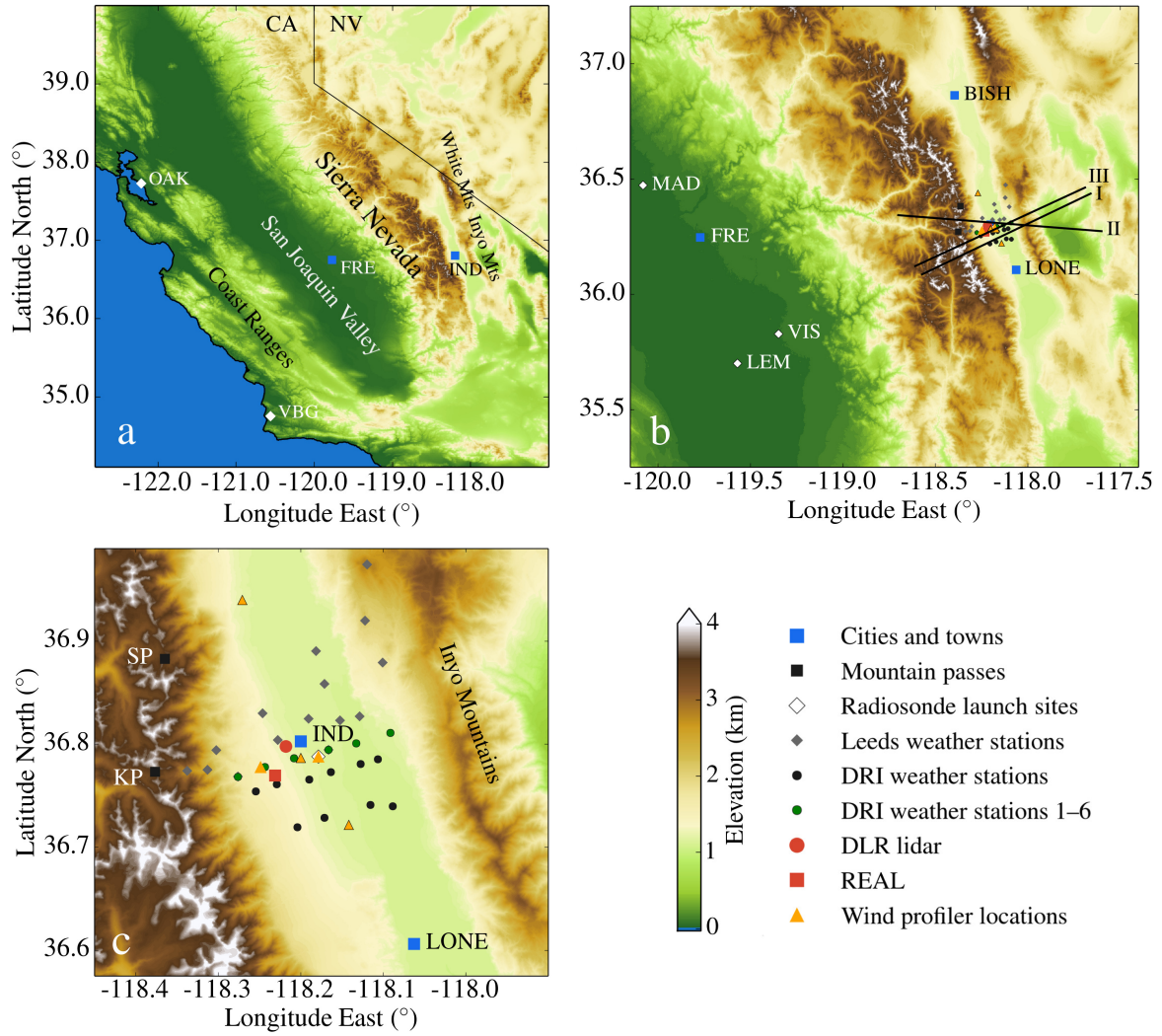


Figure 1.4: Topographic maps of California's Central Valley, the Sierra Nevada, Owens Valley and the Inyo and White Mountains. Locations of towns, sounding launch sites, and T-REX ground-based instruments are indicated with markers. Abbreviations OAK, VBG, FRE, MAD, VIS, LEM, BISH, IND, LONE stand for, respectively, Oakland, Vandenberg, Madera, Fresno, Visalia, Lemoore, Bishop, Independence, and Lone Pine. In (b), aircraft mean tracks from several T-REX IOPs are indicated with solid black lines. Roman numerals stand for flight tracks during IOP 1a (I), IOP 3a (II), and IOPs 4a, 6b-c, and 13c (III). In (c), the Kearsarge and Sawmill Passes are abbreviated as KP and SP, respectively.

instruments and data relevant for this work is contained in Section 4.2.

T-REX findings

The overarching goal of T-REX was to study the interaction and coupling between rotors, mountain waves, and boundary layer dynamics (Grubišić et al. 2008). However, the scientific questions addressed in the experiment extended well beyond its principal scope. This is perhaps best evidenced by the rich variety of contributions to the Special Collection of T-REX publications, hosted by the American Meteorological Society (cited 2015), that has expanded

ever since the completion of the T-REX experimental phase. In the following, a selection of the scientific findings from T-REX that are of interest in this work is presented.

Internal rotor structure

Ground-based remote sensors, in particular three scanning lidars, were deployed in Owens Valley to confirm the existence of subrotors, predicted in preliminary 2D and 3D rotor simulations. During T-REX IOPs 3, 6, and 13, observations of intense small-scale vortices in the valley were made on several occasions. Using the estimates of vertical motion and Doppler spectrum width from upward-looking wind profilers, Cohn et al. (2011) revealed a series of updraught-downdraught couplets beneath the first wave crest downwind of the Sierra Nevada during IOP 3. In IOP 13, the REAL aerosol backscatter lidar (Fig. 1.4c) detected Kelvin-Helmholtz billows forming and overturning in a layer of elevated strong downslope flow above the valley (Doyle et al. 2009). Doppler velocities provided by the Doppler lidar operated by the Deutsche Zentrum für Luft- und Raumfahrt (DLR) confirmed that the breaking billows were associated with couplets of positive and negative radial velocity toward the lidar with a size of roughly 500-1000 m. For both IOP 3 and 13 these signatures were attributed to subrotors. For IOP 13, further support for this interpretation came from idealized large-eddy simulations, using the measured upstream soundings as inflow conditions and a two-dimensional representation of the Sierra Nevada main ridge (Doyle et al. 2009).

The most quantitative insight into the intensity and evolution of subrotors was achieved by the combination of co-planar vertical-slice scans conducted by the DLR and University of Arizona (ASU) Doppler lidars, allowing a dual-Doppler lidar retrieval of wind vectors and streamlines vertical cross-section spanning across the valley. A few hours before the severe downslope windstorm of IOP 6, Hill et al. (2010) detected subrotors and were able to track them along their path using the vorticity and swirling strength. One of their observations is of more general interest: While their two-dimensional snapshots of the flow field showed that “subrotors unambiguously populate these flows”, only “time- or ensemble-averaged streamlines [...] may indicate a large-scale rotor, even though large-scale rotors may be undetectable instantaneously”. In conclusion, lidar observations from the three IOPs produced ultimate proof of the existence of subrotors, but also pointed to the difficulty in finding an appropriate definition of a rotor in what appears to be a rather chaotic system at any given instant in time.

Complexity of valley flow patterns

Persistent systems of slope and valley winds can be expected in Owens Valley due to its extent and the steepness of the Sierra lee slopes delimiting the valley to its west. Complex interactions between thermally and dynamically induced slope flows and along-valley flows were noted by several authors. For example, in the evening and night of 11-12 March 2006, De Wekker and Mayor (2009) observed a rather dramatic collision and mixing of drainage and along-valley flows under otherwise quiescent conditions. The great resistance of the along-valley flow to strong westerly downslope winds during a strongly dynamically-driven

episode was documented by Kühnlein et al. (2013). During the onset phase of the IOP 6 windstorm, the transition to in-valley westerly winds did not occur smoothly. Rather, it took the form of erratic pulses of strong westerly momentum competing with the up-valley winds for several hours until they were finally flushed out.

Another element of complexity of the flow in Owens Valley is related to the existence of a few mountain passes in the main ridge line of the Sierra Nevada, most notably Kearsarge Pass (3600 m MSL), located west of the town of Independence. The analysis of real-case simulations of the IOP 6 downslope windstorm by Sheridan and Vosper (2012) indicated a significant variability of the storm severity along the mountain ridge, with the Independence area standing out for its particularly high winds. Gap jets downstream of the Sawmill and Kearsarge Passes extending down to the Owens Valley floor were also present in simulations of the SRP IOP 8 windstorm event (Grubišić and Billings 2007).

Diurnal variation of downslope winds in Owens Valley

The diurnal variation of the amplitude of mountain waves generated by the Sierra Nevada has been notorious among glider pilots familiar with the region and was also paid attention to by scientists already during the Sierra Wave Project in the 1950s (Holmboe and Klieforth 1957; Kuettner 1959). Subsequent to T-REX, the importance of diurnal forcings in Owens Valley for *downslope winds* was shown in several studies. Jiang and Doyle (2008) investigated an SRP downslope wind event, during which cross-valley winds exhibited a strong diurnal variation even if upstream westerlies at and above the mountaintop remained largely unaltered. They suggested that different states of penetration of downslope winds occurred in the valley in the course of a day, with the deepest penetration typically realized in the late afternoon. Mayr and Armi (2010) and Armi and Mayr (2011) studied the onset of downslope flows at the valley bottom during T-REX IOPs 1 and 11. They found that the diurnal heating of the valley atmosphere gradually removed valley inversions which had formed during the previous night. Only when the potential temperature at all levels in the valley was higher than that at the Sierra crest or mountain pass level were downslope winds able to advance to the valley floor.

All of the SRP and T-REX cases examined in the above contributions, however, do not rank among the strongest westerly wind events observed during both SRP and T-REX. In the latter cases, in-valley westerlies can occur independent of the time of day, as already recognized by Jiang and Doyle (2008). In all cases, the thermal mechanism may act to facilitate the onset of westerlies in the valley (Billings and Grubišić 2008a,b). Indeed, recent work by Grubišić et al. (2015b) supports these findings on the basis of the climatological frequency of occurrence of westerly wind events in the Independence area from an extended five-year period of DRI Mesonet data.

Numerical simulations of mountain-wave and downslope-windstorm events and implications for mesoscale predictability

One of the core scientific objectives of T-REX was the improvement of the numerical modelling and predictability of dynamically-induced mountain-wave phenomena (Grubišić et al.

2008). An important contribution to this goal was the reproduction of the SRP and T-REX observations with mesoscale and high-resolution real-case numerical simulations. Several authors contributed to these efforts, with variable success and a few surprising results.

Grubišić and Billings (2007) investigated the lee-wave-rotor event of SRP IOP 8. Their high-resolution simulation reproduced the changes in lee-wave regimes and the formation of a rotor that had occurred rather well. On the other hand, the timing of flow transitions, such as the development of the daytime thermally-forced flow in the valley or the passage of a cold front over the Sierra Nevada, was slower than observed. Sheridan and Vosper (2012) delivered an extensive observational analysis of T-REX IOP 6, which included the experiment's most severe downslope windstorm, coinciding with rapid changes in the phase, wavelength, and amplitude of the waves aloft. The reproduction of the event using a high-resolution mesoscale model was, however, of limited success. Both large-amplitude waves over the Sierra and westerly winds in the valley were simulated, but the wave phase and its shift to the east was not reproduced correctly. The winds in the model were more thermally determined and seemingly lacking the link to the wave motion aloft. Both case studies from SRP and T-REX pointed to the great challenge of simulating correctly the conjunction of mechanisms involved in generating the windstorms, including the arrival of a cold-frontal system at the main Sierra Nevada ridge line and its interaction with the terrain, as well as the diurnal evolution of the downstream environment.

Two different perspectives on the predictability of mountain waves and downslope windstorms were taken by Doyle et al. (2011b) and Reinecke and Durran (2009). In an effort to examine the sensitivity of windstorm and mountain-wave predictions to numerical model characteristics, Doyle et al. (2011b) compared the results of 11 different non-hydrostatic numerical models initialized with a pre-windstorm upstream sounding of IOP 6. Their results revealed a strikingly diverse spectrum of simulated mountain-wave characteristics, ranging from lee waves to gravity-wave breaking, which implied a surprisingly low predictability of such events. Reinecke and Durran (2009) tested the sensitivity of downslope windstorm forecasts by a single mesoscale model on small variations in the initial conditions. The ensemble forecasts of the T-REX windstorm events of IOP 6 and 13 were examined. The predictability time scale of the IOP 13 case, associated with upstream stability layering, seemed somewhat longer than that of the IOP 6 case, involving a large-amplitude breaking mountain wave. However, the authors concluded that “neither case suggests that much confidence should be placed in the intensity of downslope winds forecast 12 or more hours in advance”.

Observations of fully-developed rotors

Interestingly, only two studies documenting coherent rotor circulations in Owens Valley have emerged from T-REX observations. During IOP 3, non-stationary lee waves shifted toward the east across Owens Valley and past the vertical line of sight of two wind profilers, allowing a large portion of the low-level turbulence zone underneath the wave crests to be sampled. Using these data, Cohn et al. (2011) documented the presence of several typical characteristics of the lee-side low-level turbulence zone: enhanced shear-generated turbulence below the upstream

edge of the wave crest, couplets of positive and negative velocity within the turbulence zone, and weak ($<5 \text{ m s}^{-1}$) but sustained easterly winds in its lowest portion, all supporting the idea of a rotor being present.

The most direct observation of a fully-developed rotor during T-REX was provided by the DLR Doppler lidar during the final stages of the windstorm episode of IOP 6. Kühnlein et al. (2013) showed the rapid temporal evolution of a large rotor at the leading edge of the downslope windstorm, having a horizontal and vertical extent of 6-8 km and 2-3 km, respectively. The rotor contained distinct regions of reversed flow with an easterly wind component of up to 10 m s^{-1} and quickly retreated westward in time. Although rather well defined in size and extent, the rotor flow was highly transient, intermittent, and three-dimensional and exhibited significant interaction with the along-valley flow (Kühnlein et al. 2013).

1.3 Scope of this work

T-REX has excited a new wave of research on mountain waves and rotors. A multitude of new findings have emerged, representing a significant step ahead in our understanding of the interaction of mountain waves and the boundary layer. Certainly, as with any field experiment, not all objectives formulated in the design phase of the experiment have been met. For example, observational evidence of gravity-wave breaking in the upper troposphere-lower stratosphere was not found, with the exception of an encounter with clear-air turbulence along a single GV flight leg at 13.7 km over the southernmost part of the Sierra Nevada during IOP 6 (Doyle et al. 2011a). On the other hand, a few fortuitous discoveries of new phenomena were made, for instance, the secondary generation of downward-propagating mountain waves near the tropopause (Smith et al. 2008; Woods and Smith 2010).

The rich T-REX data set, consisting of data from both surface and airborne sensors and mesoscale model output, is yet to be exploited to its full extent. Also, some of the observations from T-REX still remain poorly understood. Others have led to entirely new questions. The purpose of this work is to fill in some of the remaining blanks and to contribute to the resolution of a few of the outstanding questions regarding mountain-induced turbulence and real-world rotors.

1.3.1 Open questions

(i) Origin of the unsteadiness of mountain flows

During T-REX, hopes were high that UWKA and the high-resolution dual-Doppler capabilities of WCR would allow to sample the turbulent structures in Owens Valley and provide a two-dimensional depiction of the rotor flow across the valley. However, due to the lack of low-level moisture in Owens Valley, in particular during the mountain-wave events of interest, only little additional insight could be gained from the radar measurements. This excludes a few occasions on which the cap cloud over the mountains and the roll cloud over the valley were

reasonably well covered by the radar (Grubišić et al. 2006; Haimov et al. 2008).

Only two months prior to T-REX, however, in January and February 2006, the NASA Orographic Clouds Experiment (NASA06) was conducted over the Medicine Bow Mountains (MBM) in southeastern Wyoming in a wintertime, moist mid-latitude environment.⁵ On several days of the campaign, UWKA performed cross-mountain legs aligned with the ambient wind direction. The main objective of NASA06 was to study the orographic enhancement of wintertime precipitation over the MBM. During two days of the campaign, however, large-amplitude mountain waves and enhanced low-level turbulence were detected in coincidence with significant cloud cover over the MBM, allowing WCR to sample the airflow over the mountains from flight level all the way to the ground.

Preliminary analysis of the observations revealed boundary-layer separation and near-surface reversed flow in the lee of the MBM on both wave days, strongly suggestive of the presence of rotors. A striking feature of the events was their rapid temporal evolution. In both cases, the primary wave updraughts in the lee and the low-level turbulence region underneath them displayed a significant upstream movement (e.g., 7 km within 30 min on 26 January), well beyond the usual rates of change in wavelength or phase of non-stationary lee waves, reported previously (e.g., Ralph et al. 1997a). This aspect makes the NASA06 events quite similar to T-REX IOPs 3 and 6, in which non-stationary waves and rotors were observed as well.

The preliminary results clearly ask for a deeper analysis aiming at elucidating the driving dynamic factors of the strong degree of unsteadiness in the mountain-wave patterns and related turbulence.

(ii) Structure and intensity of mountain-wave-induced turbulence

Several studies in the past have underlined the usefulness of high-rate aircraft measurements of wind, temperature, and humidity for the study of small-scale atmospheric variability and turbulence over and around mountains (cf. Table 1.1). Deriving quantitative turbulence parameters, for instance the turbulent kinetic energy (TKE) or turbulent fluxes of heat and momentum, from measurements taken in spatially and temporally inhomogeneous conditions poses great challenges. This is particularly true for airborne remote sensors, for which the measurement of atmospheric parameters may be strongly affected by measurement uncertainties related to the remote measuring principle and the highly variable motion of the mobile platform. On the other hand, there are obvious advantages in using remote sensors for the study of severe low-level turbulence, since they allow to sample the turbulent phenomena of interest from afar, thereby avoiding the need to expose equipment and crew to the associated hazards. The latter aspect has led to a tendency of *undersampling* the regions closest to the mountain peaks and slopes, comprising some of the most interesting aspects of the atmosphere-terrain interaction, such as flow separation processes.

No definite answer exists, however, to the question whether meaningful, i.e., sufficiently

⁵ A topographic map of the region is shown in Chapter 2, Fig. 1.

accurate and statistically significant turbulence parameters can be derived from airborne remotely-sensed measurements in complex mountain flows.

(iii) Structure and evolution of rotors in complex terrain

Idealized conceptual models of the rotor flow were developed in the early mountain-wave experiments, but even their creators recognized substantial deviations from them for many of the observed cases. Recent observations from T-REX and NASA06 indicate the diverseness of *real-world* rotors that may form in dependence of the meteorological conditions causing them and of the surrounding topography. The influence of topography downstream of the primary mountain ridge on rotor formation has received relatively little attention. On the other hand, evidence of fully-developed rotors collected in Owens Valley during T-REX was unexpectedly scarce. When observed, the rapidity of their evolution was striking and their lifetime surprisingly short.

To what degree changes in the upstream meteorological conditions result in the rotor transience, and what is the relative importance of the characteristics of a valley atmosphere for the existence of rotors and their evolution, is yet to be illuminated.

In the following chapters, the above questions are addressed in three journal contributions by (i) Grubišić et al. (2015a), (ii) Strauss et al. (2015a), and (iii) Strauss et al. (2015b).

Chapter 2

Wave-induced boundary-layer separation in the lee of the Medicine Bow Mountains: numerical modelling

Airborne in situ and dual-Doppler radar measurements made during two wave events of the NASA06 experiment have provided insight into large-amplitude waves and their impact on the lee-side low-level flow in unprecedented detail. A comprehensive account of the observations has recently been given by French et al. (2015¹). High-resolution dual-Doppler syntheses of the two-dimensional velocity fields in a vertical plane along the aircraft track have revealed the presence of boundary-layer separation and rotors on both days. The most distinct characteristic of the observed cases was the rapid upstream movement of the rotors. The observational analysis points to gravity-wave breaking at mid levels above the mountains.

The objective of the study presented in this chapter is to provide the mesoscale dynamic context of the rapid temporal evolution of the events. Real-case numerical simulations with the Weather Research and Forecasting (WRF) model are used to shed light on the mechanisms behind boundary-layer separation and transient rotor formation. The results of this study contribute to our understanding of the origin of unsteadiness in mountain flows.

The main contribution to the work by the author of this thesis was the model verification by quantitative comparison with the aircraft data. WRF model runs, initialized with large-scale analyses from ECMWF, NCEP, and NOGAPS, were examined for the minimum root-mean-square deviation between measured and model-extracted aircraft data. Model runs relying on the ECMWF analysis offered the best comparison with the observations and were considered for subsequent analysis. Contributions to the journal article were made in the form of Figs. 3 and 4, text to Section 2, and the reviewing of paper drafts.

¹ French, J. R., S. Haimov, L. Oolman, V. Grubišić, S. Serafin, and L. Strauss, 2015: Wave-induced boundary-layer separation in the lee of the Medicine Bow Mountains. Part I: Observations. *J. Atmos. Sci.*, in review.

Reference

Grubišić, V., S. Serafin, L. Strauss, S. Haimov, J. R. French, and L. Oolman, 2015a: Wave-induced boundary-layer separation in the lee of the Medicine Bow Mountains. Part II: Modeling. *J. Atmos. Sci.*, accepted with minor revisions.

Wave-Induced Boundary-Layer Separation in the Lee of the Medicine Bow Mountains. Part II: Numerical Modeling

Vanda Grubišić*

National Center for Atmospheric Research, Boulder, CO, USA and

Department of Meteorology and Geophysics, University of Vienna, Vienna, Austria

Stefano Serafin and Lukas Strauss

Department of Meteorology and Geophysics, University of Vienna, Vienna, Austria

Samuel J. Haimov, Jeffrey R. French, and Larry D. Oolman

Department of Atmospheric Sciences, University of Wyoming, Laramie, WY

**Corresponding author address:* Vanda Grubišić, NCAR Earth Observing Laboratory, P.O. Box 3000, Boulder, CO 80307-3000

E-mail: grubisic@ucar.edu

ABSTRACT

13 Mountain waves and rotors in the lee of the Medicine Bow Mountains in SE
14 Wyoming are investigated in a two-part paper. Part I by French et al. (2015)
15 delivers a detailed observational account of two rotor events, one of which
16 displays characteristics of a hydraulic jump, the other of a classic lee-wave
17 rotor. In Part II, presented here, we convey results of high-resolution numeri-
18 cal simulations and examine physical processes involved in the formation and
19 dynamical evolution of these two rotor events.

20 The simulation results reveal that the origin of the observed rotors lies in
21 boundary-layer separation, induced by wave perturbations whose amplitudes
22 reach maxima at or near the mountain top. An undular hydraulic jump that
23 gave rise to a rotor in one of these events was found to be triggered by mid-
24 tropospheric wave breaking and an ensuing strong downslope windstorm. Lee
25 waves spawning rotors developed under conditions favoring wave energy trap-
26 ping at low levels in different phases of these two events. The upstream shift
27 of the boundary-layer separation zone, documented to occur over a relatively
28 short period of time in both events, is shown to be the manifestation of a tran-
29 sition in flow regimes, from downslope windstorms to trapped lee waves, in
30 response to a rapid change in the upstream environment related to the passage
31 of a short-wave synoptic disturbance aloft.

32 The model results also suggest that the secondary obstacles surrounding the
33 Medicine Bow Mountains play a role in the dynamics of wave and rotor events
34 by promoting lee-wave resonance in the complex terrain of SE Wyoming.

1. Introduction

A boundary layer is the region of fluid flow that is strongly affected by the no-slip condition along the interface with a solid boundary. The aspect of boundary-layer dynamics that represents the greatest difficulty theoretically is the flow separation (Batchelor 1967). Laboratory experiments show that boundary layers exhibit no tendency to separate where the flow external to the boundary layer accelerates. Conversely, where the external flow is strongly retarded, the boundary layer will separate from the solid surface (Lighthill 1986). In stratified fluids, such as the atmosphere, separation-causing deceleration can be triggered, among other means, by the adverse pressure gradient due to pressure perturbations induced by internal gravity waves launched in flow over complex terrain. If that is the case, boundary-layer separation (BLS) is said to be wave-induced (Scorer 1958; Baines 1997).

In orographically-forced atmospheric flows, in general, the occurrence of wave-induced boundary-layer separation is a manifestation of non-linear processes. In flows over terrain with vertically uniform stability and wind profiles, non-linearity displays itself as large-amplitude waves at or near the mountain tops. Flows in which either the stability, the wind or both change with height may too be conducive to triggering of boundary-layer separation through formation of trapped lee waves or of a hydraulic jump at low levels (Jiang et al. 2007).

Attendant to wave-induced boundary-layer separation is the occurrence of terrain-induced atmospheric rotors (Doyle and Durran 2002). The latter have been traditionally described and schematically represented as horizontal vortices with an axis parallel to a mountain ridge (Grubišić et al. 2008) and are often characterized by severe or extreme turbulence (Doyle and Durran 2002, 2007; Strauss et al. 2015). The interplay of baroclinic vorticity generation along stable layers embedded in mountain waves and shear vorticity generation within the terrain-adjointing boundary

layer has been shown to exert a significant impact on the rotor structure and strength. According to Hertenstein and Kuettner (2005), rotors tend to take the form of hydraulic jumps when baroclinically-generated vorticity prevails, whereas lee-wave-type rotors are expected to occur when shear-generated vorticity dominates.

BLS in stratified flows over two-dimensional (2D) hills has been examined in laboratory experiments (Baines and Hoinka 1985) and described by theoretical studies (Ambaum and Marshall 2005). These investigations reveal a range of separation regimes (Baines 1997), dependent on the parameters NH/u (non-linearity parameter or non-dimensional obstacle height) and H/L (aspect ratio or slope steepness), where N , u , H and L are, respectively, the buoyancy frequency, the upstream wind speed (both assumed to be constant with height), the maximum height of the mountain and its half-width. In the limit of neutral stratification ($NH/u \approx 0$) no separation occurs on shallow hills ($H/L \approx 0$). As the aspect ratio is increased ($H/L \gtrsim 0.1$), salient-edge BLS is expected to occur at the hilltop. For $0 < NH/u \lesssim 1$ and low aspect ratios, small-amplitude internal gravity waves cannot induce BLS, because the flow acceleration on the lee slope and deceleration farther downstream are rather weak. With strong stratification and nonlinearity ($NH/u \gtrsim 1$), the amplitude of the pressure perturbations related to gravity waves in the inviscid flow above the BL becomes large enough to force the flow to separate in a wide range of H/L values.

A large number of mountain wave studies emphasize the profound impact that BL dynamics may have on downslope windstorms, rotors and lee waves. For instance, a BL can effectively limit trapped lee wave propagation by absorbing the reflected, downward propagating wave beams (Jiang et al. 2006; Smith et al. 2006; Smith 2007). Furthermore, the BL diurnal cycle of diabatic heating and cooling modulates downslope windstorms, by inducing changes both in the turbulence intensity and in the horizontal buoyancy gradients within waves (Jiang and Doyle 2008). A number of studies, with a special focus on lee-wave-type rotors, examined the sensitivity of BLS and rotor

formation to several other factors such as surface roughness, wave length and amplitude (Doyle and Durran 2002; Vosper et al. 2006; Jiang et al. 2007). The role played by elevated inversions in the formation of rotors was investigated by Vosper (2004) and, with laboratory experiments, by Knigge et al. (2010). The effect of a downstream mountain range on BLS and rotor formation was investigated by Grubišić and Stiperski (2009) and Stiperski and Grubišić (2011).

Beyond numerical, laboratory and theoretical investigations, several field measurement campaigns were recently conducted to study the structure and dynamics of atmospheric rotors and their surface signatures in the lee of different mountain ranges, including the Falkland Islands (Mobbs et al. 2005), the Pennines (Sheridan et al. 2007) and the Dinaric Alps (Gohm et al. 2008). The most extensive of these are the pair of campaigns in the Sierra Nevada — the Sierra Rotors Project (Grubišić and Billings 2007) and the Terrain-induced Rotor Experiment (T-REX, Grubišić et al. 2008). Despite these significant efforts, the observational evidence of boundary-layer separation in terrain-induced flows has been lacking until now. Part I of the present study describes observations of two events of wave-induced boundary layer separation and rotors in the lee of the Medicine Bow Mountains (hereafter MBM) in Wyoming (Fig. 1). These events occurred on 26 January and 5 February 2006 and were documented during the NASA06 field campaign (French et al. 2015). In this paper, we use a mesoscale numerical model to simulate these two events in order to place Part I observations in a broader mesoscale context and to examine physical processes involved in their formation and temporal evolution.

The paper is organized as follows. The details of the modeling approach are presented in Section 2. Sections 3 and 4 contain our analysis of numerical simulation results for the 26 January and 5 February cases. Summary and conclusions are presented in Section 5.

2. Numerical simulations

a. Model setup

The simulations presented here were performed using version 3.3 of the ARW-WRF model (Skamarock and Klemp 2008), in a nested configuration with two domains having a horizontal grid spacing ($\Delta x = \Delta y$) of 2 km and 400 m in the outer ($d01$) and inner ($d02$) domains, respectively. Initial and boundary conditions for the simulations were interpolated from the operational ECMWF analyses, available at 6-hourly intervals with native TL511L62 resolution. The model top was located at the 100 hPa pressure level, roughly corresponding to an altitude of 15700 m. Rayleigh damping was applied to the vertical velocity in the upper 5000 m of the domain, in order to absorb vertically-propagating gravity waves and prevent their downward reflection from the model top, which was treated as a rigid lid.

The terrain-following grid uses the σ coordinate introduced by Laprise (1992) and features 61 vertical levels in both domains. The grid-spacing is 0.003σ near the lower boundary and increases towards higher altitudes with a constant stretching factor of $\sim 5\%$ (i.e., each model level is $\sim 5\%$ thicker than its lower neighbor). The vertical grid spacing near the lower boundary is chosen so as to be on the same order of (and not much smaller than) the maximum terrain height increment across one element of the horizontal grid (Mahrer 1984; De Wekker 2002). The former (0.003σ) corresponds to ~ 21 m in our case, while the latter ($\Delta x \tan \alpha$, α being the local slope angle) is well below 60 m throughout most of the domain. Under these conditions, the grid setup should not cause large errors in the computation of near-surface pressure gradients. Additional simulations with different near-surface vertical resolutions (0.001σ and 0.1σ) did not produce appreciably different results from those presented herein.

A third-order time-split Runge-Kutta scheme was used for the discretization of time derivatives. Spatial derivatives were treated with upwind-biased 5th- and 3rd-order schemes along the horizontal and vertical directions, respectively, providing implicit artificial diffusion. Given the fully compressible nature of the WRF solver, isotropic divergence damping and forward biasing of the vertically implicit acoustic-time-step terms were adopted, in order to damp acoustic modes in the solution.

Fluxes in the surface layer and vertical sub-grid-scale fluxes in the PBL are parameterized with the Eta Mellor-Yamada-Janjić scheme (MYJ, Janjić 2002), while horizontal diffusion is handled with a Smagorinsky first-order closure. The Morrison 2-moment scheme (Morrison et al. 2009) is used for microphysical processes and atmospheric radiation is treated with the RRTM scheme (Mlawer et al. 1997) for the longwave and the Dudhia (1989) scheme for the shortwave component.

The fairly high grid resolution of the inner domain lies in the so-called *terra incognita* range (Wyngaard 2004), where the application of traditional BL parameterizations, such as the MYJ scheme, might be questionable. Consequently, we explored the sensitivity of model results to BL parameterizations by performing a few additional runs with alternative schemes (not shown). Overall, the general characteristics of our results were unaltered, increasing our confidence in the appropriateness of the selected model setup.

The 26 January and 5 February simulations were both initialized at 0000 UTC on respective dates and carried forward for 36 hours. The first few hours of each run are regarded as spin up time and were not taken into account in the analysis of results.

b. Model verification

For model verification, simulation results were compared with available measurements from both surface-based and airborne sensors. Airborne measurements with the University of Wyoming

King Air (UWKA) were made between 2020 and 2230 UTC on 26 January and between 1350 and 1545 UTC on 5 February and include both level flight tracks as well as ramp soundings (French et al. 2015). Surface-based measurements include observations from the Medicine Bow wind profiler, located ~ 55 km north of the MBM, and a weather station at Laramie airport, some 50 km downstream of the MBM peak (Fig. 1). For comparison with the surface-based measurements, model output was extracted from the nearest-neighbor grid points to the surface sites. For the wind profiler, the model data was extracted from the outer domain, whereas for the Laramie surface station, the model data comes from the inner domain. The periods of comparison for the surface measurements for the two events extend from 1200 UTC on 26 January to 1200 UTC on 27 January and from 0600 UTC on 5 February to 0600 UTC on 6 February. For comparison with airborne measurements, the model data from the inner domain was linearly interpolated along the aircraft trajectory.

The observed and simulated vertical profiles of wind speed and direction at the Medicine Bow wind profiler are presented in Fig. 2, which shows a good agreement between simulation results and observations, in particular for 26 January. On both of these days, the passage of an upper tropospheric anomaly is apparent at altitudes between 6000 and 8000 m MSL. On 26 January, the passage of this anomaly occurs between 1400 UTC and 2200 UTC and is evident in the turning of wind from SW to NW and back to W, accompanied by a temporary drop of wind speed at these levels, all compatible with the passage of a synoptic short wave as described in French et al. (2015). The overall evolution of this event, including the timing of the wave passage, is captured well by the simulation. On 5 February, rapid wind turning from W to NNE then back to NW is evident in observations between approximately 1000 UTC and 2000 UTC. In this case, it appears there is a time lag of ~ 2 hours between the onset of the wind turning aloft in the observations and the simulation results. At low levels, the simulation results show sustained NW winds whereas

the observations display a sharp turn to the northerly wind soon after 1200 UTC and a subsequent gradual shift to the north-westerlies. By 1800 UTC, the model is starting to catch up with the observations and, by 0000 UTC the next day, the two appear to be in a fairly good agreement. Although without additional numerical experiments we cannot ascertain the cause of this delay, it is likely that the mesoscale model acquired this timing error through the initial and boundary conditions from the global model analyses.

The comparison between surface observations at the Laramie airport and model predictions for this site are shown in Fig. 3. The overall tendency of surface weather parameters is well reproduced for both events. In particular, the onset of high and sustained wind speeds between 1800 UTC on 26 January and 0000 UTC on the next day is captured almost perfectly, as is the second peak in wind speed between 0300 and 0600 UTC on 27 January. On 5 February, the simulation misses a sharp peak in wind speed at around 1400 UTC, the time of the aircraft research mission. An initial under-prediction of near-surface air temperatures is also apparent.

A comparison between the observed and simulated pseudo-vertical atmospheric profiles from the UWKA ramp soundings for the two events is shown in Fig. 4. Profiles are taken along descending flight segments, starting slightly downwind or over the top of the MBM and extending over its upwind slope. Generally, the rather coarse model resolution does not allow the small-scale spatial variability, apparent in the observations, to be resolved. However, the most important features of the 26 January event are reproduced reasonably well, including the mid-troposphere WNW wind direction, the wind veering with height in the lowest kilometer above the ground, the presence of a low-level jet with wind speeds exceeding 15 m s^{-1} (slightly overestimated by the model) and a relatively constant vertical gradient of virtual potential temperature of $\sim 4.4 \times 10^{-3} \text{ K m}^{-1}$ throughout the troposphere. The greatest differences between the model output and the ramp sounding on 26 January occur at heights above 5.5 km MSL. This range of altitudes coincides

with a flight segment in which the UWKA was flying slightly downstream of the MBM within a wave-breaking region (cf. Section 3a below).

On 5 February, there is less of an agreement between the model results and observations along the ramp sounding. Although the wind direction is reproduced reasonably well, the wind speed and temperature profiles compare less favorably. In particular, the layered structure of the observed wind speed and temperature profiles below ~ 3.2 km MSL are not captured, including a low-level jet of ~ 18 m s $^{-1}$ within a shallow neutral layer topped by a strong inversion ($\sim 16 \times 10^{-3}$ K m $^{-1}$) at 2.75 km, and a neutral layer above it with wind speed of ~ 15 m s $^{-1}$ topped by another, weaker inversion at 3.2 km MSL. Overall, at the time of the observations, the model is showing an underestimation of wind speed below 2.75 km MSL and an overestimation above this altitude. Two hours later, while the agreement of the wind speed profiles aloft improves, the discrepancy at low levels remains and even increases. Given the impact of the wind speed profile curvature (through the Scorer parameter) and of elevated inversions (Vosper 2004) on mountain wave response, it is reasonable to anticipate the simulation results for 5 February to show less favorable agreement with observations.

A comparison of observations and model output along the cross-mountain flight legs is shown in Fig. 5. To illustrate the degree of unsteadiness in the simulations, model output is represented by a set of profiles spanning a period of ± 1.5 hours around the central time. The set of simulated profiles on 26 January is centered at 2030 UTC, the time the flight leg was flown on that day, and on approximately two hours after the observations, at 1615 UTC on 5 February. The two-hour difference in the latter case accounts for the delayed evolution of the synoptic-scale flow diagnosed in that simulation.

On 26 January, the amplitude and spatial variability of vertical velocity and potential temperature perturbations along the UWKA level legs are well captured by the simulation. The descent of

potentially warmer air in the mountain wave on the lee side of the MBM, and the up- and down-draft couplet with the attendant potential temperature anomaly farther downstream, are in overall good agreement between the observations and the model output. Clearly, the observed profiles have more pronounced fine-scale structure, especially in the lee updraft/downdraft couplet of 26 January. We note also that the model underestimates the acceleration of the wind speed in the lee of the MBM.

On 5 February, both the aircraft data and the model results show evidence of short-wave perturbations along the entire flight track, both downstream of the MBM as well as upwind of it, where a short wavelength wave train generated by Elk Mountain is clearly visible. Although the amplitude of these short waves is well reproduced by the model, the horizontal wavelength appears to be less so. A large spread of the model solutions is an indication of a high degree of unsteadiness in the flow at this time. The examination of the individual model profiles shows a closer agreement between the observed and the simulated waves in the lee of Elk Mountain at the beginning of this time period, around 1630 UTC. Toward the end of this time window, a closer agreement of the observed and simulated short waves is found in the lee of the MBM. As will be discussed in Section 4, the high degree of unsteadiness in this case has implications for the location of the BL separation and the structure of the model-predicted rotors. Finally, we note that the model is predicting colder conditions upwind of the MBM and underestimating the horizontal wind speed on the lee side of the MBM in this case.

Despite the described shortcomings of the 5 February simulation, we consider the overall agreement between the observations and simulation results satisfactory. In the next two sections we use the simulation results, in particular those for the 26 January event for which the agreement is closer, to examine the dynamics of these two observed rotor events.

3. Analysis of model results: 26 January

a. Flow structure and boundary-layer separation

Vertical cross-sections of horizontal wind speed, vertical velocity, potential temperature and sub-grid-scale turbulent kinetic energy (SGS TKE) shown in Fig. 6 reveal several key features of this case. These cross-sections were extracted from the inner domain along line AB, which passes through the top of the MBM with heading of 98° from N (Fig. 1). The selected time, 2145 UTC on 26 January, best matches the time range of the available observations.

The four panels of Fig. 6 show a deep layer of the troposphere, between approximately 3 and 6 km MSL, flowing over the MBM and getting accelerated on the lee slope, forming a low-level jet that is confined to a much shallower layer underneath a deep stagnant region aloft. A warm potential temperature anomaly, near-neutral atmospheric stability, and non-zero values of SGS TKE are all associated with that deep stagnant region aloft. The almost vertical orientation of isentropes and the presence of patches of reversed flow at the height of ~ 6 km MSL (Fig. 6a), suggest that the acceleration of the downslope flow is occurring beneath a breaking mountain wave. Since there is no environmental critical level, wave breaking is likely the result of a large-amplitude mountain wave reaching the critical steepness (cf. Section 3c). The location of this model-predicted wave breaking is consistent with what was observed as described in Part I by French et al. (2015). Another region of strong downslope flow underneath a wave breaking region is evident farther downwind, on the lee slope of the Laramie Mountains.

The downslope wind front reaches some 20 km downwind from the MBM peak, where a sudden adjustment occurs through a flow region that resembles an undular hydraulic jump, with a series of short waves on top of the jump between 3 and 4 km MSL. Underneath the first of those short waves one finds a region of reversed flow near the ground. The strong flow through these short

waves appears to connect to the downslope flow on the lee slopes. These features are consistent with BLS occurring at that location at that point in time. Downward vertical motions on the steepest stretches of the lee slope, as well as strong updraft-downdraft couplets associated with short waves farther downstream ($x \approx 20$ km), are clearly visible in Fig. 6b. The structure of this vertical velocity couplet, with near-ground reversed flow underneath it, is indicative of the presence of an atmospheric rotor. While the layer of downslope flow is stably stratified, the flow within the rotor region is almost neutral (Fig. 6c). Figure 6d shows the SGS TKE and reveals higher values of SGS TKE within the boundary layer with a clearly pronounced maximum at the leading edge of the rotor region.

The vertical velocity component and SGS TKE at 2145 UTC on 26 January are shown in Fig. 7 at a horizontal plane at 3000 m MSL, which partially intersects the topography. The horizontal wind vectors in these panels clearly show a strong acceleration of the wind in the immediate lee of MBM. They also reveal a degree of flow splitting around the MBM and a distinct wake downwind of it. Strong vertical velocity perturbations are visible downwind of the MBM terrain (Fig. 7a), including a relatively wide zone of gentler downdraft that corresponds to the downslope flow, and the sharp vertical velocity couplet farther downwind associated with the rotor. The wake with reduced horizontal momentum is evident downstream of the rotor and to the north of line AB (Fig. 7a). The increased SGS TKE in the immediate lee of the mountain is most likely resulting from shear production associated with the low-level wind maximum in the downslope flow (Fig. 7b). An even more prominent SGS TKE maximum is visible farther downstream and corresponds to the leading edge of the rotor. As shown by Doyle and Durran (2002, 2007), turbulence in this zone is generated by intense shear between the detached low-level jet and the underlying approximately stagnant rotor region.

Evident in these cross-sections is the elongated structure of the vertical velocity and SGS TKE fields in the lee of the obstacle. The longitudinal axis of these bands is nearly perpendicular to the upstream wind direction and approximately parallels the mountain ridge, only the highest portion of which is visible in this figure. This suggests that three-dimensional aspects of the flow past MBM are only of secondary importance for the dynamic evolution of this event; although, not completely negligible as evidenced in the lee-side vertical velocity couplet and SGS TKE being more pronounced in the lee of the elevated northern terminal of the MBM, north of line AB, downwind of which the wake forms.

In summary, our simulation results suggest that the 26 January event is marked by the presence of a large-amplitude mountain wave over the lee slope of MBM whose breaking leads to the formation of an undular hydraulic jump at low levels, at or near the mountain top, which in turn induces the BLS and rotor formation near the surface. Given the accurate prediction of the large-amplitude mountain wave, we find that the mesoscale model simulation of this event reproduces the observed dynamical evolution of the atmospheric rotor with excellent timing. This point is further elucidated in the following section.

b. Evolution of surface fields and rotor morphology

In this section we focus our attention on the time evolution of the mountain wave and rotor signatures. Figure 8 presents a set of Hovmöller diagrams, in which the horizontal axis shows the distance along line AB (Fig. 1) and the vertical axis displays time from 1200 UTC on 26 January to 1200 UTC on 27 January, i.e., from hour 12 to hour 36 of the simulation. The MBM top is located at $x = 0$ km. The horizontal domain of these plots includes the Laramie Mountains, whose summit is at $x = 70$ km. The Laramie Valley lies between the two mountain ranges. Panels in the left column of Fig. 8 show surface fields (10-m wind and pressure perturbation), whereas panels

in the right column display vertical velocity and potential temperature at 3000 m MSL, at the horizontal surface that partially intersects the topography. The pressure perturbation in Fig. 8b is computed by reducing surface pressure to the lowest terrain height along line AB and subtracting the minimum value for all points along the line. Consequently, at all times, $p' = 0$ at the location of the pressure minima and $p' > 0$ elsewhere.

Given the along-flow orientation of cross-section AB, the normal wind component is generally negligible (not shown). Flow acceleration is apparent in the lee of both the MBM and the Laramie Mountains. Upstream blocking is visible on the windward side of both ranges before 1800 UTC on 26 January and upstream of the MBM after 0300 UTC the next day. Stationary bands of alternating positive and negative horizontal wind speed, evident after 0300 UTC over the Laramie Valley, are signatures of trapped lee waves that form there. The signature of these resonant waves is also evident in the pressure perturbation field (Fig. 8b) and vertical velocity and potential temperature fields (Figs. 8c and 8d).

Zooming in on the lee side of the MBM, one can see that the BLS point — the downslope wind front being its proxy — is anything but stationary before 0300 UTC on 27 January. On 26 January, the front extends as far as $x = 30$ km before 1800 UTC, retreats to $x = 15$ km between 1800 UTC and 2100 UTC and even farther back to $x = 10$ km shortly after 2100 UTC. This movement of the BLS point agrees remarkably well with the observations presented in Part I (French et al. 2015). The most intense near-surface reverse flow occurs immediately downstream of the BLS point at 2100 UTC, in combination with the strongest up- and downdrafts (Fig. 8c). The absence of the downdraft in the immediate lee of the MBM at 3000 m MSL around 0000 UTC 27 January is consistent with the BLS point lying farther upwind at this time, causing the flow to detach from the ground at a higher elevation. The downdraft, and the attendant downslope wind, at 3000 m MSL set in again at 0300 UTC 27 January, in connection with the onset of lee waves. It is worthwhile to

point out that the upstream shift of the BLS point in the lee coincides with a pulse of stronger wind speed on the upstream side, between 1800 UTC 26 January and 0000 UTC 27 January (Fig. 8a).

The time evolution of the near-surface winds is strongly correlated with the surface pressure perturbations and potential temperature at or near the MBM top. Strong downslope winds in the lee of the MBM persist as long as there is a significant pressure gradient across the MBM, a positive pressure anomaly upwind of the MBM and a lee-side minimum over the Laramie Valley (Fig. 8b) contributing to it. The attendant wave-induced pressure gradient force favors the flow acceleration to the west of the pressure minimum and the sharp deceleration, and eventually the detachment of the BL, to the east of it. The flow reattaches again farther downwind in the Laramie Valley. Another area of strong flow acceleration is evident in the lee of the Laramie Mountains ($x > 70$ km). The upstream shift of the BLS point is correlated with the upwind retreat of the lee-side pressure minimum in the lee of the MBM. Concurrent with that is a contraction and disappearance of a pronounced lee-side warm potential temperature anomaly, which is clearly evident at 3000 m MSL before 1800 UTC on 26 January. After that time, a much colder air mass appears to move into the area, in conjunction with a strong pulse of momentum between 1800 UTC 26 January and 0000 UTC 27 January.

The results presented so far suggest that the unsteadiness in the low-level flow around 2145 UTC on 26 January documented by French et al. (2015), coincides with a change in the mountain wave regime, i.e., with a transition from a large-amplitude mountain wave (up to ~ 2100 UTC 26 January) to resonant trapped lee waves (after ~ 0300 UTC 27 January). The observed upstream shift of the BLS point happens as the primary wave vanishes and before steady resonant lee waves develop.

In Fig. 9 we illustrate and contrast these two wave regimes. Whereas at 2000 UTC 26 January (Fig. 9a) the lee side flow is characterized by the breaking gravity wave above the MBM

lee slopes and the hydraulic jump at low levels, at 0400 UTC 27 January (Fig. 9b) the isentropes over the Laramie Valley show a regular structure of trapped lee waves. From these cross-sections it is evident that the MBM and the Laramie Mountains form a double ridge, which shapes the flow response over the Laramie Valley and on the lee side of both mountain ranges. As shown by Grubišić and Stiperski (2009), the horizontal wavelength of lee waves that form in between two ridges that are close or equal in height corresponds to one of higher harmonics of the primary orographic wavelength, which is equal to the ridge separation distance. This process produces a lee wave spectrum that, while dictated by the atmospheric vertical structure, is fine-tuned by the orographic spectrum, and leads to an integer number of wave crests over the valley. Although the ratio of heights of the two ridges here is closer to 1/3, the same dynamics appears to be at play, causing five wave crests to form in between the two ridges at this time (Fig. 9b). Furthermore, a strongly asymmetric flow in the lee of the downstream ridge, associated with high drag, is indicative of constructive interference of lee wave trains generated by the two obstacles (Stiperski and Grubišić 2011).

In order to illustrate vorticity dynamics in these two wave regimes, in Fig. 9 we show also the span-wise vorticity component, $\eta = \partial u / \partial z - \partial w / \partial x$. In both of these regimes, strong shear-generated positive (clockwise) BL vorticity is evident. The positive vorticity sheet conforms to the terrain up to the lee-side separation point. At that location, the BL vortex sheet detaches from the ground and becomes a free vortex sheet that forms the leading edge of the rotor. In Fig. 9b, the identity of that detached BL vortex sheet can be traced through several lee-wave crests and rotors downwind. Above the boundary layer in both of these regimes, one finds negative values of vorticity embedded within the waves. Negative (counterclockwise) vorticity is generated there by strong positive buoyancy gradients across the stable layer, between the strongly accelerated downslope flow and the weaker flow above it. The magnitude of the baroclinically-generated

vorticity is much higher within the large-amplitude mountain wave than within the resonant lee waves. As a consequence, the former overturns and breaks, as evidenced by a patchy structure of vorticity and isentropes that curl backward over themselves (Fig. 9a), as opposed to isentropes that smoothly follow the wave pattern in the lee waves (Fig. 9b).

c. Upstream environment and downstream response

The dynamical evolution of the lee-side flow, described in the previous section, can be understood by examining the time evolution of the upstream environment. To aid in this examination, Figs. 10 and 11 display the temporal change of the wind speed and stability profiles at points $p1$ and $p3$ (Fig. 1), upstream and downstream of the MBM, respectively. Point $p3$ corresponds to the location where a rapid upstream motion of the rotor was detected between 2130 and 2200 UTC in the UWKA measurements (French et al. 2015).

At point $p1$ (Fig. 10), the rotation of the horizontal wind vector, due to the passage of a short wave described in Section 2b, causes the cross-section parallel wind component to increase in strength in a deep layer between 3 and 5 km between 1800 UTC 26 January and 0300 UTC the next day. An attendant low-level jet is also evident as a pulse of stronger wind around 2100 UTC on 26 January with a maximum of $\sim 18 \text{ m s}^{-1}$ at $\sim 3000 \text{ m MSL}$. The near-surface flow appears to react quickly to this forcing. While both before 1800 UTC on 26 January and after 0300 UTC on 27 January, blocking is present at $p1$ below 3000 m MSL due to stable stratification in the BL, in between these times, enhanced BL shear due to the low-level jet and the downward mixing of momentum seem sufficient to erode the stable layer near the surface. Consequently, the whole upstream air column flows over the MBM.

The results reported in Section 3b suggest that a large-amplitude mountain wave forms above the lee slopes of MBM and breaks there at mid-tropospheric altitudes between 1800 UTC and 2100

UTC 26 January. The upstream wind was approximately parallel to line AB during this time and the cross-section-parallel wind component shown in Fig. 10a confirms that there is no mean-state critical level for gravity waves above $p1$. Before 1800 UTC, on the other hand, it appears as if there is a mean-state critical level at 8 km MSL with small negative values of cross-section-parallel wind between 8 and 10 km MSL. However, given that the upper- and lower-level winds at that time were, respectively, from S and WSW, the zero wind line in this cross-section does not represent a critical level for gravity waves generated by the flow over the MBM at that time. Consequently, as previously hypothesized, wave breaking between 1800 and 2100 UTC on 26 January must have resulted from waves reaching their critical steepness and overturning above the lee slopes.

The local non-dimensional mountain height NH/u shown in Fig. 10c, which is computed by keeping H constant (and equal to 1350 m, the approximate height difference between the MBM top and the surrounding plain) and by using the local values of section-parallel wind speed u and stratification N , confirms this conjecture. Since flow past the MBM shows some three-dimensional characteristics, we assume that NH/u exceeding a threshold value of unity is a good indicator that wave breaking aloft can be expected (Baines 1997). From Fig. 10c, it is evident that NH/u is larger than unity throughout the air column before 1900 UTC, in fair agreement with the estimate of $NH/u \approx 1.3$ obtained from the UWKA ramp soundings (French et al. 2015). Subsequently, and starting at low levels, NH/u decreases below the critical threshold due to a combined effect of increasing wind speed and decreasing stratification and leads to the cessation of mid-tropospheric wave breaking.

The onset of lee waves hours later is likely related to the presence of an almost neutral layer above 6000 m MSL between 2100 UTC 26 January and 0600 UTC 27 January, which appears right after the passage of the upper-tropospheric wave. In conjunction with the positive vertical

shear of the wind profile (Fig. 10b), the neutral layer aloft acts to trap wave energy at lower levels, leading to the formation of lee waves.

The response of the flow downstream of the MBM peak, at point $p3$, is illustrated in Fig. 11. Shallow, stably stratified, strong downslope flow is apparent there until 2100 UTC 26 January. The strength of the downslope flow increases with the onset of wave breaking at this location between 1800 and 2100 UTC on 26 January. Wave breaking is evidenced through stagnation, static instability and a low gradient Richardson number ($Ri_g = (g/\theta)(\partial\theta/\partial z)/[(\partial u/\partial z)^2 + (\partial v/\partial z)^2]$) between 4 and 6 km MSL. As wave breaking ceases, the downstream extent of the downslope flow decreases and remains confined to higher levels on the mountain flank. As a consequence, point $p3$, which was embedded in downslope flow until ~ 2100 UTC, finds itself within the rotor region later on. Low wind speeds, high turbulence and neutral stability within the rotor region are apparent between 2100 UTC 26 January and 0300 UTC 27 January. During this period, the separated BL flow is clearly evident above the rotor.

The preceding discussion emphasizes the role that the *upstream* environment plays in the wave and rotor dynamics. However, recent studies point out that a significant modulation of these phenomena can be caused by changes in the atmospheric environment on the *downstream* side of the primary orographic obstacle. In particular, the diurnal cycle of the downstream BL, with the attendant periodic variations of the lee-side atmospheric stability, has been shown to have a dramatic impact on the penetration of downslope winds along the lee slope and on the amplitude of mountain waves (Jiang and Doyle 2008; Mayr and Armi 2010), in particular in the afternoon hours.

Given that the local sunrise and sunset in this area on January 26 occur at 1415 UTC and 0015 UTC, the most interesting part of the 26 January event fell during the afternoon hours. In order to examine whether the BL diurnal cycle plays a role in the 26 January event, a sensitivity test with

zero surface heat fluxes was performed. The results (not shown) were not appreciably different from the control run. Both the intensity of the downslope flow and the overall evolution of the event were substantially unchanged. Given low sensible heat fluxes (generally $< 50 \text{ W m}^{-2}$) on a cold winter day, this result is not surprising.

4. Analysis of model results: 5 February

As discussed in Section 2b, the simulation of the 5 February event agrees less favorably with observations (Figs. 2–5). Bearing in mind discrepancies between the observations and the simulation results described in Section 2b, we focus the discussion here on the overall dynamic evolution of this event.

Vertical cross-sections along line CD, which is parallel to the mean flow and the cross-mountain flight legs on 5 February (Fig. 1), are shown in Fig. 12 at four different times during the course of this event. Two additional orographic obstacles are visible in this transect: Elk Mountain, located $\sim 35 \text{ km}$ upstream, and Sheep Mountain, $\sim 25 \text{ km}$ downstream of the MBM (centered at $x = 0$). At the time of airborne observations on 5 February (1430 UTC, Fig. 12a), there are only minor perturbations in the flow over the three peaks. Partially blocked flow upstream of the Sheep Mountain is apparent, but there is no evidence of flow reversal there or anywhere else between the MBM and Sheep Mountain. Two hours later (1630 UTC, Fig. 12b), the flow is much more perturbed, with short waves in the lee of Elk Mountain, an incipient wave overturning and the flow stagnation between 5000 and 6000 m MSL over the MBM lee slope, and another strong set of perturbations in the lee of Sheep Mountain. At this time, the model is predicting near-surface flow reversal in the lee of both the MBM and Sheep Mountain. Taking the two-hour delay in the onset of the simulated short-wave passage into account, this flow should roughly correspond to what was observed. Yet, at this time, there is no evidence in the simulation results of smooth lee

waves between the MBM and Sheep Mountain as reported by French et al. (2015). Furthermore, the location of the flow reversal and the simulated rotor do not appear to match the observations either, i.e., the model places the rotor at ~ 20 km downstream of the MBM summit instead of ~ 10 km as indicated by the measurements (cf. Fig. 5 and Fig. 9 in French et al. (2015)).

The examination of the temporal evolution of the key atmospheric parameters along line CD, shown in Fig. 13, provides further insight into the temporal evolution of the simulated flow. From Fig. 13 it is evident that the reversed flow at this particular location ($x \approx 20$ km) in the lee of the MBM is strongest at 1630 UTC and that the front of the downslope flow, which forms the leading edge of the rotor at 1630 UTC, shifts upwind in time and weakens between 1600–1800 UTC (Fig. 13a). As is the case with the January 26 event, this retreat is concurrent with the erosion of a pressure minimum (Fig. 13b) and the dissolution of an elevated positive potential temperature anomaly in the lee of the MBM after 1630 UTC (Fig. 13d). Both of these are associated with a large-amplitude mountain wave that becomes critically steep and overturns in the altitude range 4000–6000 m MSL above the MBM lee slopes between 1600–1800 UTC. In addition, an overall cooling starts at that time as a much colder air mass moves into the area (Fig. 13d). Concurrent with the wave breaking occurring aloft above the MBM lee slopes, the flow over the valleys, both upwind and downwind of the MBM, rearranges into a series of shorter trapped lee waves (1800 UTC, Fig. 12c). These simulated short waves are not strong enough to induce BLS and surface flow reversal in either the lee of Elk Mountain or the MBM (Fig. 13b). Although lacking the smoothness and strength of the observed waves, these short wave perturbations in the lee of the MBM bear more resemblance to the flow documented by French et al. (2015) than the flow at the time of the aircraft observations. As noted in Section 2b, the horizontal wavelength of short waves in the lee of Elk Mountain is closer to that observed at 1630 UTC, and in the lee of the MBM at 1800 UTC, although the flow in the lee of the MBM continues to be unsettled at that

time. The BLS and the surface flow reversal in the lee of the MBM re-emerge again around 1930 UTC on the upper MBM lee slopes, after a steady short lee wave pattern has set up there as well, over the valley in between the MBM and Sheep Mountain (1930 UTC, Fig. 12d). These trapped lee waves are shorter than those observed and persist throughout the remainder of the simulation period, producing intermittent surface reversals there (Fig. 13a).

As in the January 26 case, the upwind retreat of the BLS point is associated with mid-tropospheric wave breaking. In this case, the timing of the wave breaking is determined by the changing characteristics of the upstream environment aloft, after approximately 1500 UTC. Those characteristics include the wind speed that decreases with height (Fig. 14a), a stable layer centered at approximately 5 km MSL, and a layer of low stability above it (Fig. 14b). These elements combined lead to the increase of local non-linearity in the 4000–6000 m MSL layer, which promotes wave breaking (Fig. 14c).

To further elucidate the differences between the observed and the simulated vertical atmospheric structure on 5 February as it pertains to conditions conducive to trapped lee wave formation, in Fig. 15 we compare the observed and simulated vertical profiles of the wind speed and the Scorer parameter at point *p4*, above the Saratoga Valley, at 1430 UTC and 1630 UTC on 5 February with the profile derived from the observations. The Scorer parameter, which depends on the first derivative of potential temperature and on the second derivative of wind speed, was estimated after treating the original profiles with a low-pass filter. The observations on 5 February suggest that trapped lee waves were present downstream of the MBM between 1400 UTC and 1500 UTC and that the ducting mechanism was related to the curvature (a minimum) of the wind profile, causing a marked decrease of the squared Scorer parameter ($\ell^2 = N^2/u^2 - u^{-1} \partial^2 u / \partial z^2$) with height above 3800 m MSL (cf. Fig. 4 in French et al. (2015)). Curvature effects are indeed non-negligible in this case and, in both the profiles derived from the observations and the simulation, local minima of

the wind speed profile correlate very well with local minima of ℓ^2 . Furthermore, several elevated layers with decreasing ℓ^2 (and occasionally even with $\ell^2 < 0$) are apparent in the observed profile, which is known to lead to wave energy trapping (e.g., Crook 1986). Comparing the profiles derived from the model simulation with that derived from the observations in Figs. 15a,b, it is evident that although both the 1430 UTC and 1630 UTC model Scorer parameter profiles show a layered structure, neither matches the one derived from observations particularly well. Perhaps the closest match to the observed profile, at least qualitatively, is shown by the model around 1200 UTC, two hours ahead of the time of the observations (cf. Fig. 15c).

Finally, we comment on the structure of the lee wave field at 1930 UTC illustrated in Fig. 12d. As previously discussed, by that time the short trapped lee wave train had formed on the stable layer centered at 5 km MSL over the valleys, both upwind and downwind of the MBM peak. There appears to be a positive interference or resonance of lee waves between Elk Mountain and the MBM, which, according to Stiperski and Grubišić (2011), produces a strong asymmetric flow field in the lee of the second mountain (here MBM) and a large-amplitude wave response there. In contrast, flow downwind of Sheep Mountain is rather disorganized and flat at times, suggesting that a negative interference occurs there.

5. Summary and Conclusions

The present study reports on the numerical simulations of complex mountain-wave and rotor events observed in the lee of the Medicine Bow Mountains (MBM) in southeastern Wyoming on 26 January and 5 February 2006, and complements the description of observational results provided in Part I (French et al. 2015).

Using high-resolution numerical simulations with the WRF model, we demonstrate that the documented rotor events occurred during a complex transitional phase between different flow regimes

in the lee of the MBM. The transition between strong downslope winds with hydraulic jumps and trapped lee waves in the lee of the MBM occurred in both of the examined events in response to a rapid change in the upstream environment, associated with the passage of a short-wave synoptic disturbance aloft. The rotor and the attendant surface flow reversal in the 26 January case formed underneath an undular hydraulic jump, at the downstream end of a downslope windstorm. In the 5 February case, the same type of rotor was simulated in the early stages of the event. Yet, it appears that the observations on this day were collected during the subsequent transition into the trapped lee-wave regime. In both of these events, the lee-side rotors and surface-flow reversal were associated with wave-induced boundary-layer separation. The observed and simulated upwind shift of the boundary-layer separation point was related to the erosion of the pressure minimum on the lee side of the MBM, in response to the evolution of the wave field aloft.

The model simulation successfully reproduced the dynamical evolution of the 26 January event and generated results that are in good agreement with the observations, both in space and in time. The simulation of the 5 February event, which evolves in a strikingly similar manner to the 26 January one, is in poorer agreement with the observations. In part, this disagreement stems from the delay in the model simulation of the passage of the synoptic short wave — a timing error that the mesoscale model likely acquired through the initial and boundary conditions from the global model analyses. The difference in the fidelity of these two simulations, in both of which the predicted transition between different wave regimes is related to the wave breaking aloft, is an excellent illustration of a strong sensitivity that numerical simulations of the terrain-induced flows display to initial conditions (Doyle and Reynolds 2008; Reinecke and Durran 2009; Doyle et al. 2011)

In both of these events, the simulation results indicate that the secondary orographic obstacles surrounding the Medicine Bow Mountains, including Elk Mountain, Sheep Mountain and the

Laramie Mountains, play a role in promoting the resonance of lee waves that are well known to form frequently in flow over the complex terrain of SE Wyoming (Marwitz and Dawson 1984).

Acknowledgments. This study was initiated under the collaborative NSF grants between the University of Wyoming (ATM-0742147) and the Desert Research Institute (ATM-0742110). Additional support was provided by the NASA EPSCoR-3412 grant to the University of Wyoming and by the FWF (Austrian Science Fund) grant P24726-N27 (Stable Boundary Layer Separation and Turbulence - STABLEST) to the University of Vienna. Access to the ECMWF data was provided through the Zentralanstalt für Meteorologie und Geodynamik, Austria. The authors thank Rich Rotunno and Jimmy Dudhia for helpful discussions and their suggestions and three anonymous reviewers for their comments. NCAR is sponsored by the National Science Foundation.

References

- Ambaum, M. H., and D. P. Marshall, 2005: The effects of stratification on flow separation. *J. Atmos. Sci.*, **62**, 2618–2625.
- Baines, P. G., 1997: *Topographic Effects in Stratified Flows*. Cambridge University Press, 500 pp.
- Baines, P. G., and K. P. Hoinka, 1985: Stratified flow over two-dimensional topography of fluid of infinite depth: A laboratory simulation. *J. Atmos. Sci.*, **42**, 1614–1630.
- Batchelor, G., 1967: *An introduction to fluid dynamics*. Cambridge University Press.
- Crook, N. A., 1986: The effect of ambient stratification and moisture on the motion of atmospheric undular bores. *J. Atmos. Sci.*, **43**, 171–181.
- De Wekker, S. F. J., 2002: Structure and morphology of the convective boundary layer in mountainous terrain. Ph.D. thesis, Department of Earth and Ocean Sciences, University of British Columbia, Vancouver.

- Doyle, J. D., and D. R. Durran, 2002: The dynamics of mountain-wave-induced rotors. *J. Atmos. Sci.*, **59**, 186–201.
- Doyle, J. D., and D. R. Durran, 2007: Rotor and subrotor dynamics in the lee of three-dimensional terrain. *J. Atmos. Sci.*, **64**, 4202–4221.
- Doyle, J. D., and C. A. Reynolds, 2008: Implications of regime transitions for mountain-wave-breaking predictability. *Mon. Wea. Rev.*, **136**, 5211–5223.
- Doyle, J. D., and Coauthors, 2011: An intercomparison of T-REX mountain-wave simulations and implications for mesoscale predictability. *Mon. Wea. Rev.*, **139**, 2811–2831.
- Dudhia, J., 1989: Numerical study of convection observed during the Winter Monsoon Experiment using a mesoscale two-dimensional model. *J. Atmos. Sci.*, **46**, 3077–3107.
- French, J., S. Haimov, L. Oolman, V. Grubišić, S. Serafin, and L. Strauss, 2015: Wave-induced boundary-layer separation in the lee of the Medicine Bow Mountains. Part I: Observations. *J. Atmos. Sci.*, submitted.
- Gohm, A., G. J. Mayr, A. Fix, and A. Giez, 2008: On the onset of bora and the formation of rotors and jumps near a mountain gap. *Quart. J. Roy. Meteor. Soc.*, **134**, 21–46.
- Grubišić, V., and B. J. Billings, 2007: The intense lee-wave rotor event of Sierra Rotors IOP 8. *J. Atmos. Sci.*, **64**, 4178–4201.
- Grubišić, V., and Coauthors, 2008: The Terrain-induced Rotor Experiment. *Bull. Amer. Meteor. Soc.*, **89**, 1513–1533.
- Grubišić, V., and I. Stiperski, 2009: Lee-wave resonances over double bell-shaped obstacles. *J. Atmos. Sci.*, **66**, 1205–1228.

- Hertenstein, R. F., and J. P. Kuettner, 2005: Rotor types associated with steep lee topography: Influence of the wind profile. *Tellus A*, **57**, 117–135.
- Janjić, Z. I., 2002: Nonsingular implementation of the Mellor-Yamada level 2.5 scheme in the NCEP meso model. Tech. rep., NCEP, National Centers for Environmental Prediction, Office Note No. 437.
- Jiang, Q., and J. D. Doyle, 2008: Diurnal variation of downslope winds in Owens Valley during the Sierra Rotor experiment. *Mon. Wea. Rev.*, **136**, 3760–3780.
- Jiang, Q., J. D. Doyle, and R. B. Smith, 2006: Interaction between trapped waves and boundary layers. *J. Atmos. Sci.*, **63**, 617–633.
- Jiang, Q., J. D. Doyle, S. Wang, and R. B. Smith, 2007: On boundary layer separation in the lee of mesoscale topography. *J. Atmos. Sci.*, **64**, 401–420.
- Knigge, C., D. Etling, A. Paci, and O. Eiff, 2010: Laboratory experiments on mountain-induced rotors. *Quart. J. Roy. Meteor. Soc.*, **136**, 442–450.
- Laprise, R., 1992: The Euler equations of motion with hydrostatic pressure as an independent variable. *Mon. Wea. Rev.*, **120**, 197–207.
- Lighthill, J., 1986: *An informal introduction to theoretical fluid mechanics*. Clarendon Press.
- Mahrer, Y., 1984: An improved numerical approximation of the horizontal gradients in a terrain-following coordinate system. *Mon. Wea. Rev.*, **112**, 918–922.
- Marwitz, J. D., and P. J. Dawson, 1984: Low-level airflow in southern Wyoming during winter-time. *Mon. Wea. Rev.*, **112**, 1246–1262.

- Mayr, G. J., and L. Armi, 2010: The influence of downstream diurnal heating on the descent of flow across the Sierras. *J. Appl. Meteor. Climatol.*, **49**, 1906–1912.
- Mlawer, E., S. Taubman, P. Brown, M. Iacono, and S. Clough, 1997: Radiative transfer for inhomogeneous atmospheres: RRTM, a validated correlated-k model for the longwave. *J. Geophys. Res.*, **102(D14)**, 16 663–16 682.
- Mobbs, S. D., and Coauthors, 2005: Observations of downslope winds and rotors in the Falkland Islands. *Quart. J. Roy. Meteor. Soc.*, **131**, 329–351.
- Morrison, H., G. Thompson, and T. V., 2009: Impact of cloud microphysics on the development of trailing stratiform precipitation in a simulated squall line: Comparison of one- and two-moment schemes. *Mon. Wea. Rev.*, **137**, 991–1007.
- Reinecke, P. A., and D. R. Durran, 2009: Initial-condition sensitivities and the predictability of downslope winds. *J. Atmos. Sci.*, **66**, 3401–3418.
- Scorer, R., 1958: *Natural Aerodynamics*. Pergamon Press, 312 pp.
- Sheridan, P. F., V. Horlacher, P. Rooney, G. G. ad Hignett, S. D. Mobbs, and S. B. Vosper, 2007: Influence of lee waves on the near-surface flow downwind of the Pennines. *Quart. J. Royal. Meteor. Soc.*, 1353–1369.
- Skamarock, W., and J. Klemp, 2008: A time-split nonhydrostatic atmospheric model for weather research and forecasting applications. *J. Comput. Phys.*, **227**, 3465–3485.
- Smith, R. B., 2007: Interacting mountain waves and boundary layers. *J. Atmos. Sci.*, **64**, 594–607.
- Smith, R. B., Q. Jiang, and J. D. Doyle, 2006: A theory of gravity wave absorption by a boundary layer. *J. Atmos. Sci.*, **63**, 774–781.

- Stiperski, I., and V. Grubišić, 2011: Trapped lee wave interference in the presence of surface friction. *J. Atmos. Sci.*, **68**, 918–936.
- Strauss, L., S. Serafin, S. Haimov, and V. Grubišić, 2015: Turbulence in breaking mountain waves and atmospheric rotors from airborne in situ and Doppler radar measurements. *Quart. J. Royal. Meteor. Soc.*, Conditionally Accepted.
- Vosper, S. B., 2004: Inversion effects on mountain lee waves. *Quart. J. Roy. Meteor. Soc.*, **130**, 1723–1748.
- Vosper, S. B., P. F. Sheridan, and A. Brown, 2006: Flow separation and rotor formation beneath two-dimensional trapped lee waves. *Quart. J. Roy. Meteor. Soc.*, **132**, 2415–2438.
- Wyngaard, J. C., 2004: Toward numerical modeling in the “Terra Incognita”. *J. Atmos. Sci.*, **61**, 1816–1826.

LIST OF FIGURES

- Fig. 1.** Map of the area of the Medicine Bow Mountains (MBM), Wyoming. The gray shading represents the ground elevation. The inner domain ($d02$) is enclosed within a dashed rectangle. The thick black lines AB and CD are parallel to the cross-mountain flight legs flown, respectively, on 26 January and 5 February 2006, and mark the position of vertical cross sections presented later in the paper. Points $p1$, $p2$ and $p3$ along cross-section AB mark the locations of three vertical profiles extracted from the model output for 26 January. $p1$, upstream of the MBM, coincides with the Saratoga airport, $p2$ is at the top of the MBM, $p3$ is the point at which unsteady wave-induced BLS was observed in the lee. Point $p4$ refers to the location of upstream profiles taken on 5 February. Surface-based observations are available at points LAR (Laramie airport) and MBWW4 (Medicine Bow wind profiler). Cross-section CD intersects two secondary orographic obstacles, the Elk Mountain and the Sheep Mountain located, respectively, NW and SE of the MBM. 33
- Fig. 2.** Observations from the Medicine Bow wind profiler (top) and vertical profiles of model output at the nearest-neighbor grid point in the outer domain ($d01$) (bottom). The panels display 24-hour periods starting at 12 UTC on 26 January (left) and at 06 UTC on 5 February 2006 (right). The color bar shows horizontal wind speed in m s^{-1} 34
- Fig. 3.** Comparison of measured (red) and simulated (blue) atmospheric parameters at the Laramie airport surface weather station (LAR in Fig. 1) for 24-hour periods starting at 12 UTC on 26 January (left) and at 06 UTC on 5 February 2006 (right). 35
- Fig. 4.** Comparison of measured (red) and simulated (blue) atmospheric parameters along the descending ramp soundings flown over the Medicine Bow Range between 1925 and 1939 UTC on 26 January 2006 (top) and between 1422 and 1435 UTC on 5 February 2006 (bottom). A slight kink at 4000 m MSL in the measured profiles for 26 January corresponds to a short stretch of horizontal flight by the UWKA at that altitude. For the 5 February 2006 case, the continuous and dashed blue lines refer to model output respectively at the time of observations and two hours later. 36
- Fig. 5.** Comparison of measured (red) and simulated (blue) atmospheric parameters along cross-mountain flight legs over the Medicine Bow Range between 2026 and 2037 UTC on 26 January (left) and between 1407 and 1422 UTC on 5 February 2006 (right). The model output is shown every 15 minutes in a ± 1.5 hrs window centered at the time of the observations (2030 UTC) on 26 January and two hours after the time of observations (1615 UTC) on 5 February. 37
- Fig. 6.** Vertical cross-sections from inner domain along line AB at 2145 UTC on 26 January 2006. (a) cross-section parallel wind component (m s^{-1}), (b) vertical velocity (m s^{-1}), (c) vertical gradient of potential temperature (K m^{-1}), and (d) **SGS** TKE ($\text{m}^2 \text{s}^{-2}$). Isentropes at the interval of 2K are shown in all panels. Red dashed line indicates the height of the horizontal flight legs on 26 January (~ 5200 m MSL). 38
- Fig. 7.** Horizontal cross-sections at $z = 3000$ m MSL from inner domain at 2145 UTC on 26 January 2006. (a) Vertical velocity (m s^{-1}), and (b) **SGS** TKE ($\text{m}^2 \text{s}^{-2}$). Hatching indicates the intersection of $z = 3000$ m surface with the topography. Horizontal wind vectors at $z = 3000$ m MSL are overlaid in both panels. 39
- Fig. 8.** Hövmöller diagrams ($x-t$) illustrating the evolution of atmospheric parameters on 26 January 2006 along line AB. (a) Section-parallel 10-m wind speed (m s^{-1}), (b) surface pressure perturbation (hPa), (c) vertical velocity (m s^{-1}), and (d) potential temperature (K). Fields

- in panels (c) and (d) are shown at $z = 3000$ MSL. Hatching in these two panels indicates the intersection with the terrain. The MBM top lies at $x = 0$. Horizontal lines in all panels delimit the period during which airborne measurements were taken. 40
- Fig. 9.** Isentropes (K) and spanwise vorticity component η (s^{-1}) in the vertical cross-section along line AB from inner domain at (a) 2000 UTC on 26 January, and (b) 0400 UTC on 27 January 2006. 41
- Fig. 10.** Hövmöller diagrams (t - z) of the temporal evolution of the upstream atmospheric structure on 26 January 2006 at point $p1$ (Fig. 1). (a) Wind component parallel to section AB (m s^{-1}), (b) Brunt-Väisälä frequency (s^{-1}), and (c) local nonlinearity parameter NH/u . Vertical lines delimit the period during which airborne measurements were taken. 42
- Fig. 11.** As in Fig. 10 but for point $p3$. Panel (c) shows the gradient Richardson number Ri_g 43
- Fig. 12.** Vertical cross-sections of the wind component parallel to line CD at (a) 1430 UTC, (b) 1630 UTC, (c) 1800 UTC, and (d) 1930 UTC on 5 February 2006. Red lines indicate the height of horizontal flight legs on 5 February (~ 4200 m MSL). 44
- Fig. 13.** As in Fig. 8 but for line CD on 5 February 2006. Horizontal lines in all panels delimit the time period from 1350 UTC to 1545 UTC, during which airborne measurements were taken. Hatched vertical line at $x = -50$ km represents Elk Mountain. 45
- Fig. 14.** As in Fig. 10 but for point $p4$ on 5 February 2006. 46
- Fig. 15.** Vertical profiles of (a) track-parallel wind speed (m s^{-1}), and (b) Scorer parameter ℓ^2 (m^{-2}) on 5 February 2006 at point $p4$ in the Saratoga Valley. Thick red lines show observations at ~ 1430 UTC. Thin black lines show model predictions at 1430 UTC (solid) and 1630 UTC (dashed). (c) Hövmöller diagram of the temporal evolution of the Scorer parameter in the model simulation. Vertical lines mark the times of the model profiles shown in panels (a) and (b). 47

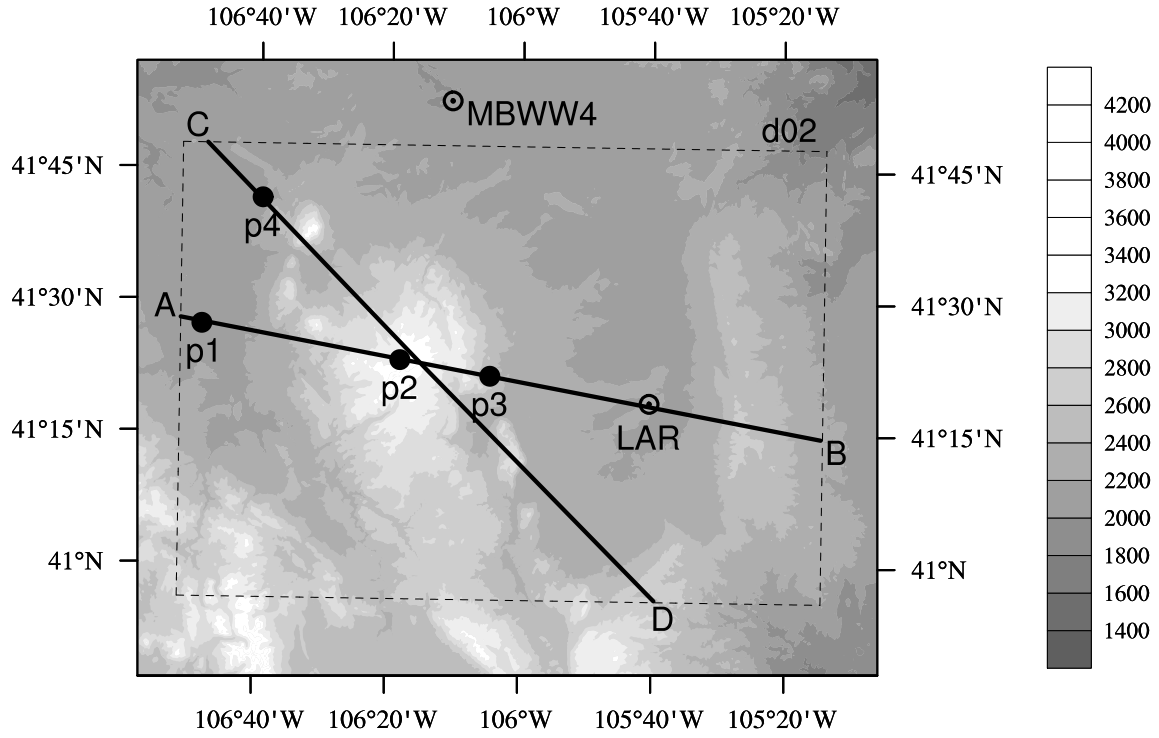


FIG. 1. Map of the area of the Medicine Bow Mountains (MBM), Wyoming. The gray shading represents the ground elevation. The inner domain (*d02*) is enclosed within a dashed rectangle. The thick black lines AB and CD are parallel to the cross-mountain flight legs flown, respectively, on 26 January and 5 February 2006, and mark the position of vertical cross sections presented later in the paper. Points *p1*, *p2* and *p3* along cross-section AB mark the locations of three vertical profiles extracted from the model output for 26 January. *p1*, upstream of the MBM, coincides with the Saratoga airport, *p2* is at the top of the MBM, *p3* is the point at which unsteady wave-induced BLS was observed in the lee. Point *p4* refers to the location of upstream profiles taken on 5 February. Surface-based observations are available at points LAR (Laramie airport) and MBWW4 (Medicine Bow wind profiler). Cross-section CD intersects two secondary orographic obstacles, the Elk Mountain and the Sheep Mountain located, respectively, NW and SE of the MBM.

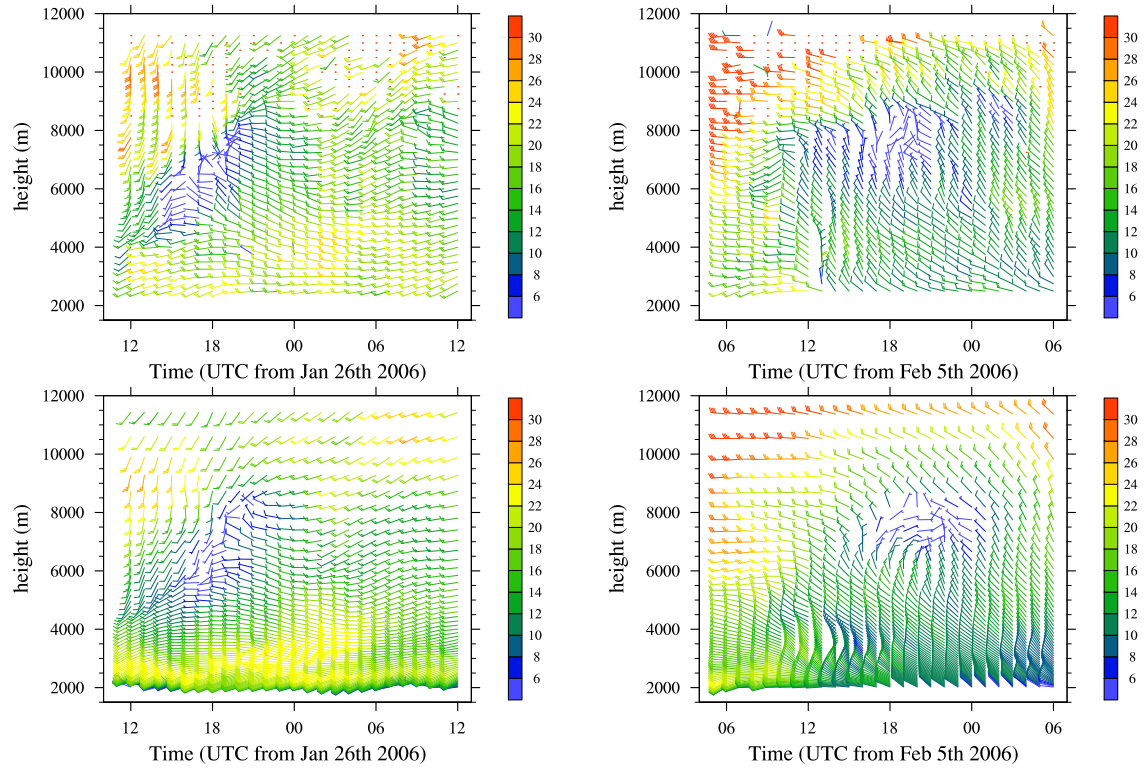


FIG. 2. Observations from the Medicine Bow wind profiler (top) and vertical profiles of model output at the nearest-neighbor grid point in the outer domain (*d01*) (bottom). The panels display 24-hour periods starting at 12 UTC on 26 January (left) and at 06 UTC on 5 February 2006 (right). The color bar shows horizontal wind speed in m s^{-1} .

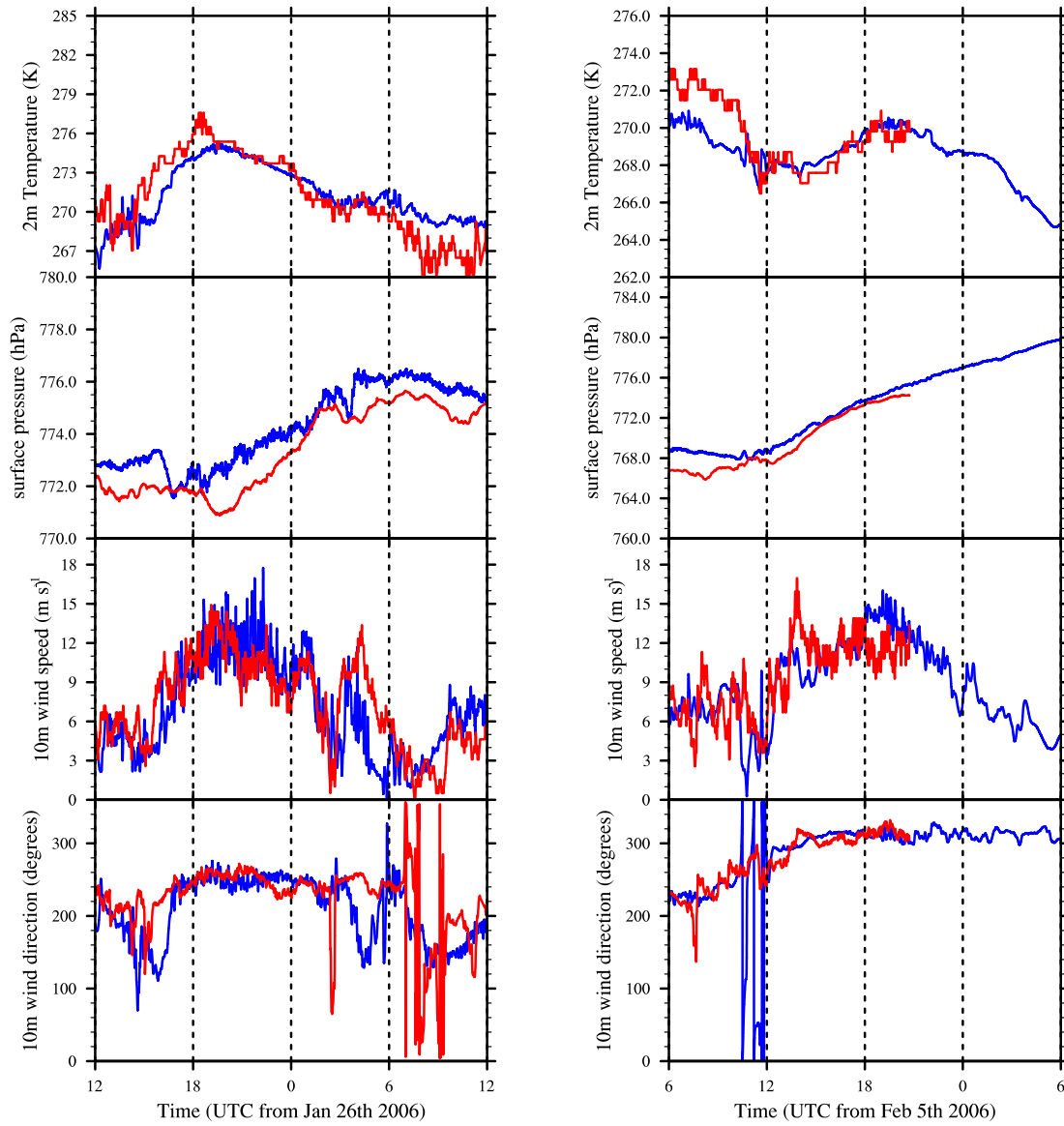


FIG. 3. Comparison of measured (red) and simulated (blue) atmospheric parameters at the Laramie airport surface weather station (LAR in Fig. 1) for 24-hour periods starting at 12 UTC on 26 January (left) and at 06 UTC on 5 February 2006 (right).

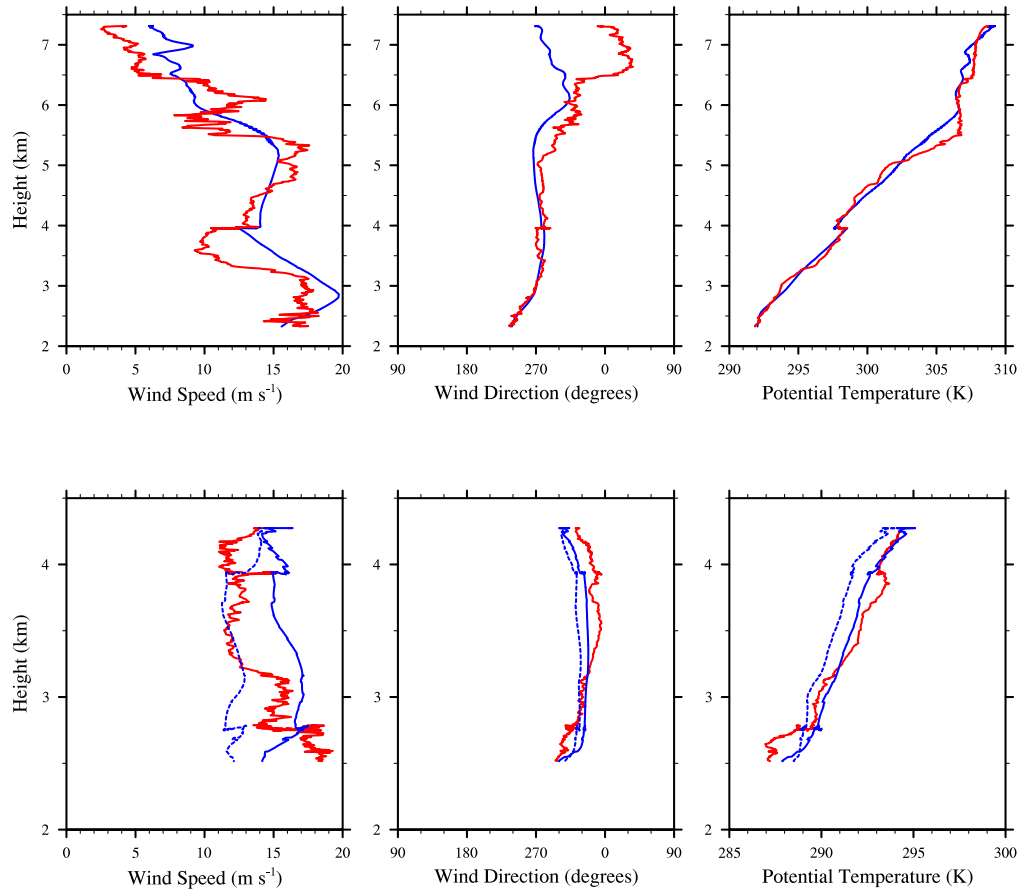


FIG. 4. Comparison of measured (red) and simulated (blue) atmospheric parameters along the descending ramp soundings flown over the Medicine Bow Range between 1925 and 1939 UTC on 26 January 2006 (top) and between 1422 and 1435 UTC on 5 February 2006 (bottom). A slight kink at 4000 m MSL in the measured profiles for 26 January corresponds to a short stretch of horizontal flight by the UWKA at that altitude. For the 5 February 2006 case, the continuous and dashed blue lines refer to model output respectively at the time of observations and two hours later.

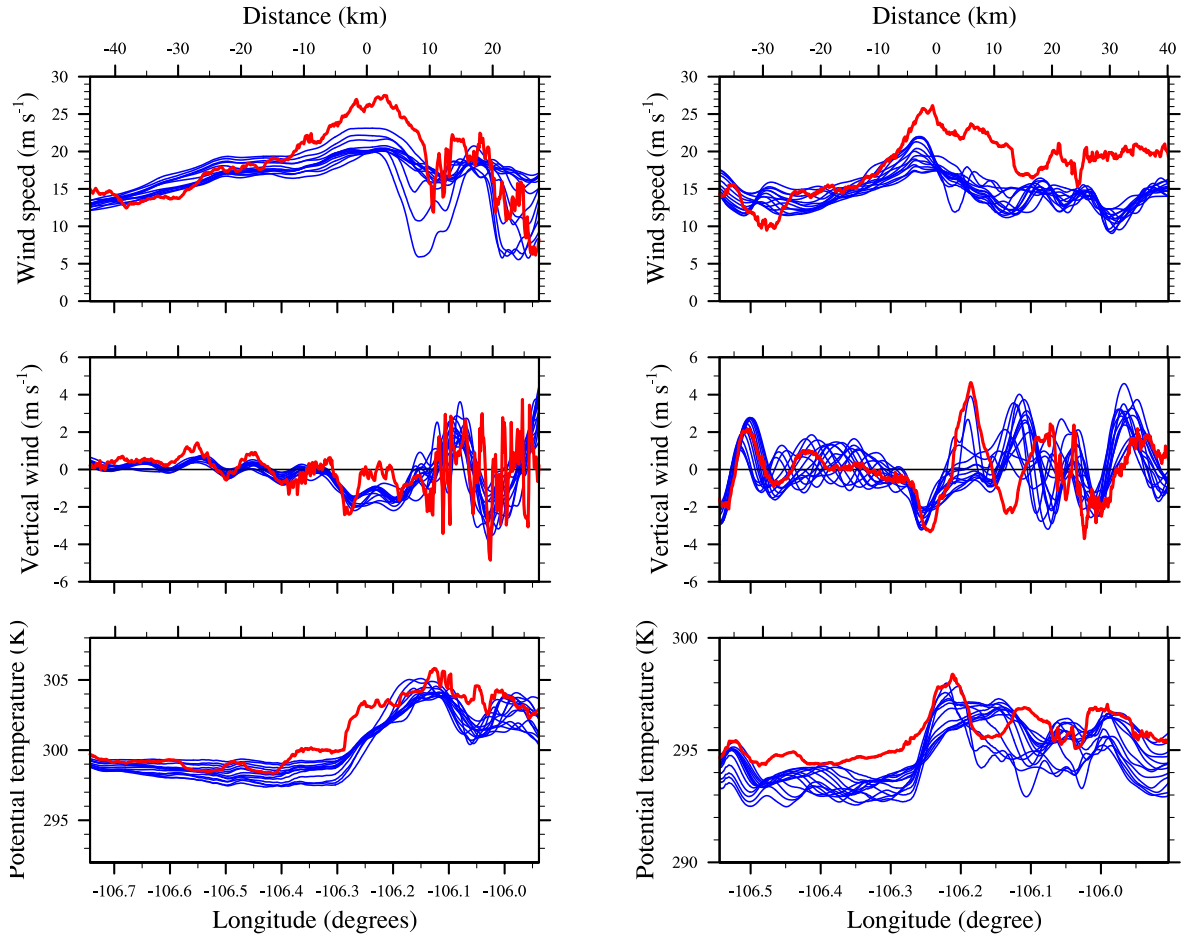


FIG. 5. Comparison of measured (red) and simulated (blue) atmospheric parameters along cross-mountain flight legs over the Medicine Bow Range between 2026 and 2037 UTC on 26 January (left) and between 1407 and 1422 UTC on 5 February 2006 (right). The model output is shown every 15 minutes in a ± 1.5 hrs window centered at the time of the observations (2030 UTC) on 26 January and two hours after the time of observations (1615 UTC) on 5 February.

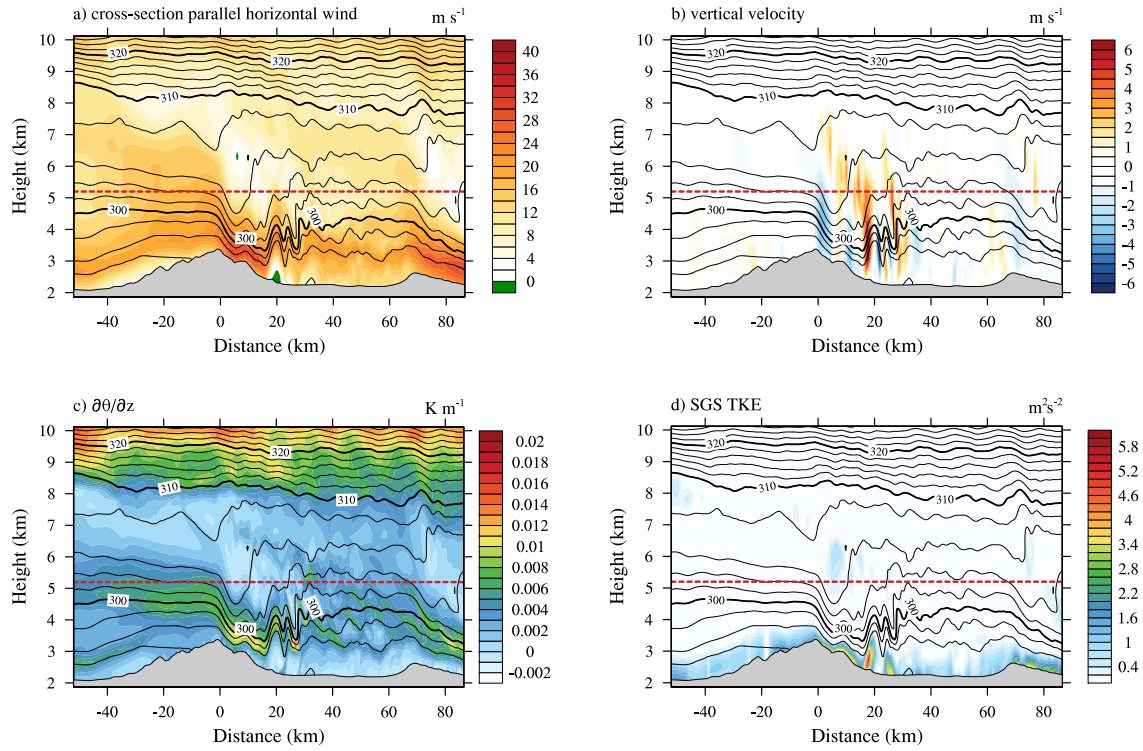


FIG. 6. Vertical cross-sections from inner domain along line AB at 2145 UTC on 26 January 2006. (a) cross-section parallel wind component (m s^{-1}), (b) vertical velocity (m s^{-1}), (c) vertical gradient of potential temperature (K m^{-1}), and (d) **SGS** TKE ($\text{m}^2 \text{s}^{-2}$). Isentropes at the interval of 2K are shown in all panels. Red dashed line indicates the height of the horizontal flight legs on 26 January (~ 5200 m MSL).

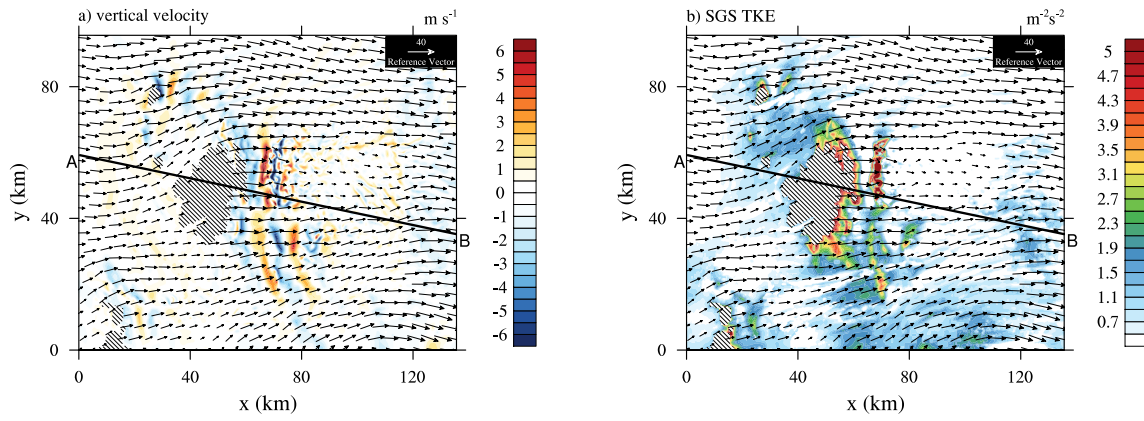


FIG. 7. Horizontal cross-sections at $z = 3000$ m MSL from inner domain at 2145 UTC on 26 January 2006. (a) Vertical velocity (m s^{-1}), and (b) **SGS TKE** ($\text{m}^2 \text{s}^{-2}$). Hatching indicates the intersection of $z = 3000$ m surface with the topography. Horizontal wind vectors at $z = 3000$ m MSL are overlaid in both panels.

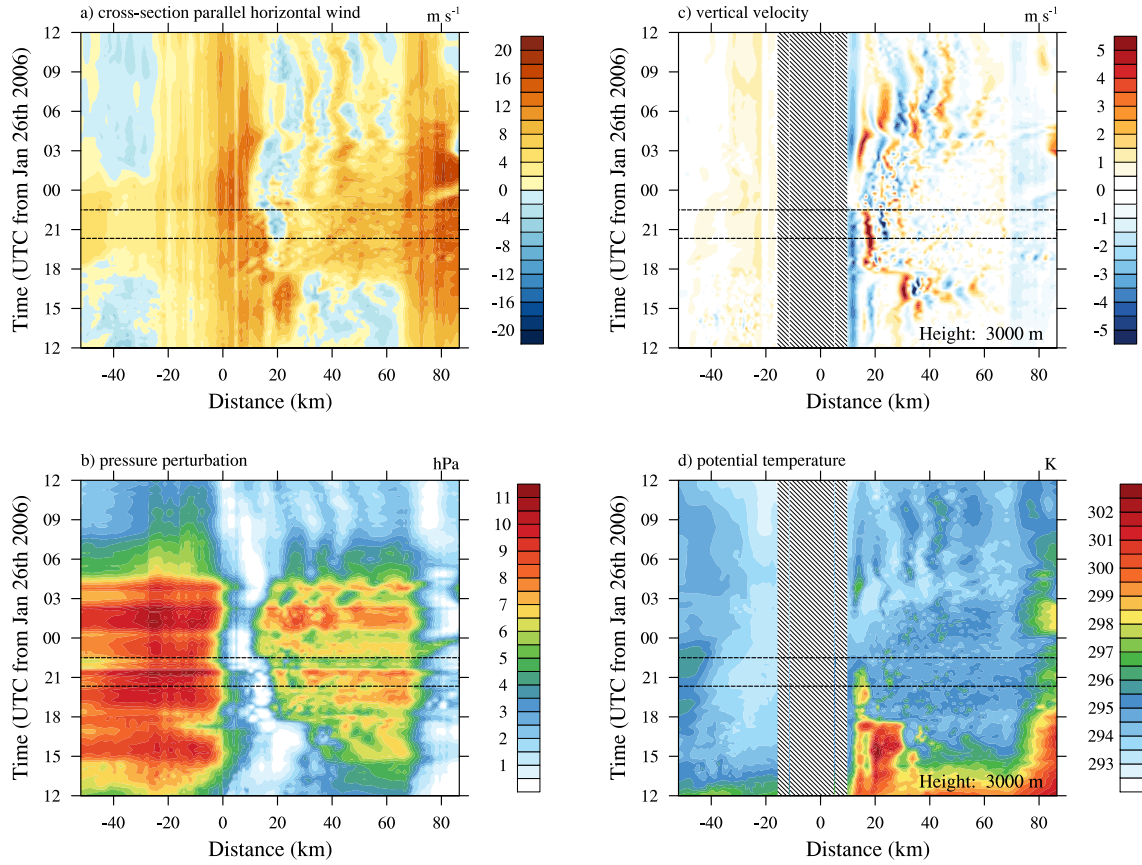


FIG. 8. Hövmöller diagrams (x - t) illustrating the evolution of atmospheric parameters on 26 January 2006 along line AB. (a) Section-parallel 10-m wind speed (m s^{-1}), (b) surface pressure perturbation (hPa), (c) vertical velocity (m s^{-1}), and (d) potential temperature (K). Fields in panels (c) and (d) are shown at $z = 3000$ MSL. Hatching in these two panels indicates the intersection with the terrain. The MBM top lies at $x = 0$. Horizontal lines in all panels delimit the period during which airborne measurements were taken.

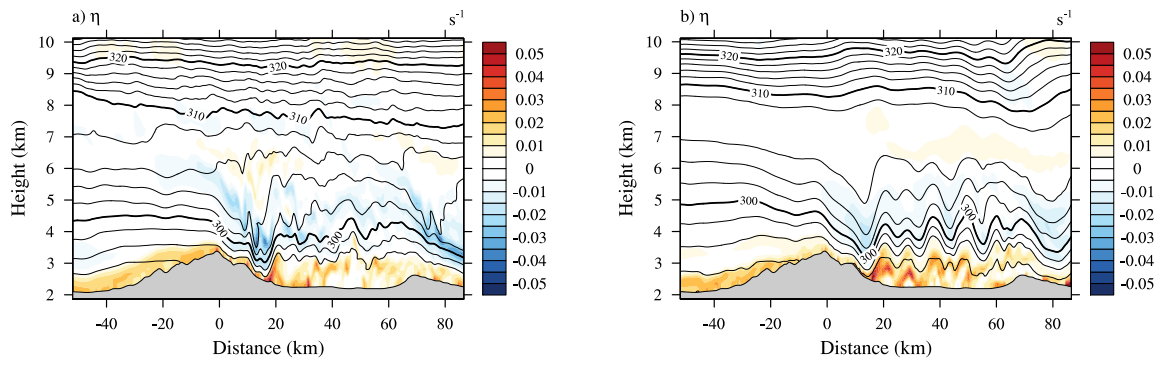


FIG. 9. Isentropes (K) and spanwise vorticity component η (s^{-1}) in the vertical cross-section along line AB from inner domain at (a) 2000 UTC on 26 January, and (b) 0400 UTC on 27 January 2006.

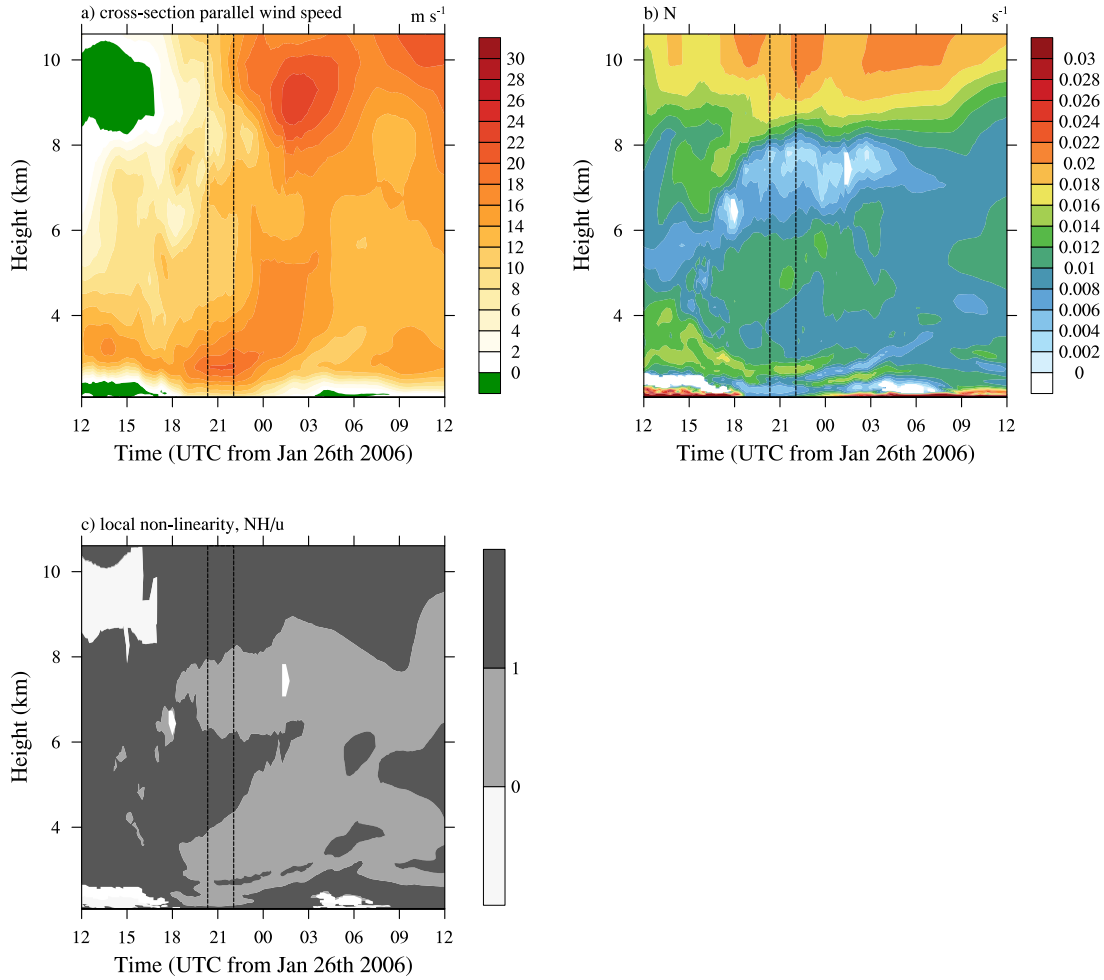


FIG. 10. Hövmöller diagrams (t - z) of the temporal evolution of the upstream atmospheric structure on 26 January 2006 at point $p1$ (Fig. 1). (a) Wind component parallel to section AB (m s^{-1}), (b) Brunt-Väisälä frequency (s^{-1}), and (c) local nonlinearity parameter NH/u . Vertical lines delimit the period during which airborne measurements were taken.

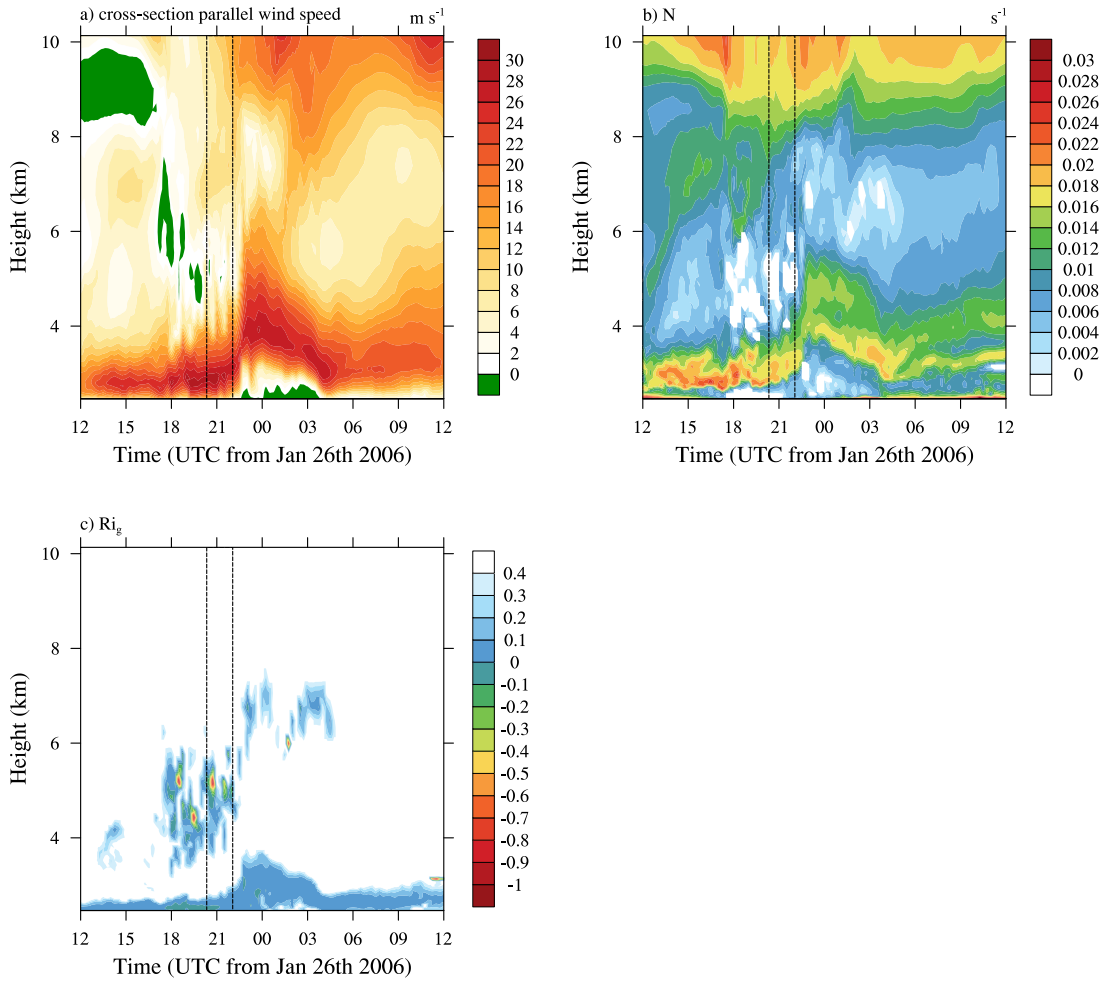


FIG. 11. As in Fig. 10 but for point $p3$. Panel (c) shows the gradient Richardson number Ri_g .

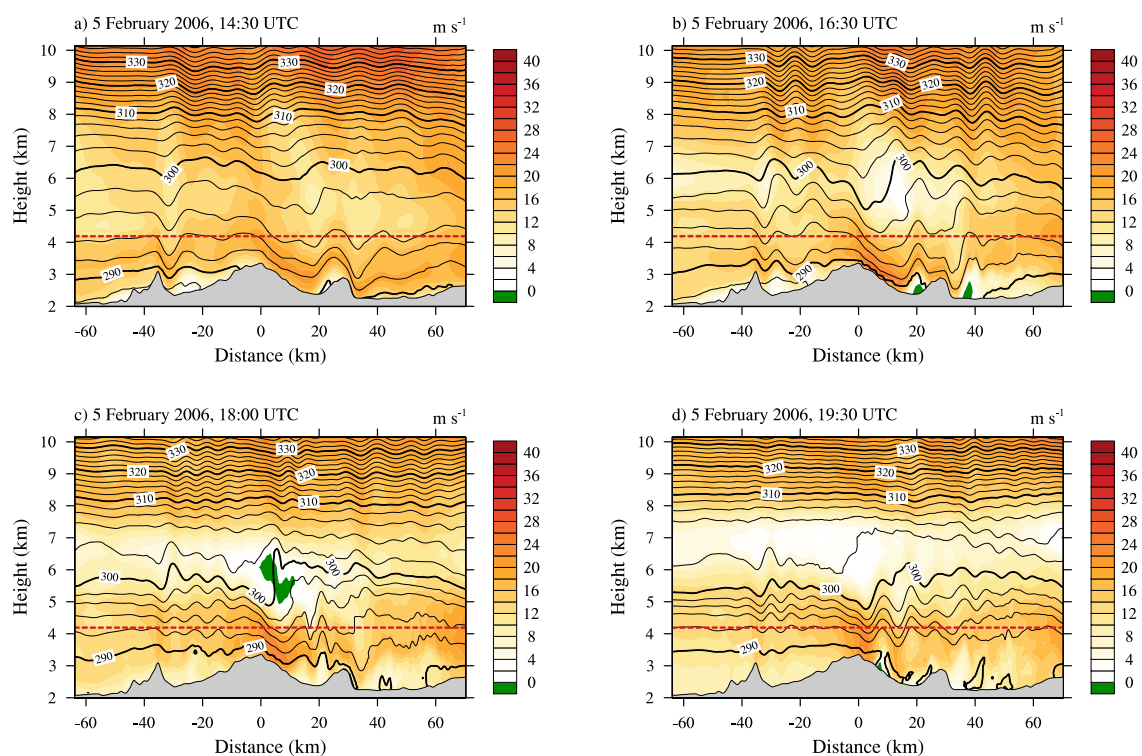


FIG. 12. Vertical cross-sections of the wind component parallel to line CD at (a) 1430 UTC, (b) 1630 UTC, (c) 1800 UTC, and (d) 1930 UTC on 5 February 2006. Red lines indicate the height of horizontal flight legs on 5 February (~ 4200 m MSL).

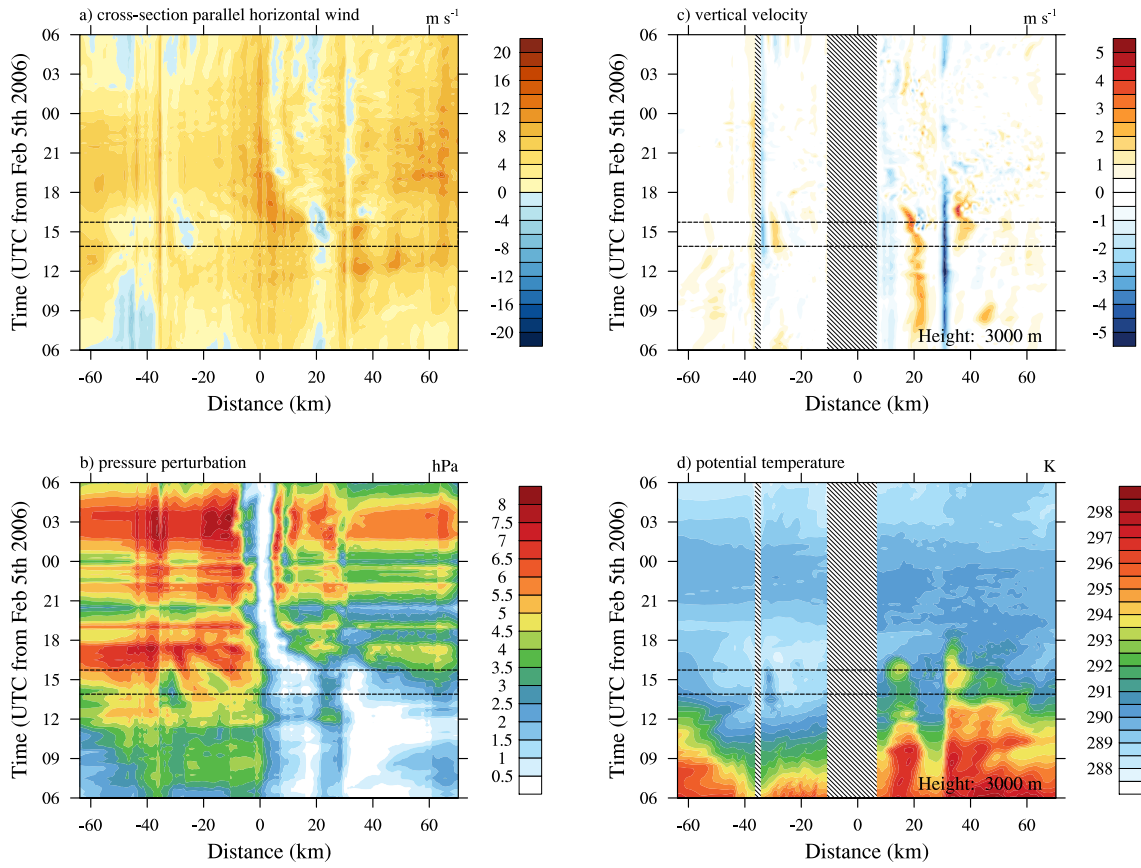


FIG. 13. As in Fig. 8 but for line CD on 5 February 2006. Horizontal lines in all panels delimit the time period from 1350 UTC to 1545 UTC, during which airborne measurements were taken. Hatched vertical line at $x = -50$ km represents Elk Mountain.

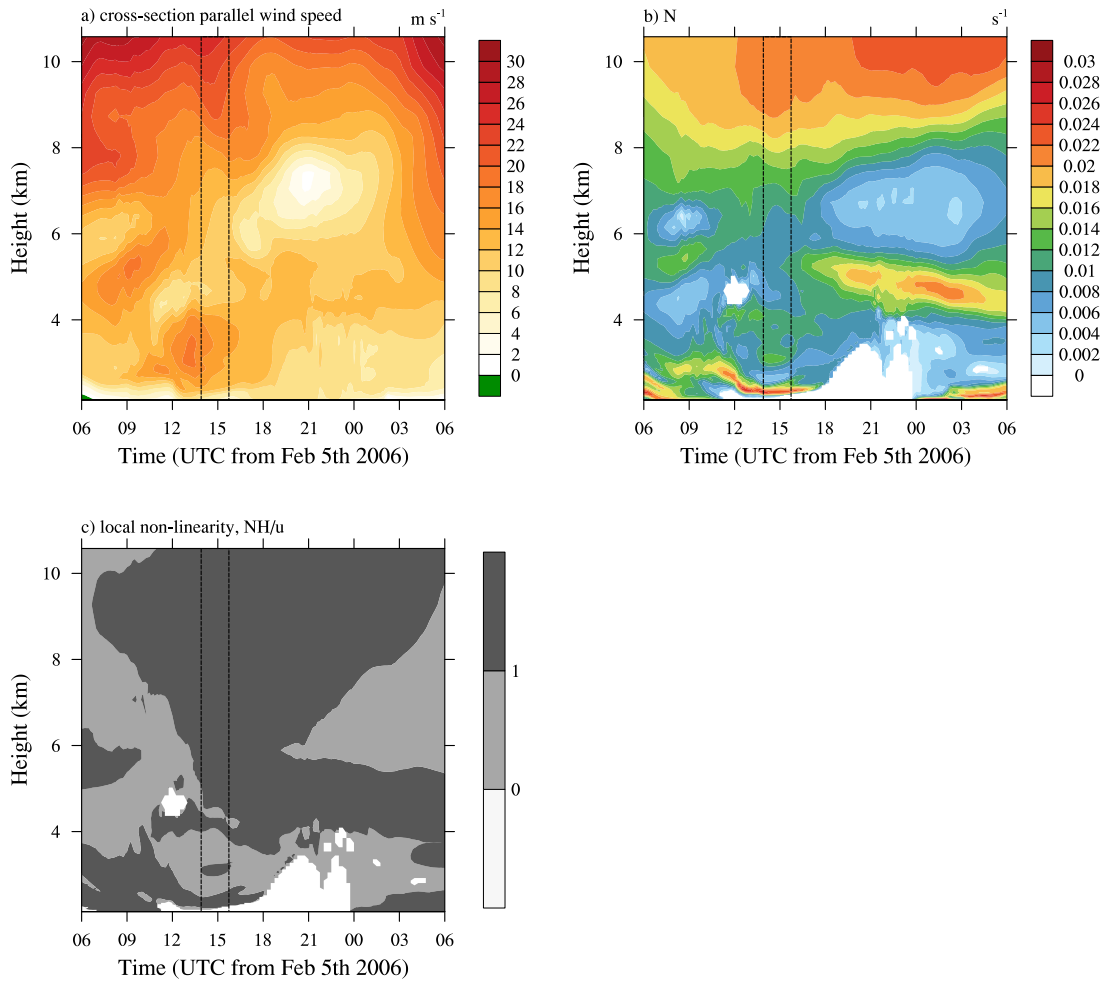


FIG. 14. As in Fig. 10 but for point $p4$ on 5 February 2006.

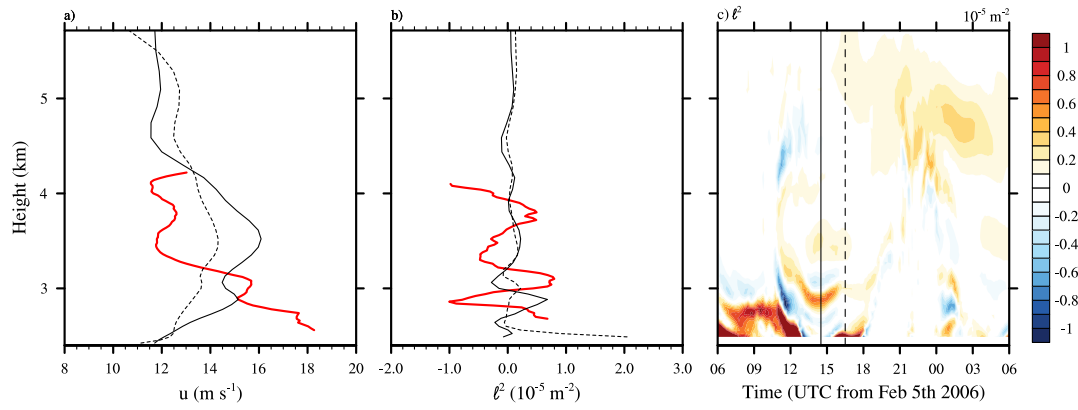


FIG. 15. Vertical profiles of (a) track-parallel wind speed (m s⁻¹), and (b) Scorer parameter ℓ^2 (m⁻²) on 5 February 2006 at point $p4$ in the Saratoga Valley. Thick red lines show observations at ~1430 UTC. Thin black lines show model predictions at 1430 UTC (solid) and 1630 UTC (dashed). (c) Hövmöller diagram of the temporal evolution of the Scorer parameter in the model simulation. Vertical lines mark the times of the model profiles shown in panels (a) and (b).

Chapter 3

Turbulence in breaking mountain waves and atmospheric rotors estimated from airborne in situ and Doppler radar measurements

French et al. (2015) analysed aircraft in situ and dual-Doppler radar data collected during two NASA06 events with large-amplitude waves and transient rotors over the Medicine Bow Mountains. Their investigation focused on radar-derived mean-field variables, in particular the along-track and vertical components of the wind and the horizontal vorticity, allowing to assess the flow variations across the underlying topography.

In the study presented in this chapter, emphasis is instead placed on the evaluation of the spatial distribution and intensity of turbulence across the mountains. We re-examine the airborne data collected on three days of the NASA06 campaign, including the two wave events described previously by French et al. (2015) and Grubišić et al. (2015a). Our investigation has two main goals: first, to devise a method that allows to derive quantitative estimates of turbulence intensity from airborne in situ and Doppler radar measurements; second, to apply this method to the NASA06 data set and characterize the structure and magnitude of turbulence in regions of gravity-wave breaking, boundary-layer separation and rotors. The results of this study extend existing procedures of aircraft data analysis and provide new estimates of turbulence intensity for a variety of mountain-induced turbulent processes.

The author's contributions to this work were the development of the turbulence analysis technique, its application to the case studies, the interpretation of results and their comparison with previous studies. Contributions to the journal article included the selection of the material to be presented, structuring and writing of the manuscript, and preparation of all tables and figures except Fig. 7.

Reference

Strauss, L., S. Serafin, S. Haimov, and V. Grubišić, 2015a: Turbulence in breaking mountain waves and atmospheric rotors estimated from airborne in situ and Doppler radar measurements. *Q.J.R. Meteorol. Soc.*, doi:[10.1002/qj.2604](https://doi.org/10.1002/qj.2604), in press.



Turbulence in breaking mountain waves and atmospheric rotors estimated from airborne *in situ* and Doppler radar measurements

Lukas Strauss^{a*}, Stefano Serafin^a, Samuel Haimov^b, Vanda Grubišić^{a,c}

^a Department of Meteorology and Geophysics, University of Vienna, Vienna, Austria

^b Department of Atmospheric Science, University of Wyoming, Laramie, Wyoming

^c Earth Observing Laboratory, National Center for Atmospheric Research, Boulder, Colorado

*Correspondence to: L. Strauss, Department of Meteorology and Geophysics, University of Vienna, Althanstrasse 14, 1090 Vienna, Austria. Email: lukas.strauss@univie.ac.at

Atmospheric turbulence generated by flow over mountainous terrain is studied using airborne *in situ* and cloud radar measurements over the Medicine Bow Mountains in SE Wyoming, USA. During the NASA Orographic Clouds Experiment (NASA06) in 2006, two complex mountain flow cases were documented by the University of Wyoming King Air research aircraft carrying aboard the Wyoming Cloud Radar.

The structure of turbulence and its intensity across the mountain range are described using the variance of vertical velocity σ_w^2 and the cube root of the energy dissipation rate $\varepsilon^{1/3}$ (EDR). For a quantitative analysis of turbulence from the cloud radar, the uncertainties in the Doppler wind retrieval have to be taken into account, such as the variance of hydrometeor fall speed and the contamination of vertical Doppler velocity by the horizontal wind. A thorough analysis of the uncertainties shows that 25% accuracy or better can be achieved in regions of moderate to severe turbulence in the lee of the mountains, while only qualitative estimates of turbulence intensity can be obtained outside of the most turbulent regions.

Two NASA06 events exhibiting large-amplitude mountain waves, mid-tropospheric wave breaking, and rotor circulations are examined. Moderate turbulence is found in a wave breaking region with σ_w^2 and EDR reaching $4.8 \text{ m}^2 \text{ s}^{-2}$ and $0.25 \text{ m}^{2/3} \text{ s}^{-1}$, respectively. Severe turbulence is measured within the rotor circulations with σ_w^2 and EDR respectively in the ranges of $7.8\text{--}16.4 \text{ m}^2 \text{ s}^{-2}$ and $0.50\text{--}0.77 \text{ m}^{2/3} \text{ s}^{-1}$. A unique result of this study is the quantitative estimation of the intensity of turbulence and its spatial distribution in the interior of atmospheric rotors, provided by the radar-derived turbulence fields.

Key Words: mountain waves; wave breaking; boundary layer separation; rotors; airborne Doppler radar; energy dissipation rate; aviation turbulence

Received ...

1. Introduction

Atmospheric flow over mountainous terrain can give rise to a variety of turbulent atmospheric processes. Glider pilots, soaring along mountain waves to reach higher altitudes, were among the first to recognize that the air in the vicinity of a mountain range is likely to bear considerable turbulence (Hirth 1933). Early glider pilot reports of severe turbulence encounters at low altitudes soon sparked the interest of atmospheric scientists (Küttner 1938). Since the 1950s, various observational efforts have been undertaken to further the understanding of mountain waves and associated turbulent phenomena. During the Sierra Wave Project (Sierra Nevada, California, 1951–55), Holmboe and Klieforth (1957) and Kuettner (1959) identified low-level circulation regions in the lee of the Sierra Nevada, referred to

as ‘atmospheric rotors’, as the origin of severe turbulence below large-amplitude lee waves.

Mountain-induced turbulence is, however, not limited to the lowest layers of the troposphere. When mountain waves propagate upward, they can steepen due to decreasing air density or as they approach a critical level, start to overturn, and eventually break, leading to vigorous turbulent mixing (Dörnbrack 1998; Sharman *et al.* 2012). Wave breaking at the tropopause or in the lower stratosphere has been observed occasionally by research aircraft and ground-based remote sensors (e.g., Lilly and Kennedy 1973; Lilly and Lester 1974; Ralph *et al.* 1997; Doyle *et al.* 2005). In contrast, to the best of our knowledge, only four studies documenting aircraft encounters of mid-tropospheric wave breaking exist to date (Lilly 1978; Smith 1987; Jiang and Doyle 2004; Elvidge *et al.* 2014), including observations from the Alpine

Experiment (ALPEX Project Homepage 2015) and the Mesoscale Alpine Programme (MAP, Bougeault *et al.* 2001).

In most of the above-mentioned studies, research aircraft were key in characterizing atmospheric turbulence over mountainous terrain. Use of aircraft near mountains, however, frequently represents a delicate tradeoff between flying through the regions of scientific interest and ensuring safety of crew and equipment aboard. The actual hazard posed by mountain-induced turbulent phenomena has been underlined by several investigations of severe turbulence encounters (e.g., Doyle *et al.* 2005; Ólafsson and Ágústsson 2009; Ágústsson and Ólafsson 2014) and by reports of more serious aviation incidents, for instance, the forced emergency landing of a DC-8 cargo jet during the 1992 Colorado Front Range windstorm (Carney *et al.* 1995; Clark *et al.* 2000).

In recent years, the advancement of modern remote-sensing instruments, and the possibility of operating them aboard aircraft, has offered new measurement approaches for the study of mountain airflows (Banta *et al.* 2013). By the nature of their measuring principle, these instruments lend themselves to the study of atmospheric turbulence from afar, thereby avoiding the need of flying directly into the turbulent regions of interest.

In this study, we make use of measurements by the Wyoming Cloud Radar (WCR), a W-band Doppler and polarimetric pulsed radar, carried aboard the University of Wyoming King Air (UWKA) research aircraft. Previous deployments of WCR include the Dynamics and Chemistry of Marine Stratocumulus Experiment (DYCOMS-II, Stevens *et al.* 2003) and the Terrain-induced Rotor Experiment (T-REX, Grubišić *et al.* 2008). T-REX (Sierra Nevada, California, 2006) was the most recent, major effort organized to investigate aspects of mountain-induced turbulence related to mountain waves, rotors, and boundary-layer dynamics. Unfortunately, due to the lack of moisture in Owens Valley and consequent unsatisfactory radar backscatter, only limited additional insight into these phenomena could be gained from WCR measurements in T-REX.

Prior to T-REX, in January and February 2006, the NASA Winter Orographic Clouds Experiment (NASA06) was conducted over the Medicine Bow Mountains (MBM) in southeastern Wyoming, deploying UWKA and WCR in a moist mid-latitude wintertime environment. Recently, French *et al.* (2015) and Grubišić *et al.* (2015, hereafter FHO15 and GSS15, respectively) provided a detailed analysis of two NASA06 events exhibiting large-amplitude mountain waves. In their studies, they revealed the presence of large atmospheric rotors and the key role of mid-tropospheric gravity wave breaking in steering the flow dynamics on both days. In the present work, we re-examine the observational data set collected during the two wave cases and extend previous analyses by the estimation of the intensity and spatial distribution of turbulence in mountain wave-induced turbulent processes.

WCR measurements have previously been used for quantitative estimation of turbulence parameters; however, the application was limited to the marine boundary layer. There, vertical profiles of the variance of vertical air velocity and energy dissipation rate obtained by Lothon *et al.* (2005) were in good agreement with complementary aircraft *in situ* measurements. In our study, the inherent inhomogeneity of the flow field over mountainous terrain and the changes in attitude of the aircraft when encountering turbulence at flight level pose significant challenges for the data analysis, which we will address in detail.

The goal of this paper is twofold: First, to show that Doppler velocities from airborne single-Doppler radar can effectively be used to detect locations of strong turbulence across mountain ranges and to obtain quantitative measures of turbulence, including upper bounds of the measurement uncertainty. Second, to apply this newly-devised technique to the NASA06 data set,

covering several complex mountain flow cases involving a rich variety of mountain-induced turbulent processes.

The rest of this paper is organized as follows: In Section 2, we give a brief overview of the NASA06 campaign and the relevant characteristics of the aircraft instrumentation and radar. In Section 3, we describe the parameters that we use to quantify turbulence and provide a detailed analysis of their uncertainties. Section 4 contains results from three days of the NASA06 campaign. In Section 5, we discuss the observed mountain-induced turbulent processes. Conclusions are drawn in Section 6.

2. Field campaign and airborne instruments

FHO15 provide an extensive overview of the NASA06 experiment, including the topographic setting, airborne instruments, and their features and limitations. Geerts *et al.* (2011) also discuss data from NASA06 and provide details of the design of this and similar experiments over the MBM from 2006 to 2009. In this section, we summarize the observed cases and discuss the characteristics of the airborne instrumentation that are relevant for our study.

2.1. Field campaign

The NASA06 experiment took place over the MBM in southeastern Wyoming in January and February 2006. Figure 1 gives an overview of the MBM topography and a sketch of the orientation of research flights on the interesting days of the campaign.

During NASA06, UWKA flights consisted of series of straight-and-level legs crossing the highest elevations of the MBM approximately in and against the mean wind direction. Data from three of these flights is analysed here.

By design, the NASA06 experiment focused primarily on the fine structure of deep wintertime orographic clouds and the role of aerosols in the formation of orographic precipitation (Geerts *et al.* 2011). However, on two days of the campaign, 26 January and 5 February 2006, stable upstream conditions and favourable mesoscale dynamic forcing led to enhanced atmospheric response to the underlying topography, including large-amplitude lee waves, gravity wave breaking, and strong low-level turbulence. In addition to the two wave events, a third day, 2 February 2006, is included in the analysis as a reference case for non-wave-induced boundary-layer turbulence.

2.2. Measurement platform and instruments

A comprehensive characterization of the aircraft *in situ* instrumentation and the cloud radar is provided in FHO15 and, more generally, in Wang *et al.* (2012) and on the UWKA Homepage (2015) for UWKA, and Damiani and Haimov (2006) and on the WCR Homepage (2015) for WCR.

2.2.1. UWKA research aircraft

The UWKA research aircraft is a specially instrumented Beechcraft Super King Air 200T. For the estimation of turbulence parameters in this study, we make use of high-rate (25 Hz) measurements of the three components of the wind, obtained from a 5-hole ‘gust’ probe, located on an extended nose boom, and measurements of air temperature and static pressure (Brown *et al.* 1983). The precision of the wind measurement is approx. $\pm 0.1 \text{ m s}^{-1}$ for the horizontal along-track and cross-track wind components u and v and $\pm 0.05 \text{ m s}^{-1}$ for the vertical wind component w (FHO15).

The second relevant instrument aboard UWKA is the Universal Indicated Turbulence System (UITS), commonly referred to as ‘MacCready Turbulence Meter’. The UITS design is based on

a method proposed by MacCready Jr. (1962, 1964) for the determination of the rate of dissipation of turbulent kinetic energy. On UWKA, the MacCready Turbulence Meter is used primarily as a real-time, on-flight indicator of turbulence (Feng 2001). In this study, data from the instrument is used as a term of comparison for dissipation rates obtained from spectral analysis of high-rate wind data.

2.2.2. Wyoming Cloud Radar (WCR)

The Wyoming Cloud Radar (WCR) is a 95 GHz pulsed, fixed multi-antenna Doppler radar, designed to provide high-resolution data of the structure and dynamics of clouds. During NASA06, WCR was operated in three-antenna mode, with beams pointing to the zenith, nadir and 30° down-forward directions when the aircraft flew straight and level. The dwell time of the radar (the time it takes to collect one radar profile) was approximately 32 ms, resulting in an along-track sampling distance of approx. 3 m at an average true airspeed of roughly 100 ms⁻¹. The radar resolution in the vertical (distance between range gates) was 30 m and the radar pulse volume at 1 km had a size of approx. 10 × 10 × 30 m³. Radar backscattered reflectivity during NASA06 was predominantly from homogeneous ice clouds, consisting mostly of spherically-shaped ice particle aggregates (FHO15). In the analysis of Doppler velocities, contamination by ground clutter was avoided by using radar data starting at 100 m above ground level.

FHO15 combined the signals from the radar nadir and down-fore beam for dual-Doppler analysis in order to determine the flow across the MBM in the along-track measurement plane. In the present work, however, only data from the nadir and zenith beams is used and it is shown that quantitative estimates of turbulence intensity can be obtained from single-Doppler measurements alone.

3. Quantitative turbulence estimates from airborne *in situ* and Doppler radar measurements

In situ measurements from UWKA have previously been used to study boundary-layer turbulence in mountainous environments (Darby and Poulos 2006; Jiang *et al.* 2010; Geerts *et al.* 2011). In the present work, we extend these studies, determining the intensity and spatial distribution of turbulence in mountain wave-induced phenomena from both UWKA and WCR data.

Quantitative estimation of turbulence requires the selection of suitable turbulence metrics. For the data at hand, the turbulent kinetic energy TKE, the variance of vertical velocity σ_w^2 , and the rate of dissipation of turbulent kinetic energy to the power of one third $\epsilon^{1/3}$, or EDR, have emerged as appropriate turbulence parameters.

3.1. Turbulence analysis approach

The mountain airflow cases under consideration are characterized by highly inhomogeneous turbulent fields forced from aloft by the presence of gravity waves. Thus, in contrast to more uniform boundary-layer flows studied by Geerts *et al.* (2011) and Lothon *et al.* (2005), the assumption of horizontal homogeneity cannot be made here.

Wavelet transforms would lend themselves naturally to the analysis of inhomogeneous mountain flows, since they allow to resolve the structure of waves and turbulence simultaneously in both spatial and wave-number domains (Torrence and Compo 1998). However, despite more recent developments (e.g.,

Terradellas *et al.* 2005; Woods and Smith 2010), a well-established method for determining turbulence parameters, such as TKE, quantitatively from wavelets does not exist to date.

In their review of experimental investigation of atmospheric boundary-layer turbulence, Druilhet and Durand (1997) commented on the issue of inhomogeneous data stating that ‘no general method exists for analysing inhomogeneous time-series’ but that a ‘sample can be divided into more homogeneous sub-samples and thus analysed by conventional techniques such as short Fourier transform’. We thus deal with the inherent inhomogeneity of the flow field by subdividing UWKA and WCR data into short segments, each of which is subjected to turbulence analysis individually.

The choice of the length of these segments must be made with care. Choosing the right segment length represents a trade-off between obtaining statistically meaningful estimates of turbulence parameters and maintaining the homogeneity of turbulence within each data segment. This choice is tightly linked to the question of what scale separates the turbulent and mean parts of the flow. Once a segment length has been chosen, atmospheric motions with only smaller scales can be resolved.

Figures 2a,b illustrate how the spatial series of the vertical wind component w change upon application of a high-pass filter (subtraction of the equally-weighted moving average from the raw signal) with decreasing filter scale. Obvious features of the mesoscale flow (e.g., upstream waves and lee-side up- and downdraughts) are apparent from all filtered w series except for scales 1.5 km and 1 km. Figures 2c,d reveal the effect of the high-pass filtering on TKE, which we compute as half of the sum of variances of the filtered wind components $\frac{1}{2}(\sigma_u^2 + \sigma_v^2 + \sigma_w^2)$ along the leg. At and below a scale of 1.5 km, the largest portion of the variance of the signal due to mesoscale motions has been removed.

This test serves as a guideline for the choice of the minimum length of the segments that are cut from the spatial series. For subsequent turbulence analysis, we proceed with a segment length of 1.5 km.

3.2. Variance of vertical velocity

Estimates of the variance of the horizontal along-track (u) and cross-track (v) wind components (for UWKA) and the vertical wind component (w , for both UWKA and WCR) are obtained from the linearly detrended wind data for each 1.5 km segment. For WCR, data from each radar range gate is used as individual spatial series.

Any complete measurement of a physical quantity requires the specification of the measurement uncertainty. Prior to this study, it was not clear whether the inherent inaccuracies in the measured wind velocities from airborne Doppler radar permit quantitative estimation of turbulence parameters in a spatially inhomogeneous airflow and in conditions of moderate flight-level turbulence. In the following, we thoroughly consider all possible uncertainties in the computed variances.

As a first step, we inspect the power spectra of measured quantities for their noise level. Figures 3a,c refer to UWKA wind measurements taken in the relatively quiescent region upstream of the mountain and in the strongly turbulent region downstream of it. Spectra from the downstream region follow a $-5/3$ power law (indicative of the inertial subrange) from scales of roughly 400 m down to 15 m, while those from the upstream region display a flattening at the high-wavenumber end, commonly associated with instrumental white noise. Similarly, Figures 3b,d refer to WCR vertical Doppler velocity from different regions of the flow. Most WCR spectra, from both up- and downstream of the mountain, exhibit an approximate $-5/3$ power law behaviour at

scales between 400 m and 40 m, while they only contain white noise at wavelengths shorter than 20 m. The level of uncorrelated white noise is highly variable, which is attributed to the Doppler radar system signal-to-noise (SNR) ratio.

In order to correct the measured variances for the contribution of noise to them, the level of white noise σ_{noise}^2 is extracted from the power spectra in each series segment. σ_{noise}^2 is then subtracted from the measured variance $\sigma_{w, \text{meas.}}^2$.

Beyond the noise contributions, which are readily determined from power spectra, there are a number of uncertainties pertaining to the moving measurement platform and to characteristics of the remote sensing instrument: (i) the uncertainty in the determination of aircraft motion and attitude, (ii) the limited accuracy of the beam-pointing angle calibration, (iii) the variance of hydrometeor fall speed, (iv) the radar pulse-volume averaging effect (PVA effect), and (v) the contamination of Doppler velocity by the horizontal wind.

The error in the determination of aircraft motion and attitude (Haimov and Rodi 2013) contributes an uncertainty of $\sigma_{\text{ac}}^2 \simeq 0.01 \text{ m}^2 \text{ s}^{-2}$ to the measured vertical wind velocity. Calibration of the radar beam pointing angle is needed to correctly remove the aircraft motion from measured Doppler velocities. For NASA06, a realistic estimate of its error and the consequent uncertainty is $\sigma_{\text{ba}}^2 \lesssim 0.09 \text{ m}^2 \text{ s}^{-2}$, based on considerations by Haimov and Rodi (2013). The variance of hydrometeor fall speed contributes to the measured variance $\sigma_{w, \text{meas.}}^2$. FHO15 obtained an estimate of the fall velocity v_t of ice particle aggregates of 1 m s^{-1} and standard deviation of 0.2 m s^{-1} , leading to a maximum positive bias in the radar-measured variance of $\sigma_{v_t}^2 \simeq 0.04 \text{ m}^2 \text{ s}^{-2}$.

The averaging effect of the finite radar pulse volume (Srivastava and Atlas 1974; Lothon *et al.* 2005) is responsible for the bending-down of spectral energy density at the higher wave numbers for WCR spectra (Figs. 3b,d). Lothon *et al.* (2005) corrected for this effect assuming a von Kármán energy spectrum and measuring the integral scale of turbulence L . In the present study, reliable estimates of L cannot be obtained from short data segments. We thus compensate for the PVA effect, which implies a loss of variance σ_{PVA}^2 , assuming that it depends linearly on the along-track (longitudinal) pulse-averaging filter width. The latter is in turn proportional to the distance from the radar. In absence of a suitable estimate of L , σ_{PVA}^2 , added to the measured variance in each leg segment, is only a rough correction and we set a conservative estimate for the error of this correction to $\sigma_{\text{PVA, err.}}^2 \simeq \pm 0.25 \sigma_{\text{PVA}}^2$.

Finally, cross-contamination of velocity components occurred because a steady aircraft attitude could not always be maintained during NASA06 flights, in particular when UWKA encountered moderate, or stronger, turbulence at flight level. Under such conditions, the fixed up/down-pointing radar beams deviated from zenith/nadir, leading to a contamination of the vertical Doppler velocity v_r by the horizontal along-track and cross-track wind components. Far from flight level, however, these are unknown and can differ by as much as 30 m s^{-1} and 10 m s^{-1} , respectively. This adds an additional uncertainty in the estimation of σ_w^2 . The maximum contribution of the horizontal wind contamination (HC) to the measured variance $\sigma_{v_r}^2$ is highly variable along each flight leg and depends on the pitch and roll angle variation in each leg segment. As shown in Appendix A, variances of pitch and roll along a leg segment tend to cause a positive bias in the measured variance ($+\sigma_{\text{HC, A}}^2$), while non-zero mean pitch and roll can lead to both an increase and decrease in the variance ($\pm\sigma_{\text{HC, B}}^2$).

Summing up all of the above uncertainties, the variance of vertical velocity σ_w^2 is given by

$$\sigma_w^2 = \sigma_{w, \text{meas.}}^2 - \sigma_{\text{noise}}^2 + \begin{cases} 0 \\ -\sigma_{\text{ac}}^2 \end{cases} \quad (1)$$

for UWKA measurements and by

$$\sigma_w^2 = \sigma_{v_r, \text{meas.}}^2 - \sigma_{\text{noise}}^2 + \sigma_{\text{PVA}}^2 + \begin{cases} +\sigma_{\text{PVA, err.}}^2 & +\sigma_{\text{HC, B}}^2 \\ -\sigma_{\text{PVA, err.}}^2 & -\sigma_{\text{HC, A}}^2 - \sigma_{\text{HC, B}}^2 - \sigma_{\text{ac}}^2 - \sigma_{\text{ba}}^2 - \sigma_{v_t}^2 \end{cases} \quad (2)$$

for WCR measurements, where the upper and lower lines in braces represent the upper and lower uncertainty bounds, respectively. For WCR, the relative uncertainty of σ_w^2 is defined as

$$R = \frac{\sigma_{\text{PVA, err.}}^2 + \sigma_{\text{HC, A}}^2 + \sigma_{\text{HC, B}}^2 + \sigma_{\text{ac}}^2 + \sigma_{\text{ba}}^2 + \sigma_{v_t}^2}{\sigma_{v_r, \text{meas.}}^2 - \sigma_{\text{noise}}^2 + \sigma_{\text{PVA}}^2}, \quad (3)$$

where the numerator and denominator stand for the maximum uncertainty and the signal, respectively. In the following sections, quantitative statements on turbulence intensity will be made only in regions of the flow with $R \leq 25\%$.

3.3. Energy dissipation rate

The second turbulence metric that we use is the cube root of the rate of dissipation of the turbulent kinetic energy EDR. Beyond its use in the scientific community, EDR has recently been established as an aircraft-independent objective measure for turbulence intensity (International Civil Aviation Organization 2007; Sharman *et al.* 2014). EDR is related to the standard deviation of the vertical acceleration $\sigma_{\ddot{z}}$ on aircraft (MacCready Jr. 1964; Cornman *et al.* 1995; International Civil Aviation Organization 2007) and thus provides the link to the subjective feel of turbulence experienced by aircraft passengers and crew. In civil aviation, EDR values are linked to ‘turbulence categories’ used in pilot reports. Following newly-proposed guidelines for medium-sized commercial aircraft by Sharman *et al.* (2014), we adopted EDR thresholds of 0.014, 0.050, 0.125, 0.220, 0.350, $0.500 \text{ m}^{2/3} \text{ s}^{-1}$, respectively, for turbulence categories ‘smooth-light’, ‘light’, ‘light-moderate’, ‘moderate’, ‘moderate-severe’, and ‘severe’.

For the estimation of EDR, we make use of the inertial dissipation technique (IDT) (Champagne 1978; Piper and Lundquist 2004; Večenaj *et al.* 2012). The IDT is based on the Kolmogorov form of the turbulent energy spectrum in the inertial subrange (Kolmogorov 1941a,b) stating that, under conditions of local isotropy and large Reynolds numbers, a range of wave numbers exists for which

$$S_i(k) = \alpha_i \varepsilon^{2/3} k^{-5/3}, \quad (4)$$

where $S_i(k)$ is the spectral energy density of velocity component $u_i = \{u, v, w\}$ and α_i is the Kolmogorov constant $\alpha_i = \{0.53, 0.707, 0.707\}$ (Oncley *et al.* 1996; Piper and Lundquist 2004).

One of the advantages of using EDR as a turbulence indicator instead of σ_w^2 or TKE arises from the EDR being estimated from the energy at smaller turbulent scales, which are affected to a lesser degree by preliminary filtering or the choice of the segment length. A disadvantage of the method is the more stringent requirement of the presence of a ‘ $-5/3$ region’ in the spectra and of local isotropy, limiting its applicability. For this work, we implemented the IDT as follows:

1. The raw wind data from each 1.5 km leg segment is linearly detrended and the power spectral density is computed using Welch’s method (Welch 1967).
2. Contrary to other studies (Oncley *et al.* 1996; Piper and Lundquist 2004) we do not define a fixed wavenumber range from which EDR is extracted. Instead, for each spectrum, we determine the region of the spectrum with

the best correspondence to the $-5/3$ slope, based on several least-squares fits to the spectrum within the wavenumber limits that are indicated by the vertical lines in Fig. 3. The input parameters to this procedure are: the wavenumber limits of the fit ($2\pi/400$ to $2\pi/15$ m^{-1} for UWKA and $2\pi/400$ to $2\pi/40$ m^{-1} for WCR data), the minimum window width for the fit ($\Delta(\log_{10} k) = 0.7$), and the maximum allowed deviation from the $-5/3$ slope (10%). The freedom in determining the inertial subrange is needed in order to handle varying scales of turbulence, depending on the region of the mountain flow under consideration. It also helps to deal with the range-dependent pulse-volume averaging effect of the Doppler radar.

3. EDR_i is estimated from the spectrum of each wind component u_i as

$$\text{EDR}_i = \varepsilon_i^{1/3} = \left(\frac{\overline{S_i(k)k^{5/3}}}{\alpha_i} \right)^{1/2}, \quad (5)$$

where the overline bar stands for the arithmetic mean taken over all wave numbers k within the detected inertial subrange.

Figure 4 includes the cross-mountain variation of EDR at flight level along flight legs on 26 January and 5 February. Very good agreement can be seen between the EDR measurement by the MacCready Turbulence Meter (EDR_{MC}) and the ‘log-mean’ EDR estimate, which we define as

$$\overline{\text{EDR}} = 10^{[\log_{10}(\text{EDR}_u) + \log_{10}(\text{EDR}_v) + \log_{10}(\text{EDR}_w)]/3}. \quad (6)$$

Considerable scattering of individual EDR estimates around $\overline{\text{EDR}}$ is also visible. This scatter is particularly pronounced in the region of relatively low turbulence upstream of the mountain top. There are several possible origins of this scatter: anisotropic turbulence, statistical scatter of EDR estimates (related to the limited extent of the leg segments), and uncertainty in the determination of the inertial subrange. Figure 5 contains two scatter diagrams consisting of EDR estimates from all legs flown on 26 January and 5 February, respectively. For values of $\overline{\text{EDR}} < 0.05 \text{ m}^{2/3} \text{ s}^{-1}$, corresponding to the hatched region, a clear tendency of the EDR estimate from the along-track horizontal wind component (EDR_u) to be larger than those from the vertical wind component (EDR_w) can be seen. This points to anisotropic turbulence as the cause of EDR scatter upstream of the mountain, where the atmosphere was stably stratified. For values of $\overline{\text{EDR}} \geq 0.05 \text{ m}^{2/3} \text{ s}^{-1}$, the scatter is rather uniform, showing no general tendency of one EDR_i component prevailing over another. We conclude that the low EDR values should not be used, since the inertial dissipation technique cannot be applied in conditions of anisotropic turbulence. The scatter of EDR values exceeding $0.05 \text{ m}^{2/3} \text{ s}^{-1}$ is instead ascribed to statistical scatter and to possible shortcomings in the procedure of determining the inertial subrange. To obtain an estimate of the uncertainty in the measurement of EDR due to the scatter, we determine the percentage interval around $\overline{\text{EDR}}$ that includes 95% ($\pm 2\sigma$) of all $\text{EDR}_i \geq 0.05 \text{ m}^{2/3} \text{ s}^{-1}$. The scatter for the flight legs from both days is almost identical and amounts to $\pm 29\%$ uncertainty of the individual EDR_i and $\pm 16\%$ uncertainty of the mean $\overline{\text{EDR}}$.

For the estimation of EDR_w from WCR data, two other possible sources of error have to be considered: the contamination of $\sigma_{v_i}^2$ by the horizontal wind and the deviation of the along-track wind in a given radar range gate from the wind at flight level. The evaluation of these two terms is contained in Appendix B.

For UWKA, the total uncertainty in the estimation of EDR is thus given by

$$\text{EDR} = \overline{\text{EDR}} \pm 16\% \quad (7)$$

and for WCR, according to Appendix B, by

$$\begin{aligned} \text{EDR} &= (\text{EDR}_w^{+9\%}_{-11\%}) \pm 29\% \\ &= \begin{cases} \text{EDR}_w^{+41\%}_{-23\%} & \text{for a tailwind} \\ \text{EDR}_w^{+15\%}_{-37\%} & \text{for a headwind} \end{cases} \end{aligned} \quad (8)$$

Note that the UWKA EDR estimate is based on three wind components, while that from WCR is based only on w . This is reflected in the uncertainty bounds.

4. Case studies

In this section, we analyse the spatial distribution of turbulence and its intensity across the MBM on three days of the NASA06 campaign. The impact of wave forcing on low-level turbulence on 26 January and 5 February is contrasted with in-cloud turbulence on 2 February. Table 1 lists the flight legs from these days that are examined in the following.

4.1. 26 January 2006 – a hydraulic jump-type rotor

26 January 2006 represents the day of NASA06 with the strongest mesoscale dynamic forcing. Detailed observational analysis by FHO15 and numerical modelling by GSS15 have shown that this day can be characterized as a complex mountain flow event involving a large breaking wave in the mid-troposphere, strong downslope winds over the lee slope of the mountain and a *hydraulic jump-type* rotor (Lester and Fingerhut 1974) that rapidly moved upstream.

Figures 4a,b and 6a,b show UWKA measurements of w , θ , u , and TKE and EDR from two flight passes on 26 January, revealing the rapid evolution of the event. In Fig. 6a, corresponding to Leg 3, three distinct regions of the flow can be identified from flight-level measurements: Region I upstream of the mountain peak is characterized by approximately constant along-track horizontal wind u , zero vertical motion w and constant potential temperature θ . At the downstream end of Region I, a transition to downward motion and increasing θ is evident, which is associated with the descending branch of the wave. Region II exhibits increased but approximately constant θ , rapidly varying w and a sudden decrease of u from approx. 20 m s^{-1} to 0 m s^{-1} and even negative values. Region III is characterized by a sudden, strong updraught and a slightly weaker downdraught on the order of $+12 \text{ m s}^{-1}$ and -9 m s^{-1} , respectively. The updraught coincides with a strong negative θ anomaly and re-strengthened u . The changes in u , w , and θ along the leg are also reflected in TKE and EDR. Turbulence is ‘light’ (TKE and $\overline{\text{EDR}}$ below $0.06 \text{ m}^2 \text{ s}^{-2}$ and $0.05 \text{ m}^{2/3} \text{ s}^{-1}$, respectively) in Region I and sharply increases as the aircraft penetrates into Region II (cf. Peaks 1 and 2). The strongest turbulence (TKE $\simeq 12.1 \text{ m}^2 \text{ s}^{-2}$ and $\text{EDR} \simeq 0.38 \text{ m}^{2/3} \text{ s}^{-1}$) is found in Region III, collocated with the main up- and downdraught (Peaks 3 and 4). The two peaks are separated by a region of ‘light’ turbulence (TKE $< 0.6 \text{ m}^2 \text{ s}^{-2}$ and $\text{EDR} < 0.05 \text{ m}^{2/3} \text{ s}^{-1}$).

Figure 6b, corresponding to Leg 5 passing over the MBM around 25 min later, shows a similar pattern in w , θ and u , but the main features in w and TKE have weakened considerably. Also notable is the upstream shift of the main updraught-downdraught couplet by approx. 7 km. Another remarkable change from Leg 3 to Leg 5 is the clear absence of turbulence in Region II preceding the updraught.

More insight into the dynamics behind the observed evolution of the event has been gained by GSS15 through high-resolution numerical modelling with the Weather Research and Forecasting (WRF) Model, using a horizontal grid spacing of 400 m. Model cross-sections at the time of the observations show

that the measurements along Legs 3 and 5 were taken during a period of ceasing wave breaking at mid-tropospheric levels and consequent upstream shift of the rotor (GSS15, their Figs. 8 and 11). One of the model cross-sections is shown in Fig. 7a. Underneath the wave-breaking region, a shooting flow over the lee of the MBM formed and was terminated by an internal hydraulic jump approx. 13 km downstream of the MBM top. Note, however, that the model hydraulic jump is positioned farther upstream than that encountered by the aircraft (approx. 22 km downstream of the MBM top). Regardless, the model helps link Region II in Fig. 6a (and Peaks 1 and 2 in turbulence intensity) to mid-level wave breaking. Despite the misplacement of the jump, the simulation also provides a hint at the origin of Peaks 3 and 4: At flight level, the aircraft encountered the upper edge of the hydraulic jump, giving rise to the strong up- and downdraught and a broad region of less coherent, but very turbulent air motion downstream of it.

Figures 8 and 9 show radar data and derived turbulence parameters along Legs 3 and 5. The first panel in both figures shows radar reflectivity Z and provides information on the distribution of cloud ice particles across the MBM. Due to poor radar coverage along Leg 3, only little additional insight can be gained from Fig. 8, except for the dome-like structure of the cloud distribution approx. 22 km downstream of the mountain top, marking the location of the hydraulic jump. Also note the good agreement between the variance estimates from the *in situ* and radar data right above and below the flight track between 26 and 38 km (Fig. 8c), where radar backscatter was good. We proceed with the analysis of radar data from Leg 5, which provides better radar coverage.

Radar reflectivity in Fig. 9a reveals a continuous layer of return signal of up to 3 km in depth upstream of the MBM and gradually decreasing depth in the downstream direction, reminiscent of compressed airflow in the accelerating downslope windstorm. At around 13 km downstream of the mountain top, the cloud layer is lifted from the surface and carried aloft to approx. 4.2 km MSL. The radar vertical Doppler velocity in Fig. 9b reveals a strong updraught and a more diffuse downdraught (on the order of $\pm 10 \text{ m s}^{-1}$) within this region, associated with a large hydraulic jump-type rotor extending over at least 1.5 km in the vertical (FHO15). Figures 9c,d, showing the radar-derived σ_w^2 and EDR_w , provide insight into the near-surface levels of turbulence. Note that the fields of EDR_w are generally patchier than those of σ_w^2 , i.e., some radar data segments in the EDR plot remain grey while valid estimates were obtained for σ_w^2 . This can be attributed to: (i) low turbulence, or (ii) the procedure of computing EDR (including the determination of the inertial subrange), which failed in some instances.

Upstream of and above the mountain top, turbulence decreases with distance from the ground, pointing to turbulence being shear-generated. Turbulence is generally ‘light’ to ‘light-moderate’ upstream of and above the MBM, but suddenly switches to ‘moderate-severe’ and ‘severe’ at around 12 km down the lee slope. This sharp transition in turbulence intensity is collocated with the detachment of the boundary layer (FHO15) followed by a large rotor downstream of it. Maximum σ_w^2 and EDR_w in the separation region are $9.4 \text{ m}^2 \text{ s}^{-2}$ and $0.51 \text{ m}^{2/3} \text{ s}^{-1}$, respectively. Highest turbulence intensities are detected inside the rotor. While the updraught itself appears ‘moderately’ turbulent, ‘severe’ turbulence is encountered in the downdraught region, with maximum σ_w^2 and EDR_w of $16.4 \text{ m}^2 \text{ s}^{-2}$ and $0.77 \text{ m}^{2/3} \text{ s}^{-1}$, respectively. The relative uncertainty of σ_w^2 , shown in Fig. 9e, remains within the 25% threshold in the separation region and inside the rotor. Unfortunately, the upstream side of the main updraught, which was detected to be most strongly turbulent in the *in situ* measurements (cf. Peak 3’), is missing in the radar data due to insufficient return signal.

4.2. 5 February 2006 – a lee-wave rotor

Observations and modelling of the 5 February 2006 case (FHO15 and GSS15) have shown that the flow on this day is characterized by large-amplitude waves in the lee of the MBM and a *lee-wave* rotor (Lester and Fingerhut 1974) with some degree of transitional behaviour, displaying a similar upstream movement of the rotor as in the 26 January case.

Our focus is again on the spatial distribution and magnitude of turbulence. Figures 4c,d and 6c,d show UWKA measurements of w , θ , u , and TKE and EDR from Legs 1 and 3 on 5 February. Unlike the passes flown on 26 January, legs on this day were not flown at the same altitude (cf. Table 1). We again subdivide measurements along Leg 1 into Regions I–III. Region I bears some resemblance with that on 26 January. Along-track horizontal wind u is approximately constant, while w transitions from near zero to negative (-3 m s^{-1}) at the downstream end of Region I, where θ increases rapidly by approx. 3 K. This again points to the fact that UWKA was first sampling in the relatively undisturbed upstream environment and then penetrated into a wave trough downstream of Region I. Region II is characterized by stronger variations in w , a drop in u by around 10 m s^{-1} , and a remarkably sharp, localized increase in θ of another 2 K. This feature coincides with the strongest peak (Peak 1 in Figs. 4c and 6c) in TKE and EDR of $5.4 \text{ m}^2 \text{ s}^{-2}$ and $0.25 \text{ m}^{2/3} \text{ s}^{-1}$, respectively. Region III lacks the strong updraught and downdraught couplet present along Leg 3 of 26 January but has a secondary positive θ anomaly of approx. 2 K and local minimum in u collocated with a local turbulence maximum (Peak 2), whose origin, however, is not entirely understood.

The presence and origin of Peak 1 in turbulence intensity has remained unaddressed in previous studies. Closer inspection of a model cross-section from 5 February (Fig. 7b) indicates a relatively warm and stagnant region of air at and above flight level slightly downstream of the mountain top, whose location exactly matches the observed θ and turbulence maximum. Thus, it is plausible that the observations made along Leg 1 of 5 February document another aircraft encounter with a wave breaking region. UWKA measurements along Leg 3 of that day largely differ from those along Leg 1, owing to the fact that the aircraft crossed the MBM at an approx. 1 km lower altitude. The variation of w and θ along Leg 3 evidences a smooth lee wave. Turbulence intensities remain below $0.3 \text{ m}^2 \text{ s}^{-2}$ and $0.07 \text{ m}^{2/3} \text{ s}^{-1}$.

Figures 10 and 11 show radar data and derived fields along Legs 1 and 3. Leg 1 of 5 February is the leg with the best radar coverage of all legs on 26 January and 5 February. Above the lee slope of the MBM, radar vertical Doppler velocities reveal strong descending motion (-4 m s^{-1}), followed by upward ($+4.5 \text{ m s}^{-1}$) and weaker downward (-2 m s^{-1}) motion, associated with a lee wave. Right below the lee wave crest, speckled, positive and negative vertical velocities indicate enhanced levels of turbulence. Using dual-Doppler analysis, FHO15 detected near-surface reversed flow in this region, revealing the presence of a lee-wave rotor. Small-scale variations in w , indicative of turbulence, extend farther downstream towards the upwind slope of Sheep Mountain. A strong downdraught (up to -8 m s^{-1}) is detected on the lee side of Sheep Mountain. Radar-derived turbulence intensities reveal several regions of ‘moderate’ to ‘severe’ turbulence upstream and downstream of the MBM. The rather large patch of turbulence on the western edge of the stretch can be attributed to turbulence generated at the flanks of Elk Mountain (Karacostas and Marwitz 1980), which is located approx. 35 km upstream of the MBM (cf. Fig. 1).

Turbulence on the lee side of the MBM exhibits a complex spatial structure. A small patch of ‘moderate-severe’ turbulence can be found in the immediate lee of Medicine Bow Peak (1–3 km downstream of it), with maximum turbulence intensities σ_w^2

and EDR_w of $10.4 \text{ m}^2 \text{ s}^{-2}$ and $0.41 \text{ m}^{2/3} \text{ s}^{-1}$, respectively. Such strong turbulence right behind a steep peak is often associated with *bluff-body separation* of the boundary-layer, occurring even without wave forcing from aloft (Baines 1997). The largest region of strong turbulence is found in the rotor, beneath the lee wave crest. Turbulence is strongest in the westernmost part of the rotor, with maximum turbulence intensities reaching $7.8 \text{ m}^2 \text{ s}^{-2}$ and $0.50 \text{ m}^{2/3} \text{ s}^{-1}$. In the region of strong downslope winds in the lee of Sheep Mountain a maximum in σ_w^2 of $9.5 \text{ m}^2 \text{ s}^{-2}$ is detected, but no reliable estimate of EDR is available.

In the analysis of UWKA measurements, we pointed to the two peaks (Peak 1 and 2) in TKE at flight level and briefly discussed the possible origin of Peak 1. The variance σ_w^2 from *in situ* and radar measurements reveals that turbulence at flight-level is clearly separated from strong turbulence closer to the ground by a region of low, i.e. undetectable turbulence (grey colour in Figs. 10c,d). This underpins the distinct origins of turbulence in these regions and, indirectly, supports the conjecture of mid-tropospheric wave breaking on 5 February.

Figure 11 contains the radar turbulence analysis for Leg 3, crossing the MBM around 40 min later. The first lee wave crest has moved upstream and a train of waves (apparent from the combined UWKA and WCR measurements of w in Fig. 11b) has formed. In response to the relocation of the first lee wave crest, the region of strong turbulence has retreated upstream, decreased in size and weakened somewhat (maximum turbulence intensities around $5.7 \text{ m}^2 \text{ s}^{-2}$ and $0.45 \text{ m}^{2/3} \text{ s}^{-1}$).

The evolution of the 5 February event is further evidenced in Fig. 12 by the composite analysis of Legs 1–4. The gradual retreat of the location of turbulence on 5 February bears some resemblance with the upstream shift of the rotor and its turbulence on 26 January. Unfortunately, along Legs 2–4, no data at the flight level of Leg 1 (5150 m MSL) is available. Thus, observational evidence of the evolution of gravity wave breaking is lacking and, judging from the aircraft measurements alone, we can only speculate about the reason for the ceasing and retreating rotor turbulence. Model cross-sections on 5 February after 1630 UTC (GSS15, their Fig. 12), however, do support the idea that the evolution of the flow at mid-levels, i.e., the onset and cessation of wave breaking, is the likely cause of the upstream shift of the rotor, as with the 26 January event. Note that the model runs for this case did reproduce the upstream shift too, although with a time delay of 3–4 hours.

4.3. 2 February 2006 – a reference case with no indication of gravity waves

For comparison, we also include the analysis of radar data collected along one cross-mountain pass on 2 February 2006. Upstream conditions on this day were characterized by moderate mean wind speed and considerably lower static stability relative to the two wave cases (Geerts *et al.* 2011). No gravity waves were excited by the MBM on this day.

Figure 13 shows the radar data analysis collected along Leg 2 of 2 February. The upstream part of the flow exhibits ‘light-moderate’ turbulence (σ_w^2 and EDR_w up to $1.8 \text{ m}^2 \text{ s}^{-2}$ and $0.18 \text{ m}^{2/3} \text{ s}^{-1}$, respectively). Right upstream of the mountain top, ‘moderate’ turbulence (up to $3.9 \text{ m}^2 \text{ s}^{-2}$ or $0.32 \text{ m}^{2/3} \text{ s}^{-1}$) is detected in a region of enhanced vertical air motion. ‘Moderate-severe’ turbulence (up to $6.7 \text{ m}^2 \text{ s}^{-2}$ or $0.43 \text{ m}^{2/3} \text{ s}^{-1}$) is detected in the immediate lee of a steep peak at mountain top, as with Leg 1 on 5 February.

5. Turbulence intensities in mountain-induced turbulent processes

In the previous section, detailed analysis of three distinct mountain flow cases has revealed a variety of mountain-induced

turbulent processes, ranging from in-cloud turbulence to wave-induced boundary-layer separation and rotor formation. Table 2 summarizes the turbulence intensities for each of the processes studied in this work, including the measurement uncertainties. Table 3 lists observations of the same processes documented in the literature. The comparison of our results to turbulence intensities reported in the literature reveals the sensitivity of turbulence measures to the chosen filter scale. It is worth stressing that, for the cases considered in this work, the choice of a filter scale of 1.5 km was made on the basis of high-pass filtering tests that remove apparent features of mesoscale motion from the spatial series, leaving us with the turbulent component of the signal.

5.1. Mid-tropospheric gravity wave breaking

Direct observations of mid-tropospheric gravity wave breaking through aircraft encounters are quite rare. We are only aware of four studies examining direct aircraft measurements of turbulent wave breakdown at mid-levels. Lilly (1978) investigated the ‘mid-tropospheric turbulence zone’ during the Boulder windstorm of 11 January 1972. A case of gravity wave breaking over the Central Alps during MAP on 21 October 1999 was documented by Jiang and Doyle (2004). Elvidge *et al.* (2014) described low-level wave breaking at a wave-induced critical level during a foehn event over the Antarctic Peninsula. A case of severe Bora flow on the Adriatic coast of Croatia was observed on 7 March 1982 during ALPEX (Smith 1987). Figure 6b of Smith (1987) shows the breakdown of a large-amplitude gravity wave at mid-levels (around 3000 m MSL), roughly 2000 m above the top of the Dinaric Alps. Underneath the turbulent breakdown region of the ALPEX case, steepened isentropes evidence a hydraulic jump-like feature. Turbulence estimates from the latter two studies compare best with our estimates of TKE in regions of wave breaking and hydraulic jumps, in particular in the 26 January case.

5.2. Internal hydraulic jumps

Direct aircraft measurements in hydraulic jumps are relatively rare, too. We are only aware of another study by Armi and Mayr (2011) documenting a jump-like feature in the lee of the Sierra Nevada, California, on 9–10 April 2006, during Intensive Observing Period 11 of T-REX. The maximum EDR value of $0.35 \text{ m}^{2/3} \text{ s}^{-1}$ reported for that event is in striking agreement with $0.38 \text{ m}^{2/3} \text{ s}^{-1}$ in the updraught part of the jump in the 26 January case, obtained in this study.

5.3. Atmospheric rotors

On 26 January and 5 February, rotor circulations were captured by WCR along several passes across the MBM, allowing the documentation of the quasi-instantaneous spatial distribution and intensity of turbulence in the rotors’ interior. Unfortunately, radar data from the rotor is incomplete for 26 January due to insufficient radar backscatter at lower levels. Nevertheless, turbulence intensities from Leg 5 (Fig. 9) suggest that the strongest turbulence (of the ‘severe’ category) is located right downstream of the leading updraught of this hydraulic jump-type rotor. On 5 February, a similar picture is obtained from Leg 1 passing over the fully-developed lee-wave rotor (Fig. 10) and from Leg 3 (Fig. 11) during its later stages. The detected spatial distribution of turbulence within the rotor is in agreement with previous observations by Lester and Fingerhut (1974) and Cohn *et al.* (2011).

Using numerical simulation and ground-based remote sensing, Doyle and Durran (2002, 2007), and Doyle *et al.* (2009) studied the inner flow field of rotors and attributed patches of strong turbulence inside the rotor to intermittent smaller-scale vortical

structures with characteristic length scales of 500 to 1000 m. These ‘subrotors’ were found to originate from Kelvin-Helmholtz instability in the separated boundary layer. The presence of subrotors on 26 January and 5 February was confirmed by FHO15 considering the cross-track vorticity along the rotor crest, derived from dual-Doppler analysis. Owing to the chosen leg segment length, our turbulence analysis approach does not allow to explicitly resolve subrotor structures. Separate patches of ‘moderate’ to ‘severe’ turbulence in the rotor interior, however, are apparent from the fields of turbulence intensity and attributing these to subrotors seems a plausible explanation.

There are only a few observational studies providing quantitative estimates of turbulence intensity in a rotor. For instance, Lester and Fingerhut (1974) report approximate values for the variance of the longitudinal velocity σ_u^2 and EDR. Our results are also in good agreement with a more recent study by Darby and Poulos (2006), making use of UWKA measurements to study the evolution of lee-wave rotor activity in the lee of Pikes Peak, Colorado.

5.4. Bluff-body boundary-layer separation

Another turbulent process covered by the radar observations is the bluff-body separation of the boundary-layer in the immediate lee of steep peaks. This phenomenon, occurring in both neutrally and stably stratified fluids, is well known in aeronautical engineering and has occasionally been observed in the atmosphere, for example, in the Sierra Nevada during T-REX (Grubišić *et al.* 2006; Haimov *et al.* 2008). Of the numerous turbulence-related aviation incidents in the vicinity of mountains (Carney *et al.* 1995), some are likely related to the phenomenon.

Bluff-body boundary-layer separation was observed on 2 February and 5 February downstream of Medicine Bow Peak, with ‘moderate-severe’ maximum σ_w^2 and EDR_w in the range 6.7–10.3 m² s⁻² and 0.41–0.43 m^{2/3} s⁻¹, respectively.

6. Summary and conclusions

Airborne *in situ* and single-Doppler radar measurements over the Medicine Bow Mountains in SE Wyoming have been used to study atmospheric turbulence induced by the presence of mountainous terrain. Measurements during several complex mountain flow cases were conducted by UWKA and WCR during the NASA06 campaign. The collected data offers the opportunity to study a variety of turbulent mountain flow processes, ranging from gravity wave breaking to atmospheric rotors.

Our analysis focuses on describing the spatial distribution of turbulence and on providing quantitative estimates of turbulence intensity, in terms of turbulent kinetic energy (TKE), variance of vertical velocity (σ_w^2) and cube root of the energy dissipation rate (EDR). The main findings of this study are twofold, pertaining to the turbulence measurement technique and to the quantification of atmospheric turbulence over complex terrain.

Prior to this study, it was not clear whether the inherent inaccuracies in measured single-Doppler velocities from airborne fixed-antenna radar, related to the motion of the measurement platform, would allow quantitative turbulence estimates in spatially inhomogeneous airflow. By carrying out a thorough analysis of potential sources of error in the Doppler wind retrieval and their effect on the uncertainty of the turbulence estimates, we have shown here that this question can be answered in the affirmative.

In the estimation of the variance of vertical air motion from the radar, the following sources of uncertainty needed to be taken into account: (i) Uncertainty in the determination of aircraft motion and attitude, (ii) limited accuracy of the beam-pointing angle calibration, (iii) variance of hydrometeor fall speed, (iv) loss

of variance due to the radar pulse-volume averaging effect, and (v) contamination of radar Doppler velocity by the horizontal wind.

For the cases we analysed, we found that the sum of these terms remains sufficiently small to allow a quantitative measurement of turbulence with the airborne Doppler radar. While only qualitative estimates of turbulence intensity could be obtained outside of the most turbulent regions, 25% accuracy and better was achieved in regions of ‘moderate’ to ‘severe’ turbulence in the lee of the mountains. The minimum detectable turbulence in the cases under consideration was limited to approximately 0.1 m² s⁻² and 0.05 m^{2/3} s⁻¹ for σ_w^2 and EDR, respectively. However, turbulence estimates were reliable, i.e., affected by reasonably small uncertainty levels, only for values greater than 0.5 m² s⁻² and 0.15 m^{2/3} s⁻¹ for σ_w^2 and EDR, respectively. It is also worth pointing to the good agreement between *in situ* and radar-derived turbulence estimates, which is apparent, for example, in Figs. 8, 9, and 13. While detailed comparisons between *in situ* and remotely-sensed turbulence estimates have been made in other studies (e.g., Istok and Doviak 1986; Meischner *et al.* 2001; Lothon *et al.* 2005), a systematic analysis using the NASA06 data set is not possible due to generally poor radar backscatter right above and below flight level.

We stress that the thresholds of minimum detectable turbulence and uncertainty provided above strictly apply to the data under consideration here. Future application of the analysis technique to a different data set will necessitate careful re-evaluation of each of the terms contributing to the uncertainty. Some of these terms are tightly linked to properties of the instruments used (for instance, the aircraft motion correction or the pulse-volume averaging effect) and their re-evaluation can largely follow what has been proposed in this work. Special attention, however, will have to be dedicated to the uncertainties associated with environmental parameters, expected to display a large variability from case to case. This applies in particular to the contamination of vertical Doppler velocity by the horizontal wind and the variance of hydrometeor fall speed, the latter of which was found to considerably limit the quality of results in other cases (Lothon *et al.* 2005).

Two days of the NASA06 campaign with strong gravity wave forcings have been analysed. Results are summarized in Table 2, providing maximum turbulence intensities and relative uncertainties for each observed mountain-induced process. On both days, a region of turbulent breakdown of a large gravity wave was observed approx. 1600 m above mountain top; ‘moderate’ turbulence was detected in the breaking regions (maximum TKE and EDR of 5.4 m² s⁻² and 0.25 m^{2/3} s⁻¹, respectively). These observations add to barely a handful of observations of mid-tropospheric gravity wave breaking documented in the literature.

A unique result of this study is the quantitative estimation of the intensity of turbulence and its spatial distribution in the interior of atmospheric rotors, provided by the radar-derived turbulence fields. Maximum turbulence intensities in both the hydraulic jump-type rotor and the lee wave-type rotor have been detected below the updraught of the main wave aloft, in agreement with past observations and numerical studies of rotor turbulence. In both cases, turbulence in the rotor is ‘severe’, with σ_w^2 and EDR ranging between 7.8–16.4 m² s⁻² and 0.50–0.77 m^{2/3} s⁻¹, respectively. The spatial distribution of turbulence maxima inside the rotor seems patchy, reminiscent of individual smaller-scale vortices (subrotors, Doyle *et al.* 2009). Apart from wave-induced processes, ‘moderate-severe’ turbulence (6.7–10.3 m² s⁻² and 0.41–0.43 m^{2/3} s⁻¹) was also detected leeward of steep peaks, underscoring the threat for aircraft to approach mountain slopes too closely.

In conclusion, it has been demonstrated that combined aircraft *in situ* and Doppler radar measurements allow the

documentation of mountain-induced turbulence at unprecedented spatial resolution and reasonable accuracy. The compiled list of mountain-induced processes and associated turbulence intensities (Table 2) including civil aviation turbulence categories, can provide updated turbulence reference values for these processes to the community of aviation weather forecasters. In this context, it is hoped that this study can further the knowledge of the hazards involved in flying in the vicinity of mountains, thereby contributing to improved turbulence avoidance strategies.

Acknowledgements

This study was supported in part by the FWF (Austrian Science Fund) grant P24726-N27 to the University of Vienna (“STABLEST, Stable boundary layer separation and turbulence”). Visits of the first two authors to NCAR were supported by the Faculty of Earth Sciences, Geography and Astronomy of the University of Vienna. NCAR is sponsored by the National Science Foundation. The authors are grateful to Željko Večenaj, Branko Grisogono, Bob Sharman, Don Lenschow, Jothiram Vivekanandan, and Scott Ellis for useful discussions and valuable advice and to Jeff French and Qun Miao for help with the data. The authors also thank two anonymous reviewers for their careful review and constructive comments.

Appendix A

Uncertainty in the variance of vertical velocity σ_w^2 due to contamination by the horizontal wind

Along the NASA06 flight legs under consideration, UWKA encountered moderate turbulence at flight level, leading to considerable deviations from mean pitch and zero roll and drift angles. As a result, the fixed radar beams were not pointing perfectly vertical, causing a possible contamination of vertical Doppler velocity v_r by the horizontal wind. It is not possible to accurately correct for this contamination since the along-track wind in a given radar range deviates up to 30 m s^{-1} from the one at flight altitude but is not known exactly. In this section, we evaluate the effect of the contamination on the uncertainty of the variance of vertical wind velocity σ_w^2 .

To estimate the contamination, we relate the components of the wind \tilde{u} , \tilde{v} , and \tilde{w} in the aircraft-fixed reference system (ACRS) to the components u , v , and w in the along-track reference system (ATRS). In the ACRS, the unit vector $\tilde{\mathbf{e}}_x$ is parallel to the aircraft longitudinal axis, $\tilde{\mathbf{e}}_y$ is 90° to the right of the longitudinal axis, and $\tilde{\mathbf{e}}_z$ is pointing down. In the ATRS, \mathbf{e}_x points in the along-track direction, \mathbf{e}_y points 90° horizontally right from it in the cross-track direction, and \mathbf{e}_z points nadir.

The velocity vector of an air parcel \mathbf{v} can be expressed as

$$\mathbf{v} = \tilde{u}\tilde{\mathbf{e}}_x + \tilde{v}\tilde{\mathbf{e}}_y + \tilde{w}\tilde{\mathbf{e}}_z = u\mathbf{e}_x + v\mathbf{e}_y + w\mathbf{e}_z. \quad (9)$$

The components of \mathbf{v} in the ATRS and the ACRS are related by a transformation, given by a series of rotations. Following Wendisch and Brenguier (2013), we use the Tait-Bryan sequence of rotations: (i) rotation \mathbf{R} about $\tilde{\mathbf{e}}_x$ by roll angle (ϕ , right wing down positive); (ii) rotation \mathbf{P} about $\tilde{\mathbf{e}}_y$ by pitch angle (θ , nose up positive); and (iii) rotation \mathbf{D} about $\tilde{\mathbf{e}}_z$ by drift angle (γ , positive in clockwise direction), with the rotation matrices being defined

as

$$\mathbf{R} = \begin{pmatrix} 1 & 0 & 0 \\ 0 & \cos \phi & -\sin \phi \\ 0 & \sin \phi & \cos \phi \end{pmatrix}, \quad \mathbf{P} = \begin{pmatrix} \cos \theta & 0 & \sin \theta \\ 0 & 1 & 0 \\ -\sin \theta & 0 & \cos \theta \end{pmatrix}, \quad (10)$$

$$\mathbf{D} = \begin{pmatrix} \cos \gamma & -\sin \gamma & 0 \\ \sin \gamma & \cos \gamma & 0 \\ 0 & 0 & 1 \end{pmatrix}.$$

The transformation from the ACRS to the ATRS is then given by

$$\begin{pmatrix} u & v & w \end{pmatrix}^T = \mathbf{D} \mathbf{P} \mathbf{R} \begin{pmatrix} \tilde{u} & \tilde{v} & \tilde{w} \end{pmatrix}^T. \quad (11)$$

Inverting this equation for the vertical component in the ACRS \tilde{w} and identifying \tilde{w} with the radial Doppler velocity v_r , we get the expression for the contamination by the horizontal wind as

$$v_r = \tilde{w} = u(\sin \gamma \sin \phi + \sin \theta \cos \gamma \cos \phi) + v(\sin \gamma \sin \theta \cos \phi - \sin \phi \cos \gamma) + w \cos \phi \cos \theta. \quad (12)$$

Approximating sines and cosines for small aircraft attitude angles (maximum $\phi, \theta, \gamma \leq 6^\circ \simeq 0.11 \text{ rad}$), and neglecting products of small angles, this can be simplified to a good approximation to

$$v_r = \tilde{w} = u\theta - v\phi + w. \quad (13)$$

To relate the variance of radial Doppler velocity $\sigma_{v_r}^2$ and the variance of vertical velocity σ_w^2 , all relevant quantities are split into their mean and fluctuation parts ($x = \bar{x} + x'$; $x = \{u, v, w, \phi, \theta\}$), to be evaluated along individual leg segments.

Inserting these into Eq. (13) and averaging leads to:

$$\overline{(v_r + v_r')^2} = \overline{[(\bar{\theta} + \theta')(\bar{u} + u') - (\bar{\phi} + \phi')(\bar{v} + v') + (\bar{w} + w')]^2}. \quad (14)$$

Expanding Eq. (14) results in a total of 55 terms involving first- to fourth-order moments of the perturbation variables. The number of terms can be reduced substantially by making the following simplifications and assumptions:

- $\bar{v}_r = \bar{u}\bar{\theta} - \bar{v}\bar{\phi} + \bar{w}$.
- $\bar{v}_r' = \bar{u}' = \bar{v}' = \bar{w}' = \bar{\theta}' = \bar{\phi}' = 0$.
- Roll and pitch angle perturbations $\{\theta', \phi'\}$ are uncorrelated with wind fluctuations $\{u', v', w'\}$; e.g., $\overline{w'\theta'} = 0$.
- Assuming that perturbations follow normal distributions, Isserlis' theorem (Isserlis 1918) applies to third- and fourth-order moments; e.g., $\overline{\theta'u'v'} = 0$ and $\overline{\theta'\phi'u'v'} = \overline{\theta'\phi'}\overline{u'v'} + \overline{\theta'u'}\overline{\phi'v'} + \overline{\theta'v'}\overline{\phi'u'} = \overline{\theta'\phi'}\overline{u'v'}$.

With $\sigma_x^2 \equiv \overline{x'^2}$ for the variance of a quantity x , we finally obtain an equation relating $\sigma_{v_r}^2$ to σ_w^2 ,

$$\begin{aligned} \sigma_{v_r}^2 = & \sigma_w^2 + \sigma_{\theta}^2 \bar{u}^2 + \bar{\theta}^2 \sigma_u^2 + \sigma_{\phi}^2 \sigma_u^2 \\ & + \sigma_{\phi}^2 \bar{v}^2 + \bar{\phi}^2 \sigma_v^2 + \sigma_{\phi}^2 \sigma_v^2 \\ & + 2\bar{\theta} \overline{u'w'} - 2\bar{\phi} \overline{v'w'} - 2\theta' \phi' \overline{u'v'} \\ & - 2\theta' \phi' \bar{u}\bar{v} - 2\bar{\theta}\bar{\phi} \overline{u'v'}. \end{aligned} \quad (15)$$

Terms 2–7 on the right-hand side of Eq. (15) consist of (positive semi-definite) products of squares of the mean variables and variances of perturbations, by which the true variance σ_w^2 tends to be overestimated. For example, upon variation of pitch angle, part of the mean along-track wind \bar{u} is sampled and this effect appears as an additional contribution $\sigma_{\theta}^2 \bar{u}^2$ to the true variance σ_w^2 . Terms 8–12 of Eq. (15) consist of products of mean variables

3 Turbulence in breaking mountain waves and rotors

10

L. Strauss *et al.*

and covariances of the perturbation variables, which can assume either sign.

Since the horizontal along-track and cross-track components of the wind u and v in each radar range gate are not known, it is not possible to evaluate these terms exactly. Instead, we must seek an upper bound for the uncertainty in the estimation of σ_w^2 that they cause. We define the upper bounds of terms 2–7 and terms 8–12 of Eq. (15) as, respectively,

$$\begin{aligned} \sigma_{\text{HC}, A}^2 &= \sigma_\theta^2 \bar{u}^2 + \bar{\theta}^2 \sigma_u^2 + \sigma_\theta^2 \sigma_u^2 + \\ &\quad \sigma_\phi^2 \bar{v}^2 + \bar{\phi}^2 \sigma_v^2 + \sigma_\phi^2 \sigma_v^2, \\ \sigma_{\text{HC}, B}^2 &= |2\bar{\theta} \overline{u'w'}| + |2\bar{\phi} \overline{v'w'}| + |2\bar{\theta}' \overline{\phi' u'v'}| + \\ &\quad |2\bar{\theta}' \overline{\phi' uv}| + |2\bar{\theta} \overline{\phi' u'v'}|. \end{aligned} \quad (16)$$

All quantities printed in boldface are unknowns and we approximate them by making the following assumptions:

- $\bar{u} \leq \bar{u}_{\text{max}} \approx 30 \text{ m s}^{-1}$. The minimum and maximum along-track wind components are -5 m s^{-1} (in regions of reversed flow near the ground) and 25 m s^{-1} , respectively.
- $\bar{v} \leq \bar{v}_{\text{max}} \approx 10 \text{ m s}^{-1}$, which corresponds to the maximum cross-track wind component.
- $\sigma_u^2 \approx \sigma_v^2 \approx \sigma_{v_r}^2$.
- $|u'v'| \approx 2\sigma_{r_{uv}} \cdot \sigma_{v_r}^2$, where $2\sigma_{r_{uv}}$ is two times the standard deviation of correlation coefficients $r_{uv} = \overline{u'v'}/(\sigma_u \sigma_v)$ obtained from the *in situ* data. Accordingly, $|u'w'| \approx 2\sigma_{r_{uw}} \sigma_{v_r}^2$ and $|v'w'| \approx 2\sigma_{r_{vw}} \sigma_{v_r}^2$. We determined $\sigma_{r_{uv}}$, $\sigma_{r_{uw}}$, and $\sigma_{r_{vw}}$ as 0.305, 0.294, and 0.291, respectively, considering *in situ* measurements from all flights on 26 January and on 5 February.

The approximated upper bounds $\sigma_{\text{HC}, A}^2$ and $\sigma_{\text{HC}, B}^2$ to the horizontal wind contamination are now given by

$$\begin{aligned} \sigma_{\text{HC}, A}^2 &= \sigma_\theta^2 \bar{u}_{\text{max}}^2 + \bar{\theta}^2 \sigma_{v_r}^2 + \sigma_\theta^2 \sigma_{v_r}^2 + \\ &\quad \sigma_\phi^2 \bar{v}_{\text{max}}^2 + \bar{\phi}^2 \sigma_{v_r}^2 + \sigma_\phi^2 \sigma_{v_r}^2, \\ \sigma_{\text{HC}, B}^2 &= 2|\bar{\theta}| \cdot 2\sigma_{r_{uw}} \sigma_{v_r}^2 + 2|\bar{\phi}| \cdot 2\sigma_{r_{vw}} \sigma_{v_r}^2 + \\ &\quad 2|\bar{\theta}' \phi'| \cdot 2\sigma_{r_{uv}} \sigma_{v_r}^2 + 2|\bar{\theta}' \phi'| \cdot \bar{u}_{\text{max}} \bar{v}_{\text{max}} + \\ &\quad 2|\bar{\theta} \phi'| \cdot 2\sigma_{r_{uv}} \sigma_{v_r}^2, \end{aligned} \quad (17)$$

and the upper and lower uncertainty bounds of σ_w^2 due to the horizontal wind contamination can be written, respectively, as

$$\sigma_w^2 = \sigma_{v_r}^2 + \begin{cases} +\sigma_{\text{HC}, A}^2 \\ -\sigma_{\text{HC}, B}^2 \end{cases}. \quad (18)$$

It is apparent from Eq. (17) that the (upper-bounded) uncertainty in the estimation of σ_w^2 due to the horizontal wind contamination of $\sigma_{v_r}^2$ is highly variable and mainly depends on aircraft pitch θ and roll ϕ and on $\sigma_{v_r}^2$ itself. The main contribution to the uncertainty can be traced back to the terms $\sigma_\theta^2 \bar{u}_{\text{max}}^2$, $2|\bar{\theta}| \cdot 2\sigma_{r_{uw}} \sigma_{v_r}^2$ and $2|\bar{\phi}| \cdot 2\sigma_{r_{vw}} \sigma_{v_r}^2$ in Eq. (17), making up for roughly 90% of the total. Figure A1 shows two examples of the relative uncertainty of σ_w^2 due to the horizontal wind contamination, defined as $(\sigma_{\text{HC}, A}^2 + \sigma_{\text{HC}, B}^2)/\sigma_{v_r}^2$. Regions in the lower-level flow with increased relative uncertainty are associated with patches of moderate turbulence at flight level. The relative uncertainty can be substantial if the sampled atmospheric turbulence is low, but it remains below 20% in the most turbulent regions of the flow.

Appendix B

Uncertainty in the estimation of energy dissipation rate from radar data

In Section 3.3, we link the primary uncertainty in the estimation of EDR from aircraft *in situ* and Doppler radar measurements to the

scatter of individual EDR_i estimates around the mean $\overline{\text{EDR}}$. The uncertainties of individual EDR_i estimates and the mean $\overline{\text{EDR}}$ are found to be $\pm 29\%$ and $\pm 16\%$ respectively.

For EDR estimates from radar data, two additional possible sources of error have to be taken into account: the contamination of $\sigma_{v_r}^2$ by the horizontal wind and the uncertainty in the along-track wind in a given radar range gate. The first term contributes less than 0.5% uncertainty. In fact, with the assumption of locally isotropic turbulence, the spectral power densities $S_w(k)$ and $S_{v_r}(k)$ only differ by a factor $S_w(k)/S_{v_r}(k) = 4/3[1 + 1/3 \cos^2(\theta)]^{-1}$, which never exceeds 1.0038 for a maximum pitch angle of $\theta_{\text{max}} \approx 6^\circ \approx 0.11 \text{ rad}$. We thus neglect this term.

The second uncertainty results from the error made in the estimation of EDR from the vertical Doppler velocity,

$$\text{EDR}_w = \varepsilon_w^{1/3} = \left[\frac{2\pi}{\text{TAS}} \left(\frac{S_{v_r}(f) f^{5/3}}{\alpha_w} \right)^{3/2} \right]^{1/3}, \quad (19)$$

due to the conversion of WCR time series to spatial series using aircraft true airspeed TAS at flight level,

$$\text{TAS} = \text{GSPD} - u_{\text{fl}}. \quad (20)$$

GSPD is the aircraft speed relative to the ground and u_{fl} is the along-track wind component at flight level. Far from flight level, u deviates up to 30 m s^{-1} from u_{fl} , giving rise to a maximum relative error in EDR_w of

$$\begin{aligned} \frac{\text{EDR}_w}{\overline{\text{EDR}}} - 1 &= \left(\frac{\text{TAS} \pm 30 \text{ m s}^{-1}}{\text{TAS}} \right)^{1/3} - 1 \\ &\approx \begin{cases} +9\% & \text{for a tailwind} \\ -11\% & \text{for a headwind} \end{cases}, \end{aligned} \quad (21)$$

for an average TAS of 100 m s^{-1} . The total uncertainty in the estimation of EDR_w from radar data is thus given by

$$\begin{aligned} \text{EDR} &= (\text{EDR}_w^{+9\%/-11\%}) \pm 29\% \\ &= \begin{cases} \text{EDR}_w^{+41\%/-23\%} & \text{for a tailwind} \\ \text{EDR}_w^{+15\%/-37\%} & \text{for a headwind} \end{cases}. \end{aligned} \quad (22)$$

References

- Ágústsson H, Ólafsson H. 2014. Simulations of observed lee waves and rotor turbulence. *Mon. Wea. Rev.* **142**: 832–849, doi:10.1175/MWR-D-13-00212.1.
- ALPEX Project Homepage. Cited 2015. Alpine Experiment (ALPEX). https://www.eol.ucar.edu/field_projects/alpex.
- Armi L, Mayr GJ. 2011. The descending stratified flow and internal hydraulic jump in the lee of the Sierras. *J. Appl. Meteor. Climatol.* **50**: 1995–2011, doi: 10.1175/JAMC-D-10-05005.1.
- Baines PG. 1997. *Topographic Effects in Stratified Flows*. Cambridge University Press.
- Banta RM, Shun CM, Law DC, Brown W, Reinking RF, Hardisty RM, Senff CJ, Brewer WA, Post MJ, Darby LS. 2013. Observational techniques: Sampling the mountain atmosphere. In: *Mountain Weather Research and Forecasting*, Chow FK, De Wekker SF, Snyder BJ (eds), Springer Netherlands, pp. 409–530, doi: 10.1007/978-94-007-4098-3_8.
- Bougeault P, Binder P, Buzzi A, Dirks R, Houze R, Kuettner J, Smith RB, Steinacker R, Volkert H. 2001. The map special observing period. *Bull. Amer. Meteor. Soc.* **82**: 433–462, doi:10.1175/1520-0477(2001)082<0433:TMSOP>2.3.CO;2.
- Brown E, Friehe C, Lenschow D. 1983. The use of pressure-fluctuations on the nose of an aircraft for measuring air motion. *J. Climate Appl. Meteor.* **22**: 171–180, doi:10.1175/1520-0450(1983)022<0171:TUOPFO>2.0.CO;2.
- Carney TQ, Bedard AJ, Brown JM, Kraus MJ, McGinley J, Lindholm TA. 1995. Hazardous mountain winds and their visual indicators. Department of Commerce/NOAA, USA.
- Champagne FH. 1978. The fine-scale structure of the turbulent velocity field. *J. Fluid. Mech.* **86**: 67–108, doi:10.1017/S0022112078001019.
- Clark TL, Hall WD, Kerr RM, Middleton D, Radke L, Ralph FM, Neiman PJ, Levinson D. 2000. Origins of aircraft-damaging clear-air turbulence during the 9 December 1992 Colorado downslope windstorm: Numerical simulations and comparison with observations. *J. Atmos. Sci.* **57**: 1105–1131, doi:10.1175/1520-0469(2000)057<1105:OAOACA>2.0.CO;2.

- Cohn SA, Grubišić V, Brown WO. 2011. Wind profiler observations of mountain waves and rotors during T-REX. *J. Appl. Meteor. Climatol.* **50**: 826–843, doi:10.1175/2010JAMC2611.1.
- Comman LB, Morse CS, Cuning G. 1995. Real-time estimation of atmospheric turbulence severity from in-situ aircraft measurements. *J. Aircraft* **32**: 171–177, doi:10.2514/3.46697.
- Damiani R, Haimov S. 2006. A high-resolution dual-Doppler technique for fixed multi-antenna airborne radar. *IEEE Trans. Geosci. Remote Sens.* **44**: 3475–3489, doi:10.1109/TGRS.2006.881745.
- Darby LS, Poulos GS. 2006. The evolution of lee-wave-rotor activity in the lee of Pike's Peak under the influence of a cold frontal passage: Implications for aircraft safety. *Mon. Wea. Rev.* **134**: 2857–2876, doi:10.1175/MWR3208.1.
- Dörnbrack A. 1998. Turbulent mixing by breaking gravity waves. *J. Fluid Mech.* **375**: 113–141, doi:10.1017/S0022112098002833.
- Doyle JD, Durran DR. 2002. The dynamics of mountain-wave-induced rotors. *J. Atmos. Sci.* **59**: 186–201, doi:10.1175/1520-0469(2002)059<0186:TDOMWI>2.0.CO;2.
- Doyle JD, Durran DR. 2007. Rotor and subrotor dynamics in the lee of three-dimensional terrain. *J. Atmos. Sci.* **64**: 4202–4221, doi:10.1175/2007JAS2352.1.
- Doyle JD, Grubišić V, Brown WOJ, De Wekker SFJ, Dörnbrack A, Jiang Q, Mayor SD, Weissmann M. 2009. Observations and numerical simulations of subrotor vortices during T-REX. *J. Atmos. Sci.* **66**: 1229–1249, doi:10.1175/2008JAS2933.1.
- Doyle JD, Shapiro MA, Jiang Q, Bartels DL. 2005. Large-amplitude mountain wave breaking over Greenland. *J. Atmos. Sci.* **62**: 3106–3126, doi:10.1175/JAS3528.1.
- Druihet A, Durand P. 1997. Experimental investigation of atmospheric boundary layer turbulence. *Atmos. Res.* **43**: 345–388, doi:10.1016/S0169-8095(96)00041-5.
- Elvidge AD, Renfrew IA, King JC, Orr A, Lachlan-Cope TA. 2014. Foehn warming distributions in non-linear and linear flow regimes: A focus on the Antarctic Peninsula. *Q. J. R. Meteorol. Soc.* doi:10.1002/qj.2489. In print.
- Feng X. 2001. Evaluation of the MacCready turbulence sensor. Master's thesis, University of Wyoming.
- French JR, Haimov S, Oolman L, Grubišić V, Serafin S, Strauss L. 2015. Wave-induced boundary-layer separation in the lee of the Medicine Bow Mountains. Part I: Observations. *J. Atmos. Sci.* In review.
- Geerts B, Miao Q, Yang Y. 2011. Boundary layer turbulence and orographic precipitation growth in cold clouds: Evidence from profiling airborne radar data. *J. Atmos. Sci.* **68**: 2344–2365, doi:10.1175/JAS-D-10-05009.1.
- Grubišić V, Armi L, Kuettner J, Haimov S, Oolman L, Damiani R, Billings B. 2006. Atmospheric rotors: Aircraft *in situ* and cloud radar measurements in T-REX. In: *12th Conference on Mountain Meteorology*. Santa Fe, NM. [Available online at <https://ams.confex.com/ams/pdfpapers/114666.pdf>].
- Grubišić V, Doyle JD, Kuettner J, Dirks R, Cohn SA, Pan LL, Mobbs S, Smith RB, Whiteman CD, Czyzyk S, Vosper S, Weissmann M, Haimov S, De Wekker SFJ, Chow FK. 2008. The Terrain-induced Rotor Experiment. *Bull. Amer. Meteor. Soc.* **89**: 1513–1533, doi:10.1175/2008BAMS2487.1.
- Grubišić V, Serafin S, Strauss L, Haimov S, French JR, Oolman L. 2015. Wave-induced boundary-layer separation in the lee of the Medicine Bow Mountains. Part II: Modeling. *J. Atmos. Sci.* Accepted with minor revisions.
- Haimov S, Grubišić V, French J, Oolman L. 2008. Multi-Doppler measurements of atmospheric rotors and turbulent mountain waves. In: *2008 IEEE International Geoscience & Remote Sensing Symposium (IGARSS)*. Boston, MA. [Available online at <http://ieeexplore.ieee.org/stamp/stamp.jsp?arnumber=4779313>].
- Haimov S, Rodi A. 2013. Fixed-antenna pointing-angle calibration of airborne Doppler cloud radar. *J. Atmos. Oceanic Technol.* **30**: 2320–2335, doi:10.1175/JTECH-D-12-00262.1.
- Hirth W. 1933. *Die hohe Schule des Segelfluges*. Klings & Co., Berlin.
- Holmboe J, Klieforth H. 1957. Investigation of mountain lee waves and the air flow over the Sierra Nevada. Department of Meteorology, UCLA Final Rep. Contract AF 19(604)728.
- International Civil Aviation Organization. 2007. Meteorological Service for International Air Navigation. Annex 3 to Convention on International Civil Aviation. [Available online at <http://www.wmo.int/pages/prog/www/ISS/Meetings/CT-MTDCF-ET-DRC.Geneva2008/Annex3.16ed.pdf>].
- Isserlis L. 1918. On a formula for the product-moment coefficient of any order of a normal frequency distribution in any number of variables. *Biometrika* **12**: 134–139, doi:10.2307/2331932.
- Istok MJ, Doviak RJ. 1986. Analysis of the relation between Doppler spectral width and thunderstorm turbulence. *J. Atmos. Sci.* **43**: 2199–2214, doi:10.1175/1520-0469(1986)043<2199:AOTRBD>2.0.CO;2.
- Jiang Q, Doyle JD. 2004. Gravity wave breaking over the Central Alps: Role of complex terrain. *J. Atmos. Sci.* **61**: 2249–2266, doi:10.1175/1520-0469(2004)061<2249:GWBOTC>2.0.CO;2.
- Jiang Q, Doyle JD, Grubišić V, Smith RB. 2010. Turbulence characteristics in an elevated shear layer over Owens Valley. *J. Atmos. Sci.* **67**: 2355–2371, doi:10.1175/2010JAS3156.1.
- Karacostas TS, Marwitz JD. 1980. Turbulent kinetic energy budgets over mountainous terrain. *J. Appl. Meteor.* **19**: 163–174, doi:10.1175/1520-0450(1980)019<0163:TKEBOM>2.0.CO;2.
- Kolmogorov AN. 1941a. Dissipation of energy in the locally isotropic turbulence. *Comptes rendus de l'Académie des Sciences de l'URSS* **32**: 16–18.
- Kolmogorov AN. 1941b. The local structure of turbulence in incompressible viscous fluid for very large Reynolds numbers. *Comptes rendus de l'Académie des Sciences de l'URSS* **30**: 301–305.
- Kuettner J. 1959. The rotor flow in the lee of mountains. Geophysics Research Directorate (GRD) Research Notes No. 6, AFCRC-TN-58-626, Air Force Cambridge Research Center, USA.
- Küttner J. 1938. Moazagotl und Föhnwelle. *Beitr. Phys. fr. Atmos.* **25**: 79–114.
- Lester PF, Fingerhut WA. 1974. Lower turbulent zones associated with mountain lee waves. *J. Appl. Meteor.* **13**: 54–61, doi:10.1175/1520-0450(1974)013<0054:LTZAWM>2.0.CO;2.
- Lilly DK. 1978. A severe downslope windstorm and aircraft turbulence event induced by a mountain wave. *J. Atmos. Sci.* **35**: 59–77, doi:10.1175/1520-0469(1978)035<0059:ASDWAA>2.0.CO;2.
- Lilly DK, Kennedy PJ. 1973. Observations of a stationary mountain wave and its associated momentum flux and energy dissipation. *J. Atmos. Sci.* **30**: 1135–1152, doi:10.1175/1520-0469(1973)030<1135:OOASMW>2.0.CO;2.
- Lilly DK, Lester PF. 1974. Waves and turbulence in stratosphere. *J. Atmos. Sci.* **31**: 800–812, doi:10.1175/1520-0469(1974)031<0800:WATITS>2.0.CO;2.
- Lothorn M, Lenschow DH, Leon D, Vali G. 2005. Turbulence measurements in marine stratocumulus with airborne Doppler radar. *Q. J. R. Meteorol. Soc.* **131**: 2063–2080, doi:10.1256/qj.04.131.
- MacCready Jr PB. 1962. The inertial subrange of atmospheric turbulence. *J. Geophys. Res.* **67**: 1051–1059, doi:10.1029/JZ067i003p1051.
- MacCready Jr PB. 1964. Standardization of gustiness values from aircraft. *J. Appl. Meteor.* **3**: 439–449, doi:10.1175/1520-0450(1964)003<0439:SOGVFA>2.0.CO;2.
- Meischner P, Baumann R, Hiller H, Jank T. 2001. Eddy dissipation rates in thunderstorms estimated by Doppler radar in relation to aircraft *in situ* measurements. *J. Atmos. Oceanic Technol.* **18**: 1609–1627, doi:10.1175/1520-0426(2001)018<1609:EDRITE>2.0.CO;2.
- Ólafsson H, Ágústsson H. 2009. Gravity wave breaking in easterly flow over Greenland and associated low level barrier- and reverse tip-jets. *Meteorol. Atmos. Phys.* **104**: 191–197, doi:10.1007/s00703-009-0024-9.
- Onley SP, Friche CA, Larue JC, Busingier JA, Itsweire EC, Chang SS. 1996. Surface-layer fluxes, profiles, and turbulence measurements over uniform terrain under near-neutral conditions. *J. Atmos. Sci.* **53**: 1029–1044, doi:10.1175/1520-0469(1996)053<1029:SLFPAT>2.0.CO;2.
- Piper M, Lundquist JK. 2004. Surface layer turbulence measurements during a frontal passage. *J. Atmos. Sci.* **61**: 1768–1780, doi:10.1175/1520-0469(2004)061<1768:SLTMDA>2.0.CO;2.
- Ralph FM, Neiman PJ, Levinson D. 1997. Lidar observations of a breaking mountain wave associated with extreme turbulence. *Geophys. Res. Lett.* **24**: 663–666, doi:10.1029/97GL00349.
- Sharman RD, Comman LB, Meymaris G, Pearson J, Farrar T. 2014. Description and derived climatologies of automated *in situ* eddy-dissipation-rate reports of atmospheric turbulence. *J. Appl. Meteor. Climatol.* **53**: 1416–1432, doi:10.1175/JAMC-D-13-0329.1.
- Sharman RD, Trier SB, Lane TP, Doyle JD. 2012. Sources and dynamics of turbulence in the upper troposphere and lower stratosphere: A review. *Geophys. Res. Lett.* **39**: L12 803, doi:10.1029/2012GL051996.
- Smith RB. 1987. Aerial observations of the Yugoslavian Bora. *J. Atmos. Sci.* **44**: 269–297, doi:10.1175/1520-0469(1987)044<0269:AOTYB>2.0.CO;2.
- Srivastava RC, Atlas D. 1974. Effect of finite radar pulse volume on turbulence measurements. *J. Appl. Meteor.* **13**: 472–480, doi:10.1175/1520-0450(1974)013<0472:EOFRPV>2.0.CO;2.
- Stevens B, Lenschow DH, Vali G, Gerber H, Bandy A, Blomquist B, Brenguier JL, Bretherton CS, Burnet F, Campos T, Chai S, Falona I, Friesen D, Haimov S, Laursen K, Lilly DK, Loehrer SM, Malinowski SP, Morley B, Petters MD, Rogers DC, Russell L, Savic-Jovic V, Snider JR, Straub D, Szumowski MJ, Takagi H, Thornton DC, Tschudi M, Twohy C, Wetzel M, van Zanten MC. 2003. Dynamics and chemistry of marine stratocumulus - DYCOMS-II. *Bull. Amer. Meteor. Soc.* **84**: 579–593, doi:10.1175/BAMS-84-5-579.
- Terradellas E, Soler MR, Ferreres E, Bravo M. 2005. Analysis of oscillations in the stable atmospheric boundary layer using wavelet methods. *Bound.-Layer Meteor.* **114**: 489–518, doi:10.1007/s10546-004-1293-y.
- Torrence C, Compo GP. 1998. A practical guide to wavelet analysis. *Bull. Amer. Meteor. Soc.* **79**: 61–78, doi:10.1175/1520-0477(1998)079<0061:APGTWA>2.0.CO;2.
- UWKA Homepage. Cited 2015. University of Wyoming King Air research aircraft. <http://atmos.uwyo.edu/n2uw>.
- Večenaj Ž, Belušić D, Grubišić V, Grisogono B. 2012. Along-coast features of Bora-related turbulence. *Bound.-Layer Meteor.* **143**: 527–545, doi:10.1007/s10546-012-9697-6.
- Wang Z, French J, Vali G, Wechsler P, Haimov S, Rodi A, Deng M, Leon D, Snider J, Peng L, Pazmany AL. 2012. Single aircraft integration of remote sensing and *in situ* sampling for the study of cloud microphysics and dynamics. *Bull. Amer. Meteor. Soc.* **93**: 653–668, doi:10.1175/BAMS-D-11-00044.1.
- WCR Homepage. Cited 2015. Wyoming Cloud Radar. <http://atmos.uwyo.edu/wcr>.
- Welch PD. 1967. Use of Fast Fourier transform for estimation of power spectra – a method based on time averaging over short modified periodograms. *IEEE Transactions on Audio and Electroacoustics* **AU15**: 70–73, doi:10.1109/TAU.1967.1161901.
- Wendisch M, Brenguier JE. 2013. *Airborne Measurements for Environmental Research*. Wiley-VCH Verlag, Weinheim, Germany.
- Woods BK, Smith RB. 2010. Energy flux and wavelet diagnostics of secondary mountain waves. *J. Atmos. Sci.* **67**: 3721–3738, doi:10.1175/2010JAS3285.1.

3 Turbulence in breaking mountain waves and rotors

12

L. Strauss *et al.*

Table 1. List of NASA06 research flight legs discussed in this paper.

Date	Leg	Time (UTC)	Altitude (m)	Heading (°)
26 Jan 2006	3	2121–2131	5200	101
	5	2154–2208	5180	100
5 Feb 2006	1	1354–1404	5150	128
	2	1407–1423	4270	319
	3	1442–1451	4220	129
	4	1454–1508	4220	318
2 Feb 2006	2	1915–1924	4250	101

Table 2. List of turbulent processes encountered on three days of NASA06 and associated maximum turbulence intensities, including their upper and lower uncertainty bounds (referred to as *relative uncertainty* R in the text, cf. Eq. 3). The last column provides the associated *turbulence category* used in pilot reports (PIREPs) in civil aviation. Turbulence categories ‘smooth-light’, ‘light’, ‘light-moderate’, ‘moderate’, ‘moderate-severe’, and ‘severe’ correspond, respectively, to EDR thresholds of 0.014, 0.050, 0.125, 0.220, 0.350, $0.500 \text{ m}^{2/3} \text{ s}^{-1}$ (Sharman *et al.* 2014).

Event	Mountain-induced process	TKE ($\text{m}^2 \text{ s}^{-2}$)	σ_w^2 ($\text{m}^2 \text{ s}^{-2}$)	EDR ($\text{m}^{2/3} \text{ s}^{-1}$)	Turbulence category
26 Jan 2006	mid-tropospheric wave breaking	$4.6^{+0.0\%}_{-0.3\%}$	$4.8^{+0\%}_{-0.2\%}$	$0.25^{+16\%}_{-16\%}$	moderate
	internal hydraulic jump (updraught)	$12.1^{+0\%}_{-0.3\%}$	$12.7^{+0\%}_{-0.2\%}$	$0.38^{+16\%}_{-16\%}$	moderate-severe
	internal hydraulic jump (downdraught)	$6.4^{+0\%}_{-0.3\%}$	$6.2^{+0\%}_{-0.2\%}$	$0.33^{+16\%}_{-16\%}$	moderate-severe
	wave-induced boundary-layer separation	–	$9.4^{+11\%}_{-15\%}$	$0.51^{+41\%}_{-23\%}$	severe
	hydraulic jump-type rotor	–	$16.4^{+8\%}_{-9\%}$	$0.77^{+41\%}_{-23\%}$	severe
5 Feb 2006	mid-tropospheric wave breaking	$5.4^{+0\%}_{-0.3\%}$	$2.3^{+0\%}_{-0.2\%}$	$0.25^{+16\%}_{-16\%}$	moderate
	bluff-body boundary-layer separation	–	$10.3^{+9\%}_{-10\%}$	$0.41^{+41\%}_{-23\%}$	moderate-severe
	lee-wave rotor (fully developed)	–	$7.8^{+8\%}_{-10\%}$	$0.50^{+41\%}_{-23\%}$	severe
	lee-wave rotor (retreating)	–	$5.7^{+6\%}_{-9\%}$	$0.47^{+41\%}_{-23\%}$	moderate-severe
	downdraught windstorm (Sheep Mountain)	–	$9.4^{+7\%}_{-9\%}$	–	–
2 Feb 2006	in-cloud turbulence	–	$1.8^{+5\%}_{-15\%}$	$0.18^{+41\%}_{-23\%}$	light-moderate
	bluff-body boundary-layer separation	–	$6.7^{+6\%}_{-8\%}$	$0.43^{+41\%}_{-23\%}$	moderate-severe

Table 3. Summary of past aircraft observations of mountain-induced turbulent processes, documented by (a) Lilly (1978), (b) Jiang and Doyle (2004), (c) Smith (1987), (d) Elvidge *et al.* (2014), (e) Armi and Mayr (2011), (f) Lester and Fingerhut (1974), (g) Darby and Poulos (2006), and (h) Cohn *et al.* (2011).

Mountain-induced process	Case	Mountain range	Reported turbulence intensity	Filter scale (km)
mid-tropospheric gravity-wave breaking	11 Jan 1972 (a)	Front Range, CO	$\text{TKE} \simeq 150 \text{ m}^2 \text{ s}^{-2}$	18
	21 Oct 1999 (MAP) (b)	Central Alps, Austria	$\text{TKE} \simeq 10.5 \text{ m}^2 \text{ s}^{-2}$	5
	7 Mar 1982 (ALPEX) (c)	Dinaric Alps, Croatia	$\sigma_w^2 \simeq 5\text{--}10 \text{ m}^2 \text{ s}^{-2}$	1.26
	5 Feb 2011 (d)	Antarctic Peninsula, Antarctica	$\text{TKE} \simeq 5\text{--}9 \text{ m}^2 \text{ s}^{-2}$	3
internal hydraulic jump	7 Mar 1982 (ALPEX) (c)	Dinaric Alps, Croatia	$\sigma_w^2 \simeq 10\text{--}15 \text{ m}^2 \text{ s}^{-2}$	1.26
	9 Apr 2006 (T-REX) (e)	Sierra Nevada, CA	$\text{EDR} \simeq 0.35 \text{ m}^{2/3} \text{ s}^{-1}$	–
atmospheric rotors	8 Oct 1970 (f)	Front Range, CO	$\sigma_u^2 \simeq 2.6 \text{ m}^2 \text{ s}^{-2}$ $\overline{\text{EDR}} \simeq 0.19\text{--}0.34 \text{ m}^{2/3} \text{ s}^{-1}$	0.85 –
	1 Apr 1997 (g)	Front Range, CO	$\text{EDR} \simeq 0.33 \text{ m}^{2/3} \text{ s}^{-1}$	–
	9 Mar 2006 (T-REX) (h)	Sierra Nevada, CA	$\text{EDR} \simeq 0.21 \text{ m}^{2/3} \text{ s}^{-1}$	–

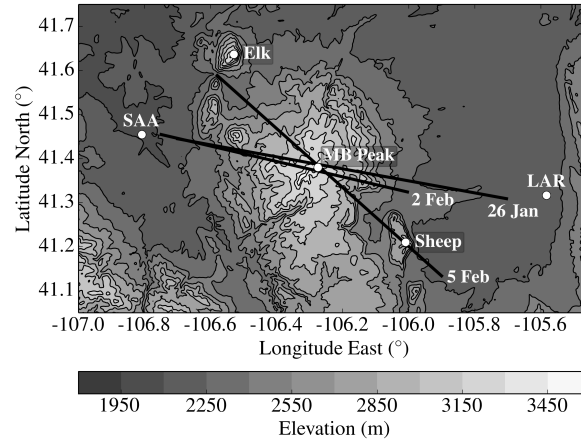


Figure 1. Topographic map of the Medicine Bow Mountains, southeastern Wyoming. White circles mark the location of Elk Mountain, Medicine Bow (MB) Peak (3662 m MSL), Sheep Mountain, Shively Field Airport in Saratoga (SAA) and Laramie Regional Airport (LAR). Black solid lines indicate the orientation of research flights on 26 January, 2 February, and 5 February 2006.

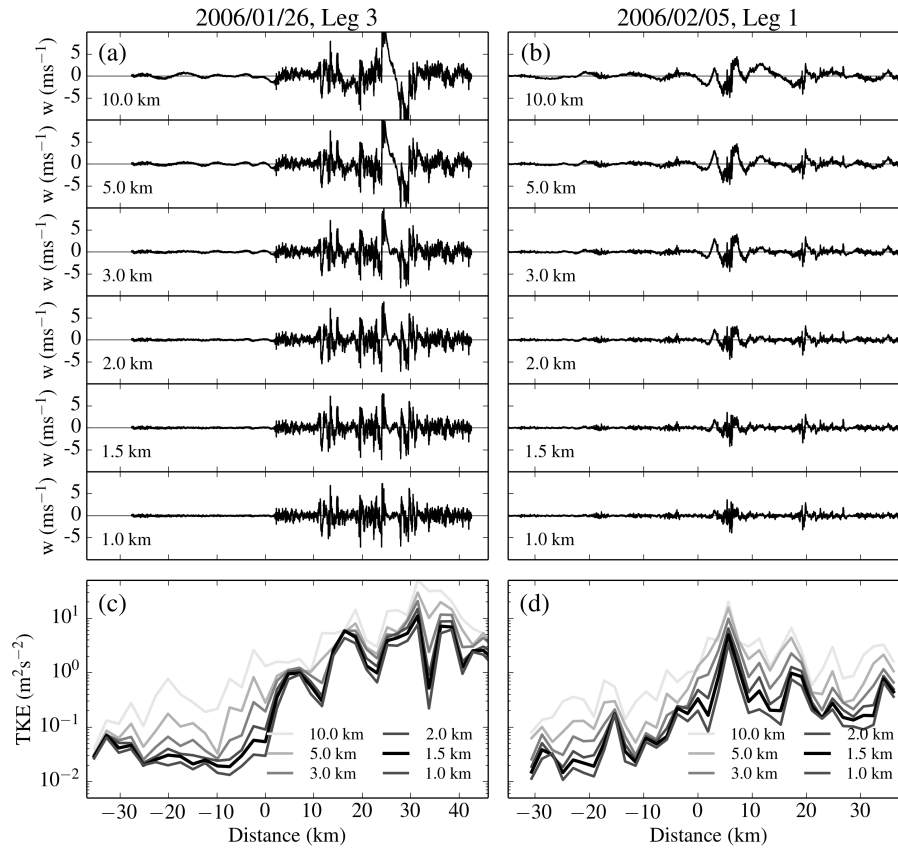


Figure 2. The effect of high-pass filtering, using an equally-weighted moving average with different window widths. (a,b) series of vertical velocity w for Leg 3 on 26 January and Leg 1 on 5 February, for filter scales ranging from 10 km to 1 km. (c,d) turbulent kinetic energy TKE for the same flight legs and filter scales. TKE at filter scale 1.5 km, used throughout this work, is indicated in black. In this and later figures, distance is upwind (< 0) or downwind (> 0) of the MBM top. The times and altitudes of all flight legs are summarized in Table 1.

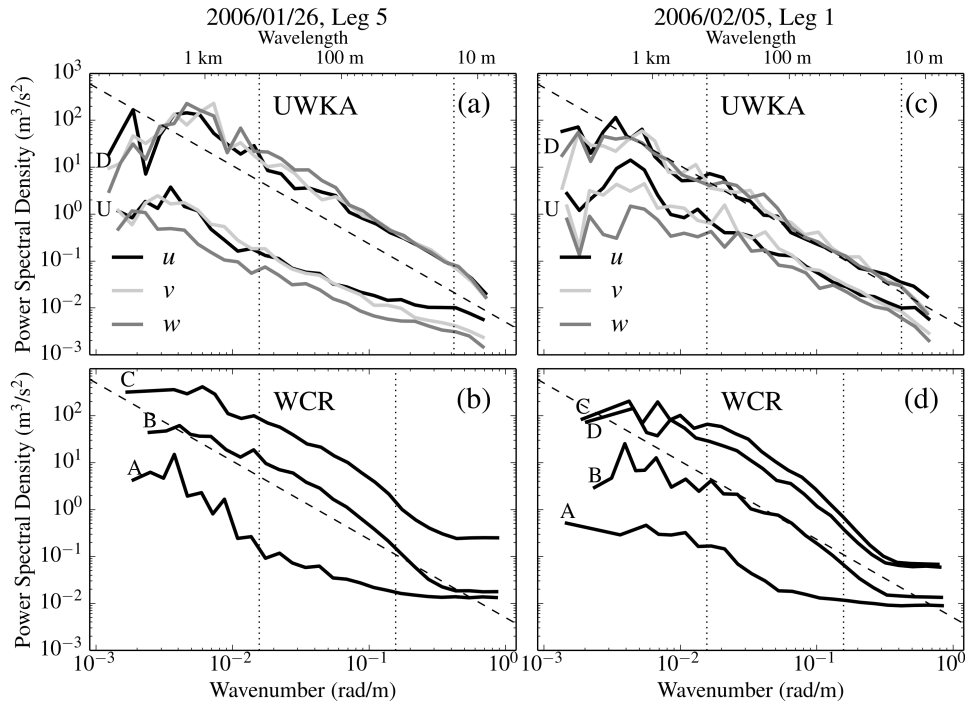


Figure 3. Example Fourier spectra computed from *in situ* wind components and radar Doppler velocity, measured along Leg 5 on 26 January (a,b) and Leg 1 on 5 February (c,d) in different regions of the flow. Panels (a) and (c) show averaged spectra from flight-level data from stretches upstream (U) and downstream (D) of Medicine Bow Peak. Panels (b) and (d) contain averaged spectra from WCR data from regions A, B, C marked in Fig. 9b and regions A, B, C, D marked in Fig. 10b. Raw spectra have been spectrally averaged using ten equal-log-interval bins per decade ($\Delta(\log_{10} k) = 0.1$). Vertical dotted lines indicate the range of wavenumbers k , from which the energy dissipation rate is extracted (see Section 3.3 for more information). Dashed solid lines mark the $-5/3$ spectral slope, expected for the inertial subrange. For the discussion of spectrum shapes, see Section 3.2.

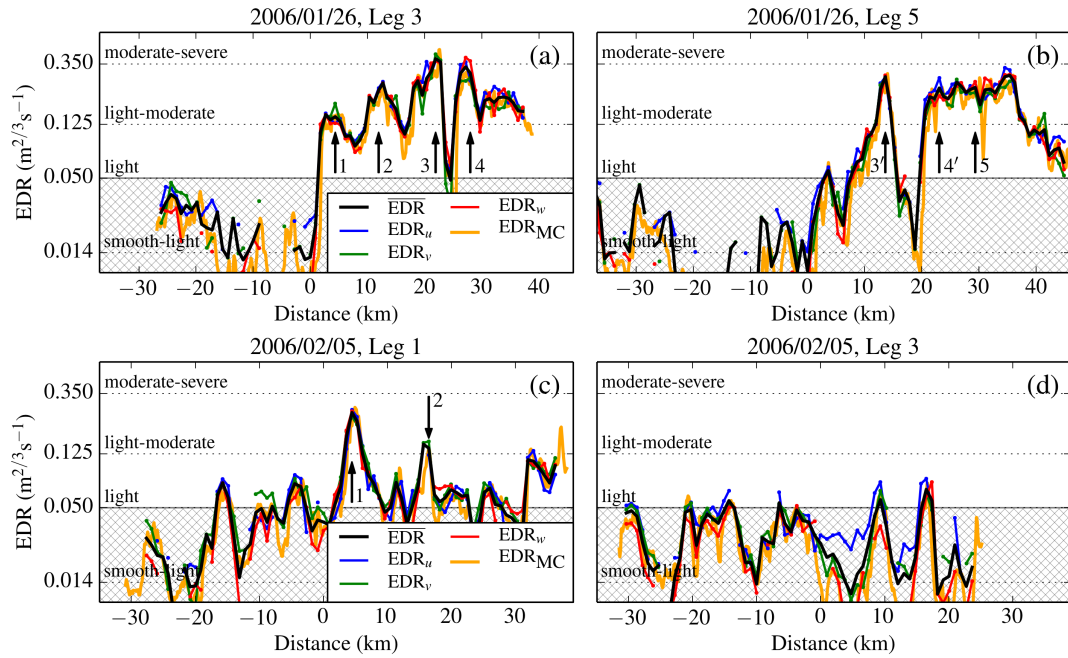


Figure 4. Aircraft *in situ* measurements of dissipation rate ($\epsilon^{1/3}$, or EDR) along flight legs crossing the MBM on 26 January (a,b) and 5 February (c,d). EDR_u , EDR_v , and EDR_w are the dissipation rate estimates from the three wind components and $\overline{\text{EDR}}$ is their mean. EDR_{MC} corresponds to dissipation rates from the MacCready Turbulence Meter, used for comparison. Vertical arrows mark the location of peaks in turbulence intensity, discussed in Section 4. Arrows labelled with primed numbers refer to the same peak in turbulence intensity but at a later point in time. Hatched regions indicate values lower than $0.05 \text{ m}^{2/3} \text{ s}^{-1}$ which are not reliable (see Fig. 5).

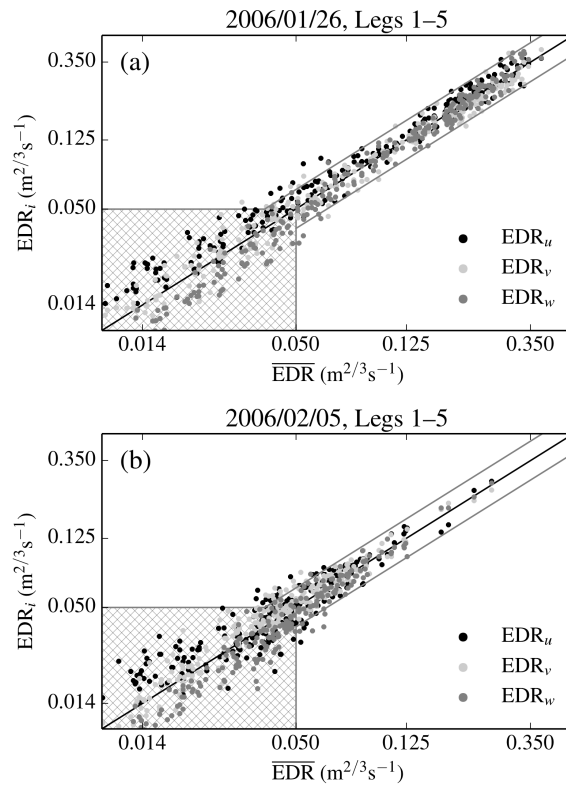


Figure 5. Scatter of individual estimates EDR_u , EDR_v , and EDR_w around their log-mean $\overline{\text{EDR}}$ (black solid line) for all flight legs on (a) 26 January and (b) 5 February, respectively. The hatched regions indicate low EDR estimates ($< 0.05 \text{ m}^{2/3} \text{s}^{-1}$), which are not reliable (see discussion in the text). The grey solid lines mark the 95% ($\pm 2\sigma$) interval around $\overline{\text{EDR}}$, representative of the uncertainty of individual EDR estimates.

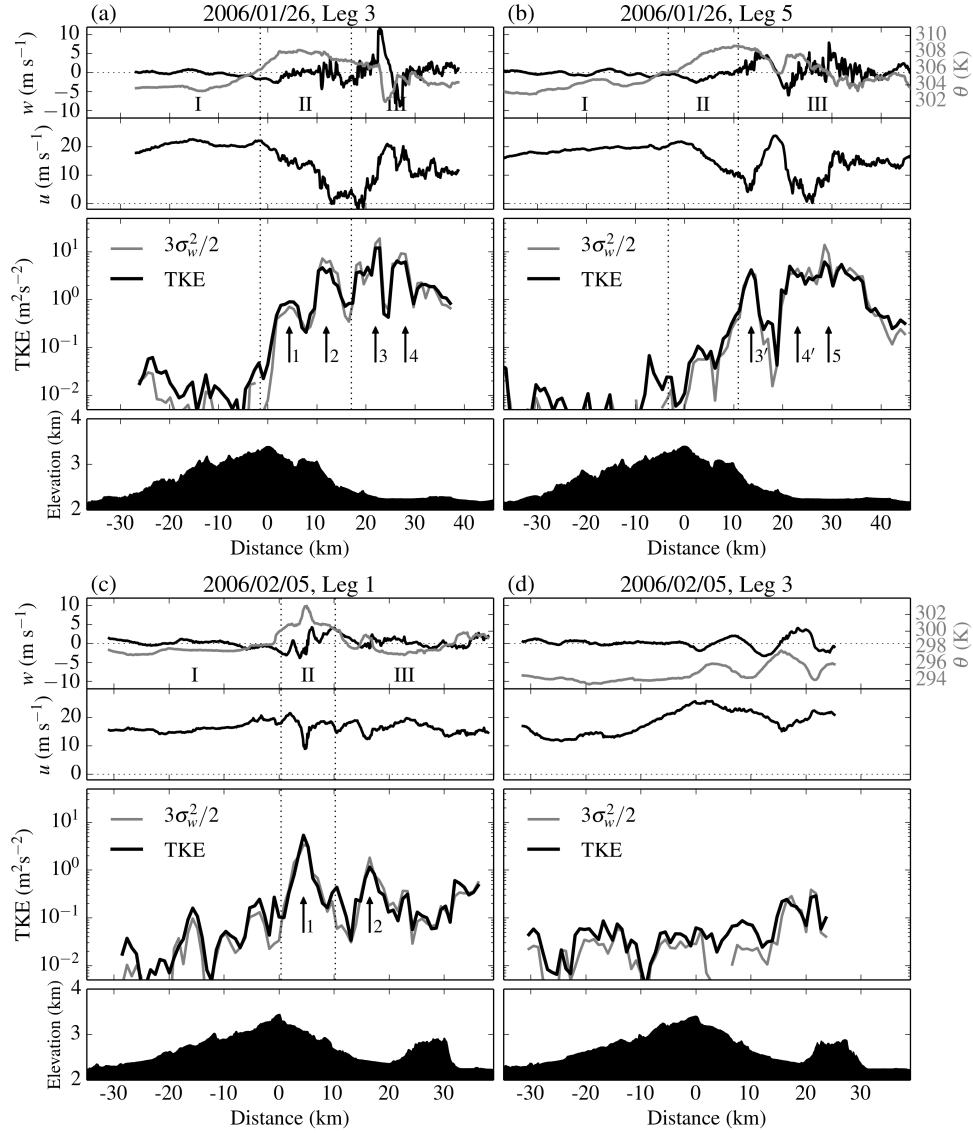


Figure 6. Aircraft *in situ* measurements of vertical velocity w (black solid), potential temperature θ (grey solid), along-track horizontal velocity u , TKE and $3\sigma_w^2/2$, and the underlying terrain along flight legs crossing the MBM on 26 January (a,b) and 5 February 2006 (c,d). Vertical dotted lines plus letters I–III delimit distinct regions of the flow at flight level, discussed in Section 4. Vertical arrows mark the location of peaks in turbulence intensity (also see Fig. 4).

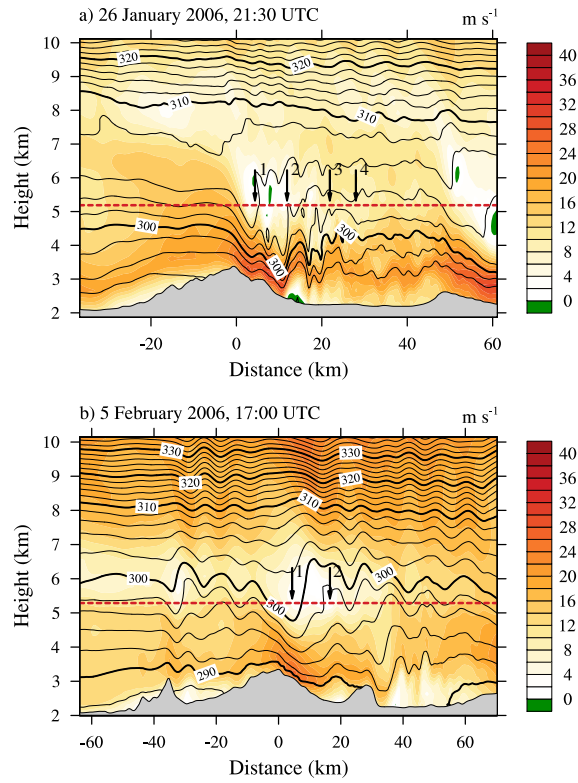


Figure 7. Numerical model cross-sections showing along-track horizontal wind component and isentropes. (a) Cross-section along Leg 3 on 26 January for model output time 2130 UTC, indicating reversed flow along the lee slope close to the ground and steepened isentropes and stagnant flow at flight level. (b) Cross-section along Leg 1 on 5 February for model output time 1700 UTC, providing a similar picture, however without clear indication of a near-surface recirculation region. Note that the model output time of 1700 UTC has been chosen to account for the observed delayed timing of the model for the 5 February case (GSS15). Dashed horizontal lines indicate the altitude of the straight-and-level flight legs. Vertical arrows in both panels mark the location of peaks in turbulence intensity at flight level (Fig. 6).

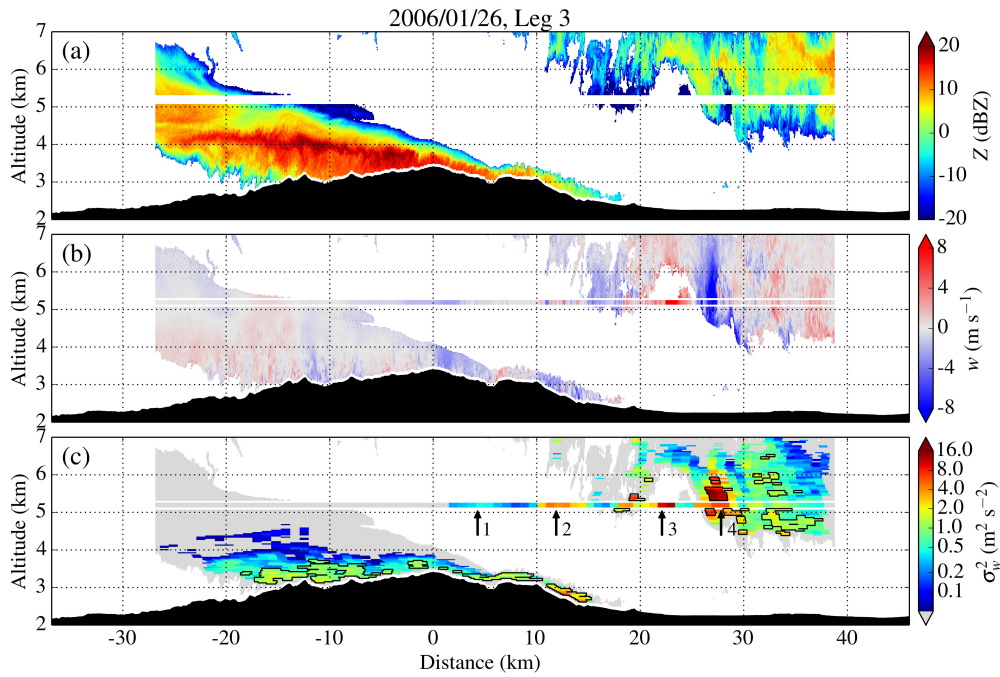


Figure 8. Radar data and derived turbulence parameters collected along Leg 3 on 26 January, crossing the MBM at approx. 5200 m MSL between 2121 and 2131 UTC. (a) Radar reflectivity Z , (b) vertical Doppler velocity w , and (c) variance of vertical velocity σ_w^2 . White colour corresponds to missing data due to insufficient radar backscatter from clouds. The white stripe in panel (a) corresponds to the ‘radar blind zone’, extending across ± 100 m around flight level, which is filled with aircraft *in situ* measurements in panels (b) and (c). Raw vertical Doppler velocity w has been corrected for a mean hydrometeor fall speed of 1 m s^{-1} . A logarithmically scaled colour bar is used for σ_w^2 . Grey areas in the display of σ_w^2 correspond to an undetectable level of turbulence (greater than 100% relative uncertainty). The black contour line marks the region in which the relative uncertainty of the σ_w^2 estimate is lower than 25%. Arrows in panel (c) indicate local maxima in σ_w^2 , corresponding to the peaks in TKE in Fig. 6a.

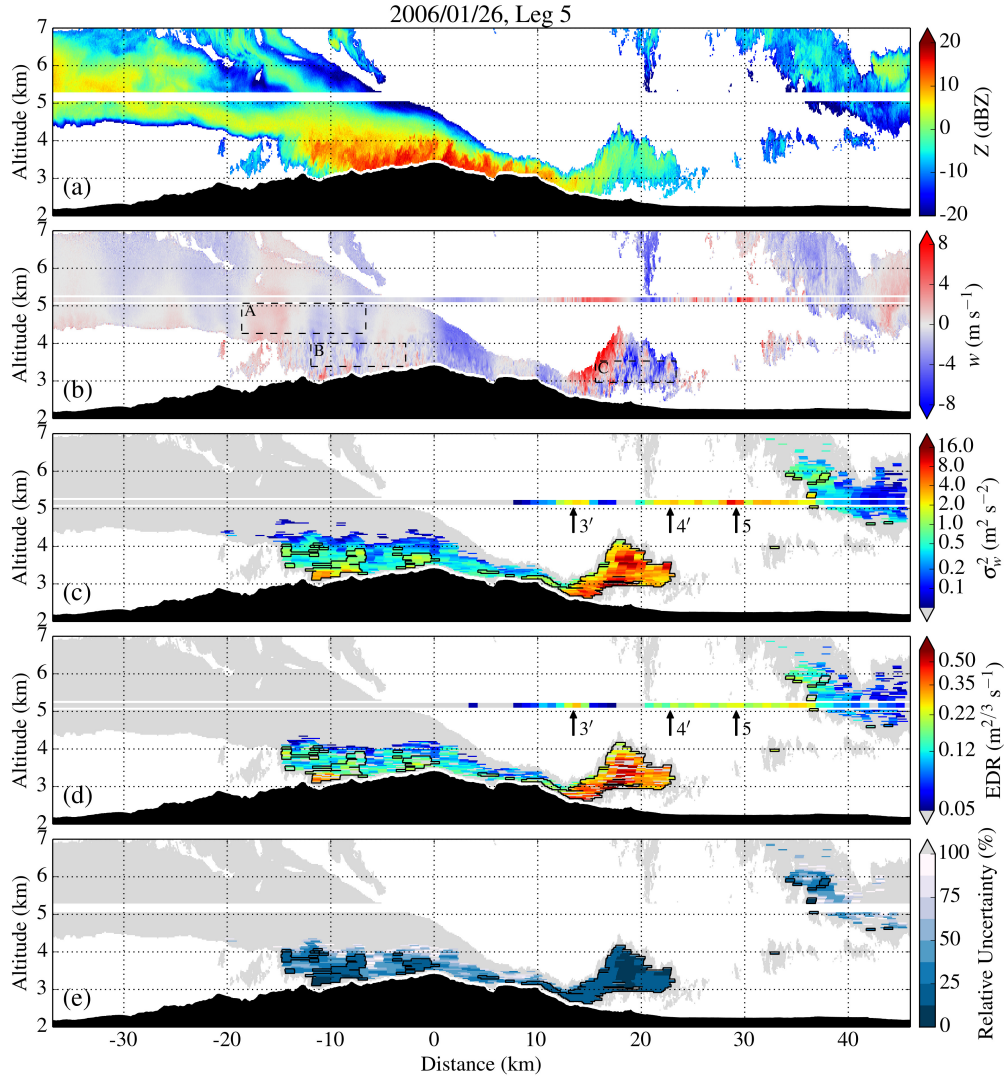


Figure 9. Radar data and derived turbulence parameters collected along Leg 5 on 26 January, crossing the MBM at approx. 5200 m MSL between 2154 and 2208 UTC. (a) Radar reflectivity Z , (b) vertical Doppler velocity w , (c) variance of vertical velocity σ_w^2 , (d) dissipation rate EDR_w , and (e) relative uncertainty of the σ_w^2 estimate. The black contour line in panels (c)–(e) marks the region in which the relative uncertainty of the σ_w^2 estimate is lower than 25%. Arrows in panels (c) and (d) indicate local maxima in σ_w^2 and EDR_w , corresponding to the peaks in TKE in Fig. 6b. Boxes A–C in panel (b) delimit regions of the flow from which example radar spectra are shown in Fig. 3b.

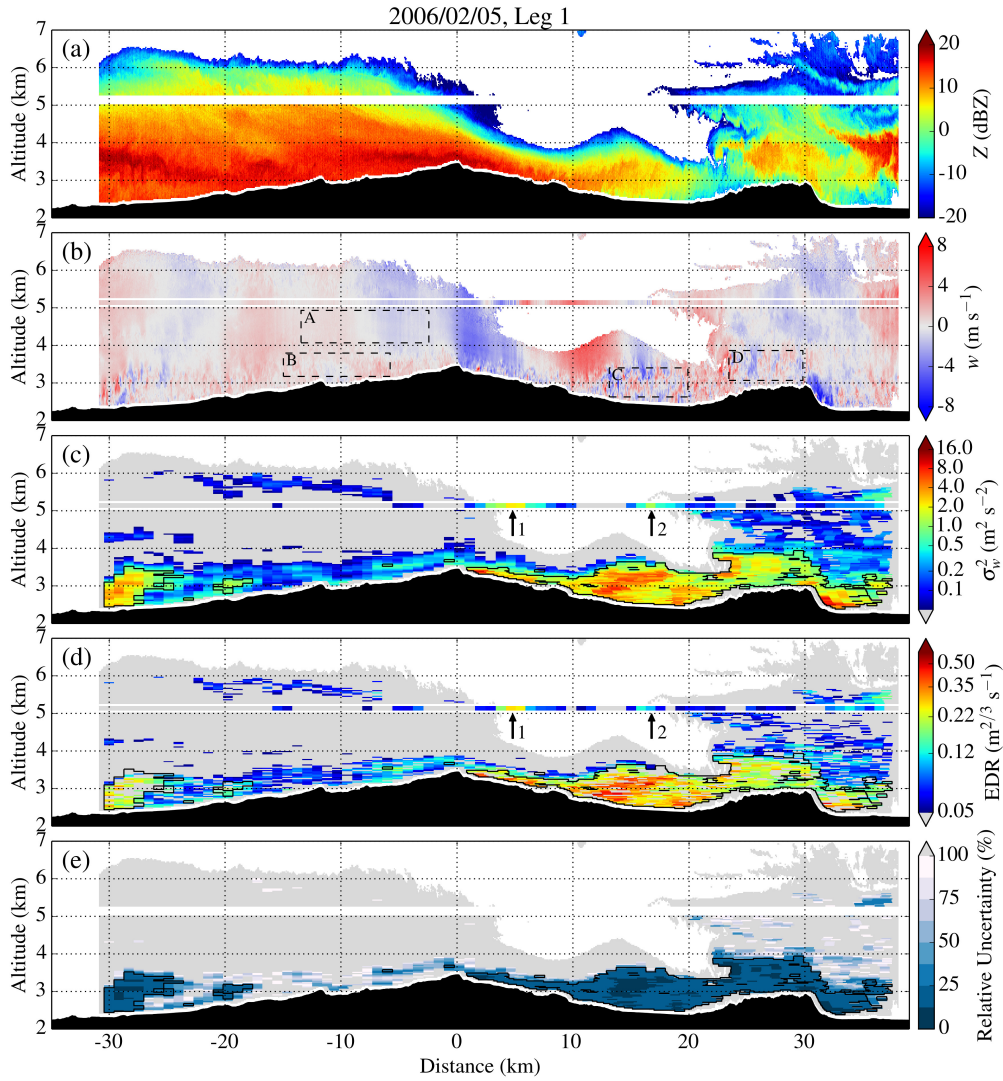


Figure 10. Same as Fig. 9 but for Leg 1 on 5 February, crossing the MBM and Sheep Mountain at approx. 5150 m MSL between 1354 and 1404 UTC. Boxes A–D in panel (b) delimit the regions of the flow of which example radar spectra are shown in Fig. 3d. Arrows in panels (c) and (d) indicate local maxima in σ_w^2 and EDR, corresponding to the peaks in TKE in Fig. 6c.

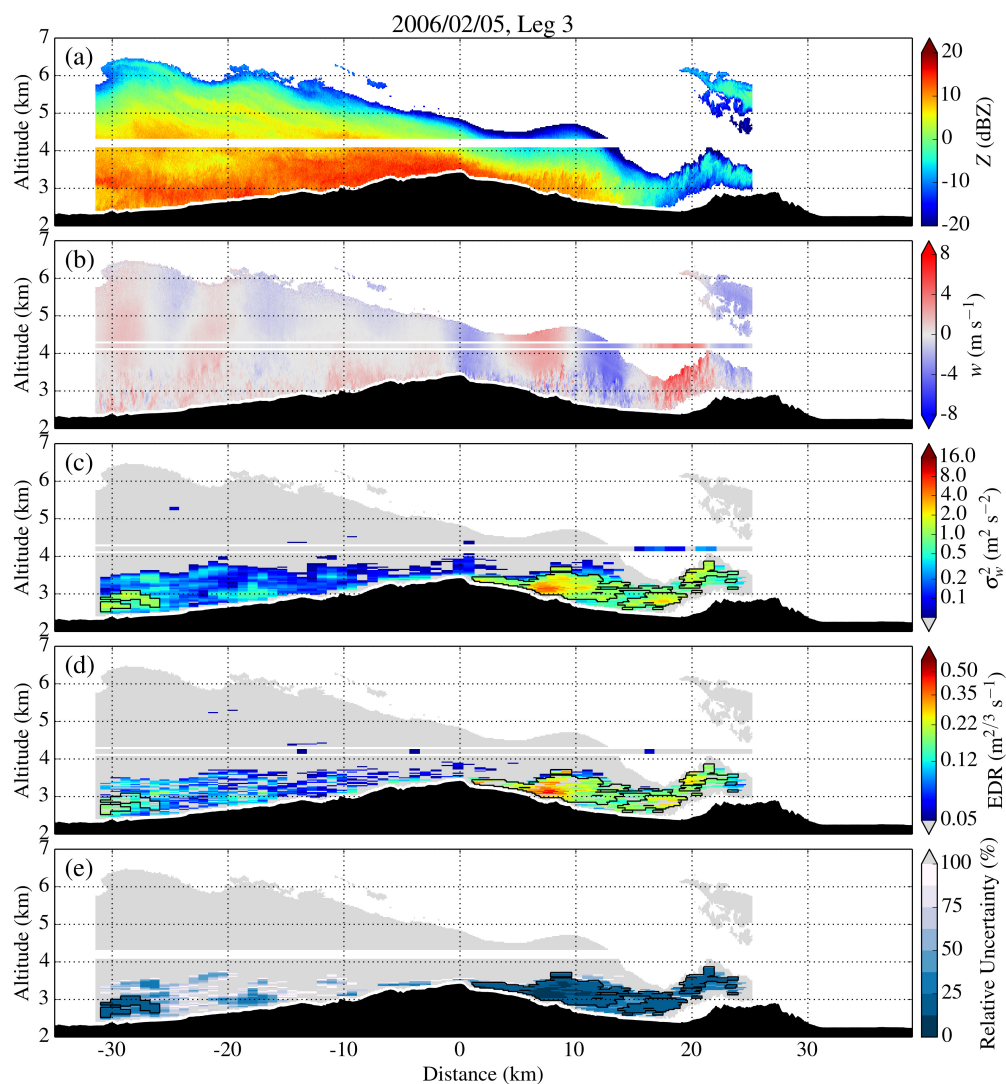


Figure 11. Same as Fig. 9 but for Leg 3 on 5 February, crossing the MBM and Sheep Mountain at approx. 4200 m MSL between 1442 and 1451 UTC.

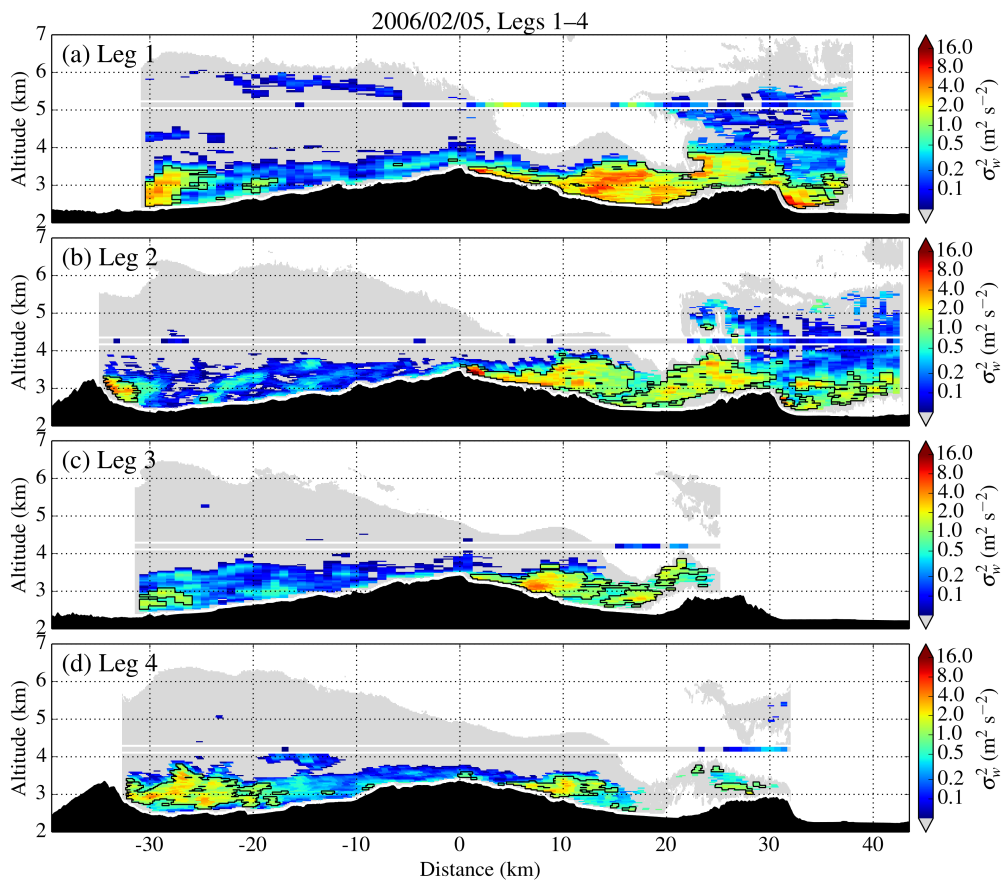


Figure 12. Variance of vertical Doppler velocity σ_w^2 for Legs 1–4 (top to bottom) on 5 February, crossing Elk Mountain, the MBM, and Sheep Mountain between 1354 and 1508 UTC. Note that all flight legs crossed the peak region of the MBM but Legs 2 and 4 were flown at a somewhat larger heading (approx. $+10^\circ$), thereby passing over the top of Elk Mountain at the western end of the transect.

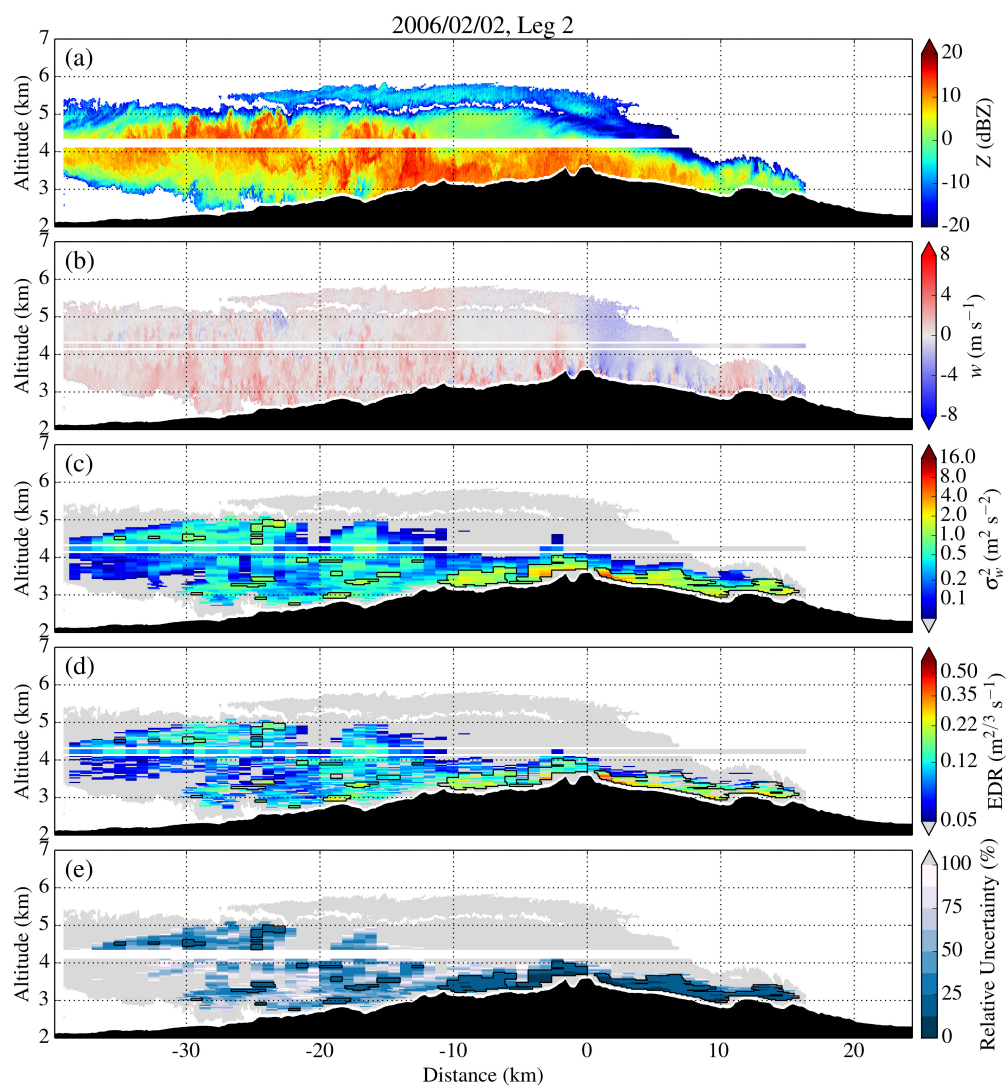


Figure 13. Same as Fig. 9 but for Leg 2 on 2 February crossing the MBM at approx. 4250 m MSL between 1915 and 1923 UTC.

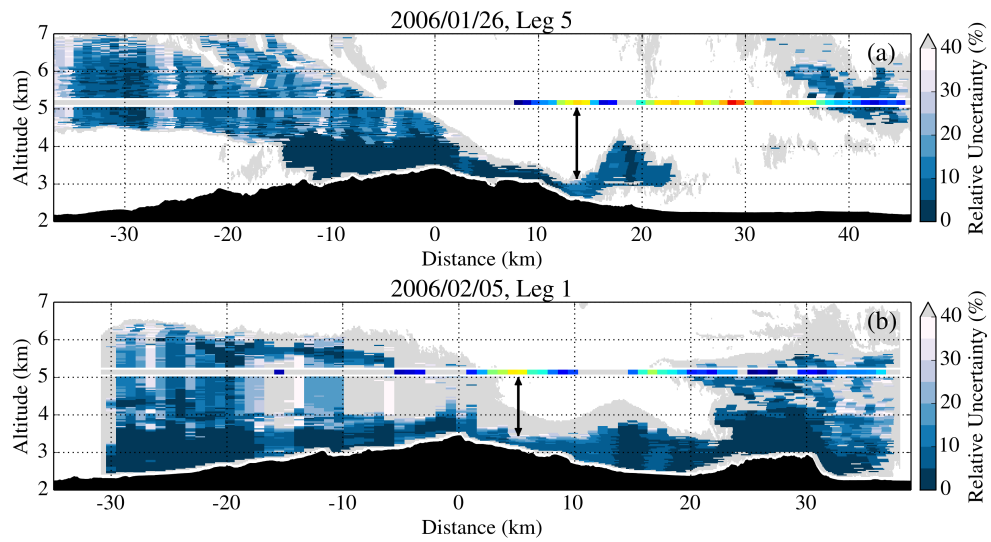


Figure A1. Relative uncertainty of the variance of vertical velocity σ_w^2 due to the contamination by the horizontal wind. Coloured stripes, inserted at flight level, correspond to *in situ*-measured σ_w^2 (cf. Figs 9c and 10c). Vertical arrows indicate the collocation of enhanced flight-level turbulence and increased relative uncertainty in the estimation of σ_w^2 in the lower-level flow.

Chapter 4

Atmospheric rotors and severe turbulence in a deep valley

Using the observational data collected during the Terrain-induced Rotor Experiment (T-REX), a number of authors have studied the effects of lee waves on the flow in Owens Valley, California. The predictions of the existence of intense subrotor vortices in the turbulence zone underneath the lee-wave crests have been largely confirmed. However, coherent rotor circulations were rarely observed in the valley during T-REX and, when present, rotors were found to be of very transient character and to display a strong interaction with the along-valley flow.

The objective of the study presented in this chapter is to shed new light on the T-REX observations by a systematic investigation of the impact of the downstream atmospheric environment and secondary topography on the formation of rotors and severe turbulence in Owens Valley. To this end, a selection of T-REX cases with enhanced mountain-wave activity is examined to understand better the conditions under which rotors or similar turbulent structures form in the valley. The results allow to extend the traditional conceptual models of the rotor flow to a deep elongated valley.

The author's contributions to this work were the detailed examination of the seven T-REX IOPs exhibiting the strongest wave activity, large parts of the analysis of data from T-REX ground-based and airborne instruments, and the interpretation of results. Contributions to the journal manuscript, currently in review at the *Journal of the Atmospheric Sciences*, included the selection of results for presentation, their composition, the writing of the manuscript and preparation of all tables and figures except Figs. 3 and 18.

Reference

Strauss, L., S. Serafin, and V. Grubišić, 2015b: Atmospheric rotors and severe turbulence in a deep valley. Submitted to *J. Atmos. Sci.*.

Atmospheric rotors and severe turbulence in a deep valley

Lukas Strauss*

Department of Meteorology and Geophysics, University of Vienna, Vienna, Austria

Stefano Serafin

Department of Meteorology and Geophysics, University of Vienna, Vienna, Austria

Vanda Grubišić

Earth Observing Laboratory, National Center for Atmospheric Research, Boulder, Colorado and

Department of Meteorology and Geophysics, University of Vienna, Vienna, Austria

**Corresponding author address:* Lukas Strauss, Department of Meteorology and Geophysics, University of Vienna, Althanstrasse 14, 1090 Vienna, Austria

E-mail: lukas.strauss@univie.ac.at

ABSTRACT

The conceptual model of an atmospheric rotor is re-examined in the context of a deep valley, using data from the Terrain-induced Rotor Experiment (T-REX) conducted in 2006 in the southern Sierra Nevada and Owens Valley, California. All T-REX cases with strong mountain-wave forcing have been examined and four of them (IOPs 1, 4, 6, and 13) are presented in detail. Their analysis reveals a rich variety of rotor-like turbulent structures that may form in the valley during periods of strong cross-mountain winds. Typical flow scenarios in the valley include elevated turbulence zones, downslope flow separation at a valley inversion, turbulent interaction of in-valley westerlies and along-valley flows, and highly transient mountain waves and rotors. The scenarios can be related to different stages of the passage of mid-latitude frontal systems across the region.

The observations show that the elements of the classic rotor concept are modulated and, at times, largely overridden by dynamically and thermally driven processes in the valley. For instance, strong lee-side pressure perturbations induced by large-amplitude waves, commonly regarded as the prerequisite for flow separation, are found to be only one of the factors controlling rotor formation and severe turbulence generation in the valley. Buoyancy perturbations in the thermally layered valley atmosphere prove to be a major player in many of the observed cases.

Based on observational evidence from the T-REX cases, extensions to the classic rotor concept, appropriate for a deep elongated valley, are proposed.

1. Introduction

Mountain waves are frequently accompanied by enhanced low-level turbulence. Early studies of such phenomena documented the occurrence of stationary cloud formations, for instance along the Adriatic coast of Croatia (Mohorovičić 1889; Grubišić and Orlić 2007) or over the Sudetes in Central Europe (Koschmieder 1920). Inspired by these studies and by reports of severe turbulence encounters by glider pilots (Hirth 1933), Wolf Hirth and Joachim Kuettner coordinated the first systematic measurements in mountain waves and low-level turbulence zones in the lee of the Riesengebirge (Sudetes; Küttner 1938, 1939). In his seminal work, Kuettner coined the term *rotor*, referring to the seemingly rotating lines of cumulus clouds underneath the smooth lenticular wave clouds.

From the 1950s to the 1970s, several observational programs devoted to the study of mountain waves and rotors were organized in the US and Europe: the Sierra Wave Project in the southern Sierra Nevada and Owens Valley, California (Holmboe and Klieforth 1957; Grubišić and Lewis 2004), a study of lee waves in the French Alps (Gerbier and Berenger 1961), and the Colorado Lee Wave Program in the Rocky Mountains (Lilly and Toutenhoofd 1969). From these field programs and related theoretical studies (Queney et al. 1960), conceptual models of the mountain wave-rotor system emerged and soon became integral part of mountain meteorology textbooks and aviation handbooks (e.g., Whiteman 2000; WMO 1993).

A schematic depiction of a lee-wave rotor, reproduced from Lester and Fingerhut (1974), is shown in Fig. 1a. The rotor flow is described as a turbulent low-level circulation zone underneath the lee-wave crest. The rotor is capped by a *rotor or roll cloud*; near the surface, the flow occasionally recirculates back toward the mountain. Some of the most severe occurrences of lee-side turbulence have been ascribed to mountain flows of hydraulic type (Fig. 1b). In the presence of a

strong crest-level inversion or a mid-level critical layer (Durran 1990), a shooting flow can form over the mountain lee slope followed by an internal hydraulic jump. The hydraulic jump-type rotor farther downstream typically extends beyond the mountaintop level. The rotor flow poses a significant aeronautical hazard (Carney et al. 1997): aircraft penetrating into the rotor typically encounter a sharp transition to severe turbulence in its leading updraft.

The conceptual models of rotors are, however, simplistic. Specifically, they are inherently two-dimensional and steady-state and represent only the average characteristics of the rotor flow, as noted in early studies (Holmboe and Klieforth 1957; Vergeiner and Lilly 1970). Also, they often neglect the importance of the atmospheric environment and topography downstream of the mountain ridge. For instance, in the case of two parallel mountain ridges separated by a valley, a number of processes can be expected to modify the rotor flow. These include diurnal heating in the valley and resultant thermally-driven slope and valley winds (Zardi and Whiteman 2013), terrain-forced and pressure-driven channeling of flow in the valley (Whiteman and Doran 1993; Kossmann and Sturman 2003), the modulation of lee wave characteristics by the presence of secondary topography (Stiperski and Grubišić 2011), and along-ridge variations in crest height or valley width (Mayr et al. 2007; Gohm et al. 2008).

A new opportunity to study the effects of the downstream environment on rotor formation was offered by the Terrain-induced Rotor Experiment (T-REX, Grubišić et al. 2008), conducted in 2006 in Owens Valley, California. The core objective of T-REX was to study the interaction of mountain waves, rotors, and the boundary layer. During the experiment, novel ground-based and airborne in situ and remote sensing instrumentation allowed to document both cross-mountain and in-valley flows and their interactions, at unprecedented temporal and spatial resolution.

Subsequent to T-REX, a few authors have challenged the conceptual models of atmospheric rotors (e.g., Doyle and Durran 2007; Doyle et al. 2009; Cohn et al. 2011; Kühnlein et al. 2013).

A systematic comparison of different T-REX cases, however, is yet to be achieved and is the main objective of this study. In this work, we review the existing T-REX literature and present a set of observations of rotors and similar turbulent structures in Owens Valley, with the aim of collecting comprehensive evidence of how the characteristics of the downstream environment modify the rotor flow. Furthermore, we propose extensions to the current conceptual models, appropriate for a deep elongated valley.

The rest of this paper is organized as follows. In Section 2, we provide the T-REX geographical context and discuss the observing systems relevant for this study. In Section 3, we present four case studies revealing different flow responses to the Sierra Nevada and turbulent flow patterns in Owens Valley. In Section 4, we discuss typical flow scenarios and possible transitions between them. Conclusions are drawn in Section 5.

2. The Terrain-induced Rotor Experiment

a. Geographical context

Topographic maps of the Sierra Nevada and Owens Valley are shown in Fig. 2. The Sierra Nevada stretches approximately 640 km from south-southeast to north-northwest and is about 110 km wide. Some of its peaks reach 4000 m and more, the highest one being Mt. Whitney (4421 m MSL). Gentle westward and steep eastward slopes characterize the southern section of the range. There, the average elevation drop between the main ridge line and the floor of Owens Valley to its east is about 3000 m, with a 30° slope. The southern Sierra Nevada exhibits relatively little along-ridge variation in crest height, but a few high passes exist. Kearsarge Pass (3600 m MSL, right west of Independence) and Sawmill Pass (3460 m MSL) lie in the T-REX measurement area.

The highest density of T-REX ground-based instrumentation was located in Owens Valley around the town of Independence. Owens Valley runs approximately 150 km parallel to and east of the southern Sierra Nevada, and is bound by the Inyo and White Mountains to its east. Its bottom and crest-to-crest widths are approximately 15 km and 30 km, respectively. The valley floor gently ascends from Owens (Dry) Lake at 1084 m MSL to the town of Bishop at 1260 m MSL, from where it rises more rapidly for another 30 km to the north up to 1850 m MSL.

b. T-REX observing systems

T-REX field activities took place in March and April 2006. Ground-based and airborne in situ and remote sensing measurements were made during 15 Intensive Observing Periods (IOPs). The locations of ground-based instruments and the orientation and extent of aircraft flight tracks are indicated in Fig. 2b,c.

Upwind radiosondes were launched from the Naval Air Station Lemoore and by the NCAR Mobile GPS Advanced Upper Air Sounding System (Mobile GAUS) near the cities of Visalia or Madera (Fig. 2b). Downwind radiosondes were launched in Owens Valley southeast of Independence from the NCAR Integrated Sounding System (ISS, Parsons et al. 1994), which included a GAUS.

Coordinated flight missions were flown with up to three research aircraft. The NSF-NCAR Gulfstream V (HIAPER, or GV), the UK-NCAS BAe-146, and the University of Wyoming King Air (UWKA) flew stacked cross-valley flight legs aligned with the mean wind direction at altitudes from 150 m above the valley floor to 14 km MSL (Grubišić et al. 2008, their Fig. 3 and Table III). High-rate (25 Hz) in situ measurements were taken of the three wind components, temperature, humidity, and pressure. On UWKA, additional measures of the energy-dissipation rate to the power of one third (EDR) were recorded by the MacCready Turbulence Meter (MacCready Jr. 1964), al-

lowing to estimate turbulence intensity at and below the Sierra Nevada crest level. EDR estimates show good agreement with those obtained from spectral analysis of high-rate wind measurements for turbulence scales of 15–400 m (Strauss et al. 2015). Recently, EDR has been established as an aircraft-independent objective measure of turbulence intensity in civil aviation (International Civil Aviation Organization 2007; Sharman et al. 2014). UWKA was also equipped with the dual-Doppler Wyoming Cloud Radar (WCR), providing insight into the two-dimensional wind field in cap clouds over the Sierra Nevada and roll clouds over Owens Valley. Here, measurements from the three research aircraft are displayed in composite vertical cross-sections. Interpolated contours of vertical velocity and potential temperature, derived from the composite data using natural neighbor interpolation based on Delaunay triangulation (Sibson 1981), allow to visualize the wave fields and stratification.

A network of 32 automatic weather stations (AWS) covered the floor and slopes of Owens Valley around the town of Independence. AWS by the Desert Research Institute (DRI) were arranged in three west-east oriented arrays south of Independence. AWS by the University of Leeds (UL) were distributed to the north and up on the slopes of the Sierra Nevada and the Inyo Mountains. All AWS measured the horizontal wind, wind direction, temperature and humidity every 30 s.

Three boundary-layer wind profilers were deployed as part of the NCAR ISS. ISS2 was located on the western slope of the valley, a Multiple Antenna Profiler (MAPR, Cohn et al. 2001) was situated at the valley center, and a Mobile ISS (MISS) was relocated along the valley axis between IOPs. The wind profilers measured horizontal wind speed and direction and vertical velocity up to 5000 m above ground level, at 30 min (ISS2/MISS) and 5 min (MAPR) intervals.

Finally, several scanning Doppler lidars were deployed. Here, data from the lidar operated by the Deutsche Zentrum für Luft- und Raumfahrt (DLR) (Kühnlein et al. 2013) is used. Vertical-slice *range-height indicator* scans were performed at azimuthal angles of 50°, 80°, and 170° east

of north (referred to as RHI-50, RHI-80, and RHI-170, respectively) to sample cross-valley and along-valley flows. Conical *plan position indicator* (PPI) scans were carried out at multiple elevation angles ranging from 3° to 60° (PPI-03 to PPI-60). Lidar-measured fields include the aerosol backscatter intensity, radial Doppler velocity and Doppler spectral width.

In addition to the observational data sets, 700 hPa analyses from the European Centre for Medium-Range Weather Forecasts (ECMWF) Integrated Forecast System (IFS) are used here to provide the context of the large-scale synoptic flow.

3. Observations

The primary objective of this work is to re-examine the conceptual model of a rotor for a deep valley. To this end, we analyzed T-REX IOPs 1, 2, 3, 4, 6, and 13, exhibiting the strongest response of the flow to the underlying topography (in terms of, e.g., the amplitude of vertical air motion at the Sierra Nevada crest level, or the strength of downslope winds over the mountain lee slope). In the following section, we summarize the general upstream synoptic and downstream in-valley conditions during the chosen IOPs. Four selected cases, displaying different types of rotor flow and mechanisms of turbulence generation in Owens Valley, are presented in more detail in Section 3b.

a. Synoptic conditions during T-REX IOPs

The Sierra Nevada is well known for launching large-amplitude mountain waves. The generation of mountain waves in its lee is typically associated with the passage of frontal systems (Holmboe and Klieforth 1957). From October to May, with the shift of the polar jet to the south, mid-latitude synoptic systems tend to travel past the Sierra Nevada, directing strong southwesterly to northwesterly, stably-stratified flow towards the ridge, thereby favoring the generation of large-amplitude mountain waves and rotors. The frequency of occurrence of mountain-wave events in

the lee of the Sierra Nevada peaks in April (Grubišić and Billings 2008), which led to the planning of T-REX field activities in spring 2006.

T-REX IOPs, aiming for periods of enhanced flow response to the Sierra Nevada, were thus scheduled when medium-range forecasts predicted the approach of a frontal system toward the US West Coast, as is evident from 700 hPa ECMWF analyses (Fig. 3). Intense IOPs typically featured shortwave synoptic troughs to the west of the Sierra Nevada. The exception is IOP 3, which stands out for its particularly strong flow being part of the core of the polar jet extending from Alaska to the coast of California.

A set of upstream and downstream vertical profiles of wind speed, wind direction, and virtual potential temperature θ_v during the IOPs is shown in Fig. 4. Common characteristics of the *upstream* profiles (colored in blue) include low wind speed and wind direction considerably deviating from the cross-mountain direction ($\sim 255^\circ$) below ridge height (indicative of upstream blocking), increased stability at and above crest level, and weaker stability and rapid increase in wind speed in the free atmosphere. Such a vertically layered atmosphere corresponds to a Scorer parameter (defined as $N^2/U^2 - (1/U)(\partial^2 U/\partial z^2)$, where N and U are the upstream stability and cross-mountain wind speed, respectively) that decreases with height, favoring the formation of trapped lee waves (Scorer 1949).

Upon close inspection of the profiles, a few differences between the cases become apparent. These include, for example, stronger crest-level stratification but weaker increase in wind speed aloft for IOPs 1 and 2 compared to IOPs 4 and 13. The resultant differences in the Scorer parameter have been linked previously to the tendency of two wave types (lee waves vs. propagating mountain waves) to form in the lee of the Sierra Nevada (Grubišić and Billings 2008). Apart from case-to-case differences, another cause of differing vertical profiles seems to be the timing of radiosonde launches with respect to the approaching cold front, making the IOP 1 and 2 profiles

representative of the early prefrontal environment, while the others correspond to the stages when the front has already reached the Sierra Nevada.

The differences in the *downstream* in-valley profiles (Fig. 4, colored in red) are generally larger, however the profiles share the tendency of the low-level flow in the valley to be south-southeasterly (up-valley). This characteristic is explained by the position of the synoptic-scale pressure low to the (north-)northwest of the mountain range, which gives rise to pressure-driven channeling of the flow along the valley from south to north ahead of cold fronts (Zhong et al. 2008). Once again, IOP 3 is different in this respect from the other soundings.

A complex layered structure of stability is evident from the valley profiles for some IOPs (e.g., 1 and 4), in contrast to a rather well-mixed valley atmosphere in others (e.g., 3 and 6), related mainly to the timing of the radiosonde launch with respect to the local time of day (early morning for the former vs. afternoon for the latter). In-valley profiles are further characterized by marked shear (up to $20 \text{ m s}^{-1} \text{ km}^{-1}$) in the layer $\pm 1000 \text{ m}$ around the mountaintop height. Aloft, most downstream soundings closely follow their upstream counterparts.

While important predictors for wave launching by the Sierra Nevada can be found in upstream profiles (e.g., enhanced crest-level stability), several authors have investigated the additional role of properties of the downstream atmosphere for wave generation and penetration of westerly winds into Owens Valley (Jiang and Doyle 2008; Billings and Grubišić 2008a,b; Mayr and Armi 2010). For example, moderate downslope winds may be present at the Owens Valley floor despite weak or no waves aloft, due to the difference between upwind and downwind potential temperatures, allowing the cooler upstream air to flow over the mountain gaps and undercut the valley atmosphere (Raab and Mayr 2008; Mayr and Armi 2010). These potential temperature differences arise from and are modulated by the relative timing of approaching frontal systems (leading to

blocking and gradual build-up of cold air upstream of the Sierra Nevada) and the diurnal heating cycle in the valley.

b. Case studies

In Section 1, processes typical of a valley atmosphere have been introduced. In the majority of the selected IOPs, several of these processes (sometimes all of them) were at play, influencing rotor formation and turbulence generation and their temporal evolution. The impact of a single process on rotor formation thus cannot be studied in isolation from the others. This aspect of the data analysis represented a particular challenge, which we aimed to alleviate by selecting cases dominated by a limited set of processes. In the following, four of such cases are presented in detail. The upstream conditions and the strengths and scales of the downstream response during these cases are summarized in Table 1.

1) THE ELEVATED TURBULENCE ZONE

IOP 1 was conducted from 0000 UTC 2 March to 1500 UTC 3 March 2006. The IOP involved flight missions by UWKA and GV in the morning (IOP 1a) and afternoon (IOP 1b) of 2 March. Mayr and Armi (2010) previously investigated the onset of shallow foehn in Owens Valley during this case. Here, we focus on the UWKA turbulence measurements during the morning flight.

IOP 1a was timed well ahead of the passage of a mid-latitude synoptic system (Fig 3a). Upstream conditions were typical of the prefrontal environment, with strong crest-level stability and enhanced lee-side shear, but moderate wind speeds and decreasing stability farther aloft (Fig. 4a), providing optimal conditions for moderate-amplitude lee waves. Up-valley flow with wind speeds on the order of $5\text{-}10\text{ m s}^{-1}$ was found in the valley, topped by a sharp inversion ($\Delta\theta \approx 5\text{-}6\text{ K}$) roughly 1500 m above the valley floor.

In situ measurements made by UWKA are shown in Fig. 5. Raw and interpolated vertical velocities (Fig. 5a,b) exhibit a sequence of vertically coherent up- and downdrafts on the order of $\pm 4.5 \text{ m s}^{-1}$, strongly suggestive of lee waves. A distinct characteristic of the waves is the rapid decay of their amplitude downwind of the second downdraft. This feature may be attributed to destructive interference of lee waves generated by the primary and secondary ridges (Grubišić and Stiperski 2009; Stiperski and Grubišić 2011), or to critical-level or viscous absorption of wave energy by the valley atmosphere (Smith et al. 2002; Jiang et al. 2006).

Along the primary lee-wave crest and below the layer of increased stability, “moderate” ($\text{EDR} \geq 0.22 \text{ m}^{2/3} \text{ s}^{-1}$; Sharman et al. 2014) to “moderate-severe” ($\text{EDR} \geq 0.35 \text{ m}^{2/3} \text{ s}^{-1}$) turbulence and enhanced mixing in the otherwise stably stratified downstream atmosphere is detected (Fig. 5e). Below that region, the inversion-capped valley atmosphere remains largely undisturbed. A core of non-turbulent air flowing up the valley east of its axis is revealed by aircraft measurements below 3000 m MSL.

Jiang et al. (2010) suggested that strong crest-level turbulence in this IOP results from the interaction of the waves with the enhanced vertical shear, as will be further discussed in Section 4a. In the remainder, this type of turbulence structure over the valley is referred to as *elevated turbulence zone*, as opposed to the *low-level turbulence zone* near the ground (Fig. 1a).

2) DOWNSLOPE FLOW SEPARATION AT A LOW-LEVEL VALLEY INVERSION

One of the strongest windstorms of T-REX occurred on 16 April 2006 (IOP 13, Reinecke and Durran 2009). During the local morning and early afternoon (IOP 13c), scanning lidars sampled the turbulent interaction of strong westerly winds and pressure-driven channeled up-valley flow, providing some of the best evidence of subrotor vortices in T-REX (Doyle et al. 2009; De Wekker

and Mayor 2009). A few hours earlier (IOP 13b), another remarkable event was observed by the DLR lidar, which has not received attention thus far.

With the approach of the frontal system, cold air was building up upwind of the Sierra Nevada and started to flow through the mountain gaps towards the valley floor at 0800 UTC 16 April. About 7 km west of the DLR lidar, the strong ($>15 \text{ m s}^{-1}$) downslope flow terminated abruptly, detaching from the surface and flowing over another air mass in the core of the valley. The flow at the valley bottom had an upslope component but was mainly directed up-valley, as revealed by Fig. 6 for 1115 UTC. This configuration persisted for more than 5 hours (0800–1330 UTC). At various times during this period, wavy features reminiscent of Kelvin-Helmholtz billows (Fig. 7, couplets of positive and negative radial velocity) formed along the directionally-sheared interface between the westerly flow and the lower-level up-valley flow. The couplets were collocated with turbulent intrusions into the otherwise non-turbulent valley air, similar to, albeit not as vigorous as, the subrotor vortices observed during IOP 13c.

Further insight into the dynamics of the event can be gained from a comparison of upstream and in-valley vertical profiles (Fig. 8), similar to the analysis by Mayr and Armi (2010). Upstream profiles are again characterized by blocking, extending to 2300 m MSL, while up-valley flow dominates in the valley. The θ_v profile (Fig. 8c) reveals that the upstream flow above the blocked layer is cooler than the valley atmosphere and is thus able to penetrate well below crest level on the lee side. Its initially negative buoyancy, however, vanishes as it encounters the low-level valley inversion ~ 700 m above the valley floor. This level coincides almost exactly with the height at which the flow separates in the lidar images (Figs. 6, 7), pointing to the key role of the thermodynamic structure of the valley atmosphere in determining the position of the separation point.

Since no aircraft measurements are available for this period, direct evidence of waves at and above crest-level is missing. Measurements by the wind profilers, however, indicate sustained upward motion up to 4 m s^{-1} above the ISS2 site between 3 km and 4.5 km MSL (Fig. 6). In addition, enhanced downward motion above the eastern part of the valley is evidenced by the temporary re-descent of the radiosonde (Fig. 6) launched at 1100 UTC from the valley center (cf. Wang et al. 2009). However, in the absence of spatially more extensive aircraft measurements, no satisfactory answer can be given as to the type and amplitude of the waves.

The *nighttime flow separation* of IOP 13b bears some similarity to the elevated turbulence zone of IOP 1a. A major difference, however, is the considerably deeper penetration of westerly flow in IOP 13b, which is due to the different timing of the frontal passage with respect to the diurnal cycle in the valley. In IOP 1a, the flow through the passes started in the local morning, after nocturnal cooling in the valley had led to a strong, elevated inversion $\sim 1500 \text{ m}$ above the valley floor. In IOP 13b, the overflow set in early in the night, when a low-level inversion $\sim 700 \text{ m}$ above the valley floor had just formed, resulting in a penetration deeper by almost 1000 m and a well-defined separation of the flow at the low-level inversion. Another distinguishing feature of the two cases seem to be the turbulence production mechanisms, as discussed in Section 4a.

3) TURBULENT INTERACTION OF IN-VALLEY WESTERLIES WITH ALONG-VALLEY FLOW

Some of the highest turbulence intensities in Owens Valley were encountered by UWKA on its morning flight on 14 March 2006 (IOP 4a). Upstream profiles (Fig. 4d) were characterized by prefrontal to frontal conditions. Both the strengthening of upper-level winds and diurnal heating in the valley led to considerable transience of wave patterns throughout the IOP (Armi and Mayr 2015).

Composite cross-sections of in situ measurements made by UWKA during 1700–1930 UTC are shown in Fig. 9. Large-amplitude, long waves are detected in the lee of the Sierra Nevada (Table 1). In contrast to IOP 1a (Fig. 5), westerly momentum and strong vertical motion are present well below crest level above the lee slope and the valley center (Fig. 9a,d). The turbulence structure in and above the valley is fairly complex. Strong turbulence right above the mountain tops (Arrow 1 in Fig. 9e) is related to the top of the cap cloud, which was particularly well developed and “spilled over” into the valley (Fig. 9a,c). A second region of severe turbulence at crest level (Arrow 2 in Fig. 9e) could be explained by both in-cloud turbulence and vertical wind shear. The most interesting turbulent region is located at lower levels in the valley and tilts upward across the valley from west to east (Fig. 9d,e). Fig. 9d shows wind direction and reveals that the low-level turbulence is localized at the directionally-sheared interface, between the in-valley westerlies and the strong up-valley flow in the valley. The magnitude of turbulence in the third region falls into the “moderate-severe” category, comparable to that reported for the interior of rotors (e.g., Darby and Poulos 2006; Strauss et al. 2015).

The end of IOP 4a and the subsequent evolution of the event, extending beyond the available aircraft measurements, was covered by lidar observations. DLR lidar data from the 2.5 hours (1920–2200 UTC) after the flight mission is shown in Figs. 10 and 11. The spatial distribution of turbulence (Fig. 10c) is consistent with that in the composite cross-section (Fig. 9e). Note that the lidar was situated roughly 2 km west of Independence, which serves as the origin of aircraft composite cross-sections. The PPI-20 scan at 1926 UTC (Fig. 10d) indicates a strong up-valley flow ($10\text{--}20\text{ m s}^{-1}$), beneath the cross-mountain flow. Within an hour, the flow in the valley changes significantly (Fig. 10, right panels). At 2025 UTC, shallow westerly downslope flow is present down to 3 km east of the lidar, where it encounters the strong up-valley flow. The period 2000–2130 UTC coincided with the appearance of roll and wave clouds over the eastern portion of the valley, as

visible from GOES-10 satellite images (not shown). The transition continues until the up-valley flow is completely replaced by westerlies (Fig. 11b,d). The vertical structure of the flow in the valley throughout this period is quite complex. Above the relatively shallow cross-valley current, up-valley and upslope-directed flow, interacting strongly with the crest-level westerlies, is detected southwest of the lidar in the 4-6 km range (Figs. 10f,h and 11d).

A photograph taken near the DLR lidar site at 2130 UTC, shown in Fig. 12, provides an impressive snapshot of this event. The nicely formed line of roll clouds east of the valley axis might suggest the presence of a rotor. Lidar scans, instead, reveal that the cumulus clouds formed along the line of encounter of cross-valley and up-valley flows (Fig. 10e,f,h).

4) TRANSIENT MOUNTAIN WAVES AND ROTORS

The most severe downslope windstorm of T-REX occurred on 25 and 26 March 2006 (IOP 6). Maximum wind gusts of 35.8 m s^{-1} were recorded at DRI Station 2 around 0240 UTC 26 March. Damage was caused in the town of Independence and severe turbulence over Owens Valley was encountered by a private aircraft crossing the valley en route from San Francisco to Las Vegas. Owing to the severity of the event, IOP 6 became the subject of many observational and numerical modeling studies (e.g., Reinecke and Durran 2009; Hill et al. 2010; Jiang et al. 2011; Doyle et al. 2011; Sheridan and Vosper 2012; Kühnlein et al. 2013).

IOP 6 lasted from 2000 UTC 24 March to 0500 UTC 26 March. Sheridan and Vosper (2012) have documented the dynamic evolution of this event, including details of the cold-frontal passage, using observations and real-case simulations. The marked transience of the flow in Owens Valley during the second phase of IOP 6 (1600 UTC 25 March to 0500 UTC 26 March, IOP 6b-c) has been analyzed by Kühnlein et al. (2013), using data from the DLR lidar. The objective of this

section is to re-examine the observations and link them to the evolution of waves above Owens Valley.

Soundings from IOP 6b-c (Fig. 4e) are characterized by frontal to postfrontal conditions. Cross-mountain winds above the mountaintop height continue to increase with time, reaching 30 m s^{-1} at crest level and exceeding 50 m s^{-1} at the tropopause in the 2258 UTC sounding. Initial upstream blocking is gradually reduced and enhanced crest-level stability yields to more uniform stratification. Crest-level shear increases, peaking at $\sim 20 \text{ m s}^{-1} \text{ km}^{-1}$ in the 2000 UTC downstream profile.

Two flight missions were conducted on 25 March, the first one involving all three research aircraft. A composite cross-section of aircraft measurements from the first mission is shown in Fig. 13a-c. A strongly nonlinear mountain wave is present downstream of the Sierra Nevada, with isentropes bending downward by $\sim 2 \text{ km}$ in the lee and quickly recovering their original height over the valley center. The aircraft measurements coincide with a period of alternating up-valley flow and eastward-propagating pulses of high-momentum air, with hydraulic jump-like turbulent structures similar to a rotor at their front (Kühnlein et al. 2013, their Figs. 3 and 5). From 2130 UTC onwards, westerly winds at the valley floor prevail, possibly aided by the diurnal temperature cycle in the valley (Jiang and Doyle 2008; Sheridan and Vosper 2012; Billings and Grubišić 2008a). The vertical velocity above the ISS2 wind profiler (Fig. 14) changes sign at 1730–1830 UTC, likely related to the shift of the primary wave updraft to the east. By the time of the afternoon flights, the horizontal wavelength of the wave has increased, placing the leading updraft of the wave over the windward slope of the Inyos (Fig. 13d,e; Table 1).

From 2200 UTC 25 March to 0300 UTC 26 March westerlies dominate at the valley floor, continuously gaining strength and exceeding 20 m s^{-1} by 0200 UTC. The most severe downslope windstorm of T-REX occurs from 0200 to 0330 UTC 26 March. By 0230 UTC, lofted dust becomes visible in the DLR lidar RHI-80 scans over the eastern part of the valley, reaching a vertical

extent of 2.5 km within only 10 min (Fig. 15a,c). In the next 30 min, the leading edge of this feature rapidly moves upstream across the valley (Fig. 15c,e), gradually decelerating and lingering over the lidar site for the next hour (also cf. Kühnlein et al. 2013, their Fig. 9).

The above observations represent the best evidence of boundary-layer separation and the associated development of a large rotor in T-REX. Radial velocities away from the lidar in excess of 20 m s^{-1} are found near the rotor edge (Fig. 15c). Distinct zones of easterly (i.e., reversed) flow of up to 10 m s^{-1} are located eastward of the separation point and underneath the rotor edge, resulting in strong shear and severe turbulence (Fig. 15d), which is typical of the separated boundary layer (Doyle and Durran 2002). Once the rotor fully developed (Fig. 15e), its downwelling branch, characterized by flow-away from the lidar and increased turbulence intensity (Fig. 15f), becomes visible and seems to re-attach to the ground.

Despite its strong similarities to the idealized rotor, the flow displays a high degree of three-dimensionality and transience (Kühnlein et al. 2013). Beyond a region with a marked easterly flow component, immediately downstream of the separation point, wind vectors in the eastern portion of the valley are predominantly down-valley. Also, not always is the rotor structure as well defined as in Fig. 15e. The strong interaction with the along-valley flow perturbs its average shape continuously. After 0330 UTC, the rotor retreats upstream and eventually decays. At the same time, upward motion re-appears above the ISS2 site (Fig. 14), suggesting that the leading updraft of the wave in the valley has shifted back to the west.

In summary, the gradual onset and rapid cessation of the IOP 6 downslope windstorm appear to be tightly linked to the eastward and westward shifts of the waves aloft. As the waves moves to the east and downslope winds gradually follow, a rotor-like turbulent structure is found at their front. As the wave updraft reaches the secondary ridge, this structure is suppressed, but resurrects

as a fully developed rotor downwind of the retreating windstorm as the waves move back towards the Sierra Nevada.

The last phase of IOP 6 bears striking resemblance to two events observed on 26 January and 5 February 2006 in the lee of the Medicine Bow Mountains, SE Wyoming. A detailed observational analysis (French et al. 2015; Strauss et al. 2015) and high-resolution numerical modeling (Grubišić et al. 2015) have identified transient mid-tropospheric wave breaking as the key mechanism behind the movement of the rotors in those cases. Indeed, in an investigation of the predictability of the IOP 6 severe downslope windstorm (Reinecke and Durran 2009), only those ensemble members reproduced severe downslope windstorms that involved the upper-tropospheric turbulent breakdown of a large-amplitude mountain wave above the Sierra Nevada. It is thus plausible that the nonstationary waves and transient rotors of IOP 6b-c are closely related to wave breaking and concomitant changes in the flow across the Sierra Nevada.

4. Discussion

The above case studies reveal a rich variety of turbulent flow patterns over the Sierra Nevada and Owens Valley. The analysis shows that the classic elements of the rotor concept, and the types of rotor-like structures that may form from their combination, are dramatically affected by the characteristics of the downstream atmosphere. In Fig. 16, we present schematic diagrams that describe the typical flow scenarios related to frontal passage across the region. Table 2 provides a classification of these and other T-REX cases.

a. Categorization of turbulent structures in Owens Valley

A schematic of the *elevated turbulence zone* (Scenario A) is shown in Fig. 16a. Trapped lee waves of moderate amplitude are present over the Sierra Nevada. Below the lee wave crest, “mod-

erate” to “moderate-severe” turbulence is found. The inversion-capped up-valley flow in the valley remains decoupled. Lines of roll clouds similar to rotor clouds occasionally form in the wave crests over the valley.

It is tempting to think of this case as an “elevated rotor”, induced by the detachment of the flow at the elevated valley inversion. However, turbulence intensity is equally high below the upwelling and downwelling branches of the wave. This is in contrast to previous findings showing that the strongest rotor turbulence is located along its upstream edge (generated from the shear of the separated boundary-layer), while it is generally weaker and more diffuse on its downstream side (Lester and Fingerhut 1974; Doyle and Durran 2002). Here instead, turbulence is likely generated by the interaction of waves with enhanced crest-level shear, resulting in a local decrease (increase) of Richardson number in wave crests (troughs) and consequent promotion (suppression) of shear instability (Jiang et al. 2010).

A depiction of *downslope flow separation at a low-level valley inversion* (Scenario B) is shown in Fig. 16b. At nighttime, the cold upstream air mass starts to flow over the Sierra Nevada but is prevented from progressing to the valley bottom by the presence of even colder and more stable air. The downslope flow separates from the lee slope well above the valley floor and flows over the stably stratified up-valley flow. Kelvin-Helmholtz billows that form at the directionally-sheared interface between the two air masses are advected and break down into turbulence, reminiscent of subrotors observed for other T-REX cases. Scenario B highlights the importance of potential temperature differences between the upstream and downstream air masses for the location of flow separation. This case displays several characteristics of a classic rotor: flow separation, shear at the lower edge of the separated flow, Kelvin-Helmholtz instability, and the associated formation of billows and enhanced turbulence. On the other hand, a horizontal vortex line below the separated flow is absent and is replaced by channeled up-valley flow.

The schematics of Scenarios A and B are somewhat similar to two of those by Jiang and Doyle (2008, their Fig. 12). The latter, however, refer to a weak westerly wind event during SRP IOP 12, primarily determined by thermal forcing in the valley.

A schematic of daytime *turbulent interaction of in-valley westerlies with channeled up-valley flow* (Scenario C) is shown in Fig. 16c. The wave amplitude tends to be considerably larger than in Scenarios A and B. This may be attributed in part to the well-mixed valley atmosphere: compared to the latter scenarios, the absence of a valley inversion results in a larger effective mountain height (Smith et al. 2002; Armi and Mayr 2015). Frequently, a convective cap cloud is present over the Sierra Nevada. In the course of the day, the valley atmosphere becomes increasingly well-mixed, permitting the cross-mountain flow to reach the valley floor. Severe turbulence is found on top of the cap cloud and where the penetrating westerlies interact with the up-valley flow, with intensities similar to those in the interior of rotors. At times, a rather well-defined line of (directional) shear at the interface between the westerly and up-valley winds is present in the valley and roll clouds form east of the valley axis. The scenario typically lasts until westerlies become strong enough to flush out the valley air (IOP 4a), but along-valley winds may also continue to resist for several hours (IOP 13c).

The class of strongest events (Scenario D) is presented in Fig. 16d. This scenario is characterized by the highest cross-mountain winds and largest-amplitude waves, capable of fully controlling the flow in the valley. In response, a large rotor can form, whose leading edge is aligned with the updraft of the wave aloft. The wave field, however, exhibits a high degree of transience. It strongly responds to the strengthening (weakening) of cross-mountain winds by extending (shortening) its wavelength and shifting across the valley to the east (west), thereby steering the downslope windstorm with the rotor at its leading edge. In the strongest phase of the event, the wave updraft is located over the windward slope of the secondary ridge and rotor formation is temporarily

suppressed. The scenario contains all elements of the classic rotor, in particular a rather well-defined reversed flow downstream of the boundary-layer separation point. The distinct additional element to the steady-state traditional concept is the rapid rotor evolution on a temporal scale of only a few hours, likely related to the onset and cessation of mountain wave-breaking at mid- to upper levels (cf. Jiang et al. 2007; Grubišić et al. 2015).

b. Stages of frontal passage over the Sierra Nevada and Owens Valley

The essential characteristics of the upstream and downstream soundings associated with the above four scenarios are shown in Fig. 17. Close inspection of the idealized profiles indicates that they may be related to different *stages* of the passage of frontal systems across the region. The following description of the idealized soundings focuses on three aspects: the effect of the frontal passage on the upstream environment, its impact on wind speed and direction within the valley, and the distinct effect of diurnal heating within the valley on the downstream profile of potential temperature.

The upstream environment in Scenarios A and B (identical in the idealized profiles) is characterized by prefrontal conditions. The upstream flow is blocked (as evident in both wind speed and direction below 2 km MSL), wind shear is strong at the mountaintop level and moderate aloft. Stability is enhanced at and above crest level but weaker aloft. In Scenario C, associated with prefrontal to frontal conditions, the upstream flow is more deeply blocked at low levels. Winds are stronger at the ridge height and continue increasing up to the tropopause. The layer of increased stability has shifted upwards. In Scenario D, displaying significant transience, upstream profiles of wind speed and direction transition from frontal to postfrontal conditions. Initial upstream blocking is gradually reduced and winds amplify throughout the troposphere. The low-level wind switches from initially southerly to westerly and finally to north-northwesterly, as the front passes.

At the same time, the potential temperature profiles remain mostly unaltered, with the rather uniform stability profile favoring the generation of upward-propagating mountain waves.

The kinematic characteristics of the valley atmosphere in the four scenarios are mainly determined by pressure-driven channeling of the flow towards the pressure low to the north of the Sierra Nevada. As the front approaches the mountain range, the up-valley flow strengthens (Scenarios A/B to C). In Scenario D, in-valley winds finally switch to westerly and then north-northwesterly.

The thermodynamic structure within the valley is primarily determined by the diurnal heating cycle. Low or elevated valley inversions (Scenarios B or A, respectively) can be generated through nocturnal cooling. Daytime warming leads to an increasingly well-mixed valley atmosphere (Scenario C). The diurnal cycle can, however, be largely superseded when cold-frontal air reaches the center of Owens Valley from the north (Scenario D).

The four scenarios and the associated schematic diagrams (Fig. 16) can thus be interpreted as representative of different stages of the pre- to postfrontal evolution of gravity waves launched by the Sierra Nevada. An individual wave event may run through a sequence of these stages. The specific combination of the upstream conditions with the thermodynamic and kinetic characteristics of the valley atmosphere appear to predetermine the evolution of each individual case. The evolution depends crucially on the relative timing of the approach and passage of the frontal system with respect to the diurnal cycle in the valley. For example, despite similar upstream conditions (Scenarios A, B, C), nighttime cooling (A, B) and daytime warming (C) in the valley can lead to distinct downstream flow responses.

Beyond the timing of the front, a large case-to-case variability of upstream and downstream conditions exists, regarding, for instance, the strength of crest-level stability or the magnitude of up-valley winds. The resultant predominance of a particular process can alter the evolution of an individual event and can give preference to one scenario over another despite similar initial

conditions. For example, in IOP 13c (Doyle et al. 2009), the along-valley flow was too strong to be completely replaced by the incoming westerlies, in contrast to IOP 6 (Kühnlein et al. 2013, and Section 3b4).

It is thus not possible to provide a unique prototypical sequence of in-valley flow patterns during a frontal passage. Frequently, however, two or three of the four scenarios are met along the evolution of an event. Examples from T-REX include IOP 1 (A–C), IOP 6 (A–C–D), IOP 13 (A–B–C; Table 2). Another notable event is the Sierra Rotors Project (SRP) IOP 8 (24–27 March 2004). From observations and numerical modeling, Grubišić and Billings (2007) showed striking similarities of this case with T-REX IOP 6, involving mid-level wave breaking and rotor formation and the same sequence of stages (A–C–D). Similar flow patterns are also observed in the Alps. For example, Scenario B is well known in the Inn Valley, Austria, where shallow south foehn frequently separates on top of a wintertime valley cold pool, inhibiting its breakthrough at the valley floor (Gohm and Mayr 2004; Mayr et al. 2007).

c. Role of surface pressure gradients for rotor formation in a valley

Lyra (1943) was the first to note that pressure perturbations induced by trapped lee waves may produce regions of adverse pressure gradient force and decelerate the flow sufficiently to make it separate from the surface (Queney et al. 1960). Much later, Doyle and Durran (2002) corroborated Lyra’s conjecture, showing the key role of wave-induced boundary-layer separation in rotor formation. The wave-induced pressure perturbations and rotor strength in their numerical simulations revealed a threshold pressure gradient above which rotors form. A threshold value of $(|\nabla p|/\rho)/(U^2/L) \approx 2.2$, where U is the upstream wind speed (in the model) and L is the mountain half-width, was proposed. Accordingly, a rough calculation of the minimum pressure gradient required for rotor formation in Owens Valley (using $U = 20 \text{ m s}^{-1}$ as a typical value for the wind

speed of strong westerlies and $L = 7.5$ km as the half-width of the Sierra Nevada lee slope) provides an *order-of-magnitude* estimate of 1 hPa km^{-1} .

Hovmöller diagrams of pressure perturbations across DRI stations 1–6 for a selection of IOPs are shown in Fig. 18. The surface measurements do not display large pressure perturbations and the pressure gradients observed at the valley floor hardly ever exceeds the required threshold. The exception is the downslope windstorm event of IOP 6. This is remarkable, since both large-amplitude waves and rotor-like flow patterns were actually present in Owens Valley during all periods marked in Fig. 18. The lack of significant perturbations in the surface pressure is consistent with results by Parish and Oolman (2012), who noted that amplitudes of isobaric height perturbations are damped rapidly within the boundary layer, such that no appreciable wave-induced horizontal pressure gradient remains below crest level. This is also evident in composite cross-sections of flight-level pressure perturbations from four UWKA flights (Fig. 19).

Recently, Jiang et al. (2006) suggested turbulent dissipation and critical-level absorption as two possible wave absorption mechanisms in the boundary layer. They found that a stagnant boundary layer is most efficient in absorbing wave energy and momentum by critical-level absorption. Indeed, the sustained up-valley flow in Owens Valley likely acts as a critical level to waves forming in the crest-level, predominantly westerly flow. Even when strong westerlies dominate in the valley, the resultant turbulent motions may diffuse and dissipate originally coherent wave-induced pressure perturbations. We thus hypothesize that turbulence or stagnant layers in the valley tend to absorb a significant portion of the wave energy, thereby preventing large wave-induced pressure perturbations from reaching the valley floor.

The question remains as to what caused rotors and rotor-like structures in the absence of large pressure gradients. Note that the pressure-perturbation argument is based purely on the magnitude of an individual term, the pressure-gradient force, in the horizontal equations of motion. However,

in real flows evolving in complex environments, other terms in the full set of momentum equations may become equally important. For example, in the presence of very stable air in the valley, wave-induced pressure gradients and positive buoyancy forces may act in concert to make the downslope flow detach from the lee slope, well above the valley floor. This was likely the case in the IOP 13b nighttime event (Fig. 16b). A similar event has also been reported from the Persistent Cold-Air Pool Study over the Salt Lake Valley in 2010 (Lareau and Horel 2014). To elucidate the relative importance of pressure-gradient, buoyancy and other forces for flow separation, a thorough evaluation of the relevant terms in the equations of motion is required. Such an analysis does not appear possible from the observational data alone, calling for high-resolution numerical simulations.

5. Summary and conclusions

Idealized conceptual models of atmospheric rotors in the lee of mountain ranges emerged in the 1950s during the Sierra Wave Project (Holmboe and Klieforth 1957) and were refined until the 1970s (Lester and Fingerhut 1974). These models prove to be overly simplistic, in particular in the topographical setting considered in the present study, consisting of two parallel mountain ridges separated by a deep elongated valley. In such an environment, rotor formation may be influenced by thermally-driven slope and valley flows, pressure-driven flow channeling, or by the modulation of lee-wave characteristics by the presence of the secondary ridge.

In this study, we have considered observations of large-amplitude waves, low-level rotors and severe turbulence, made during IOPs 1, 2, 3, 4, 6, and 13 of T-REX. We have examined commonalities and differences in the rotor morphology and the spatial and temporal patterns of turbulence within the valley downstream of the Sierra Nevada. Four case studies reveal the rich variety of flow responses and turbulent structures during periods with strong mountain-wave activity. Schematic

diagrams, highlighting typical flow scenarios and pointing to the mechanisms of turbulence generation in the valley, have been distilled (Fig. 16). These include (A) the elevated turbulence zone, (B) separation of downslope flow at a low-level valley inversion, (C) turbulent interactions of in-valley westerlies with channeled along-valley flows, and (D) transient mountain waves and rotors.

The scenarios and their comparison show that the elements of the classic rotor concept are greatly enriched and, at times, largely overridden by dynamically and thermally induced processes in the valley. For instance, flow reversal downstream of the separation point was rarely observed, due to channeled along-valley flows prevailing in the valley, downwind of the separated surface westerlies. Conversely, individual aspects of the rotor concept may co-exist even in the absence of a fully-developed rotor. For example, roll clouds parallel to the mountain ridge appear to form even without a rotor (Scenarios A and C). Moderate to severe turbulence may be generated in the valley through other processes, such as shear instability at the interface between the separated westerlies and the up-valley flow underneath (Scenarios B and C). However, in the strongest cases, all ingredients may be in place to give rise to a vigorous rotor flow and attendant severe turbulence (Scenario D). While in Scenarios A, B, and C, turbulence structures can deviate substantially from those associated with a classic rotor, Scenario D underlines that the rotor concept may apply even in a deep valley, given a special set of conditions.

The four flow scenarios can be related to different stages of frontal passage over the valley. The evolution of individual events often runs through a sequence of these stages (Table 2). Also, the scenarios do not seem to be constrained to the Sierra Nevada and Owens Valley, as indicated by reports of similar observations in the Alps.

Despite the presence of large-amplitude waves and rotor-like structures, horizontal pressure gradients at the valley floor were often relatively weak. It is hypothesized that wave-induced pressure

perturbations are subject to critical-level absorption and/or turbulent diffusion of wave energy, preventing them from extending to the valley bottom.

In summary, while some of the observations presented in this work may seem to call into question the concept of the rotor flow as a whole, its strongest occurrences do contain most of the defining elements suggested in previous studies. Even its nonideal variants, here referred to as *rotor-like* turbulent structures, seem to bear sufficient similarity to deserve the name, not least because the term is well-known in the aviation community where it stands for the likely encounter with severe low-level turbulence underneath lenticular wave clouds.

Acknowledgments. This study was supported by the FWF (Austrian Science Fund) grant P24726-N27 to the University of Vienna (“STABLEST, Stable boundary layer separation and turbulence”). Visits by L. Strauss and S. Serafin to NCAR were funded by the Faculty of Earth Sciences, Geography and Astronomy of the University of Vienna. The primary sponsor of T-REX was the U.S. National Science Foundation (NSF). All data sets were downloaded from the T-REX data archive, which is maintained by the Earth Observing Laboratory (NCAR, cited 2015). NCAR is sponsored by NSF. Access to ECMWF data was provided through the Zentralanstalt für Meteorologie und Geodynamik, Austria. The authors thank Martin Weissmann, Andreas Dörnbrack, and Stephan De Wekker for their help with the lidar data and for sharing their insights from the field. L. Strauss is indebted to Samuel Haimov for his continuous support with the UWKA and WCR data and their careful interpretation.

References

Armi, L., and G. J. Mayr, 2015: Virtual and real topography for flows across mountain ranges. *J. Appl. Meteor. Climatol.*, **54**, 723–731, doi:10.1175/JAMC-D-14-0231.1.

- Billings, B. J., and V. Grubišić, 2008a: A numerical study of the effects of diurnal heating, moisture, and downstream topography on downslope winds within a valley. *13th Conference on Mountain Meteorology*, Whistler, BC, Canada. [Available online at <https://ams.confex.com/ams/13MontMet17AP/webprogram/Paper140812.html>].
- Billings, B. J., and V. Grubišić, 2008b: A study of the onset of westerly downslope winds in Owens Valley. *13th Conference on Mountain Meteorology*, Whistler, BC, Canada. [Available online at <https://ams.confex.com/ams/13MontMet17AP/webprogram/Paper140810.html>].
- Carney, T. Q., A. J. Bedard, J. M. Brown, M. J. Kraus, J. McGinley, and T. A. Lindholm, 1997: Hazardous mountain winds and their visual indicators. Department of Commerce, NOAA, Handbook, Federal Aviation Administration Advisory Circular AC00-57, 80 pp. [Available online at http://www.faa.gov/documentLibrary/media/Advisory_Circular/00-57.pdf].
- Cohn, S. A., W. O. J. Brown, C. L. Martin, M. E. Susedik, G. Maclean, and D. B. Parsons, 2001: Clear air boundary layer spaced antenna wind measurement with the Multiple Antenna Profiler (MAPR). *Ann. Geophys.*, **19**, 845–854, doi:10.5194/angeo-19-845-2001.
- Cohn, S. A., V. Grubišić, and W. O. J. Brown, 2011: Wind profiler observations of mountain waves and rotors during T-REX. *J. Appl. Meteor. Climatol.*, **50**, 826–843, doi:10.1175/2010JAMC2611.1.
- Darby, L. S., and G. S. Poulos, 2006: The evolution of lee-wave-rotor activity in the lee of Pike's Peak under the influence of a cold frontal passage: Implications for aircraft safety. *Mon. Wea. Rev.*, **134**, 2857–2876, doi:10.1175/MWR3208.1.
- De Wekker, S. F. J., and S. D. Mayor, 2009: Observations of atmospheric structure and dynamics in the Owens Valley of California with a ground-based, eye-safe, scanning aerosol lidar. *J. Appl.*

- Meteor. Climatol.*, **48**, 1483–1499, doi:10.1175/2009JAMC2034.1.
- Doyle, J. D., and D. R. Durran, 2002: The dynamics of mountain-wave-induced rotors. *J. Atmos. Sci.*, **59**, 186–201, doi:10.1175/1520-0469(2002)059<0186:TDOMWI>2.0.CO;2.
- Doyle, J. D., and D. R. Durran, 2007: Rotor and subrotor dynamics in the lee of three-dimensional terrain. *J. Atmos. Sci.*, **64**, 4202–4221, doi:10.1175/2007JAS2352.1.
- Doyle, J. D., V. Grubišić, W. O. J. Brown, S. F. J. De Wekker, A. Dörnbrack, Q. Jiang, S. D. Mayor, and M. Weissmann, 2009: Observations and numerical simulations of subrotor vortices during T-REX. *J. Atmos. Sci.*, **66**, 1229–1249, doi:10.1175/2008JAS2933.1.
- Doyle, J. D., Q. Jiang, R. B. Smith, and V. Grubišić, 2011: Three-dimensional characteristics of stratospheric mountain waves during T-REX. *Mon. Wea. Rev.*, **139**, 3–23, doi:10.1175/2010MWR3466.1.
- Durran, D. R., 1990: Mountain waves and downslope winds. *Atmospheric Processes over Complex Terrain*, W. Blumen, Ed., Meteorological Monographs, Vol. 23, American Meteorological Society, 59–82.
- Earth Observing Laboratory, cited 2015: T-REX Homepage. [Available online at https://www.eol.ucar.edu/field_projects/t-rex].
- French, J. R., S. Haimov, L. Oolman, V. Grubišić, S. Serafin, and L. Strauss, 2015: Wave-induced boundary-layer separation in the lee of the Medicine Bow Mountains. Part I: Observations. Submitted to *J. Atmos. Sci.*
- Gerbier, N., and M. Berenger, 1961: Experimental studies of lee waves in the French Alps. *Q.J.R. Meteorol. Soc.*, **87**, 13–23, doi:10.1002/qj.49708737103.

- Gohm, A., and G. J. Mayr, 2004: Hydraulic aspects of föhn winds in an alpine valley. *Q.J.R. Meteorol. Soc.*, **130**, 449–480, doi:10.1256/qj.03.28.
- Gohm, A., G. J. Mayr, A. Fix, and A. Giez, 2008: On the onset of bora and the formation of rotors and jumps near a mountain gap. *Q.J.R. Meteorol. Soc.*, **134**, 21–46, doi:10.1002/qj.206.
- Grubišić, V., and B. J. Billings, 2007: The intense lee-wave rotor event of Sierra Rotors IOP 8. *J. Atmos. Sci.*, **64**, 4178–4201, doi:10.1175/2006JAS2008.1.
- Grubišić, V., and B. J. Billings, 2008: Climatology of the Sierra Nevada mountain-wave events. *Mon. Wea. Rev.*, **136**, 757–768, doi:10.1175/2007MWR1902.1.
- Grubišić, V., and M. Orlić, 2007: Early observations of rotor clouds by Andrija Mohorovičić. *Bull. Amer. Meteor. Soc.*, **88**, 693–700, doi:10.1175/BAMS-88-5-693.
- Grubišić, V., and I. Stiperski, 2009: Lee-wave resonances over double bell-shaped obstacles. *J. Atmos. Sci.*, **66**, 1205–1228, doi:10.1175/2008JAS2885.1.
- Grubišić, V., and Coauthors, 2008: The Terrain-Induced Rotor Experiment. *Bull. Amer. Meteor. Soc.*, **89**, 1513–1533, doi:10.1175/2008BAMS2487.1.
- Grubišić, V., and J. M. Lewis, 2004: Sierra Wave Project revisited – 50 years later. *Bull. Amer. Meteor. Soc.*, **85**, 1127–1142, doi:10.1175/BAMS-85-8-1127.
- Grubišić, V., S. Serafin, L. Strauss, S. Haimov, J. R. French, and L. Oolman, 2015: Wave-induced boundary-layer separation in the lee of the Medicine Bow Mountains. Part II: Modeling. Submitted to *J. Atmos. Sci.*
- Hill, M., R. Calhoun, H. J. S. Fernando, A. Wieser, A. Dörnbrack, M. Weissmann, G. Mayr, and R. Newsom, 2010: Coplanar Doppler lidar retrieval of rotors from T-REX. *J. Atmos. Sci.*, **67**, 713–729, doi:10.1175/2009JAS3016.1.

- Hirth, W., 1933: Die lange Welle. *Die hohe Schule des Segelfluges*, W. Hirth, Ed., Klasing & Co., Berlin, 135–139.
- Holmboe, J., and H. Klieforth, 1957: Investigation of mountain lee waves and the air flow over the Sierra Nevada. Department of Meteorology, UCLA Final Rep. Contract AF 19(604)-728, 283 pp.
- International Civil Aviation Organization, 2007: Meteorological Service for International Air Navigation. Annex 3 to Convention on International Civil Aviation. [Available online at http://www.wmo.int/pages/prog/www/ISS/Meetings/CT-MTDCF-ET-DRC_Geneva2008/Annex3_16ed.pdf].
- Jiang, Q., and J. D. Doyle, 2008: Diurnal variation of downslope winds in Owens Valley during the Sierra Rotor Experiment. *Mon. Wea. Rev.*, **136**, 3760–3780, doi:10.1175/2008MWR2469.1.
- Jiang, Q., J. D. Doyle, V. Grubišić, and R. B. Smith, 2010: Turbulence characteristics in an elevated shear layer over Owens Valley. *J. Atmos. Sci.*, **67**, 2355–2371, doi:10.1175/2010JAS3156.1.
- Jiang, Q., J. D. Doyle, and R. B. Smith, 2006: Interaction between trapped waves and boundary layers. *J. Atmos. Sci.*, **63**, 617–633, doi:10.1175/JAS3640.1.
- Jiang, Q., J. D. Doyle, S. Wang, and R. B. Smith, 2007: On boundary layer separation in the lee of mesoscale topography. *J. Atmos. Sci.*, **64**, 401–420, doi:10.1175/JAS3848.1.
- Jiang, Q., M. Liu, and J. D. Doyle, 2011: Influence of mesoscale dynamics and turbulence on fine dust transport in Owens Valley. *J. Appl. Meteor. Climatol.*, **50**, 20–38, doi:10.1175/2010JAMC2522.1.

- Koschmieder, H., 1920: Zwei bemerkenswerte Beispiele horizontaler Wolkenschläuche (Two notable examples of horizontal cloud tubes). *Beitr. Phys. Frei. Atmos.*, **9**, 176–180.
- Kossmann, M., and A. P. Sturman, 2003: Pressure-driven channeling effects in bent valleys. *J. Appl. Meteor.*, **42**, 151–158, doi:10.1175/1520-0450(2003)042<0151:PDCEIB>2.0.CO;2.
- Kühnlein, C., A. Dörnbrack, and M. Weissmann, 2013: High-resolution Doppler lidar observations of transient downslope flows and rotors. *Mon. Wea. Rev.*, **141**, 3257–3272, doi:10.1175/MWR-D-12-00260.1.
- Küttner, J., 1938: Moazagotl und Föhnwelle (Moazagotl and foehn wave). *Beitr. Phys. Atmos.*, **25**, 79–114.
- Küttner, J., 1939: Zur Entstehung der Föhnwelle (On the origin of the foehn wave). *Beitr. Phys. Atmos.*, **25**, 251–299.
- Lareau, N. P., and J. D. Horel, 2014: Dynamically induced displacements of a persistent cold-air pool. *Boundary-Layer Meteorol.*, **154**, 291–316, doi:10.1007/s10546-014-9968-5.
- Lester, P. F., and W. A. Fingerhut, 1974: Lower turbulent zones associated with mountain lee waves. *J. Appl. Meteor.*, **13**, 54–61, doi:10.1175/1520-0450(1974)013<0054:LTZAWM>2.0.CO;2.
- Lilly, D. K., and W. Toutenhoofd, 1969: The Colorado Lee Wave Program. *Clear Air Turbulence and Its Detection*, Y.-H. Pao, and A. Goldberg, Eds., Springer US, 232–245, doi:10.1007/978-1-4899-5615-6_13.
- Lyra, G., 1943: Theorie der stationären Leewellenströmung in freier Atmosphäre (Theory of stationary lee wave flow in the free atmosphere). *Z. angew. Math. Mech.*, **23**, 1–28, doi:10.1002/zamm.19430230102.

- MacCready Jr., P. B., 1964: Standardization of gustiness values from aircraft. *J. Appl. Meteor.*, **3**, 439–449, doi:10.1175/1520-0450(1964)003\$(<\$0439:SOGVFA\$>\$2.0.CO;2.
- Mayr, G. J., and L. Armi, 2010: The influence of downstream diurnal heating on the descent of flow across the Sierras. *J. Appl. Meteor. Climatol.*, **49**, 1906–1912, doi:10.1175/2010JAMC2516.1.
- Mayr, G. J., and Coauthors, 2007: Gap flows: Results from the Mesoscale Alpine Programme. *Q.J.R. Meteorol. Soc.*, **133**, 881–896, doi:10.1002/qj.66.
- Mohorovičić, A., 1889: Interessante Wolkenbildung über der Bucht von Buccari (Interesting cloud formation above Bakar Bay). *Meteor. Z.*, **24**, 56–58.
- Parish, T. R., and L. D. Oolman, 2012: Isobaric height perturbations associated with mountain waves measured by aircraft during the Terrain-Induced Rotor Experiment. *J. Atmos. Oceanic Technol.*, **29**, 1825–1834, doi:10.1175/JTECH-D-12-00050.1.
- Parsons, D., and Coauthors, 1994: The Integrated Sounding System: Description and preliminary observations from TOGA COARE. *Bull. Amer. Meteor. Soc.*, **75**, 553–567, doi:10.1175/1520-0477(1994)075<0553:TISSDA>2.0.CO;2.
- Queney, P., G. Corby, N. Gerbier, H. Koschmieder, and J. Zierep, 1960: The airflow over mountains. World Meteorological Organization Tech. Note 34, 135 pp.
- Raab, T., and G. Mayr, 2008: Hydraulic interpretation of the footprints of Sierra Nevada windstorms tracked with an automobile measurement system. *J. Appl. Meteor. Climatol.*, **47**, 2581–2599, doi:10.1175/2008JAMC1675.1.
- Reinecke, P. A., and D. R. Durran, 2009: Initial-condition sensitivities and the predictability of downslope winds. *J. Atmos. Sci.*, **66**, 3401–3418, doi:10.1175/2009JAS3023.1.

- Scorer, R. S., 1949: Theory of waves in the lee of mountains. *Q.J.R. Meteorol. Soc.*, **75**, 41–56, doi:10.1002/qj.49707532308.
- Sharman, R. D., L. B. Cornman, G. Meymaris, J. Pearson, and T. Farrar, 2014: Description and derived climatologies of automated in situ eddy-dissipation-rate reports of atmospheric turbulence. *J. Appl. Meteor. Climatol.*, **53**, 1416–1432, doi:10.1175/JAMC-D-13-0329.1.
- Sheridan, P., and S. Vosper, 2012: High-resolution simulations of lee waves and downslope winds over the Sierra Nevada during T-REX IOP 6. *J. Appl. Meteor. Climatol.*, **51**, 1333–1352, doi:10.1175/JAMC-D-11-0207.1.
- Sibson, R., 1981: A brief description of natural neighbour interpolation. *Interpreting Multivariate Data*, V. Barnett, Ed., Wiley, New York, USA, 21–36.
- Smith, R. B., S. Skubis, J. D. Doyle, A. S. Broad, C. Kiemle, and H. Volkert, 2002: Mountain waves over Mont Blanc: Influence of a stagnant boundary layer. *J. Atmos. Sci.*, **59**, 2073–2092, doi:10.1175/1520-0469(2002)059<2073:MWOMBI>2.0.CO;2.
- Stiperski, I., and V. Grubišić, 2011: Trapped lee wave interference in the presence of surface friction. *J. Atmos. Sci.*, **68**, 918–936, doi:10.1175/2010JAS3495.1.
- Strauss, L., S. Serafin, S. Haimov, and V. Grubišić, 2015: Turbulence in breaking mountain waves and atmospheric rotors estimated from airborne in situ and Doppler radar measurements. *Q.J.R. Meteorol. Soc.*, doi:10.1002/qj.2604, in press.
- Vergeiner, I., and D. K. Lilly, 1970: The dynamic structure of lee wave flow as obtained from balloon and airplane observations. *Mon. Wea. Rev.*, **98**, 220–232, doi:10.1175/1520-0493(1970)098<0220:TDSOLW>2.3.CO;2.

- Wang, J., J. Bian, W. O. Brown, H. Cole, V. Grubišić, and K. Young, 2009: Vertical air motion from T-REX radiosonde and dropsonde data. *J. Atmos. Oceanic Technol.*, **26**, 928–942, doi:10.1175/2008JTECHA1240.1.
- Whiteman, C. D., 2000: *Mountain Meteorology. Fundamentals and Applications*. Oxford University Press, 355 pp.
- Whiteman, C. D., and J. C. Doran, 1993: The relationship between overlying synoptic-scale flows and winds within a valley. *J. Appl. Meteor.*, **32**, 1669–1682, doi:10.1175/1520-0450(1993)032<1669:TRBOSS>2.0.CO;2.
- WMO, 1993: Handbook of meteorological forecasting for soaring flight. World Meteorological Organization Tech. Note 495.
- Woods, B. K., and R. B. Smith, 2010: Energy flux and wavelet diagnostics of secondary mountain waves. *J. Atmos. Sci.*, **67**, 3721–3738, doi:10.1175/2010JAS3285.1.
- Zardi, D., and C. D. Whiteman, 2013: Diurnal mountain wind systems. *Mountain Weather Research and Forecasting*, F. K. Chow, S. F. De Wekker, and B. J. Snyder, Eds., Springer Netherlands, 35–119, doi:10.1007/978-94-007-4098-3_2.
- Zhong, S., J. Li, C. D. Whiteman, X. Bian, and W. Yao, 2008: Climatology of high wind events in the Owens Valley, California. *Mon. Wea. Rev.*, **136**, 3536–3552, doi:10.1175/2008MWR2348.1.

LIST OF TABLES

Table 1. Summary of upstream flow characteristics and strength and scales of the downstream flow response for the selected T-REX cases. Letters behind IOP numbers identify IOP sub-periods. Upward- or downward-pointing arrows behind numbers indicate the tendency of a quantity to increase or decrease during the given period. *Mid-level wind speed* refers to the average wind speed in the layer 4000–6000 m MSL. 38

Table 2. Classification of T-REX cases, according to the four scenarios presented in Section 4a and Fig. 16. (*) Documented by De Wekker and Mayor (2009). 39

TABLE 1. Summary of upstream flow characteristics and strength and scales of the downstream flow response for the selected T-REX cases. Letters behind IOP numbers identify IOP sub-periods. Upward- or downward-pointing arrows behind numbers indicate the tendency of a quantity to increase or decrease during the given period. *Mid-level wind speed* refers to the average wind speed in the layer 4000–6000 m MSL.

IOP	1a	4a	6b	6c	13b
Period (UTC, 2006)	1600–2100	1600–2200	1630–2100	0200–0500	0800–1330
	2 March	14 March	25 March	26 March	16 April
Mid-level wind speed (m s^{-1})	25	35	30	35	20
Crest-level potential temperature increase ($\text{K}/500 \text{ m}$)	5.0	5.5	3.0	3.0	2.5
Crest-level stability (N, s^{-1})	0.018	0.019	0.014	0.014	0.012
Wavelength (km)	17	19 \uparrow	16 \uparrow	30 \downarrow	n/a
Crest-level w_{\min} (m s^{-1})	−4.5	−8.5	−10	−6.5	−4
Crest-level w_{\max} (m s^{-1})	+4.5	+6.0	+10	+7.5	+4
Valley inversion height (m MSL)	2700	3200	n/a	n/a	1900
Valley inversion strength ($\Delta\theta, \text{K}/500 \text{ m}$)	5.5	3.5	n/a	n/a	4.0
Maximum strength of up-valley flow (m s^{-1})	17	21	9	n/a	9
Maximum adverse surface pressure gradient (hPa km^{-1})	n/a	0.13	0.14	1.04	0.06

TABLE 2. Classification of T-REX cases, according to the four scenarios presented in Section 4a and Fig. 16.
 (*) Documented by De Wekker and Mayor (2009).

Scenario	T-REX Cases	Date (2006)	Time (UTC)
Elevated turbulence zone (Scenario A)	IOP 1a	2 March	1600–2100
	IOP 2a	5–6 March	2100–0300
	IOP 6a	24–25 March	2100–0300
	IOP 13a	15–16 April	2200–0400
Flow separation at a low-level inversion (Scenario B)	IOP 13b	16 April	0800–1330
	non-IOP	14 April	0830–1230
Turbulent interaction of in-valley westerlies and up-valley flow (Scenario C)	IOP 1b	2–3 March	2130–0200
	IOP 4a	14 March	1600–2200
	IOP 11a	9–10 April	2230–0200
	IOP 13c	16–17 April	2100–0230
Transient mountain waves and rotors (Scenario D)	non-IOP (*)	28 February	2300–n/a
	IOP 3a	9 March	1600–2200
	IOP 6b	25 March	1630–2100
	IOP 6c	26 March	0200–0500

LIST OF FIGURES

- Fig. 1.** Schematic representations of (a) a lee-wave rotor and (b) a hydraulic-jump type rotor. (a) The “low-level turbulent zone” (LTZ), reproduced from Lester and Fingerhut (1974, their Fig. 1): “Idealized cross section of the LTZ: A, lenticular clouds; B, cap cloud; C, reversed rotor; D, region of gusty surface winds; E, region of strong updraft and extreme turbulence; F, rotor or roll cloud; G, region of strong downdraft and severe turbulence; H, lower portion of rotor circulation and occasionally reversed surface winds.” (b) Hydraulic airflow over a mountain ridge: supercritical downslope flow over the lee slope and hydraulic jump-like adjustment to the subcritical regime further downwind with a large rotor forming under the jump. Reproduced from Lester and Fingerhut (1974, their Fig. 10d). (Copyright 1974 American Meteorological Society. Used with permission.) 44
- Fig. 2.** Topographic maps of California’s Central Valley, the Sierra Nevada, Owens Valley and the Inyo and White Mountains. Locations of towns, sounding launch sites, and T-REX ground-based instruments are indicated with markers. Abbreviations OAK, VBG, FRE, MAD, VIS, LEM, BISH, IND, LONE stand for, respectively, Oakland, Vandenberg, Madera, Fresno, Visalia, Lemoore, Bishop, Independence, and Lone Pine. In (b), aircraft mean tracks, along which vertical cross-sections are shown in Figs. 5, 9, 13, and 19, are indicated with solid black lines. Roman numerals stand for flight tracks during IOP 1a (I), IOP 3a (II), and IOPs 4a, 6b-c, and 13c (III). In (c), the Kearsarge and Sawmill Passes are abbreviated as KP and SP, respectively. 45
- Fig. 3.** ECMWF 700-hPa analyses from (a) 1800 UTC 2 March (IOP 1a), (b) 0000 UTC 6 March (IOP 2a), (c) 1800 UTC 9 March (IOP 3a), (d) 1800 UTC 14 March (IOP 4a), (e) 1800 UTC 25 March (IOP 6b), and (f) 1800 UTC 16 April 2006 (IOP 13c). 700-hPa geopotential height contours are depicted as thick black lines. Shades of green indicate relative humidity in excess of 50 %. The town of Independence is marked with a red bullet. 46
- Fig. 4.** Upstream (shades of blue) and downstream (shades of red) vertical profiles of wind speed, wind direction, and virtual potential temperature θ_v for the six IOPs with strong mountain-wave activity. Horizontal black lines mark the altitudes of, from bottom to top, Owens Valley floor (1200 m MSL), Kearsarge Pass (3600 m MSL), and the Sierra Nevada crest (4000 m MSL). 47
- Fig. 5.** Composite vertical cross-section of UWKA in situ measurements made between 1700 and 1930 UTC 2 March 2006 (IOP 1a) along a cross-valley track (Fig. 2b). (a) vertical velocity, (b) interpolated vertical velocity, (c) horizontal wind speed, (d) wind direction, (e) energy-dissipation rate to the power of one third (EDR). The Sierra Nevada range is located to the left (west), the Inyo Mountains to the right (east). Distance is upwind (< 0) or downwind (> 0) of the valley axis, which runs through the town of Independence. 48
- Fig. 6.** 3D representation of a DLR lidar RHI-80 scan of radial velocity at around 1115 UTC 16 April (IOP 13b) and a PPI-06 scan about 10 min earlier. The view is to the north, with the Sierra Nevada to the west and the Inyo Mountains to the east. In the lidar scans, cool colors (blue to green) and warm colors (yellow to red) indicate, respectively, motion towards and away from the lidar (see Fig. 7 for a color bar). Range indicators are drawn every 2 km. The elevation exaggeration factor is 2. Data from the ISS2, MISS, and MAPR wind profilers are shown as three-dimensional wind vectors in vertical columns. Color shades correspond to vertical motion (red upward, gray zero, blue downward). Wind measurements by DRI and UL AWS are shown as flat, black triangles. The curved black line corresponds to the trajectory of the radiosonde launched at 1100 UTC southeast of Independence, exhibiting a

- temporary descent suggestive of enhanced downward motion. (Map data: Google, Landsat, SIO, NOAA, U.S. Navy, NGA, GEBCO) 49
- Fig. 7.** Three consecutive DLR lidar RHI-80 scans of radial velocity (v_r , left panels) and Doppler spectral width (σ_{v_r} , right panels), carried out at (a,b) 1232 UTC, (c,d) 1234 UTC, and (e,f) 1235 UTC 16 April 2006 (IOP 13b). The spectral width is given in arbitrary units (a. u.). The Sierra Nevada lee slopes are to the left, flow is from the left. The apparent flow away from the lidar to its west at low levels (shades of yellow) is a result of the projection of up-valley flow vectors on the lidar RHI-80 scan plane. Vertical arrows point to developing short-wave features along the directionally sheared interface between the strong downslope and the up-valley flows, reminiscent of Kelvin-Helmholtz billows. 50
- Fig. 8.** Same as Fig. 4f but for the period of nighttime flow separation (IOP 13b). Vertical arrows in the rightmost panel point to the maximum level of intrusion of upstream air into Owens Valley. Note that the downstream θ_v profile between gap and crest level (3500–4200 m MSL, black crosses) is affected by dominant horizontal advection and a temporary re-descent of the radiosonde over the eastern portion of the valley and should thus be interpreted with caution. 51
- Fig. 9.** Composite vertical cross-section of data from UWKA and Wyoming Cloud Radar (WCR) made between 1700 and 2000 UTC 14 March (IOP 4a). WCR data from a leg at around 1955 UTC is included in panels (a–c). Radar returns are from the cap cloud over the Sierra Nevada, which spills over into Owens Valley. Arrows 1 and 2 point in panel (e) point to regions of moderate to severe turbulence over the valley. The dashed line in panels (d) and (e) indicates another region of strong turbulence, located at the directionally sheared interface between the in-valley westerlies and strong up-valley flow. See discussion in the text. 52
- Fig. 10.** DLR lidar RHI and PPI scans conducted at around 1925 UTC (left panels) and 2025 UTC (right panels) on 14 March 2006 (IOP 4a). Panels from top to bottom show RHI-80 scans of aerosol backscatter, radial Doppler velocity, and spectral width, and PPI-20 scans of radial Doppler velocity. PPI-20 panels are overlaid with 5-min surface winds, measured by the DRI and UL AWS. Aerosol backscatter and spectral width are given in arbitrary units (a. u.). The origin of the horizontal coordinate axis corresponds to the lidar site, located about 2 km west of Independence. 53
- Fig. 11.** Same as Fig. 10 but for approx. 2155 UTC on 14 March 2006 (IOP 4a). 54
- Fig. 12.** Photograph taken near the DLR lidar site (~ 2 km west of Independence) at around 2130 UTC 14 March 2006 (IOP 4a). The view is along the valley axis to the south-southeast, i.e., flow is from the right to the left. Upper-case labels mark the terrain features, including the lee slope of the Sierra Nevada (SN), the Alabama Hills (AH), and the upwind slope of the Inyo Mountains (IM). Lower-case letters point to cloud features: (a) “spilling-over” cap cloud over the Sierra Nevada, (b) dust cloud over the eastern part of the valley, (c) line of roll clouds, and (d) wave clouds. Compare the position of the dust and roll clouds with the location of the boundary between westerly and up-valley flow in the PPI-20 lidar scans (Fig. 10, right panels). (Photo courtesy: Andreas Dörnbrack and Martin Weissmann.) 55
- Fig. 13.** Composite vertical cross-sections of UWKA and BAe-146 in situ measurements during IOP 6. Measurements were made between 1625 UTC and 1850 UTC 25 March (IOP 6b, left panels) and between 2315 UTC 25 March and 0020 UTC 26 March (prior to IOP 6c, right panels) along flight tracks crossing Independence (Fig. 2b). In (e), data has been inter-

- polated separately for the UWKA and BAe-146 flights to account for the temporal changes in the wave field. 56
- Fig. 14.** Time-height Hovmöller diagrams of (a) wind speed and wind direction and (b) vertical velocity measured by the ISS2 wind profiler between 0400 UTC 25 March to 0800 UTC 26 March, covering the transient phases of the IOP 6 windstorm. Vertical dotted lines indicate periods with nonstationary waves and rotors. 57
- Fig. 15.** 3D representation of DLR lidar RHI-80 scans of radial Doppler velocity (left panels) and Doppler spectral width (right panels) at (a,b) 0228 UTC, (c,d) 0238 UTC, and (e,f) 0328 UTC 26 March 2006 (IOP 6c). Color maps are available from Fig. 10f,g. Range indicators are drawn every 2 km. Data from the ISS2 and MAPR wind profilers is shown as three-dimensional wind vectors in vertical columns. Vector color refers to vertical motion (blue downward). Wind measurements by DRI and UL AWS are shown as flat, dark gray triangles. The elevation exaggeration is 2. (Map data: Google, Landsat, SIO, NOAA, U.S. Navy, NGA, GEBCO) 58
- Fig. 16.** Schematic diagrams of four different classes of cases of wave formation and low-level turbulence generation in Owens Valley. (a) elevated turbulence zone, (b) flow separation at a low-level valley inversion, (c) turbulent interaction of in-valley westerlies with along-valley flows, (d) transient mountain waves and rotors. Flow is from the left. The lower gray-shaded terrain indicates the presence of a mountain pass. Green solid and dashed lines depict streamlines of the flow in laminar and turbulent flow regions, respectively. Red turbulence symbols and eddies mark regions of moderate and severe turbulence and mixing. The cap cloud over the Sierra Nevada is indicated with gray eddies and delimited by a dashed gray line. Beyond cap clouds, roll clouds and lenticular wave clouds are frequently present in the wave crests over the valley; here, they are omitted for clarity. In the valley, blue solid and dashed lines stand for isentropes in undisturbed and perturbed regions, respectively. Up-valley flow is indicated by “into-the-page” circular symbols. In (d), arrows pointing left and right illustrate the movement of the wave and rotor. 59
- Fig. 17.** Idealized upstream and downstream vertical profiles (in shades of blue and red, respectively) of wind speed, wind direction and potential temperature, corresponding to the four different scenarios discussed in Section 4a and delineated schematically in Fig. 16. (a) Upstream prefrontal environment and downstream weak, inversion-capped up-valley flow, (b) upstream prefrontal environment and downstream nighttime cold pool, (c) upstream prefrontal to frontal environment and downstream daytime mixed valley atmosphere, (d) transient upstream and downstream frontal to postfrontal environment. In (d), labels 1–3 loosely refer to successive stages of frontal passage across the Sierra Nevada and Owens Valley, the last stage representing incipient postfrontal conditions. The three dotted horizontal lines indicate, from bottom to top, the approximate altitude of Owens Valley floor, Kearsarge Pass and the Sierra Nevada crest level. 60
- Fig. 18.** Hovmöller diagrams of the temporal evolution of surface flow and pressure perturbations across DRI AWS array 1–6 (Fig. 2c) for several IOPs. Periods with rotors or rotor-like turbulent structures in Owens Valley are delimited by black horizontal lines. Time is positive upward. The time and location of the maximum adverse pressure gradient force within each period is indicated by a black triangle. Maximum gradients are (a) 0.06, (b) 0.13, (c) 0.08, (d) 0.22, (e) 0.14, and (f) 1.04 hPa km⁻¹. Pressure perturbations were computed as follows: 10-min mean station pressures were reduced to the height of the lowest station using the hypsometric equation; perturbations were obtained as deviations from the mean of reduced pressures for every 10-min interval. 61

Fig. 19. Composite vertical cross-sections of UWKA and BAe-146 in situ measurements of flight-level pressure perturbations from flights during (a) 1700–1930 UTC 9 March (IOP 3a), (b) 1700–1930 UTC 14 March (IOP 4a), (c) 1630–1845 UTC 25 March (IOP 6b), and (d) 2215–0015 UTC 16–17 April (IOP 13c). Pressure perturbations were computed as follows: flight-level pressure measurements were corrected for hydrostatic variations due to deviations from the aircraft mean altitude; pressure perturbations were obtained from the corrected pressures after linear detrending (cf. Woods and Smith 2010). 62

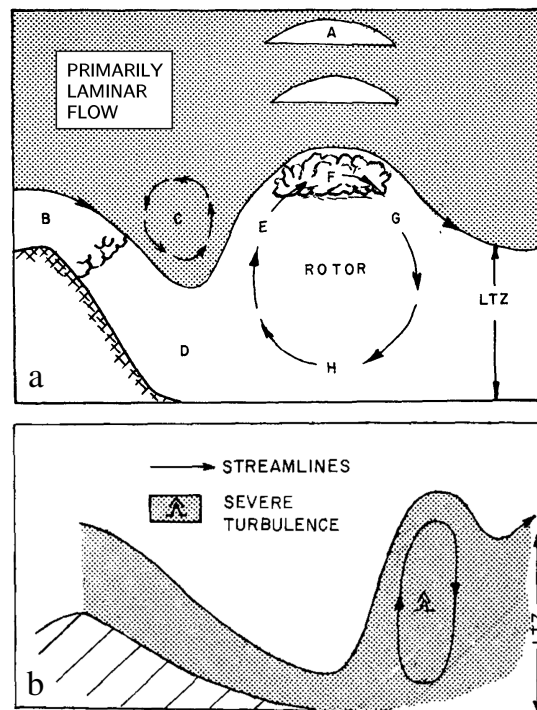


FIG. 1. Schematic representations of (a) a lee-wave rotor and (b) a hydraulic-jump type rotor. (a) The “low-level turbulent zone” (LTZ), reproduced from Lester and Fingerhut (1974, their Fig. 1): “Idealized cross section of the LTZ: A, lenticular clouds; B, cap cloud; C, reversed rotor; D, region of gusty surface winds; E, region of strong updraft and extreme turbulence; F, rotor or roll cloud; G, region of strong downdraft and severe turbulence; H, lower portion of rotor circulation and occasionally reversed surface winds.” (b) Hydraulic airflow over a mountain ridge: supercritical downslope flow over the lee slope and hydraulic jump-like adjustment to the subcritical regime further downwind with a large rotor forming under the jump. Reproduced from Lester and Fingerhut (1974, their Fig. 10d). (Copyright 1974 American Meteorological Society. Used with permission.)

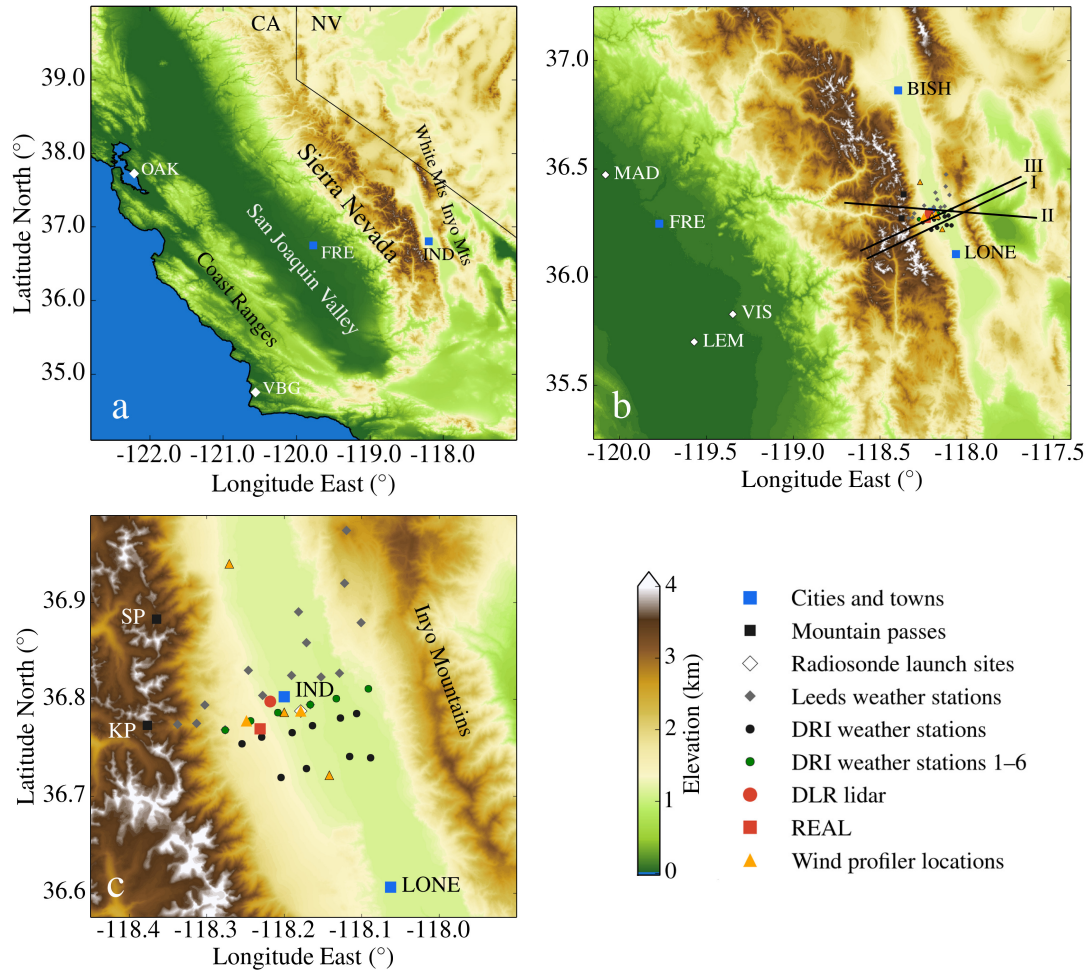


FIG. 2. Topographic maps of California's Central Valley, the Sierra Nevada, Owens Valley and the Inyo and White Mountains. Locations of towns, sounding launch sites, and T-REX ground-based instruments are indicated with markers. Abbreviations OAK, VBG, FRE, MAD, VIS, LEM, BISH, IND, LONE stand for, respectively, Oakland, Vandenberg, Madera, Fresno, Visalia, Lemoore, Bishop, Independence, and Lone Pine. In (b), aircraft mean tracks, along which vertical cross-sections are shown in Figs. 5, 9, 13, and 19, are indicated with solid black lines. Roman numerals stand for flight tracks during IOP 1a (I), IOP 3a (II), and IOPs 4a, 6b-c, and 13c (III). In (c), the Kearsarge and Sawmill Passes are abbreviated as KP and SP, respectively.

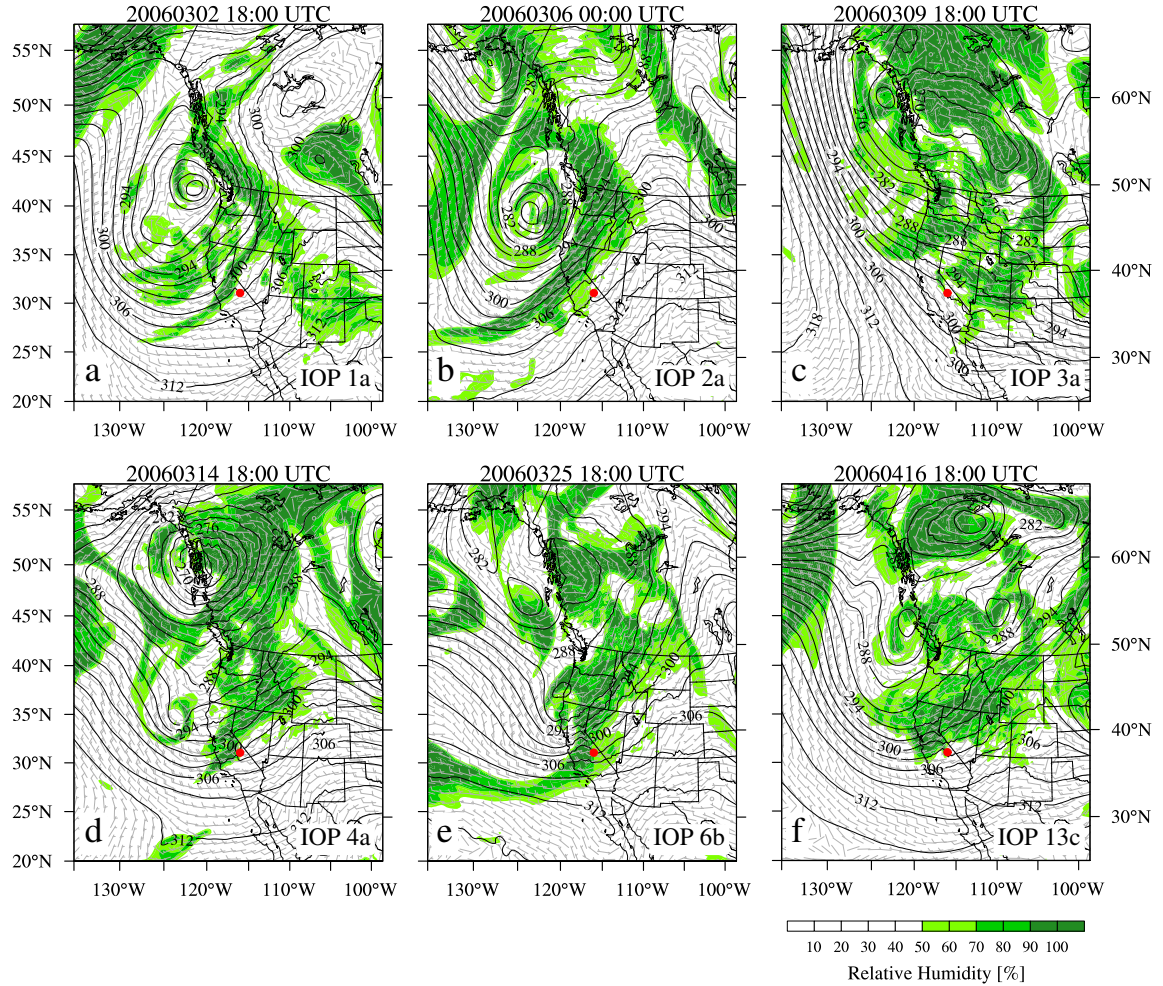


FIG. 3. ECMWF 700-hPa analyses from (a) 1800 UTC 2 March (IOP 1a), (b) 0000 UTC 6 March (IOP 2a), (c) 1800 UTC 9 March (IOP 3a), (d) 1800 UTC 14 March (IOP 4a), (e) 1800 UTC 25 March (IOP 6b), and (f) 1800 UTC 16 April 2006 (IOP 13c). 700-hPa geopotential height contours are depicted as thick black lines. Shades of green indicate relative humidity in excess of 50 %. The town of Independence is marked with a red bullet.

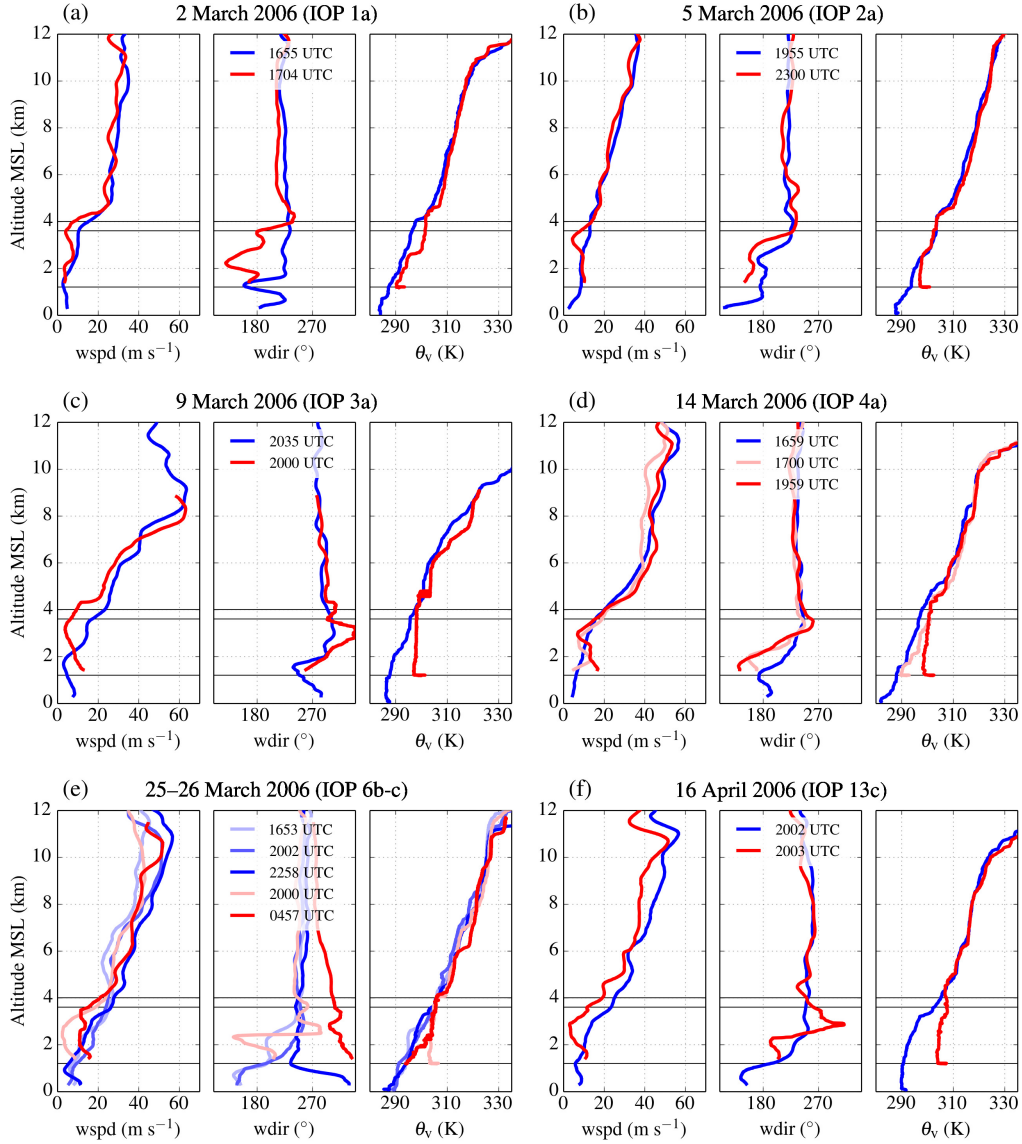


FIG. 4. Upstream (shades of blue) and downstream (shades of red) vertical profiles of wind speed, wind direction, and virtual potential temperature θ_v for the six IOPs with strong mountain-wave activity. Horizontal black lines mark the altitudes of, from bottom to top, Owens Valley floor (1200 m MSL), Kearsarge Pass (3600 m MSL), and the Sierra Nevada crest (4000 m MSL).

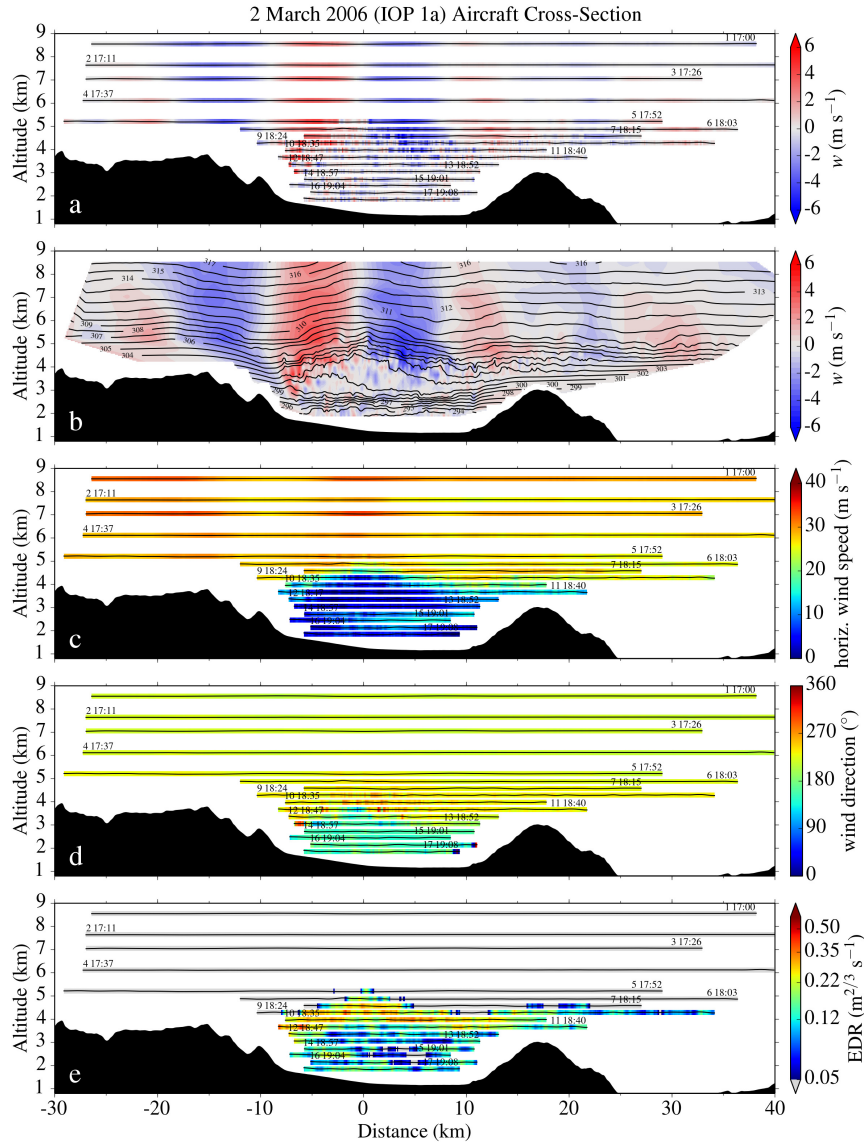


FIG. 5. Composite vertical cross-section of UWKA in situ measurements made between 1700 and 1930 UTC 2 March 2006 (IOP 1a) along a cross-valley track (Fig. 2b). (a) vertical velocity, (b) interpolated vertical velocity, (c) horizontal wind speed, (d) wind direction, (e) energy-dissipation rate to the power of one third (EDR). The Sierra Nevada range is located to the left (west), the Inyo Mountains to the right (east). Distance is upwind (< 0) or downwind (> 0) of the valley axis, which runs through the town of Independence.

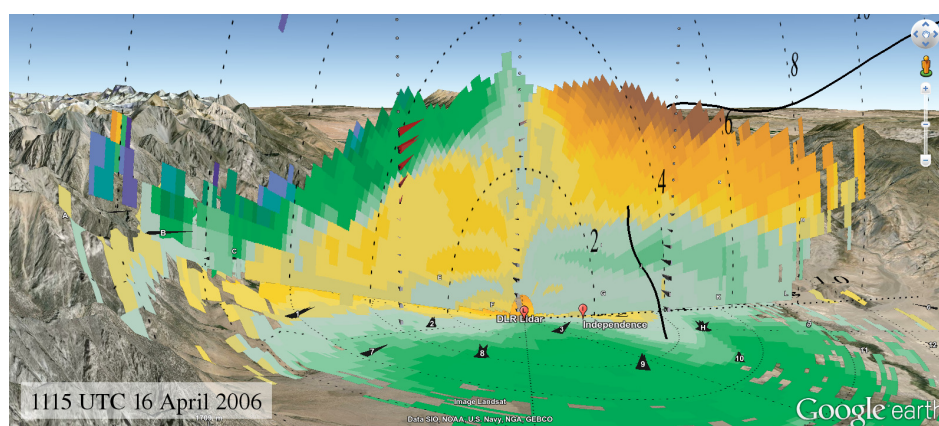


FIG. 6. 3D representation of a DLR lidar RHI-80 scan of radial velocity at around 1115 UTC 16 April (IOP 13b) and a PPI-06 scan about 10 min earlier. The view is to the north, with the Sierra Nevada to the west and the Inyo Mountains to the east. In the lidar scans, cool colors (blue to green) and warm colors (yellow to red) indicate, respectively, motion towards and away from the lidar (see Fig. 7 for a color bar). Range indicators are drawn every 2 km. The elevation exaggeration factor is 2. Data from the ISS2, MISS, and MAPR wind profilers are shown as three-dimensional wind vectors in vertical columns. Color shades correspond to vertical motion (red upward, gray zero, blue downward). Wind measurements by DRI and UL AWS are shown as flat, black triangles. The curved black line corresponds to the trajectory of the radiosonde launched at 1100 UTC southeast of Independence, exhibiting a temporary descent suggestive of enhanced downward motion. (Map data: Google, Landsat, SIO, NOAA, U.S. Navy, NGA, GEBCO)

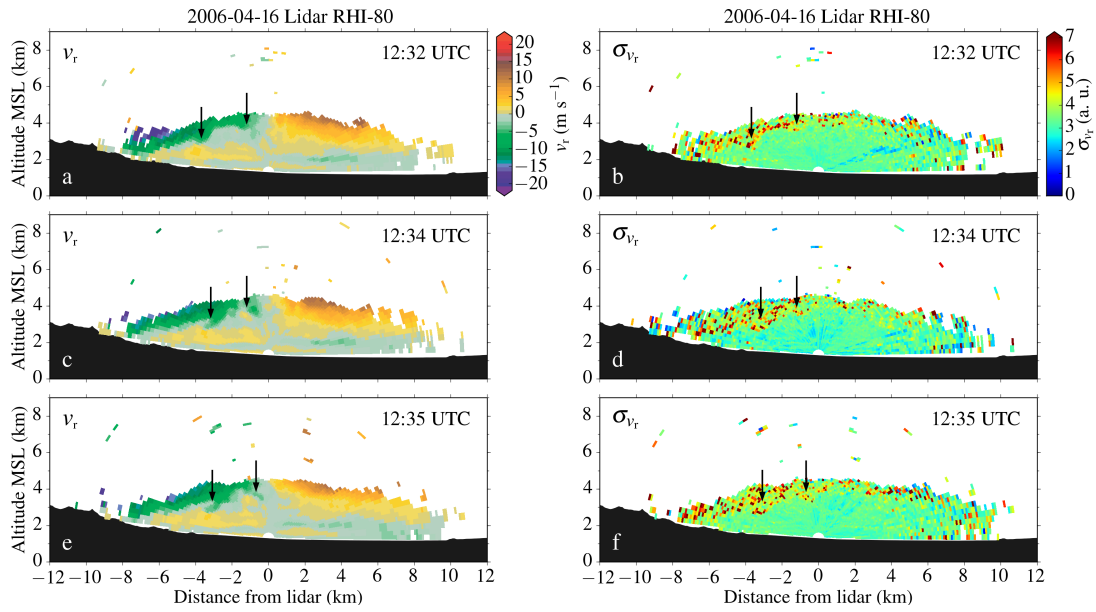


FIG. 7. Three consecutive DLR lidar RHI-80 scans of radial velocity (v_r , left panels) and Doppler spectral width (σ_{v_r} , right panels), carried out at (a,b) 12:32 UTC, (c,d) 12:34 UTC, and (e,f) 12:35 UTC 16 April 2006 (IOP 13b). The spectral width is given in arbitrary units (a. u.). The Sierra Nevada lee slopes are to the left, flow is from the left. The apparent flow away from the lidar to its west at low levels (shades of yellow) is a result of the projection of up-valley flow vectors on the lidar RHI-80 scan plane. Vertical arrows point to developing short-wave features along the directionally sheared interface between the strong downslope and the up-valley flows, reminiscent of Kelvin-Helmholtz billows.

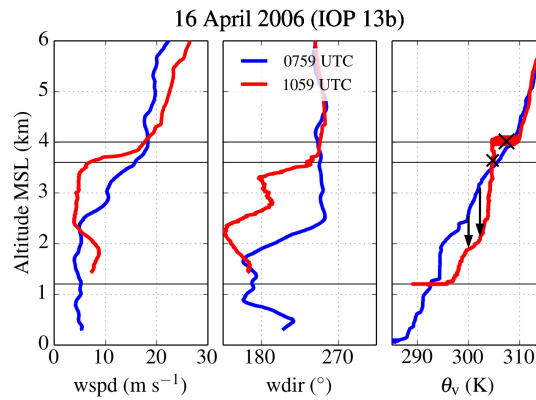


FIG. 8. Same as Fig. 4f but for the period of nighttime flow separation (IOP 13b). Vertical arrows in the rightmost panel point to the maximum level of intrusion of upstream air into Owens Valley. Note that the downstream θ_v profile between gap and crest level (3500–4200 m MSL, black crosses) is affected by dominant horizontal advection and a temporary re-descent of the radiosonde over the eastern portion of the valley and should thus be interpreted with caution.

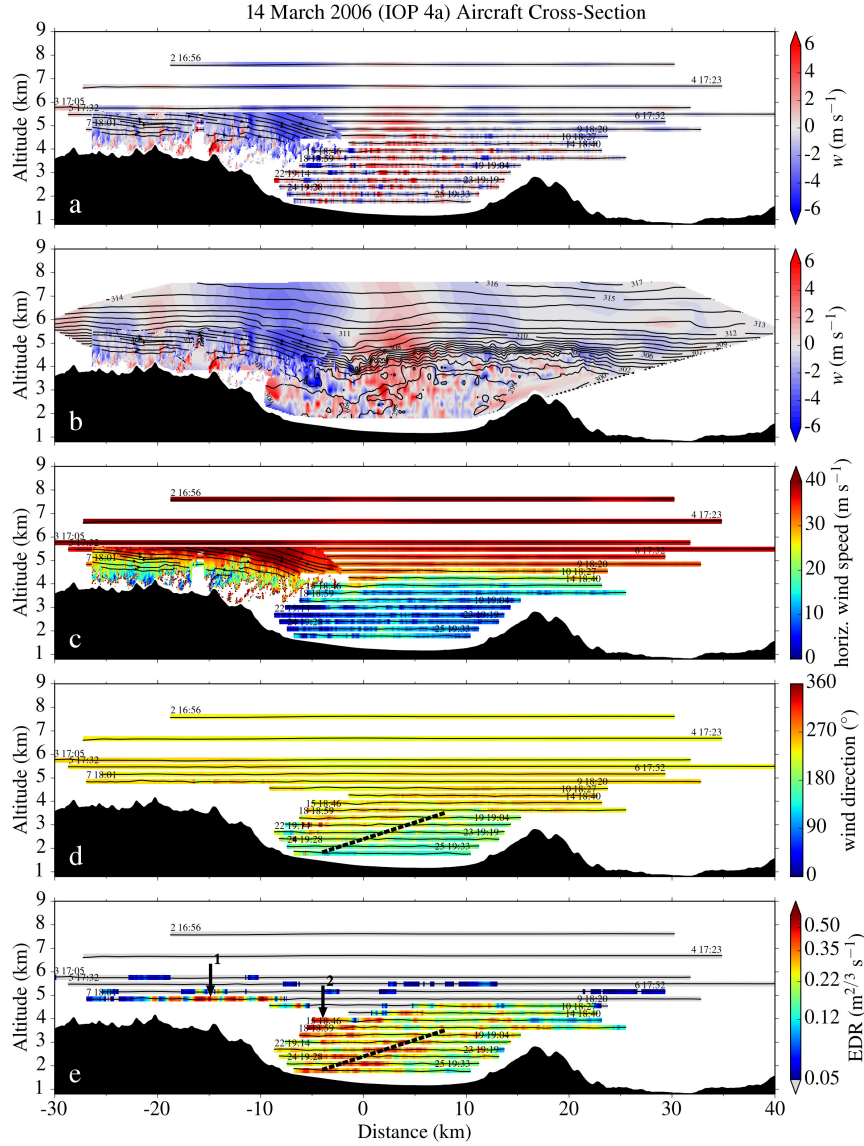


FIG. 9. Composite vertical cross-section of data from UWKA and Wyoming Cloud Radar (WCR) made between 1700 and 2000 UTC 14 March (IOP 4a). WCR data from a leg at around 1955 UTC is included in panels (a-c). Radar returns are from the cap cloud over the Sierra Nevada, which spills over into Owens Valley. Arrows 1 and 2 point in panel (e) point to regions of moderate to severe turbulence over the valley. The dashed line in panels (d) and (e) indicates another region of strong turbulence, located at the directionally sheared interface between the in-valley westerlies and strong up-valley flow. See discussion in the text.

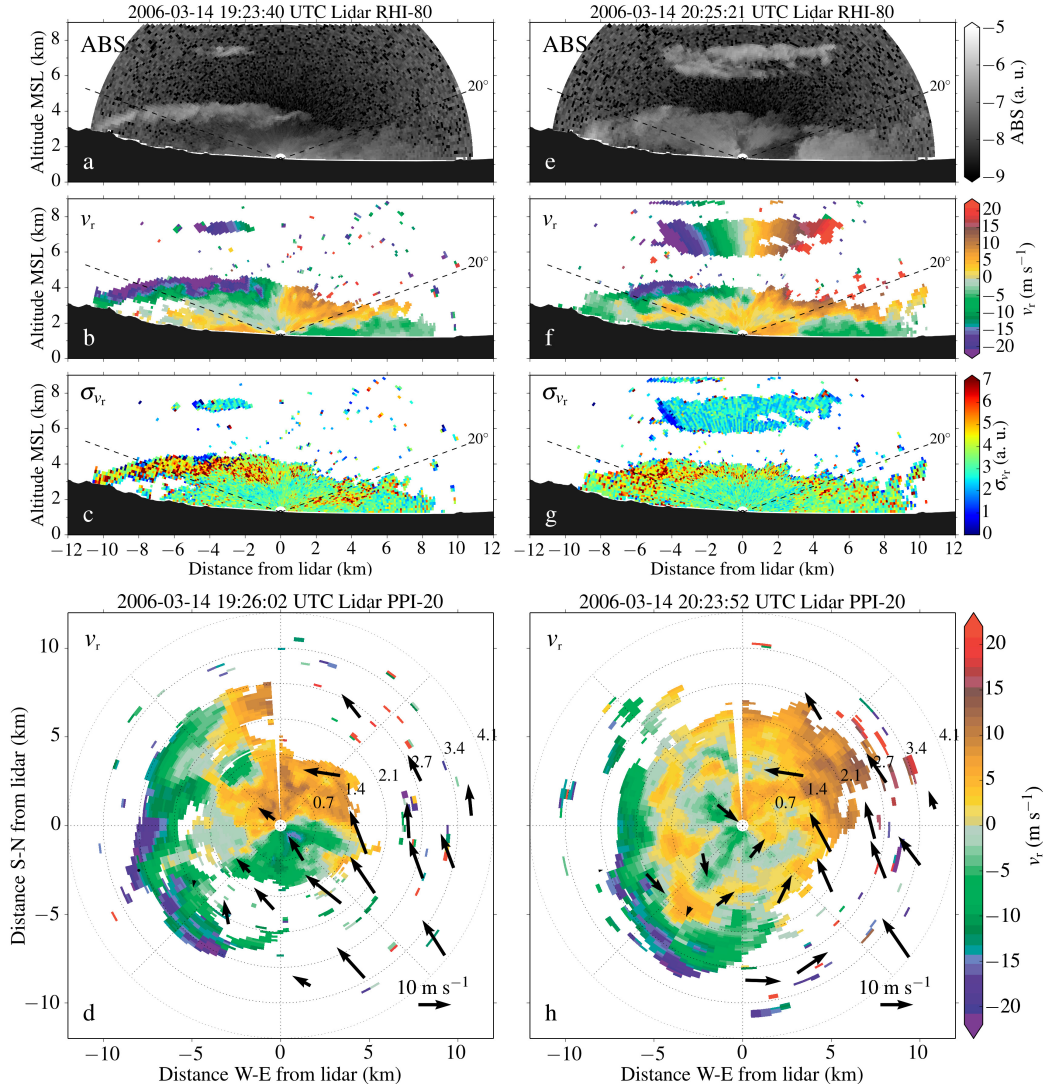


FIG. 10. DLR lidar RHI and PPI scans conducted at around 1925 UTC (left panels) and 2025 UTC (right panels) on 14 March 2006 (IOP 4a). Panels from top to bottom show RHI-80 scans of aerosol backscatter, radial Doppler velocity, and spectral width, and PPI-20 scans of radial Doppler velocity. PPI-20 panels are overlaid with 5-min surface winds, measured by the DRI and UL AWS. Aerosol backscatter and spectral width are given in arbitrary units (a. u.). The origin of the horizontal coordinate axis corresponds to the lidar site, located about 2 km west of Independence.

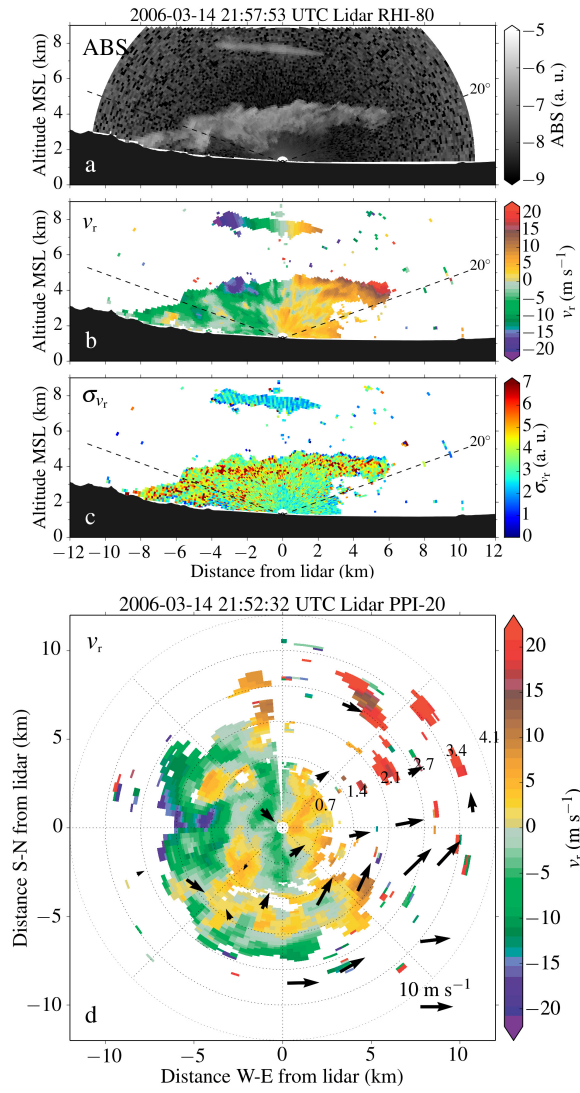


FIG. 11. Same as Fig. 10 but for approx. 2155 UTC on 14 March 2006 (IOP 4a).



FIG. 12. Photograph taken near the DLR lidar site (~ 2 km west of Independence) at around 2130 UTC 14 March 2006 (IOP 4a). The view is along the valley axis to the south-southeast, i.e., flow is from the right to the left. Upper-case labels mark the terrain features, including the lee slope of the Sierra Nevada (SN), the Alabama Hills (AH), and the upwind slope of the Inyo Mountains (IM). Lower-case letters point to cloud features: (a) “spilling-over” cap cloud over the Sierra Nevada, (b) dust cloud over the eastern part of the valley, (c) line of roll clouds, and (d) wave clouds. Compare the position of the dust and roll clouds with the location of the boundary between westerly and up-valley flow in the PPI-20 lidar scans (Fig. 10, right panels). (Photo courtesy: Andreas Dörnbrack and Martin Weissmann.)

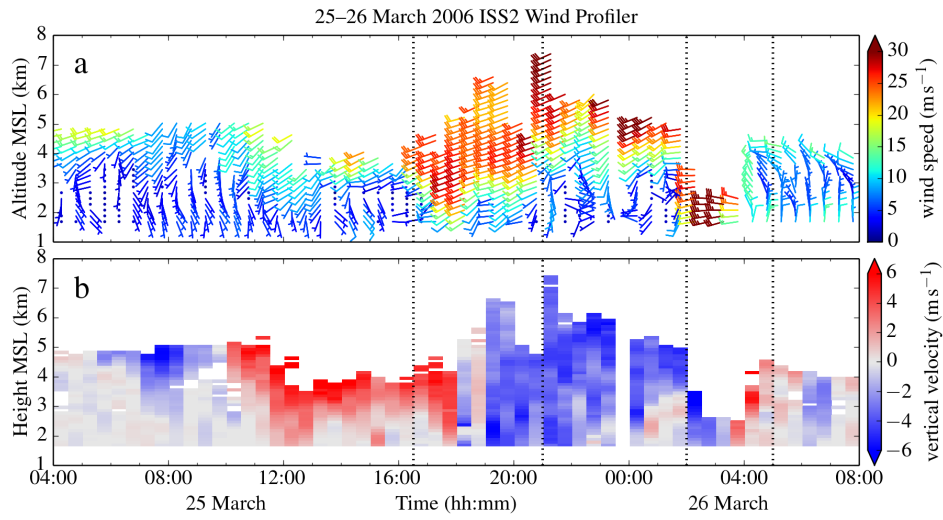


FIG. 14. Time-height Hovmöller diagrams of (a) wind speed and wind direction and (b) vertical velocity measured by the ISS2 wind profiler between 0400 UTC 25 March to 0800 UTC 26 March, covering the transient phases of the IOP 6 windstorm. Vertical dotted lines indicate periods with nonstationary waves and rotors.

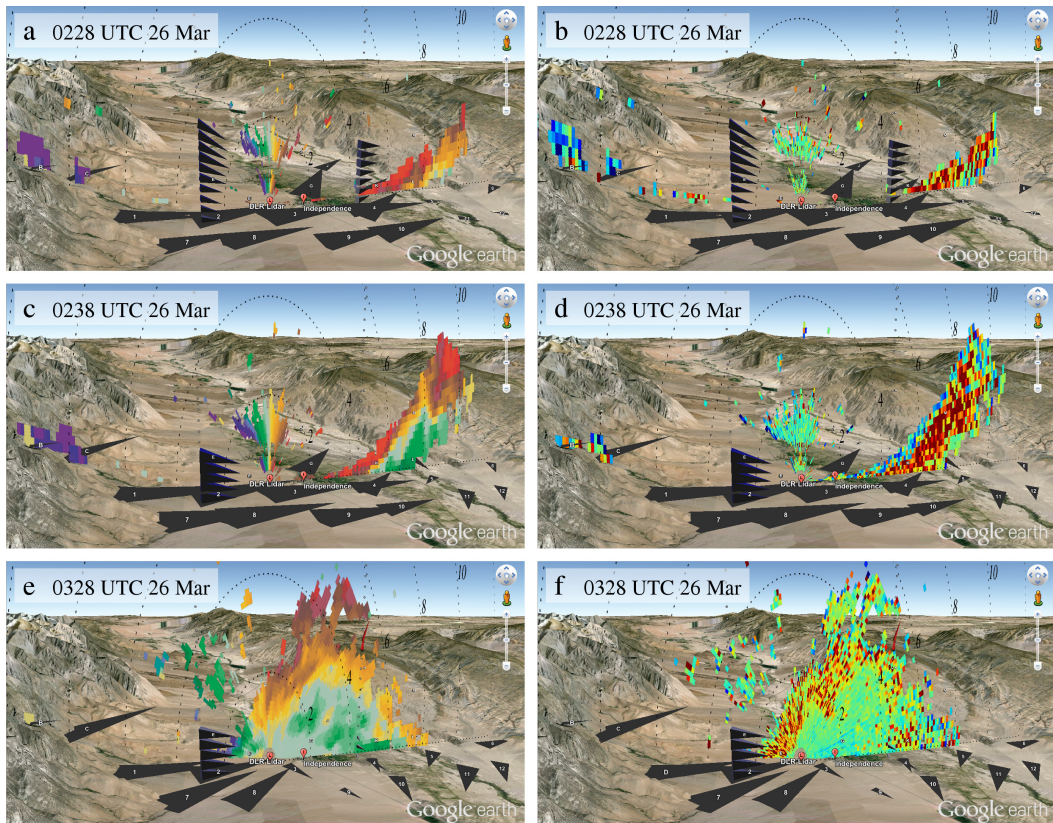


FIG. 15. 3D representation of DLR lidar RHI-80 scans of radial Doppler velocity (left panels) and Doppler spectral width (right panels) at (a,b) 0228 UTC, (c,d) 0238 UTC, and (e,f) 0328 UTC 26 March 2006 (IOP 6c). Color maps are available from Fig. 10f,g. Range indicators are drawn every 2 km. Data from the ISS2 and MAPR wind profilers is shown as three-dimensional wind vectors in vertical columns. Vector color refers to vertical motion (blue downward). Wind measurements by DRI and UL AWS are shown as flat, dark gray triangles. The elevation exaggeration is 2. (Map data: Google, Landsat, SIO, NOAA, U.S. Navy, NGA, GEBCO)

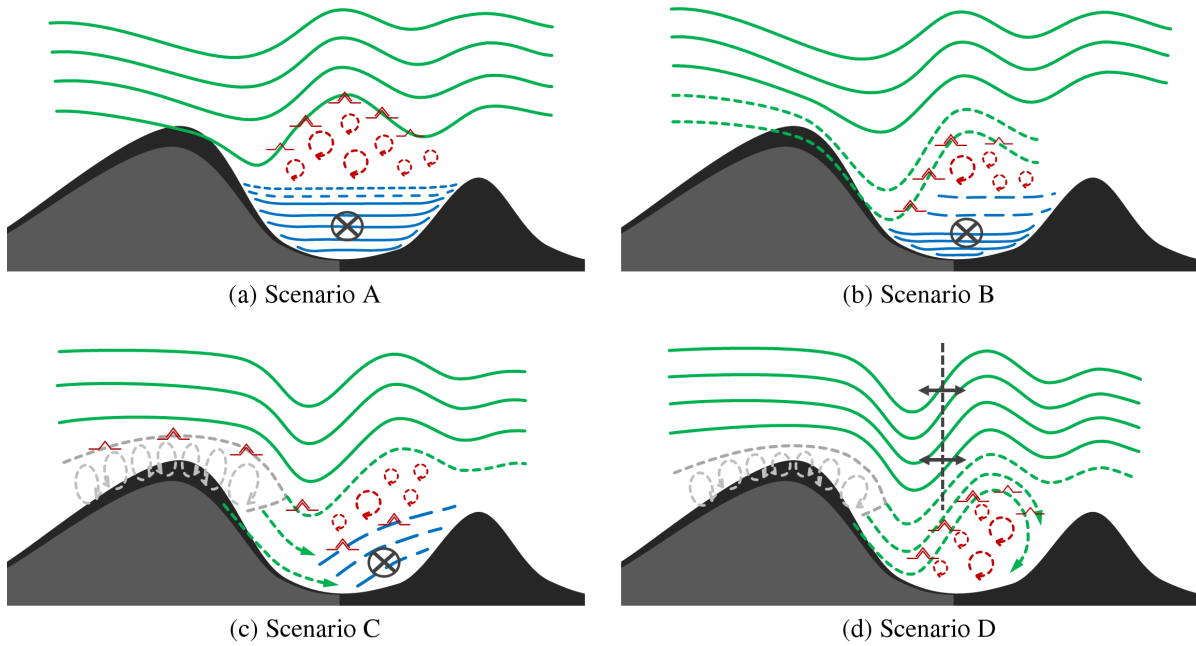


FIG. 16. Schematic diagrams of four different classes of cases of wave formation and low-level turbulence generation in Owens Valley. (a) elevated turbulence zone, (b) flow separation at a low-level valley inversion, (c) turbulent interaction of in-valley westerlies with along-valley flows, (d) transient mountain waves and rotors. Flow is from the left. The lower gray-shaded terrain indicates the presence of a mountain pass. Green solid and dashed lines depict streamlines of the flow in laminar and turbulent flow regions, respectively. Red turbulence symbols and eddies mark regions of moderate and severe turbulence and mixing. The cap cloud over the Sierra Nevada is indicated with gray eddies and delimited by a dashed gray line. Beyond cap clouds, roll clouds and lenticular wave clouds are frequently present in the wave crests over the valley; here, they are omitted for clarity. In the valley, blue solid and dashed lines stand for isentropes in undisturbed and perturbed regions, respectively. Up-valley flow is indicated by “into-the-page” circular symbols. In (d), arrows pointing left and right illustrate the movement of the wave and rotor.

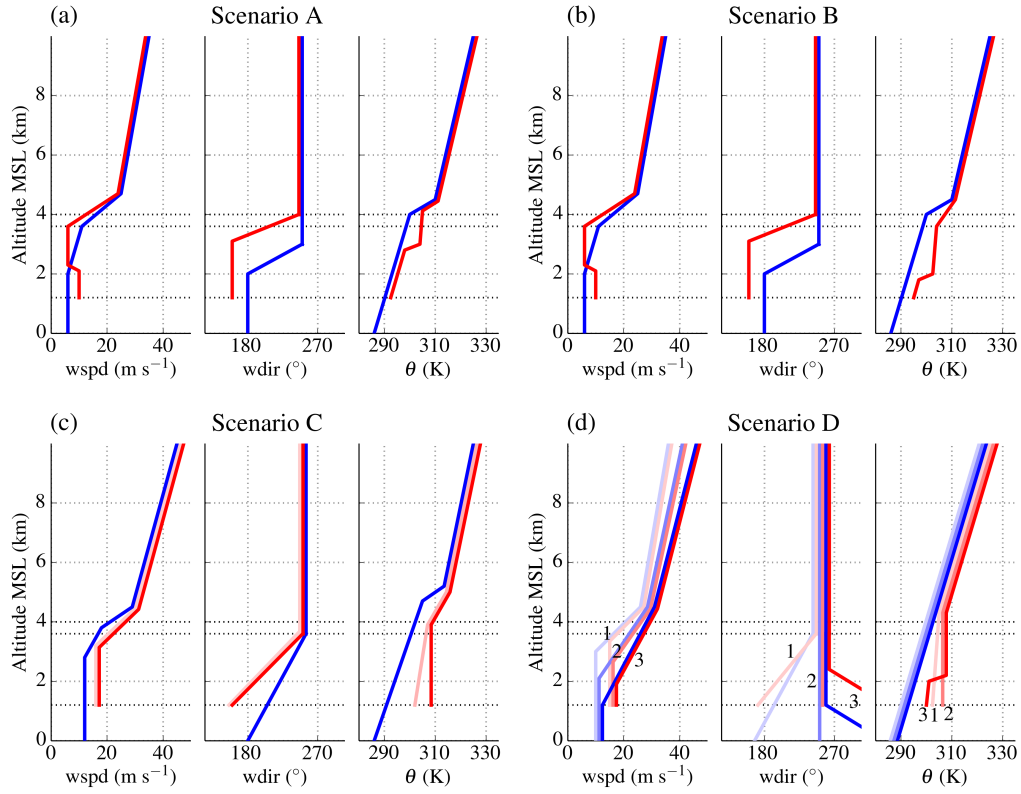


FIG. 17. Idealized upstream and downstream vertical profiles (in shades of blue and red, respectively) of wind speed, wind direction and potential temperature, corresponding to the four different scenarios discussed in Section 4a and delineated schematically in Fig. 16. (a) Upstream prefrontal environment and downstream weak, inversion-capped up-valley flow, (b) upstream prefrontal environment and downstream nighttime cold pool, (c) upstream prefrontal to frontal environment and downstream daytime mixed valley atmosphere, (d) transient upstream and downstream frontal to postfrontal environment. In (d), labels 1–3 loosely refer to successive stages of frontal passage across the Sierra Nevada and Owens Valley, the last stage representing incipient postfrontal conditions. The three dotted horizontal lines indicate, from bottom to top, the approximate altitude of Owens Valley floor, Kearsarge Pass and the Sierra Nevada crest level.

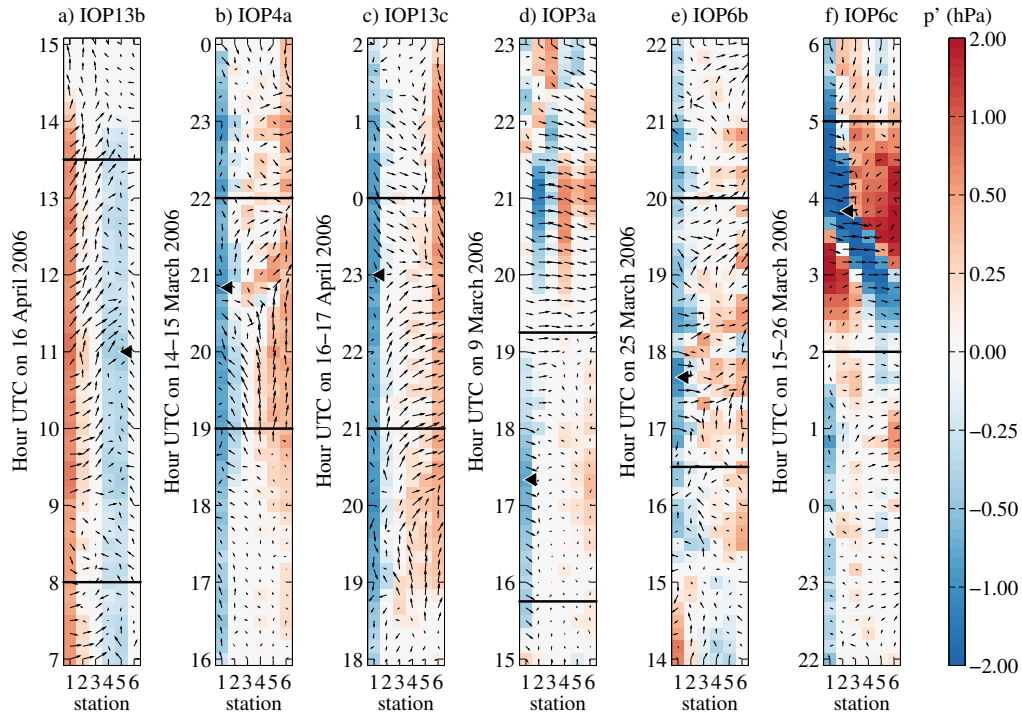


FIG. 18. Hovmöller diagrams of the temporal evolution of surface flow and pressure perturbations across DRI AWS array 1–6 (Fig. 2c) for several IOPs. Periods with rotors or rotor-like turbulent structures in Owens Valley are delimited by black horizontal lines. Time is positive upward. The time and location of the maximum adverse pressure gradient force within each period is indicated by a black triangle. Maximum gradients are (a) 0.06, (b) 0.13, (c) 0.08, (d) 0.22, (e) 0.14, and (f) 1.04 hPa km^{-1} . Pressure perturbations were computed as follows: 10-min mean station pressures were reduced to the height of the lowest station using the hypsometric equation; perturbations were obtained as deviations from the mean of reduced pressures for every 10-min interval.

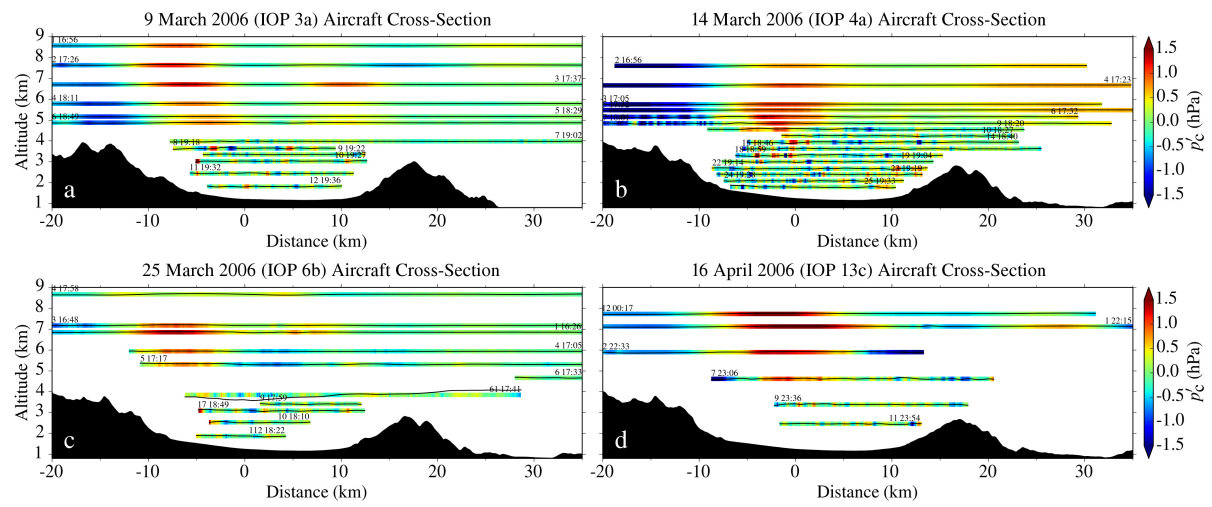


FIG. 19. Composite vertical cross-sections of UWKA and BAe-146 in situ measurements of flight-level pressure perturbations from flights during (a) 1700–1930 UTC 9 March (IOP 3a), (b) 1700–1930 UTC 14 March (IOP 4a), (c) 1630–1845 UTC 25 March (IOP 6b), and (d) 2215–0015 UTC 16–17 April (IOP 13c). Pressure perturbations were computed as follows: flight-level pressure measurements were corrected for hydrostatic variations due to deviations from the aircraft mean altitude; pressure perturbations were obtained from the corrected pressures after linear detrending (cf. Woods and Smith 2010).

Chapter 5

Conclusions

In this thesis, observations of large-amplitude mountain waves, wave breaking, atmospheric rotors and associated low-level turbulence have been analysed and reproduced using high-resolution numerical simulations. The observations were made during two field campaigns over the Medicine Bow Mountains in southeastern Wyoming and over the southern Sierra Nevada and Owens Valley in California in 2006. Analyses of data from airborne and ground-based in situ and remote sensors have revealed the spatial distribution and intensity of turbulence in the lee of the mountain ranges and their rapid temporal changes in several cases of enhanced mountain-wave activity. Numerical simulations have provided the mesoscale dynamic context for the evolution of two mountain-wave and rotor events and have served to elucidate their observed transient behaviour.

The studies presented in Chapters 2, 3, and 4 represent new contributions to some of the open questions of mountain-wave-induced turbulence and its dependence on time-varying environmental conditions upstream and downstream of a mountain range. In the following section, the main findings are summarized and discussed in the context of previous investigations. Figure 5.1 highlights the most important results. Concluding remarks are given in Section 5.2 and potential for future research is outlined in Section 5.3.

5.1 Summary and discussion

5.1.1 Quantitative estimation of turbulence intensity in complex mountain flows

A new approach to the estimation of turbulence parameters from airborne in situ and high-resolution Doppler radar measurements has been developed in the work by Strauss et al. (2015a), presented in Chapter 3. A method has been devised to derive the variance of vertical velocity (σ_w^2) and the cube root of the energy dissipation rate ($\varepsilon^{1/3}$, or EDR) from measurement data collected by UWKA and WCR. A thorough analysis of the uncertainties of σ_w^2 and EDR related to the Doppler velocity measurement by the airborne radar proves to be essential to guarantee the quality of the method. For σ_w^2 , the two most critical contributors to the

total uncertainty are, first, the relatively poorly determined effect of averaging of the air motion within the radar pulse volume and, second, the contamination of the vertical velocity measurement by the horizontal wind upon deviations of the radar beam from the vertical. For EDR, the measurement uncertainty stems mostly from statistical scatter of Fourier spectral estimates within the inertial subrange and the difficulty of determining the subrange from spectra. Despite these uncertainties, a quantitative estimation of turbulence intensity from the aircraft and radar data, that is, the estimation of turbulence parameters within reasonably small uncertainty levels, has been shown to be possible. For the cases under consideration, the minimum reliable value of σ_w^2 , affected by a relative uncertainty of 25% or less, was found to be $0.5 \text{ m}^2 \text{ s}^{-2}$, while measured values of σ_w^2 in the most turbulent regions of the mountain flow peaked at approx. $16 \text{ m}^2 \text{ s}^{-2}$, allowing turbulence intensity to be measured over a dynamic range of approx. 1.5 decades. These values apply to the radar-derived σ_w^2 , those determined from aircraft in situ measurements have generally much lower uncertainty.

The successful application of the turbulence estimation technique for the analysis of data from the NASA06 campaign underscores the potential of the combined aircraft in situ and Doppler radar measurements for the study of mountain-induced turbulence. The derived turbulence fields offer a quasi-instantaneous two-dimensional picture of the spatial variation of turbulence and its intensity across the mountain range. The analyses of measurements made on 26 January and 5 February 2006 over the Medicine Bow Mountains give rare insights into the turbulence structure in the interior of atmospheric rotors.

A large hydraulic-jump-type rotor was observed on 26 January, extending 5–10 km in the horizontal and up to 3 km in the vertical, more than two times the height of the surrounding mountains. The rotor proportions were strikingly similar to those depicted in schematics of the hydraulic-jump type. Behind the leading updraught of the hydraulic jump, maximum values of σ_w^2 and EDR of, respectively, $16.4 \text{ m}^2 \text{ s}^{-2}$ and $0.77 \text{ m}^{2/3} \text{ s}^{-1}$ indicated most intense turbulence. To the best of our knowledge, comparable quantitative measurements of turbulence in this rotor type date back to the work by Lester and Fingerhut (1974), more than 40 years ago. The results re-emphasize the great aviation hazard associated with jump-type rotors (Holmboe and Klieforth 1957; Kuettner 1959; Kuettner and Hertenstein 2002).

The turbulence analysis of the lee-wave rotor case observed on 5 February 2006 reveals a low-level region of moderate-severe turbulence that is confined below the first lee-wave crest (Fig. 5.1, upper panels). Maximum turbulence of $7.8 \text{ m}^2 \text{ s}^{-2}$ or $0.50 \text{ m}^{2/3} \text{ s}^{-1}$ is located underneath the upwelling branch of the lee wave, in good agreement with previous observations and numerical simulations (Lester and Fingerhut 1974; Doyle and Durran 2002). Data from consecutive cross-mountain flight legs on that day allow to monitor the gradual cessation of turbulence in the rotor upon its weakening and gradual retreat towards the mountaintop.

During both NASA06 wave events, considerable perturbations of the flow were also measured outside the rotor regions. At flight level, localized patches of moderate turbulence above the mountaintop support the idea of mid-level wave breaking. In the lee-wave rotor case, this region was locally distinct from the turbulence at low-levels, as revealed by the combination of turbulence estimates from the in situ and radar measurements (Fig. 5.1, upper

panels). On 5 February, flow disturbances were also found in the immediate lee of the steep Medicine Bow peak, pointing to a salient-edge separation of the boundary layer and resultant turbulence with maximum intensities of $10.3 \text{ m}^2 \text{ s}^{-2}$ and $0.41 \text{ m}^{2/3} \text{ s}^{-1}$.

The results point to the usefulness of the turbulence estimation technique for the remote detection of severe turbulence in the immediate vicinity of mountain slopes and peaks. The peak in rotor turbulence intensity on 5 February was located roughly 300 m above the lee slope of the MBM; the region of salient-edge separation downstream of Medicine Bow Peak was detected within less than 200 m above the surrounding terrain. In addition, the mountain as a whole was immersed in clouds. From an aviation safety perspective, it was out of the question to navigate the research aircraft into the cloud-covered, strongly turbulent regions to collect in situ data.

The success of the remote turbulence measurement technique obviously relies on suitable environmental parameters, in particular, on a sufficient density and suitable distribution of scattering particles detectable by the radar. In the cases under consideration, clouds were populated by a rather homogeneous distribution of ice particles, which contributed to keeping the unwanted variance of hydrometeor fall speed at a minimum. Due to its strong dependence on sufficient cloud coverage, the technique is clearly not suited for the detection of clear-air turbulence, for instance, on commercial aircraft. This deficit, however, does not impair its potential applications to research on terrain-induced turbulence. Measurements by UWKA and WCR in similar environmental conditions continue to be made. Rather recently, low-level turbulence, likely related to rotors, was detected over the Park Range of northern Colorado during the Colorado Airborne Multi-Phase Cloud Study (CAMPS, Kingsmill et al. 2014).

5.1.2 Transient mountain waves, wave breaking, and rotors

The most distinguishing feature of the large-amplitude wave and rotor events during both NASA06 and T-REX was the rapidity at which changes in wave phase, length, and amplitude and accompanying transitions in the near-surface flow occurred. On 26 January 2006, the boundary-layer separation point and the rotor downstream of it retreated 7 km towards the top of the MBM within 30 min (French et al. 2015). On 5 February 2006, a similar upstream movement was less pronounced but still appreciable (5 km in 45 min). On 26 March 2006, the final stages of a severe downslope windstorm in the lee of the Sierra Nevada were accompanied by the formation of a large, quickly evolving rotor. As the windstorm receded to the west towards the mountain lee slopes, the rotor formed at its front in the easternmost part of the valley, reaching a vertical extent of 2.5 km within only 10 minutes. Subsequently, the rotor moved upstream by 6 km within 20 min towards the valley centre, where it stayed for the next 30-40 min and decayed afterwards (Kühnlein et al. 2013).

Real-case high-resolution WRF simulations of the NASA06 events by Grubišić et al. (2015a), presented in Chapter 2, have revealed that the observed unsteadiness of the flow structure owes its origin to a transition in flow regimes. For the 26 January case, the model simulation successfully reproduced the passage of a short-wave synoptic disturbance and

5 Conclusions

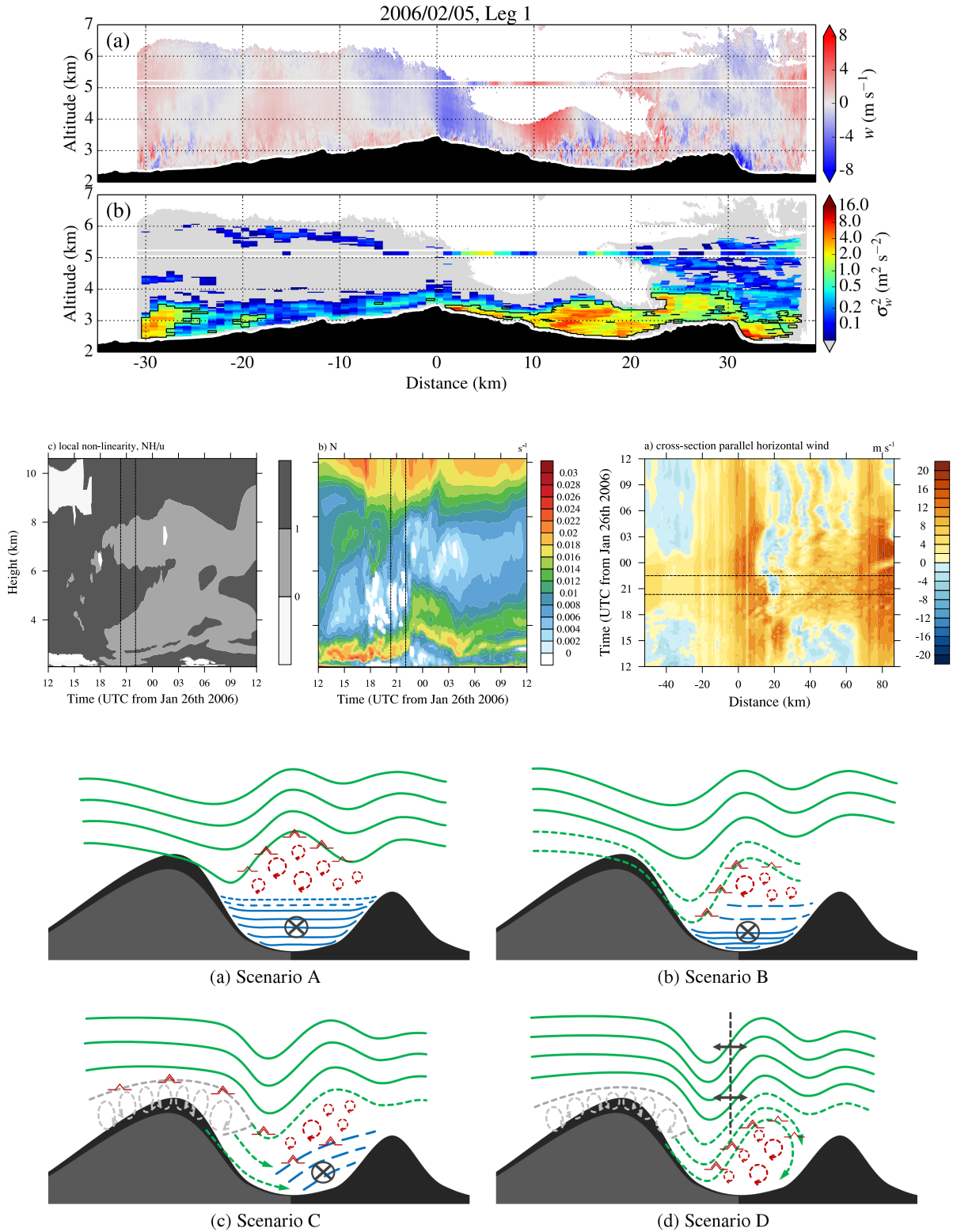


Figure 5.1: Highlights of this work. Upper panels: radar-measured vertical air velocity and derived variance of vertical velocity from UWKA Leg 1 on 5 February 2006, crossing the MBM. Reproduced from Strauss et al. (2015a, their Fig. 10). Middle panels: time-height Hovmöller diagrams of the NLP profile upstream of the MBM and the downstream stability profile on 26 January 2006, and a distance-time Hovmöller diagram of the cross-mountain surface wind speed, revealing the changes in flow regimes. Reproduced from Grubišić et al. (2015a, their Figs. 8, 10, 11). Lower panels: Schematic diagrams of four typical flow scenarios of mountain-wave and low-level turbulence generation in a deep elongated valley. Reproduced from Strauss et al. (2015b, their Fig. 16).

associated short-term changes in the flow response to the MBM. The key to the understanding of the evolution of the event were the temporal variations of the upstream local non-linearity parameter (NLP) $N(z)h/U(z)$ (Fig. 5.1, middle panels). Ahead of the short-wave passage, the upstream NLP grew appreciably larger than unity in a deep layer above the mountain range. Consequently, a large-amplitude hydrostatic mountain wave formed over the MBM, reached its critical steepness and broke, thereby generating a stagnant and almost neutrally stratified region – a self-induced critical level. Below this region, a severe downslope windstorm developed over the lee slope with an undular hydraulic jump farther downstream, triggering boundary-layer separation and rotor formation in the lee. This situation represents an almost prototypical realization of the second type of BLS predicted by Jiang et al. (2007, their Fig. 12). As the synoptic short-wave passed, the mid-level NLP fell below its critical threshold as a consequence of increasing wind speed and decreasing stability in the mid-troposphere. The subsequent transition from an undular hydraulic jump to resonant trapped lee waves caused the BLS point and rotor to shift upstream. The observed change in flow regime was reproduced by the simulation with excellent timing.

For the 5 February case, the attempt to simulate the observed lee-side changes with the numerical model was less successful. The simulation did show the passage of the upper-tropospheric anomaly and the associated changes in the NLP layering, triggering the onset of mid-tropospheric wave breaking and its subsequent cessation. However, the comparison of the model-predicted BLS and rotor with the observations, in terms of their location and the timing of their upstream shift, was poor. The lack of agreement with the observations could be a result of the delay of the passage of the synoptic disturbance in the model simulation or of the inability of the model to produce a realistic layering of the Scorer parameter, responsible for the observed lee waves and rotor during the event.

While no numerical simulation has been conducted for the IOP 6 windstorm event in this work, a hint at the origin of its rapid evolution can be found in Reinecke and Durran (2009). Only those members of their ensemble forecast of the windstorm showing low-level wave breaking reproduced the observed strength of the downslope windstorm. The subsequent evolution of the downslope windstorm has not been discussed by Reinecke and Durran, however, several authors have documented the changes in wave amplitude and wavelength as observed from aircraft measurements and wind profilers (Sheridan and Vosper 2012; Kühnlein et al. 2013; Strauss et al. 2015b). The strong resemblance of the dynamics of the IOP 6 event to that of the NASA06 cases is yet another indication of the close connection of mid-tropospheric wave breaking and the transience of low-level processes.

It appears useful to put our results into the context of previous studies. The unsteadiness of mountain lee waves has been noted since the early systematic observations of wave clouds (e.g., Manley 1945; Förchtgott 1957). Ralph et al. (1997a) gave a concise review of this topic from which some of the following discussion is drawn. Lee-wave non-stationarity has been noted to occur over a range of temporal scales. Changes in wavelength and amplitude on a time scale of several hours or more have early been attributed to the diurnal heating cycle (e.g., Kuettner 1959; Gerbier and Berenger 1961). The resultant changes in the characteristics of

the atmospheric boundary layer have a substantial effect on the position and amplitude of mountain waves and the damping of lee waves, which has only recently been sufficiently clarified (e.g., Jiang et al. 2006; Jiang and Doyle 2008).

On the other hand, a number of authors have reported changes in lee-wave characteristics to occur on time scales of an hour or less (Ralph et al. 1997a, and references therein). Here, the study by Vergeiner and Lilly (1970), using data from balloon and aircraft observations collected during the CLWP to examine the structure of lee waves downwind of the Rocky Mountains, is of interest. The authors noted that lee-side flow patterns occasionally changed from hydraulic-jump-type to lee-wave-type within 1 h. Their main conclusion that “flow pattern[s] can be very sensitive to small changes in the upstream conditions” is supported by the findings of this work.

More recently, observations of transient low-level turbulence similar to those presented here have been made. Using measurements by a scanning Doppler lidar, Clark et al. (1994) documented the presence of an unsteady jump-like structure towards the end of the 9 January 1989 Colorado Front Range windstorm. The jump and the region of reversed flow underneath it rapidly shifted westward towards the foothills by 10 km within less than 40 min. Gohm et al. (2008) investigated the onset phase of a strong Adriatic bora windstorm in the lee of a mountain gap in the Dinaric Alps on 4 April 2002. In their numerical simulation, an initially stationary hydraulic jump at the centre of the gap and lee-wave rotor at the gap edge propagated downstream and gave rise to the bora breakthrough at the coast, in association with the onset of wave breaking at an environmental critical level. Lastly, Stiperski et al. (2012) described the complex bora flow in the lee of southern Velebit during a severe bora episode on 20 December 2004. There, upstream propagating rotors underneath unsteady undular bores were, too, related to low-level wave breaking.

Changes in environmental parameters upstream of a mountain range, however, may not be the sole cause of unsteadiness of the downstream flow response. For instance, Vergeiner and Lilly (1970) also recognized that “many observed changes appear to be too fast and too large to be caused in an accountable way by variation of the basic flow”, which, according to them, supported “previous notions on the possible non-stationarity (non-uniqueness) of the flow over obstacles (Long 1953b)”. More recently, Nance and Durran (1998) shed new light on the mechanisms responsible for lee-wave non-stationarity. Their two-dimensional mountain-wave simulations showed that finite-amplitude lee-wave patterns can exhibit temporal variations in local wavelength and amplitude, even when the background flow is perfectly steady, owing to non-linear wave-wave interactions.

In summary, the transient behaviour of waves and rotors in the specific cases simulated here originated from the synoptic changes in the ambient conditions and the consequent transitions of downstream flow regimes. More generally, however, any occurrence of the above phenomena (wave breaking, flow separation, rotors etc.) must be expected to display a high degree of intrinsic non-stationarity irrespective of the evolution of the upstream environment, owing to their strongly non-linear nature. Clearly, this aspect makes them a very challenging subject for forecasting.

5.1.3 Predictability of mountain-wave-induced turbulence

While the numerical model simulation for the NASA06 26 January case reproduced the BLS and hydraulic-jump-type rotor and their upstream retreat with excellent timing, relatively poor agreement with the observations was obtained for the 5 February case. Specific shortcomings of the simulation in the second case could be the timing error the model might have acquired through the initial conditions from the global analysis and the greater challenge in reproducing correctly the fine vertical structure of the Scorer parameter and its changes with time. Similarly, the real-case modelling attempts by Grubišić and Billings (2007) of the rotor case of SRP IOP 8 and by Sheridan and Vosper (2012) for the downslope windstorm event of T-REX IOP 6 had variable success. This raises the fundamental question of the degree of confidence that should be placed in deterministic model forecasts of strongly non-linear mountain flow phenomena.

The question of predictability of gravity-wave breaking and downslope windstorms has been addressed by a few authors recently. Doyle et al. (2000) compared the results of 11 different non-hydrostatic models initialized with identical upstream profiles corresponding to the conditions during the 11 January 1972 Boulder windstorm. Mid- and upper-level wave breaking was predicted by all models in similar horizontal positions and vertical layers, however, significant differences arose between them regarding the temporal evolution of wave breaking. Also, model results displayed a large sensitivity to slight changes in upper-level upstream conditions, surface friction, or the insertion of realistic three-dimensional topography. Doyle et al. (2007) and Doyle and Reynolds (2008) explored the sensitivity of model-predicted lee-side winds on slightly perturbed upstream conditions, going from linear to strongly non-linear wave regimes by increasing the mountain height. Most interestingly, the growth of initial perturbations in the models was found to be largest at the regime boundary between ordinary lee waves and wave breaking, rather than within the more strongly non-linear breaking regime for the highest mountains. Near this boundary, the ensemble displayed a bimodal response, with one half of the ensemble members exhibiting lee-wave characteristics and the other half producing wave breaking and hydraulic jumps. Reinecke and Durran (2009) extended these studies to a fully three-dimensional model ensemble to examine the initial-condition sensitivity of the windstorm strengths of T-REX IOPs 6 and 13. Initial perturbations grew largest for the simulations of IOP 6 displaying wave breaking, resulting in a large spread of forecast downslope winds, with the mean wind strength computed from the 10 strongest and the 10 weakest members differing by as much as 28 m s^{-1} in the 6 h forecast. An astonishing detail of these studies is that the random perturbations imposed on measured soundings were within the magnitudes typical of radiosonde observational errors. Lastly, Doyle et al. (2011b) renewed their model intercomparison using two-dimensional numerical simulations with an identical initial state based on conditions during T-REX IOP 6. Results showed a strikingly diverse spectrum of simulated mountain-wave characteristics, from smooth lee waves to breaking waves, which was attributed mostly to differences in the model dynamical cores.

Overall, the sensitivities revealed in the above studies suggest that deterministic model forecasts may have great difficulty in accurately predicting the key characteristics of topograph-

ically forced flows, such as the strength of downslope winds or the timing of upper-level wave breaking. Even though the aspect of predictability has not been explicitly addressed in this work, it seems reasonable to transfer these results to the forecasting of low-level turbulence. In this context, yet another contribution to the forecast uncertainty may result from the sensitivity of model-predicted wave amplitudes, windstorm fronts, and rotors to the type and parameter settings of turbulence parametrizations (e.g., Gohm et al. 2008). In this light, the high degree of agreement between the NASA06 26 January event and the deterministic WRF run appears most remarkable, while the poorer agreement for the 5 February 2006 simulation (or for the IOP 6 simulations by Sheridan and Vosper, 2012) seems less puzzling.

5.1.4 Atmospheric rotors in a deep valley

The complexity of turbulent flow patterns in Owens Valley, during periods with enhanced mountain-wave activity as well as during more quiescent episodes, was one of the surprising findings during the T-REX field activities. The observations clearly put into question the idealized conceptual models of the mountain wave-rotor system. Following the experimental phase of T-REX, several authors have examined the flow patterns in Owens Valley during individual T-REX cases (e.g., Armi and Mayr 2011; Cohn et al. 2011; Kühnlein et al. 2013). In the study by Strauss et al. (2015b), presented in Chapter 4, a systematic analysis of the strongest T-REX mountain-wave cases has been carried out with the aim of categorizing the types of rotors and turbulent structures that may form in the complex valley atmosphere.

From the analysed T-REX IOPs 1, 2, 3, 4, 6, and 13, four distinct cases have been selected, representing different flow scenarios in Owens Valley. The scenarios depend crucially on the combination of the characteristics of the upstream and downstream environments. In the cases under consideration, the former was typically characterized by the approach and passage of a frontal system over the Sierra Nevada. The latter was primarily affected by diurnal heating processes in the valley atmosphere as well as by pressure-driven channelling of the flow in the valley in response to larger-scale synoptic pressure gradients. Four typical flow scenarios have been distilled from the selected cases (Fig. 5.1, lower panels): (A) the elevated turbulence zone, (B) flow separation at a valley inversion, (C) turbulent interaction of in-valley westerlies with the along-valley flow, and (D) transient mountain waves and rotors.

In Scenario A, lee waves do form in the lee of the Sierra Nevada and moderate crest-level turbulence is generated over the valley, however the valley atmosphere remains largely decoupled from the cross-mountain flow. In Scenario B, cold upstream air flows down the lee slopes into the valley until it reaches the top of a nighttime pool of cooler air and is forced to separate from the slope. In Scenario C, strong westerlies across the mountain range and resultant large-amplitude waves gradually advance to the valley floor but the channelled up-valley flow withstands for an appreciable amount of time. Scenarios A, B, and C are characterized by the presence of *rotor-like* turbulent structures, i.e., well-defined regions of enhanced turbulence along the interface between the strong westerly winds and the (up-valley flowing or inversion-capped) valley atmosphere, with turbulence intensities sometimes

reaching those found in the interior of rotors. Finally, in Scenario D, the mountain-wave-induced forcing is strong enough to take the full control over the flow in the valley; severe downslope winds and fully-developed rotors rapidly form and decay.

The scenarios and the schematic diagrams associated with them can be related to different stages of the passage of frontal systems across the Sierra Nevada. An individual event may run through a sequence of these stages, resulting in the change of waves in the lee of the Sierra Nevada and turbulence structures in the valley on a time scale of only a few hours as the frontal system passes the region. While each of the individual diagram again tends to provide only a snapshot of the flow, their sequential composition allows to represent the transience observed in most of the T-REX events.

A particularly interesting finding of our analysis is the presence of rotors and rotor-like structures in the absence of strong surface pressure perturbations. The pressure gradients imposed on the near-surface flow by large-amplitude waves have traditionally been suggested as the primary cause of boundary-layer separation and rotor genesis (Lyra 1943). More recently, numerical simulations of rotors suggested that the flow separates once a critical threshold of the pressure gradient is exceeded (e.g., Doyle and Durran 2002; Vosper et al. 2006). However, virtually all of these idealized studies relied on effectively two-dimensional model setups and most of them did not contain a secondary topography (with the exception of Doyle et al. 2009 and Stiperski and Grubišić 2011). With these setups, a realistic representation of the thermal characteristics of the valley atmosphere and the dominant along-valley flow – a concomitant phenomenon of periods of strong synoptically driven cross-mountain winds – is not possible.

In reality, the valley atmosphere, constituting a deep boundary layer whose characteristics substantially differ from those of the free-atmospheric flow aloft, tends to attenuate the wave-induced pressure perturbations well below the model-predicted threshold for boundary-layer separation. Nevertheless, rotor-like turbulent structures can exist in the valley, owing to the predominance of other forces, for example the buoyancy force, making the flow detach from the Sierra Nevada lee slope at the top of strongly stratified layers. Real-case three-dimensional simulations of a case with moderate-amplitude lee waves during SRP are consistent with this description (Jiang and Doyle 2008). In the cases of lee waves with exceptionally large amplitude, instead, pressure perturbations may still represent the primary forcing. The best evidence of fully-developed rotors from observations and numerical models (e.g., Kühnlein et al., 2013 and Grubišić and Billings, 2007, respectively) has indeed been found in such conditions. In summary, the original picture of rotor formation suggesting the sole effect of wave-induced pressure perturbations on the near-surface flow appears to require a revision. Future research should focus on the question to what degree both wave-induced and thermodynamic forcings lead to flow separation and rotor genesis.

Lastly, in view of the richness of turbulent structures and most evident interactions of cross-mountain and along-valley flows in Owens Valley, it is legitimate to wonder why they appear to have remained unaddressed in earlier field experiments. After all, the first mountain-wave and rotor experiments of the 1950s, the Sierra Wave Project and the Mountain Wave-Jet

Stream Project (Holmboe and Klieforth 1954, 1957) took place in the very same location and a few dozen wave cases were documented. Two answers to this puzzling question are offered here.

A close inspection of the instrumentation available during these projects reveals that several barographs and thermographs were distributed across Owens Valley and the adjacent Sierra Nevada and Inyo slopes in the Independence area, but only two instruments with wind speed and wind direction recording capability were available, one placed in the centre of the valley, the other one mobile, displaced across the valley with a car. Despite the scarcity of wind measurements, the general observation was made that “On ‘normal’ wave days the dust is often carried northward by southerly surface winds along the eastern side of the valley.” (Holmboe and Klieforth 1957, p. 176) and, for a strong lee-wave case, “The wind speeds at the surface were rather big and with large westerly components over most of the valley except the extreme east side where there was an abrupt change to southeasterly flow [...]” (Holmboe and Klieforth 1957, p. 92). Nevertheless, it appears that the evidence based on only two wind sensors did not seem overwhelming to the investigators. Also, the insufficient number of radiosondes launched from the valley did not allow to grasp the deep up-valley wind regimes, observed for many strong lee-wave cases during T-REX.

More importantly perhaps, many of the results contained in the reports were never written up in the form of scientific articles and so have remained unpublished in the journal literature, for reasons detailed by Grubišić and Lewis (2004). It was thus up to the T-REX field participants and data analysts, relying on an extensive network of surface stations and powerful remote sensors, to reveal the complexity of the strongly vertically layered and horizontally inhomogeneous structure of the flow in Owens Valley and its impact on rotor formation.

5.2 Concluding remarks

Large-amplitude mountain waves, gravity-wave breaking, and atmospheric rotors are among the most energetic phenomena arising from the interaction of the atmospheric flow with mountainous terrain. This work has offered a new perspective on the temporal variability of these phenomena and their turbulent character on the basis of high-resolution observations and numerical simulations.

Special emphasis has been placed on atmospheric rotors and associated severe low-level turbulence. Going well beyond idealized conceptual models, results allow to better comprehend many aspects of their nature. Rotors are severely turbulent phenomena, they are short-lived, strongly non-linear, intrinsically non-stationary, three-dimensional, highly sensitive to small changes in the upstream conditions, and very often modified significantly by the downstream environment. Their strongest occurrences appear to be tightly linked to transients in flow regimes, which makes them exceptionally hard to predict. Some of these aspects are not completely new – indeed, some of them were noted as early as in the 1950s during the first dedicated observations in the field, but since then have not received sufficient attention or have fallen into oblivion. This work re-emphasizes the importance of both upstream and

downstream processes in shaping lee-side turbulent processes and thereby contributes to a more comprehensive picture of the rotor flow.

Some of the observations presented in this work may seem to call into question the concept of the rotor flow as a whole. However, the strongest rotors do contain most of the defining elements suggested in previous studies, such as the near-surface reversed flow. Even their non-ideal variants, here referred to as *rotor-like* turbulent structures, seem to bear sufficient similarity to deserve the name, not least because the term is well-known in the aviation community, where it stands for the likely encounter with severe turbulence underneath lenticular wave clouds.

Airborne and ground-based remote sensors prove to be instrumental in revealing the complex spatial distribution of mountain-induced turbulence and its temporal variability. When used appropriately, quantitative estimates of turbulence intensity from these instruments are possible and can serve to study these processes from afar without the risk of exposing people and measurement equipment to the hazards associated with them.

To better understand the observations and examine the involved small-scale processes in detail, high-resolution real-case and idealized numerical simulations are the tool of choice. To correctly forecast the conjunction of dynamic and boundary-layer processes implicated in the generation of severe lee-side winds, wave-induced boundary-layer separation and rotors, however, seems a formidable challenge. Previous conclusions on the predictability of wave breaking (Doyle et al. 2011b) may apply in an analogous manner, that is, the prediction of the location and timing of rotors and associated low-level turbulence, of great importance for aviation, may only be possible through probabilistic approaches. The latter will require a skillful interpretation of mesoscale ensemble predictions by forecasters, accounting for the possibility of strongly non-Gaussian probability distributions.

5.3 Outlook

Future research may focus on two aspects that have not been addressed sufficiently here.

Firstly, the along-ridge variability of the atmospheric and topographic conditions influencing the rotor genesis and the resultant fully three-dimensional structure of the rotor flow have received relatively little attention. In one of the geographical areas of this work, the Sierra Nevada and Owens Valley, several mountain passes are present in the main ridge line. The passes seems to favour the occurrence of high westerly winds downstream of them, for instance, in the Independence area, lying downwind of Kearsarge Pass. It is not well understood to what degree this topographic configuration favours or impedes the formation of rotors in the area.

In the topographically much more complex environment of the northern Dinaric Alps of Croatia, the onset phase of strong bora seems to be associated with gap jets, starting to reach the coast through mountain gaps, as opposed to rotor-like wakes lee-side of higher terrain, where the flow separates already high up on the slopes (Gohm et al. 2008). In that region, shear lines forming between the gap jets and wake regions are of great relevance for operational forecasting of the wind on coastal roads and airports (e.g., Krk Bridge and Rijeka Airport on

the northern tip of Krk Island).

High-resolution simulations, using idealized three-dimensional topography intersected by one or several gaps, may allow to further explore the three-dimensional structure of rotors and gap jets in dependence of parameters such as the gap width and depth. The idealized simulations of the rotor shear regions and jet-wake shear lines would help to better characterize the locations of strongest turbulence associated with them. Finally, verifying the simulation results with observations by ground-based scanning Doppler lidars positioned downstream of gap flanks would be most interesting.

The second open question regards the role of dynamic and thermal in-valley processes for rotor formation. T-REX observations show that wave-induced pressure perturbations are rapidly damped in the valley atmosphere, impeding flow separation triggered purely by wave-induced pressure gradients. Flow separation did occur nevertheless in some cases, pointing to the additional role of other forces from the full set of terms in the momentum equations, such as the buoyancy force. The relative importance of pressure-gradient forces as opposed to buoyancy forces for flow separation and rotor formation in a valley could be illuminated through a set of high-resolution idealized simulations, via the detailed inspection of the relative magnitudes of the relevant terms in the momentum equations.

Finally, real-case simulations of those T-REX cases that show a strong influence of the valley atmosphere on low-level turbulence may be most interesting. Given the importance of correctly representing the concurrence of lee waves, valley stability layering and pressure-driven channelling in the valley, such simulations could prove difficult. They may also constitute, however, a new challenging test of the abilities of state-of-the-art numerical models in properly representing the plethora of atmospheric processes in complex terrain.

Bibliography

- Ágústsson, H., and H. Ólafsson, 2014: Simulations of observed lee waves and rotor turbulence. *Mon. Wea. Rev.*, **142**, 832–849, doi:[10.1175/MWR-D-13-00212.1](https://doi.org/10.1175/MWR-D-13-00212.1).
- Ambaum, M. H., and D. P. Marshall, 2005: The effects of stratification on flow separation. *J. Atmos. Sci.*, **62**, 2618–2625, doi:[10.1175/JAS3485.1](https://doi.org/10.1175/JAS3485.1).
- American Meteorological Society, cited 2015: T-REX AMS Journals Special Collection. [Available online at <http://journals.ametsoc.org/page/trex>].
- Armi, L., and G. J. Mayr, 2011: The descending stratified flow and internal hydraulic jump in the lee of the Sierras. *J. Appl. Meteor. Climatol.*, **50**, 1995–2011, doi:[10.1175/JAMC-D-10-05005.1](https://doi.org/10.1175/JAMC-D-10-05005.1).
- Attié, J.-L., A. Druilhet, B. Bénech, and P. Durand, 1999: Turbulence on the lee side of a mountain range: Aircraft observations during PYREX. *Q.J.R. Meteorol. Soc.*, **125**, 1359–1381, doi:[10.1002/qj.1999.49712555613](https://doi.org/10.1002/qj.1999.49712555613).
- Baines, P. G., 1995: *Topographic Effects in Stratified Flows*. Cambridge University Press, 482 pp.
- Baines, P. G., and K. P. Hoinka, 1985: Stratified flow over two-dimensional topography of fluid of infinite depth: A laboratory simulation. *J. Atmos. Sci.*, **42**, 1614–1630, doi:[10.1175/1520-0469\(1985\)042<1614:SFOTDT>2.0.CO;2](https://doi.org/10.1175/1520-0469(1985)042<1614:SFOTDT>2.0.CO;2).
- Banta, R. M., and Coauthors, 2013: Observational techniques: Sampling the mountain atmosphere. *Mountain Weather Research and Forecasting*, F. K. Chow, S. F. J. De Wekker, and B. J. Snyder, Eds., Springer Netherlands, 409–530, doi:[10.1007/978-94-007-4098-3_8](https://doi.org/10.1007/978-94-007-4098-3_8).
- Batchelor, G., 1967: *An Introduction to Fluid Dynamics*. Cambridge University Press, 615 pp.
- Bedard, A., 1990: A review of the evidence for strong, small-scale vortical flows during downslope windstorms. *J. Wind Eng. Ind. Aerod.*, **36**, 97–106, doi:[10.1016/0167-6105\(90\)90296-O](https://doi.org/10.1016/0167-6105(90)90296-O).
- Belušić, D., M. Hrastinski, Ž. Večenaj, and B. Grisogono, 2013: Wind regimes associated with a mountain gap at the northeastern Adriatic coast. *Appl. Meteor. Climatol.*, **52**, 2089–2105, doi:[10.1175/JAMC-D-12-0306.1](https://doi.org/10.1175/JAMC-D-12-0306.1).

- Belušić, D., M. Pasarić, and M. Orlić, 2004: Quasi-periodic bora gusts related to the structure of the troposphere. *Q.J.R. Meteorol. Soc.*, **130**, 1103–1121, doi:[10.1256/qj.03.53](https://doi.org/10.1256/qj.03.53).
- Belušić, D., M. Žagar, and B. Grisogono, 2007: Numerical simulation of pulsations in the bora wind. *Q.J.R. Meteorol. Soc.*, **133**, 1371–1388.
- Billings, B. J., and V. Grubišić, 2008a: A numerical study of the effects of diurnal heating, moisture, and downstream topography on downslope winds within a valley. *13th Conference on Mountain Meteorology*, Whistler, BC, Canada. [Available online at <https://ams.confex.com/ams/13MontMet17AP/webprogram/Paper140812.html>].
- Billings, B. J., and V. Grubišić, 2008b: A study of the onset of westerly downslope winds in Owens Valley. *13th Conference on Mountain Meteorology*, Whistler, BC, Canada. [Available online at <https://ams.confex.com/ams/13MontMet17AP/webprogram/Paper140810.html>].
- Bougeault, P., B. Benech, P. Bessemoulin, B. Carissimo, A. J. Clar, J. Pelon, M. Petitdidier, and E. Richard, 1997: PYREX: A summary of findings. *Bull. Amer. Meteor. Soc.*, **78**, 637–650, doi:[10.1175/1520-0477\(1997\)078<0637:PASOF>2.0.CO;2](https://doi.org/10.1175/1520-0477(1997)078<0637:PASOF>2.0.CO;2).
- Bougeault, P., and Coauthors, 2001: The MAP special observing period. *Bull. Amer. Meteor. Soc.*, **82**, 433–462, doi:[10.1175/1520-0477\(2001\)082<0433:TMSOP>2.3.CO;2](https://doi.org/10.1175/1520-0477(2001)082<0433:TMSOP>2.3.CO;2).
- Bretherton, F. P., 1969: Momentum transport by gravity waves. *Q.J.R. Meteorol. Soc.*, **95**, 213–243, doi:[10.1002/qj.49709540402](https://doi.org/10.1002/qj.49709540402).
- Brown, E., C. Friehe, and D. Lenschow, 1983: The use of pressure-fluctuations on the nose of an aircraft for measuring air motion. *J. Climate Appl. Meteor.*, **22**, 171–180, doi:[10.1175/1520-0450\(1983\)022<0171:TUOPFO>2.0.CO;2](https://doi.org/10.1175/1520-0450(1983)022<0171:TUOPFO>2.0.CO;2).
- Carney, T. Q., A. J. Bedard, J. M. Brown, M. J. Kraus, J. McGinley, and T. A. Lindholm, 1997: Hazardous mountain winds and their visual indicators. Department of Commerce, NOAA, Handbook, Federal Aviation Administration Advisory Circular AC00-57, 80 pp. [Available online at http://www.faa.gov/documentLibrary/media/Advisory_Circular/00-57.pdf].
- Chow, F. K., S. F. J. De Wekker, and B. J. E. Snyder, 2013: *Mountain Weather Research and Forecasting*. Springer Netherlands, 750 pp., doi:[10.1007/978-94-007-4098-3](https://doi.org/10.1007/978-94-007-4098-3).
- Clark, T. L., W. D. Hall, and R. M. Banta, 1994: Two- and three-dimensional simulations of the 9 january 1989 severe boulder windstorm: Comparison with observations. *J. Atmos. Sci.*, **51**, 2317–2343, doi:[10.1175/1520-0469\(1994\)051<2317:TATDSO>2.0.CO;2](https://doi.org/10.1175/1520-0469(1994)051<2317:TATDSO>2.0.CO;2).
- Clark, T. L., and W. R. Peltier, 1984: Critical level reflection and the resonant growth of non-linear mountain waves. *J. Atmos. Sci.*, **41**, 3122–3134, doi:[http://dx.doi.org/10.1175/1520-0469\(1984\)041<3122:CLRATR>2.0.CO;2](http://dx.doi.org/10.1175/1520-0469(1984)041<3122:CLRATR>2.0.CO;2).

- Cohn, S. A., V. Grubišić, and W. O. J. Brown, 2011: Wind profiler observations of mountain waves and rotors during T-REX. *J. Appl. Meteor. Climatol.*, **50**, 826–843, doi:[10.1175/2010JAMC2611.1](https://doi.org/10.1175/2010JAMC2611.1).
- Colson, D., 1952: Results of double-theodolite observations at Bishop, Cal., in connection with the “Bishop-Wave” phenomena. *Bull. Amer. Meteor. Soc.*, **33**, 107–116.
- Damiani, R., and S. Haimov, 2006: A high-resolution dual-Doppler technique for fixed multi-antenna airborne radar. *IEEE Trans. Geosci. Remote Sens.*, **44**, 3475–3489, doi:[10.1109/TGRS.2006.881745](https://doi.org/10.1109/TGRS.2006.881745).
- Darby, L. S., and G. S. Poulos, 2006: The evolution of lee-wave-rotor activity in the lee of Pike’s Peak under the influence of a cold frontal passage: Implications for aircraft safety. *Mon. Wea. Rev.*, **134**, 2857–2876, doi:[10.1175/MWR3208.1](https://doi.org/10.1175/MWR3208.1).
- De Wekker, S. F. J., and S. D. Mayor, 2009: Observations of atmospheric structure and dynamics in the Owens Valley of California with a ground-based, eye-safe, scanning aerosol lidar. *J. Appl. Meteor. Climatol.*, **48**, 1483–1499, doi:[10.1175/2009JAMC2034.1](https://doi.org/10.1175/2009JAMC2034.1).
- Dörnbrack, A., 1998: Turbulent mixing by breaking gravity waves. *J. Fluid Mech.*, **375**, 113–141, doi:[10.1017/S0022112098002833](https://doi.org/10.1017/S0022112098002833).
- Doyle, J. D., C. Amerault, and C. A. Reynolds, 2007: Sensitivity analysis of mountain waves using an adjoint model. *Meteor. Z.*, **16**, 607–620, doi:[10.1127/0941-2948/2007/0236](https://doi.org/10.1127/0941-2948/2007/0236).
- Doyle, J. D., and D. R. Durran, 2002: The dynamics of mountain-wave-induced rotors. *J. Atmos. Sci.*, **59**, 186–201, doi:[10.1175/1520-0469\(2002\)059<0186:TDOMWI>2.0.CO;2](https://doi.org/10.1175/1520-0469(2002)059<0186:TDOMWI>2.0.CO;2).
- Doyle, J. D., and D. R. Durran, 2004: Recent developments in the theory of atmospheric rotors. *Bull. Amer. Meteor. Soc.*, **85**, 337–342, doi:[10.1175/BAMS-85-3-337](https://doi.org/10.1175/BAMS-85-3-337).
- Doyle, J. D., and D. R. Durran, 2007: Rotor and subrotor dynamics in the lee of three-dimensional terrain. *J. Atmos. Sci.*, **64**, 4202–4221, doi:[10.1175/2007JAS2352.1](https://doi.org/10.1175/2007JAS2352.1).
- Doyle, J. D., V. Grubišić, W. O. J. Brown, S. F. J. De Wekker, A. Dörnbrack, Q. Jiang, S. D. Mayor, and M. Weissmann, 2009: Observations and numerical simulations of subrotor vortices during T-REX. *J. Atmos. Sci.*, **66**, 1229–1249, doi:[10.1175/2008JAS2933.1](https://doi.org/10.1175/2008JAS2933.1).
- Doyle, J. D., Q. Jiang, R. B. Smith, and V. Grubišić, 2011a: Three-dimensional characteristics of stratospheric mountain waves during T-REX. *Mon. Wea. Rev.*, **139**, 3–23, doi:[10.1175/2010MWR3466.1](https://doi.org/10.1175/2010MWR3466.1).
- Doyle, J. D., and C. A. Reynolds, 2008: Implications of regime transitions for mountain-wave-breaking predictability. *Mon. Wea. Rev.*, **136**, 5211–5223, doi:[10.1175/2008MWR2554.1](https://doi.org/10.1175/2008MWR2554.1).

- Doyle, J. D., and Coauthors, 2000: An intercomparison of model-predicted wave breaking for the 11 January 1972 Boulder windstorm. *Mon. Wea. Rev.*, **128**, 901–914, doi:[10.1175/1520-0493\(2000\)128<0901:AIOMPW>2.0.CO;2](https://doi.org/10.1175/1520-0493(2000)128<0901:AIOMPW>2.0.CO;2).
- Doyle, J. D., and Coauthors, 2011b: An intercomparison of T-REX mountain-wave simulations and implications for mesoscale predictability. *Mon. Wea. Rev.*, **139**, 2811–2831, doi:[10.1175/MWR-D-10-05042.1](https://doi.org/10.1175/MWR-D-10-05042.1).
- Durran, D. R., 1986: Another look at downslope windstorms. Part I: The development of analogs to supercritical flow in an infinitely deep, continuously stratified fluid. *J. Atmos. Sci.*, **43**, 2527–2543, doi:[10.1175/1520-0469\(1986\)043<2527:ALADWP>2.0.CO;2](https://doi.org/10.1175/1520-0469(1986)043<2527:ALADWP>2.0.CO;2).
- Durran, D. R., 1990: Mountain waves and downslope winds. *Atmospheric Processes over Complex Terrain*, W. Blumen, Ed., Meteorological Monographs, Vol. 23, American Meteorological Society, 59–82.
- Durran, D. R., 2003a: Downslope winds. *Encyclopedia of Atmospheric Sciences*, J. R. Holton, J. A. Curry, and J. A. Pyle, Eds., Academic Press, London, UK, 644–650.
- Durran, D. R., 2003b: Lee waves and mountain waves. *Encyclopedia of Atmospheric Sciences*, J. R. Holton, J. A. Curry, and J. A. Pyle, Eds., Academic Press, London, UK, 1161–1169.
- Eiff, O. S., and P. Bonneton, 2000: Lee-wave breaking over obstacles in stratified flow. *Phys. Fluids*, **12**, 1073–1086, doi:<http://dx.doi.org/10.1063/1.870362>.
- Förchtgott, J., 1957: Active turbulent layer downwind of mountain ridges. *Stud. Geophys. Geod.*, **1**, 173–181, doi:[10.1007/BF02585106](https://doi.org/10.1007/BF02585106).
- French, J. R., S. Haimov, L. Oolman, V. Grubišić, S. Serafin, and L. Strauss, 2015: Wave-induced boundary-layer separation in the lee of the Medicine Bow Mountains. Part I: Observations. *J. Atmos. Sci.*, in review.
- Fritts, D. C., and M. J. Alexander, 2003: Gravity wave dynamics and effects in the middle atmosphere. *Rev. Geophys.*, **41**, 1003, doi:[10.1029/2001RG000106](https://doi.org/10.1029/2001RG000106).
- Geerts, B., Q. Miao, and Y. Yang, 2011: Boundary layer turbulence and orographic precipitation growth in cold clouds: Evidence from profiling airborne radar data. *J. Atmos. Sci.*, **68**, 2344–2365, doi:[10.1175/JAS-D-10-05009.1](https://doi.org/10.1175/JAS-D-10-05009.1).
- Gerbier, N., and M. Berenger, 1961: Experimental studies of lee waves in the French Alps. *Q.J.R. Meteorol. Soc.*, **87**, 13–23, doi:[10.1002/qj.49708737103](https://doi.org/10.1002/qj.49708737103).
- Gohm, A., and G. J. Mayr, 2004: Hydraulic aspects of föhn winds in an alpine valley. *Q.J.R. Meteorol. Soc.*, **130**, 449–480, doi:[10.1256/qj.03.28](https://doi.org/10.1256/qj.03.28).
- Gohm, A., and G. J. Mayr, 2005: Numerical and observational case-study of a deep Adriatic bora. *Quart. J. Roy. Meteor. Soc.*, **131**, 1363–1392, doi:[10.1256/qj.04.82](https://doi.org/10.1256/qj.04.82).

- Gohm, A., G. J. Mayr, A. Fix, and A. Giez, 2008: On the onset of bora and the formation of rotors and jumps near a mountain gap. *Q.J.R. Meteorol. Soc.*, **134**, 21–46, doi:[10.1002/qj.206](https://doi.org/10.1002/qj.206).
- Grisogono, B., and D. Belušić, 2009: A review of recent advances in understanding the meso and microscale properties of the severe Bora wind. *Tellus*, **61A**, 1–16, doi:[10.1111/j.1600-0870.2008.00369.x](https://doi.org/10.1111/j.1600-0870.2008.00369.x).
- Grubišić, V., L. Armi, J. Kuettner, S. Haimov, L. Oolman, R. Damiani, and B. Billings, 2006: Atmospheric rotors: Aircraft in situ and cloud radar measurements in T-REX. *12th Conference on Mountain Meteorology*, Santa Fe, NM. [Available online at <https://ams.confex.com/ams/pdfpapers/114666.pdf>].
- Grubišić, V., and B. J. Billings, 2007: The intense lee-wave rotor event of Sierra Rotors IOP 8. *J. Atmos. Sci.*, **64**, 4178–4201, doi:[10.1175/2006JAS2008.1](https://doi.org/10.1175/2006JAS2008.1).
- Grubišić, V., and B. J. Billings, 2008a: Climatology of the Sierra Nevada mountain-wave events. *Mon. Wea. Rev.*, **136**, 757–768, doi:[10.1175/2007MWR1902.1](https://doi.org/10.1175/2007MWR1902.1).
- Grubišić, V., and B. J. Billings, 2008b: Summary of the Sierra Rotors Project wave and rotor events. *Atmosph. Sci. Lett.*, **9**, 176–181, doi:[10.1002/asl.200](https://doi.org/10.1002/asl.200).
- Grubišić, V., and M. Orlić, 2007: Early observations of rotor clouds by Andrija Mohorovičić. *Bull. Amer. Meteor. Soc.*, **88**, 693–700, doi:[10.1175/BAMS-88-5-693](https://doi.org/10.1175/BAMS-88-5-693).
- Grubišić, V., and I. Stiperski, 2009: Lee-wave resonances over double bell-shaped obstacles. *J. Atmos. Sci.*, **66**, 1205–1228, doi:[10.1175/2008JAS2885.1](https://doi.org/10.1175/2008JAS2885.1).
- Grubišić, V., and Coauthors, 2008: The Terrain-Induced Rotor Experiment. *Bull. Amer. Meteor. Soc.*, **89**, 1513–1533, doi:[10.1175/2008BAMS2487.1](https://doi.org/10.1175/2008BAMS2487.1).
- Grubišić, V., and J. M. Lewis, 2004: Sierra Wave Project revisited – 50 years later. *Bull. Amer. Meteor. Soc.*, **85**, 1127–1142, doi:[10.1175/BAMS-85-8-1127](https://doi.org/10.1175/BAMS-85-8-1127).
- Grubišić, V., S. Serafin, L. Strauss, S. Haimov, J. R. French, and L. Oolman, 2015a: Wave-induced boundary-layer separation in the lee of the Medicine Bow Mountains. Part II: Modeling. *J. Atmos. Sci.*, accepted with minor revisions.
- Grubišić, V., S. Serafin, and L. Strauss, 2015b: Climatology of westerly wind events in the lee of the Sierra Nevada. In preparation for *J. Appl. Meteor. Climatol.*
- Grubišić, V., and Coauthors, 2004: T-REX Terrain-induced Rotor Experiment: Scientific overview document and experiment design. Project proposal, 72 pp. [Available online at http://www.eol.ucar.edu/system/files/TREX_SOD.pdf].

- Haimov, S., V. Grubišić, J. R. French, and L. Oolman, 2008: Multi-Doppler measurements of atmospheric rotors and turbulent mountain waves. *2008 IEEE International Geoscience & Remote Sensing Symposium (IGARSS)*, Boston, MA. [Available online at <http://ieeexplore.ieee.org/stamp/stamp.jsp?arnumber=4779313>].
- Hertenstein, R. F., 2009: The influence of inversions on rotors. *Mon. Wea. Rev.*, **137**, 433–446, doi:[10.1175/2008MWR2482.1](https://doi.org/10.1175/2008MWR2482.1).
- Hertenstein, R. F., and J. P. Kuettner, 2005: Rotor types associated with steep lee topography: Influence of the wind profile. *Tellus A*, **57**, 117–135, doi:[10.3402/tellusa.v57i2.14625](https://doi.org/10.3402/tellusa.v57i2.14625).
- Hill, M., R. Calhoun, H. J. S. Fernando, A. Wieser, A. Dörnbrack, M. Weissmann, G. Mayr, and R. Newsom, 2010: Coplanar Doppler lidar retrieval of rotors from T-REX. *J. Atmos. Sci.*, **67**, 713–729, doi:[10.1175/2009JAS3016.1](https://doi.org/10.1175/2009JAS3016.1).
- Hirth, W., 1933: Die lange Welle (The long wave). *Die hohe Schule des Segelfluges (The Fine Art of Gliding)*, W. Hirth, Ed., Klasing & Co., Berlin, 135–139.
- Hoinkes, H., 1942: Wolkenbeobachtungen bei Föhn in Innsbruck (Cloud observations in Innsbruck during foehn). *Beitr. Phys. Frei. Atmos.*, **27**, 62–68.
- Holmboe, J., and H. Klieforth, 1954: Sierra Wave Project. Department of Meteorology, UCLA Final Rep. Contract AF 19(122)-263, 55 pp.
- Holmboe, J., and H. Klieforth, 1957: Investigation of mountain lee waves and the air flow over the Sierra Nevada. Department of Meteorology, UCLA Final Rep. Contract AF 19(604)-728, 283 pp.
- Jackson, P. L., G. Mayr, and S. Vosper, 2013: Dynamically-driven winds. *Mountain Weather Research and Forecasting*, F. K. Chow, S. F. J. De Wekker, and B. J. Snyder, Eds., Springer Netherlands, 121–218, doi:[10.1007/978-94-007-4098-3_3](https://doi.org/10.1007/978-94-007-4098-3_3).
- Jiang, Q., and J. D. Doyle, 2004: Gravity wave breaking over the Central Alps: Role of complex terrain. *J. Atmos. Sci.*, **61**, 2249–2266, doi:[10.1175/1520-0469\(2004\)061<2249:GWBOTC>2.0.CO;2](https://doi.org/10.1175/1520-0469(2004)061<2249:GWBOTC>2.0.CO;2).
- Jiang, Q., and J. D. Doyle, 2008: Diurnal variation of downslope winds in Owens Valley during the Sierra Rotor Experiment. *Mon. Wea. Rev.*, **136**, 3760–3780, doi:[10.1175/2008MWR2469.1](https://doi.org/10.1175/2008MWR2469.1).
- Jiang, Q., and J. D. Doyle, 2008: On the diurnal variation of mountain waves. *J. Atmos. Sci.*, **65**, 1360–1377, doi:[10.1175/2007JAS2460.1](https://doi.org/10.1175/2007JAS2460.1).
- Jiang, Q., J. D. Doyle, V. Grubišić, and R. B. Smith, 2010: Turbulence characteristics in an elevated shear layer over Owens Valley. *J. Atmos. Sci.*, **67**, 2355–2371, doi:[10.1175/2010JAS3156.1](https://doi.org/10.1175/2010JAS3156.1).

- Jiang, Q., J. D. Doyle, and R. B. Smith, 2006: Interaction between trapped waves and boundary layers. *J. Atmos. Sci.*, **63**, 617–633, doi:[10.1175/JAS3640.1](https://doi.org/10.1175/JAS3640.1).
- Jiang, Q., J. D. Doyle, S. Wang, and R. B. Smith, 2007: On boundary layer separation in the lee of mesoscale topography. *J. Atmos. Sci.*, **64**, 401–420, doi:[10.1175/JAS3848.1](https://doi.org/10.1175/JAS3848.1).
- Jiang, Q., R. B. Smith, and J. D. Doyle, 2008: Impact of the atmospheric boundary layer on mountain waves. *J. Atmos. Sci.*, **65**, 592–608, doi:[10.1175/2007JAS2376.1](https://doi.org/10.1175/2007JAS2376.1).
- Kahn, B. H., W. Chan, and P. F. Lester, 1997: An investigation of rotor flow using dfdr data. *Proc. Seventh Conf. on Aviation, Range, and Aerospace Meteorology*, Long Beach, CA. [Available online at <http://ntrs.nasa.gov/archive/nasa/casi.ntrs.nasa.gov/19970015304.pdf>].
- Kim, Y.-J., S. D. Eckermann, and H.-Y. Chun, 2003: An overview of the past, present and future of gravity-wave drag parametrization for numerical climate and weather prediction models. *Atmosphere-Ocean*, **41**, 65–98, doi:[10.3137/ao.410105](https://doi.org/10.3137/ao.410105).
- Kingsmill, D. E., P. O. G. Persson, S. Haimov, and M. Shupe, 2014: Mountain waves and orographic precipitation in a northern Colorado winter storm. *16th Conference on Mountain Meteorology*, San Diego, CA. [Available online at <https://ams.confex.com/ams/16MountMet/webprogram/Paper251865.html>].
- Knigge, C., D. Etling, A. Paci, and O. Eiff, 2010: Laboratory experiments on mountain-induced rotors. *Q.J.R. Meteorol. Soc.*, **136**, 442–450, doi:[10.1002/qj.564](https://doi.org/10.1002/qj.564).
- Knox, J. B., 1952: A preliminary report on hydraulic pressure jumps as observed with the Sierra Wave. Univ. of Calif., Meteor. Dept.
- Knox, J. B., 1954: On waves of finite amplitude. Air Force Cambridge Research Center Scientific Rep. 5, Sierra Wave Project Contract No. AF 19, (122)-263 pp.
- Koch, J. P., and A. Wegener, 1930: Wissenschaftliche Ergebnisse der Dänischen Expedition nach Dronning Louises-Land und quer über das Inlandeis von Nordgrönland (Scientific results of the Danish expedition to Dronning Louise Land and across the ice shelf of northern Greenland). *Meddelelser om Grønland*, **75 (1, 2)**, Copenhagen.
- Koschmieder, H., 1920: Zwei bemerkenswerte Beispiele horizontaler Wolkenschläuche (Two notable examples of horizontal cloud tubes). *Beitr. Phys. Frei. Atmos.*, **9**, 176–180.
- Krishnamurthy, R., R. Calhoun, and H. Fernando, 2010: Large-eddy simulation-based retrieval of dissipation from coherent Doppler lidar data. *Boundary-Layer Meteorol.*, **136**, 45–57, doi:[10.1007/s10546-010-9495-y](https://doi.org/10.1007/s10546-010-9495-y).
- Kuettner, J., 1959: The rotor flow in the lee of mountains. Geophysics Research Directorate (GRD) Research Notes No. 6, AFCRC-TN-58-626, Air Force Cambridge Research Center, USA, 20 pp.

- Kuettner, J., and R. F. Hertenstein, 2002: Observations of mountain-induced rotors and related hypotheses: A review. *10th Conference on Mountain Meteorology*, Park City, UT. [Available online at <https://ams.confex.com/ams/pdfpapers/40363.pdf>].
- Kuettner, J. P., 1986: The aim and conduct of ALPEX. Scientific results of the Alpine Experiment. GARP Publications Series No. 27, WMO/TD 108, 3-14.
- Kuettner, J. P., and D. K. Lilly, 1968: Lee waves in the Colorado Rockies. *Weatherwise*, **21**, 180–197, doi:[10.1080/00431672.1968.9932819](https://doi.org/10.1080/00431672.1968.9932819).
- Kühnlein, C., A. Dörnbrack, and M. Weissmann, 2013: High-resolution Doppler lidar observations of transient downslope flows and rotors. *Mon. Wea. Rev.*, **141**, 3257–3272, doi:[10.1175/MWR-D-12-00260.1](https://doi.org/10.1175/MWR-D-12-00260.1).
- Küttner, J., 1938: Moazagotl und Föhnwelle (Moazagotl and foehn wave). *Beitr. Phys. Atmos.*, **25**, 79–114.
- Küttner, J., 1939: Zur Entstehung der Föhnwelle (On the origin of the foehn wave). *Beitr. Phys. Atmos.*, **25**, 251–299.
- Lenschow, D., 1986: Aircraft measurements in the boundary layer. *Probing the Atmospheric Boundary Layer*, D. Lenschow, Ed., American Meteorological Society, 39–55.
- Lenschow, D. H., 1970: Airplane measurements of planetary boundary layer structure. *J. Appl. Meteor.*, **9**, 874–884, doi:[10.1175/1520-0450\(1970\)009<0874:AMOPBL>2.0.CO;2](https://doi.org/10.1175/1520-0450(1970)009<0874:AMOPBL>2.0.CO;2).
- Lenschow, D. H., J. Mann, and L. Kristensen, 1994: How long is long enough when measuring fluxes and other turbulence statistics. *J. Atmos. Oceanic Technol.*, **11**, 661–673, doi:[10.1175/1520-0426\(1994\)011<0661:HLILEW>2.0.CO;2](https://doi.org/10.1175/1520-0426(1994)011<0661:HLILEW>2.0.CO;2).
- Lester, P. F., 1993: *Turbulence: A New Perspective for Pilots*. Jeppesen Sanderson.
- Lester, P. F., and W. A. Fingerhut, 1974: Lower turbulent zones associated with mountain lee waves. *J. Appl. Meteor.*, **13**, 54–61, doi:[10.1175/1520-0450\(1974\)013<0054:LTZAWM>2.0.CO;2](https://doi.org/10.1175/1520-0450(1974)013<0054:LTZAWM>2.0.CO;2).
- Lilly, D. K., 1971: Observations of mountain-induced turbulence. *J. Geophys. Res.*, **76**, 6585–6588, doi:[10.1029/JC076i027p06585](https://doi.org/10.1029/JC076i027p06585).
- Lilly, D. K., 1978: A severe downslope windstorm and aircraft turbulence event induced by a mountain wave. *J. Atmos. Sci.*, **35**, 59–77, doi:[10.1175/1520-0469\(1978\)035<0059:ASDWAA>2.0.CO;2](https://doi.org/10.1175/1520-0469(1978)035<0059:ASDWAA>2.0.CO;2).
- Lilly, D. K., and P. F. Lester, 1974: Waves and turbulence in the stratosphere. *J. Atmos. Sci.*, **31**, 800–812, doi:[10.1175/1520-0469\(1974\)031<0800:WATITS>2.0.CO;2](https://doi.org/10.1175/1520-0469(1974)031<0800:WATITS>2.0.CO;2).

- Lilly, D. K., and W. Toutenhoofd, 1969: The Colorado Lee Wave Program. *Clear Air Turbulence and Its Detection*, Y.-H. Pao, and A. Goldberg, Eds., Springer US, 232–245, doi:[10.1007/978-1-4899-5615-6_13](https://doi.org/10.1007/978-1-4899-5615-6_13).
- Lilly, D. K., and E. J. Zipser, 1972: The Front Range windstorm of 11 January 1972. a meteorological narrative. *Weatherwise*, **25**, 56–63, doi:[10.1080/00431672.1972.9931577](https://doi.org/10.1080/00431672.1972.9931577).
- Lin, Y.-L., 2007: *Mesoscale Dynamics*. Cambridge University Press, 630 pp.
- Long, R. R., 1953a: A laboratory model resembling the “Bishop-Wave” phenomenon. *Bull. Amer. Meteor. Soc.*, **34**, 205–211.
- Long, R. R., 1953b: Some aspects of the flow of stratified fluids. I. A theoretical investigation. *Tellus*, **5**, 42–58.
- Long, R. R., 1954: Some aspects of the flow of stratified fluids. II. Experiments with a two-fluid system. *Tellus*, **6**, 97–115.
- Long, R. R., 1955: Some aspects of the flow of stratified fluids. III. Continuous density gradients. *Tellus*, **7**, 342–357.
- Lothon, M., A. Druilhet, Bénech, B. Campistron, B., S. Bernard, and F. Saïd, 2003: Experimental study of five föhn events during the Mesoscale Alpine Programme: From synoptic scale to turbulence. *Q.J.R. Meteorol. Soc.*, **129**, 2171–2193, doi:[10.1256/qj.02.30](https://doi.org/10.1256/qj.02.30).
- Lothon, M., D. H. Lenschow, D. Leon, and G. Vali, 2005: Turbulence measurements in marine stratocumulus with airborne Doppler radar. *Q. J. R. Meteorol. Soc.*, **131**, 2063–2080, doi:[10.1256/qj.04.131](https://doi.org/10.1256/qj.04.131).
- Lyra, G., 1940: Über den Einfluss von Bodenerhebungen auf die Strömung einer stabil geschichteten Atmosphäre (On the influence of surface obstacles on the flow of a stably stratified atmosphere). *Beitr. Phys. Atmos.*, **226**, 197–206.
- Lyra, G., 1943: Theorie der stationären Leewellenströmung in freier Atmosphäre (Theory of stationary lee-wave flow in the free atmosphere). *Z. angew. Math. Mech.*, **23**, 1–28, doi:[10.1002/zamm.19430230102](https://doi.org/10.1002/zamm.19430230102).
- MacCready Jr., P. B., 1964: Standardization of gustiness values from aircraft. *J. Appl. Meteor.*, **3**, 439–449, doi:[10.1175/1520-0450\(1964\)003<0439:SOGVFA>2.0.CO;2](https://doi.org/10.1175/1520-0450(1964)003<0439:SOGVFA>2.0.CO;2).
- Manley, G., 1945: The helm wind of Crossfell, 1937-1939. *Q.J.R. Meteorol. Soc.*, **71**, 197–219, doi:[10.1002/qj.49707130901](https://doi.org/10.1002/qj.49707130901).
- Marriott, W., 1886: The helm wind of August 19th, 1885. *Q.J.R. Meteorol. Soc.*, **12**, 1–10, doi:[10.1002/qj.4970125701](https://doi.org/10.1002/qj.4970125701).

- Marriott, W., 1889: Report on the helm wind inquiry. *Q.J.R. Meteorol. Soc.*, **15**, 103–118, doi:[10.1002/qj.4970157010](https://doi.org/10.1002/qj.4970157010).
- Marwitz, J. D., and P. J. Dawson, 1984: Low-level airflow in southern Wyoming during wintertime. *Mon. Wea. Rev.*, **112**, 1246–1262, doi:[10.1175/1520-0493\(1984\)112<1246:LLAISW>2.0.CO;2](https://doi.org/10.1175/1520-0493(1984)112<1246:LLAISW>2.0.CO;2).
- Mayr, G. J., and L. Armi, 2010: The influence of downstream diurnal heating on the descent of flow across the Sierras. *J. Appl. Meteor. Climatol.*, **49**, 1906–1912, doi:[10.1175/2010JAMC2516.1](https://doi.org/10.1175/2010JAMC2516.1).
- Miles, J. W., and H. E. Huppert, 1969: Lee waves in a stratified flow. Part 4: Perturbation approximation. *J. Fluid Mech.*, **35**, 497–525, doi:[10.1017/S0022112069001248](https://doi.org/10.1017/S0022112069001248).
- Mobbs, S. D., and Coauthors, 2005: Observations of downslope winds and rotors in the Falkland Islands. *Q.J.R. Meteorol. Soc.*, **131**, 329–351, doi:[10.1256/qj.04.51](https://doi.org/10.1256/qj.04.51).
- Mohorovičić, A., 1889: Interessante Wolkenbildung über der Bucht von Buccari (Interesting cloud formation above Bakar Bay). *Meteor. Z.*, **24**, 56–58.
- Nance, L. B., and D. R. Durran, 1998: A modeling study of nonstationary trapped mountain lee waves. part II: Nonlinearity. *J. Atmos. Sci.*, **55**, 1429–1445, doi:[10.1175/1520-0469\(1998\)055<1429:AMSONT>2.0.CO;2](https://doi.org/10.1175/1520-0469(1998)055<1429:AMSONT>2.0.CO;2).
- Nappo, C. J., 2002: *An Introduction to Atmospheric Gravity Waves*. Academic Press, 276 pp.
- Neiman, P. J., R. M. Hardesty, M. A. Shapiro, and R. E. Cupp, 1988: Doppler lidar observations of a downslope windstorm. *Mon. Wea. Rev.*, **116**, 2265–2275, doi:[10.1175/1520-0493\(1988\)116<2265:DLOAD>2.0.CO;2](https://doi.org/10.1175/1520-0493(1988)116<2265:DLOAD>2.0.CO;2).
- Ólafsson, H., and P. Bougeault, 1997: The effect of rotation and surface friction on orographic drag. *J. Atmos. Sci.*, **54**, 193–210, doi:[10.1175/1520-0469\(1997\)054<0193:TEORAS>2.0.CO;2](https://doi.org/10.1175/1520-0469(1997)054<0193:TEORAS>2.0.CO;2).
- Palm, E., 1955: Multiple-layer mountain wave models with constant stability and shear. Air Force Cambridge Research Center Scientific Report No. 3, Contract No. AF 19, (604)-728 pp.
- Parish, T. R., and L. D. Oolman, 2012: Isobaric height perturbations associated with mountain waves measured by aircraft during the Terrain-Induced Rotor Experiment. *J. Atmos. Oceanic Technol.*, **29**, 1825–1834, doi:[10.1175/JTECH-D-12-00050.1](https://doi.org/10.1175/JTECH-D-12-00050.1).
- Prtenjak, M. T., and Belušić, 2009: Formation of reversed lee flow over the north-eastern adriatic during bora. *Geofizika*, **26**, 145–155.

- Queney, M. P., 1936a: Recherches relatives à l'influence du relief sur les éléments météorologiques (1) (Research on the influence of orography on meteorological conditions). *La Météorologie*, 334–353.
- Queney, M. P., 1936b: Recherches relatives à l'influence du relief sur les éléments météorologiques (suite) (Research on the influence of orography on meteorological conditions). *La Météorologie*, 453–470.
- Queney, M. P., 1947: Theory of perturbations in stratified currents with application to air flow over mountain barriers. Dept. of Meteorology, University of Chicago, Misc. Rep. 23, 81 pp.
- Queney, M. P., 1955: Rotor phenomena in the lee of mountains. *Tellus*, **7**, 367–371, doi:[10.1111/j.2153-3490.1955.tb01173.x](https://doi.org/10.1111/j.2153-3490.1955.tb01173.x).
- Queney, P., G. Corby, N. Gerbier, H. Koschmieder, and J. Zierep, 1960: The airflow over mountains. World Meteorological Organization Tech. Note 34, 135 pp.
- Raab, T., and G. Mayr, 2008: Hydraulic interpretation of the footprints of Sierra Nevada windstorms tracked with an automobile measurement system. *J. Appl. Meteor. Climatol.*, **47**, 2581–2599, doi:[10.1175/2008JAMC1675.1](https://doi.org/10.1175/2008JAMC1675.1).
- Ralph, F. M., P. J. Neiman, T. L. Keller, D. Levinson, and L. Fedor, 1997a: Observations, simulations, and analysis of nonstationary trapped lee waves. *J. Atmos. Sci.*, **54**, 1308–1333, doi:[10.1175/1520-0469\(1997\)054<1308:OSAAON>2.0.CO;2](https://doi.org/10.1175/1520-0469(1997)054<1308:OSAAON>2.0.CO;2).
- Ralph, F. M., P. J. Neiman, and D. Levinson, 1997b: Lidar observations of a breaking mountain wave associated with extreme turbulence. *Geophys. Res. Lett.*, **24**, 663–666, doi:[10.1029/97GL00349](https://doi.org/10.1029/97GL00349).
- Reinecke, P. A., and D. R. Durran, 2009: Initial-condition sensitivities and the predictability of downslope winds. *J. Atmos. Sci.*, **66**, 3401–3418, doi:[10.1175/2009JAS3023.1](https://doi.org/10.1175/2009JAS3023.1).
- Richard, E., P. Mascart, and E. C. Nickerson, 1989: The role of surface friction in downslope windstorms. *J. Appl. Meteor.*, **28**, 241–251, doi:[10.1175/1520-0450\(1989\)028<0241:TROSFI>2.0.CO;2](https://doi.org/10.1175/1520-0450(1989)028<0241:TROSFI>2.0.CO;2).
- Sawada, M., and Coauthors, 2012: Transient downslope winds under the influence of stationary lee waves from the Zao mountain range. *J. Meteorol. Soc. Jpn. Ser. II*, **90**, 79–100, doi:[10.2151/jmsj.2012-105](https://doi.org/10.2151/jmsj.2012-105).
- Schweitzer, H., 1952: Versuch einer Erklärung des Föhns als Luftströmung mit überkritischer Geschwindigkeit (An attempt to explain the foehn as an airflow with supercritical speed). *Arch. Meteorol. Geophys. Bioklim.*, **5**, 350–371, doi:[10.1007/BF02247776](https://doi.org/10.1007/BF02247776).
- Scorer, R. S., 1949: Theory of waves in the lee of mountains. *Q.J.R. Meteorol. Soc.*, **75**, 41–56, doi:[10.1002/qj.49707532308](https://doi.org/10.1002/qj.49707532308).

- Scorer, R. S., 1955: Theory of airflow over mountains: IV-Separation of flow from the surface. *Q.J.R. Meteorol. Soc.*, **81**, 340–350, doi:[10.1002/qj.49708134905](https://doi.org/10.1002/qj.49708134905).
- Scorer, R. S., and H. Klieforth, 1959: Theory of mountain waves of large amplitude. *Q.J.R. Meteorol. Soc.*, **85**, 131–143, doi:[10.1002/qj.49708536406](https://doi.org/10.1002/qj.49708536406).
- Sharman, R. D., S. B. Trier, T. P. Lane, and J. D. Doyle, 2012: Sources and dynamics of turbulence in the upper troposphere and lower stratosphere: A review. *Geophys. Res. Lett.*, **39**, L12 803, doi:[10.1029/2012GL051996](https://doi.org/10.1029/2012GL051996).
- Sheridan, P., and S. Vosper, 2012: High-resolution simulations of lee waves and downslope winds over the Sierra Nevada during T-REX IOP 6. *J. Appl. Meteor. Climatol.*, **51**, 1333–1352, doi:[10.1175/JAMC-D-11-0207.1](https://doi.org/10.1175/JAMC-D-11-0207.1).
- Sheridan, P. F., V. Horlacher, G. G. Rooney, P. Hignett, Mobbs, S. D., Vosper, and S. B., 2007: Influence of lee waves on the near-surface flow downwind of the Pennines. *Q.J.R. Meteorol. Soc.*, **133**, 1353–1369, doi:[10.1002/qj.110](https://doi.org/10.1002/qj.110).
- Sheridan, P. F., and S. B. Vosper, 2006a: A flow regime diagram for forecasting lee waves, rotors and downslope winds. *Met. Apps*, **13**, 179–195, doi:[10.1017/S1350482706002088](https://doi.org/10.1017/S1350482706002088).
- Sheridan, P. F., and S. B. Vosper, 2006b: Numerical simulations of rotors, hydraulic jumps and eddy shedding in the Falkland Islands. *Atmosph. Sci. Lett.*, **6**, 211–218, doi:[10.1002/asl.118](https://doi.org/10.1002/asl.118).
- Smith, C. M., and E. D. Skillingstad, 2009: Investigation of upstream boundary layer influence on mountain wave breaking and lee wave rotors using a large-eddy simulation. *J. Atmos. Sci.*, **66**, 3147–3164, doi:[10.1175/2009JAS2949.1](https://doi.org/10.1175/2009JAS2949.1).
- Smith, R. B., 1979: The influence of mountains on the atmosphere. *Adv. Geophys.*, **21**, 87–230, doi:[10.1016/S0065-2687\(08\)60262-9](https://doi.org/10.1016/S0065-2687(08)60262-9).
- Smith, R. B., 1985: On severe downslope winds. *J. Atmos. Sci.*, **42**, 2597–2603, doi:[10.1175/1520-0469\(1985\)042<2597:OSDW>2.0.CO;2](https://doi.org/10.1175/1520-0469(1985)042<2597:OSDW>2.0.CO;2).
- Smith, R. B., 1987: Aerial observations of the Yugoslavian bora. *J. Atmos. Sci.*, **44**, 269–297, doi:[10.1175/1520-0469\(1987\)044<0269:AOOTYB>2.0.CO;2](https://doi.org/10.1175/1520-0469(1987)044<0269:AOOTYB>2.0.CO;2).
- Smith, R. B., 1989: Hydrostatic airflow over mountains. *Adv. Geophys.*, **31**, 1–41, doi:[10.1016/S0065-2687\(08\)60052-7](https://doi.org/10.1016/S0065-2687(08)60052-7).
- Smith, R. B., 2007: Interacting mountain waves and boundary layers. *J. Atmos. Sci.*, **64**, 594–607, doi:[10.1175/JAS3836.1](https://doi.org/10.1175/JAS3836.1).
- Smith, R. B., J. D. Doyle, Q. Jiang, and S. A. Smith, 2007: Alpine gravity waves: Lessons from MAP regarding mountain wave generation and breaking. *Q.J.R. Meteorol. Soc.*, **133**, 917–936, doi:[10.1002/qj.103](https://doi.org/10.1002/qj.103).

- Smith, R. B., Q. Jiang, and J. D. Doyle, 2006: A theory of gravity wave absorption by a boundary layer. *J. Atmos. Sci.*, **63**, 774–781, doi:[10.1175/JAS3631.1](https://doi.org/10.1175/JAS3631.1).
- Smith, R. B., S. Skubis, J. D. Doyle, A. S. Broad, C. Kiemle, and H. Volkert, 2002: Mountain waves over Mont Blanc: Influence of a stagnant boundary layer. *J. Atmos. Sci.*, **59**, 2073–2092, doi:[10.1175/1520-0469\(2002\)059<2073:MWOMBI>2.0.CO;2](https://doi.org/10.1175/1520-0469(2002)059<2073:MWOMBI>2.0.CO;2).
- Smith, R. B., B. K. Woods, J. Jensen, W. A. Cooper, J. D. Doyle, Q. Jiang, and V. Grubišić, 2008: Mountain waves entering the stratosphere. *J. Atmos. Sci.*, **65**, 2543–2562, doi:[10.1175/2007JAS2598.1](https://doi.org/10.1175/2007JAS2598.1).
- Staquet, C., and J. Sommeria, 2002: Internal gravity waves: From instabilities to turbulence. *Annu. Rev. Fluid. Mech.*, **34**, 559–593, doi:[10.1146/annurev.fluid.34.090601.130953](https://doi.org/10.1146/annurev.fluid.34.090601.130953).
- Stiperski, I., and V. Grubišić, 2011: Trapped lee wave interference in the presence of surface friction. *J. Atmos. Sci.*, **68**, 918–936, doi:[10.1175/2010JAS3495.1](https://doi.org/10.1175/2010JAS3495.1).
- Stiperski, I., B. Ivančan-Picek, V. Grubišić, and A. Bajić, 2012: Complex bora flow in the lee of southern velebit. *Q.J.R. Meteorol. Soc.*, **138**, 1490–1506, doi:[10.1002/qj.1901](https://doi.org/10.1002/qj.1901).
- Strauss, L., S. Serafin, S. Haimov, and V. Grubišić, 2015a: Turbulence in breaking mountain waves and atmospheric rotors estimated from airborne in situ and Doppler radar measurements. *Q.J.R. Meteorol. Soc.*, doi:[10.1002/qj.2604](https://doi.org/10.1002/qj.2604), in press.
- Strauss, L., S. Serafin, and V. Grubišić, 2015b: Atmospheric rotors and severe turbulence in a deep valley. Submitted to *J. Atmos. Sci.*
- UCAR/NCAR, cited 2015: Earth Observing Laboratory, 2005-present. NSF/NCAR GV HIAPER Aircraft. doi:[10.5065/D6DR2SJP](https://doi.org/10.5065/D6DR2SJP).
- Vergeiner, I., and D. K. Lilly, 1970: The dynamic structure of lee wave flow as obtained from balloon and airplane observations. *Mon. Wea. Rev.*, **98**, 220–232, doi:[10.1175/1520-0493\(1970\)098<0220:TDSOLW>2.3.CO;2](https://doi.org/10.1175/1520-0493(1970)098<0220:TDSOLW>2.3.CO;2).
- Večenaj, Ž., D. Belušić, V. Grubišić, and B. Grisogono, 2012: Along-coast features of bora-related turbulence. *Bound.-Layer Meteor.*, **143**, 527–545, doi:[10.1007/s10546-012-9697-6](https://doi.org/10.1007/s10546-012-9697-6).
- Večenaj, Ž., S. F. J. De Wekker, and V. Grubišić, 2011: Near-surface characteristics of the turbulence structure during a mountain-wave event. *J. Appl. Meteor. Climatol.*, **50**, 1088–1106, doi:[10.1175/2010JAMC2450.1](https://doi.org/10.1175/2010JAMC2450.1).
- Vosper, S. B., 2004: Inversion effects on mountain lee waves. *Q.J.R. Meteorol. Soc.*, **130**, 1723–1748, doi:[10.1256/qj.03.63](https://doi.org/10.1256/qj.03.63).
- Vosper, S. B., P. F. Sheridan, and A. Brown, 2006: Flow separation and rotor formation beneath two-dimensional trapped lee waves. *Q.J.R. Meteorol. Soc.*, **132**, 2415–2438, doi:[10.1256/qj.05.174](https://doi.org/10.1256/qj.05.174).

Bibliography

- Vosper, S. B., H. Wells, J. A. Sinclair, and P. F. Sheridan, 2013: A climatology of lee waves over the UK derived from model forecasts. *Met. Apps*, **20**, 466–481, doi:[10.1002/met.1311](https://doi.org/10.1002/met.1311).
- Wang, Z., and Coauthors, 2012: Single aircraft integration of remote sensing and in situ sampling for the study of cloud microphysics and dynamics. *Bull. Amer. Meteor. Soc.*, **93**, 653–668, doi:[10.1175/BAMS-D-11-00044.1](https://doi.org/10.1175/BAMS-D-11-00044.1).
- Weigel, A. P., and M. W. Rotach, 2004: Flow structure and turbulence characteristics of the daytime atmosphere in a steep and narrow Alpine valley. *Q.J.R. Meteorol. Soc.*, **130**, 2605–2627, doi:[10.1256/qj.03.214](https://doi.org/10.1256/qj.03.214).
- Weissmann, M., A. Dörnbrack, and J. D. Doyle, 2009: Vorticity from line-of-sight lidar velocity scans. *J. Atmos. Oceanic Technol.*, **26**, 2683–2690, doi:[10.1175/2009JTECHA1260.1](https://doi.org/10.1175/2009JTECHA1260.1).
- Wendisch, M., and J. E. Brenguier, 2013: *Airborne Measurements for Environmental Research*. Wiley-VCH Verlag, Weinheim, Germany, 520 pp.
- Whelan, R. F., 2000: *Exploring the Monster. Mountain Lee Waves: The Aerial Elevator*. Wind Canyon Books, 169 pp.
- Whiteman, C. D., 2000: *Mountain Meteorology. Fundamentals and Applications*. Oxford University Press, 355 pp.
- WMO, 1993: Handbook of meteorological forecasting for soaring flight. World Meteorological Organization Tech. Note 495.
- Woods, B. K., and R. B. Smith, 2010: Energy flux and wavelet diagnostics of secondary mountain waves. *J. Atmos. Sci.*, **67**, 3721–3738, doi:[10.1175/2010JAS3285.1](https://doi.org/10.1175/2010JAS3285.1).
- Woods, B. K., and R. B. Smith, 2011: Short-wave signatures of stratospheric mountain wave breaking. *J. Atmos. Sci.*, **68**, 635–656, doi:[10.1175/2010JAS3634.1](https://doi.org/10.1175/2010JAS3634.1).
- Worthington, R. M., 2014: Boundary-layer effects on mountain waves: A new look at some historical studies. *Meteorol. Atmos. Phys.*, **126**, 1–12, doi:[10.1007/s00703-014-0331-7](https://doi.org/10.1007/s00703-014-0331-7).

Acronyms and abbreviations

2D	two-dimensional
3D	three-dimensional
ACRS	aircraft-fixed reference system
ALPEX	Alpine Experiment
AMS	American Meteorological Society
ARW	Advanced Research WRF
ATRS	along-track reference system
AWS	automated weather stations
BLS	boundary-layer separation
CLWP	Colorado Lee Wave Program
DLR	Deutsches Zentrum für Luft- und Raumfahrt
DRI	Desert Research Institute
ECMWF	European Centre for Medium-Range Weather Forecasts
EDR	cube root of the energy-dissipation rate, $\varepsilon^{1/3}$
EOL	Earth Observing Laboratory (NCAR)
FHO15	French et al. (2015)
FWF	Fonds zur Förderung der wissenschaftlichen Forschung (Austria)
GAUS	GPS Advanced Upper Air Sounding System
GPS	Global Positioning System
GSS15	Grubišić et al. (2015a)
HIAPER, or GV	High-Performance Instrumented Airborne Platform for Environmental Research
IDT	inertial dissipation technique
IOP	intensive observing period
ISS	Integrated Sounding System
JSP	Mountain Wave-Jet Stream Project
Lidar	light detection and ranging
LTZ	low-level turbulence zone
MAP	Mesoscale Alpine Programme
MAPR	Multiple Antenna Profiler
MSL	above mean sea level
NASA06	NASA Orographic Clouds Experiment
NCAR	National Center for Atmospheric Research (U.S.)
NCEP	National Centers for Environmental Prediction (U.S.)
NLP	non-linearity parameter
NOGAPS	Navy Operational Global Atmospheric Prediction System (U.S.)
NSF	National Science Foundation (U.S.)
OSTIV	Organisation Scientifique et Technique du Vol à Voile

PPI	plan position indicator (lidar scan)
PYREX	Pyrénées Experiment
Radar	radio detection and ranging
REAL	Raman-shifted eye-safe aerosol lidar
RHI	range-height indicator (lidar scan)
σ_w^2	variance of vertical velocity
SRP	Sierra Rotors Project
SWP	Sierra Wave Project
TKE	turbulent kinetic energy
T-REX	Terrain-induced Rotor Experiment
UCAR	University Corporation for Atmospheric Research
UL	University of Leeds
UWKA	University of Wyoming King Air
WCR	Wyoming Cloud Radar
WMO	World Meteorological Organization
WRF	Weather Research and Forecasting model

Acknowledgements

This work would not have been possible without the support and encouragement by a lot of people surrounding me. I am indebted to ...

- ◇ my mentor Vanda Grubišić, for giving me the initial stimulus for my research on mountain waves and rotors, for providing numerous opportunities for exchange with researchers in Europe and abroad, and for granting me the necessary time to develop my own thoughts and become a scientist,
- ◇ Stefano Serafin, for providing support practically every day and helping me overcome the stumbling blocks on my way to finishing this work, through numerous scientific discussions, reviewing of manuscripts, and contributing his own ideas on how to proceed,
- ◇ Samuel Haimov, for sharing his expert knowledge of the Wyoming Cloud Radar and helping with the data analysis, and for his meticulous analysis and criticism of the turbulence estimation technique, which led to substantial improvements in the quality of the results,
- ◇ a number of other people, whom I met and talked to, for sharing their expertise and giving advice, including Željko Večenaj, Branko Grisogono, Ivana Stiperski, Karmen Babić, Volkmar Wirth, Bob Sharman, and Stephan De Wekker,
- ◇ my colleagues at the University of Vienna for good company during lunch hours and a friendly working environment, in particular my office mate Johannes Sachsperger, for lending me an ear and helping me with programming, LaTeX, and other issues whenever needed, and for heating our office with his iMac in winter,
- ♡ finally, my family and friends, in particular my girlfriend Veronika, for smoothing the wave-like and jump-like disturbances in my motivation and mood through continuous support and encouragement, for practising patience when my attention was focused on science, and for keeping me connected to other things in life.

Curriculum vitae

Lukas Strauss, Dipl.-Ing.

Vienna, Austria

lukas.strauss@univie.ac.at

<http://imgw.univie.ac.at/en/research/tm/staff/strauss>

Academic employment record

11/2010 –	Pre-doctoral university assistant and project staff, Department of Meteorology and Geophysics, University of Vienna, Austria
08–09/2010	Research trainee, Subdivision of Fluid Mechanics, Department of Mathematics, University of Oslo, Norway
01–06/2010	Project staff, Institute for Theoretical Physics, Vienna University of Technology, Austria

Education

2010 – 2015	Doctoral studies in Meteorology at the Department of Meteorology and Geophysics, University of Vienna. Supervisor: Prof. Vanda Grubišić
2004 – 2009	Studies in Physics at the Vienna University of Technology. Diploma thesis ‘Vibrations and diffusion in colloidal cluster crystals’. Thesis supervisor: Prof. Gerhard Kahl
1995 – 2003	Secondary school. Final exams in Physics, French, and Latin.

Visits & stays

08/2014, 08/2013, 07–08/2012	Visitor, Earth Observing Laboratory (EOL), National Center for Atmospheric Research (NCAR), Boulder, Colorado
08–09/2010	Intern, Subdivision of Fluid Mechanics, Department of Mathematics, University of Oslo, Norway
02–07/2008	Exchange student, École Polytechnique Fédérale de Lausanne (EPFL), Switzerland

Workshops & schools

09/2013	‘Observations and experimental methods in an inhomogeneous atmosphere’, Institute of Meteorology and Climate Research, Garmisch-Partenkirchen, Germany
10/2012	‘Bridging the Gap between Atmospheric Scales’, Wageningen University, Wageningen, Netherlands
04/2011	‘Parametrization of Subgrid-scale Physical Processes’, European Centre for Medium-Range Weather Forecast (ECMWF), Reading, UK

Teaching experience

- 2012 – Supervision of Bachelor students (M. Wind, R. Mühlgassner, A. Bergner)
- 2011 – Exercise classes in ‘Thermodynamics of the Atmosphere’ and ‘Dynamics of the Atmosphere I/II’ at the University of Vienna
- 2007 – 2008 Tutor in ‘Quantum Theory’ and ‘Mathematical Methods in Theoretical Physics’ at the TU Vienna

Scholarships and awards

- 08/2014 ‘Best Student Poster Presentation’ Award by the American Meteorological Society, 16th Conference on Mountain Meteorology, San Diego, California
- 04/2014 ‘Outstanding Student Poster’ Award by the European Geosciences Union, EGU General Assembly, Vienna, Austria
- 08/2012 ‘Best Student Poster Presentation’ Award by the American Meteorological Society, 15th Conference on Mountain Meteorology, Steamboat, Colorado
- 06/2009 Scholarship of the TU Vienna for research visits abroad

Selected conference contributions

- Strauss L., V. Grubišić, S. Serafin, R. Mühlgassner, 2014: Mountain waves and rotors – revisiting the concept of the “Lower Turbulent Zone”. Poster at the 16th AMS Conference on Mountain Meteorology 2014, San Diego, California.
- Strauss L., V. Grubišić, S. Serafin, R. Mühlgassner, 2014: Mountain wave-induced turbulence – “Lower Turbulent Zones” revisited. Poster at the EGU General Assembly 2014, Vienna, Austria.
- Strauss L., S. Serafin, V. Grubišić, 2013: Terrain-induced turbulence: insights gained from airborne in situ and remotely sensed data. Talk at the Aviation Turbulence Workshop. National Center for Atmospheric Research (NCAR), Boulder, Colorado.
- Strauss, L., S. Serafin, V. Grubišić, 2012: Measuring turbulence from airborne in situ and radar data recorded during an event of wave-induced boundary-layer separation. Poster, 15th AMS Conference on Mountain Meteorology 2012, Steamboat, Colorado.

Peer-reviewed publications

- Strauss, L., S. Serafin, S. Haimov, and V. Grubišić, 2015a: Turbulence in breaking mountain waves and atmospheric rotors estimated from airborne in situ and Doppler radar measurements. *Q.J.R. Meteorol. Soc.*, doi:10.1002/qj.2604, in press.
- Grubišić, V., S. Serafin, L. Strauss, S. Haimov, J. R. French, and L. Oolman, 2015a: Wave-induced boundary-layer separation in the lee of the Medicine Bow Mountains. Part II: Modeling. *J. Atmos. Sci.*, accepted with minor revisions.
- Coslovich, D., L. Strauss, and G. Kahl, 2011: Hopping and microscopic dynamics of ultrasoft particles in cluster crystals. *Soft Matter*, **7**, 2127–2137, doi:10.1039/C0SM00545B.

Manuscripts in review / in preparation

- Strauss, L., S. Serafin, and V. Grubišić, 2015b: Atmospheric rotors and severe turbulence in a deep valley. Submitted to *J. Atmos. Sci.*.
- Grubišić, V., S. Serafin, and L. Strauss, 2015b: Climatology of westerly wind events in the lee of the Sierra Nevada. In preparation for *J. Appl. Meteor. Climatol.*.
- French, J. R., S. Haimov, L. Oolman, V. Grubišić, S. Serafin, and L. Strauss, 2015: Wave-induced boundary-layer separation in the lee of the Medicine Bow Mountains. Part I: Observations. *J. Atmos. Sci.*, in review.

Languages

- German Native
- English Fluent (C1)
- French Fluent (B2)
- Mandarin Chinese Basic knowledge (A1)

Scientific analysis and computer skills

- Programming Python ●●●, Unix shell scripts ●●●, Fortran ●●○, Object-oriented programming ●●○, C/C++ ●○○, NCAR Command Language ●○○
- Numerical simulation Weather Research and Forecasting (WRF) Model ●●○, Cloud Model 1 (CM1) ●○○, ANSYS CFX (CFD software) ●○○
- Data analysis Remotely-sensed data (Doppler radars, lidars, wind profilers), high-rate in situ data (aircraft, towers)
Turbulence analysis, spectral analysis, wavelet analysis
- Applications Google earth, L^AT_EX, Microsoft Office, Libre Office, Virtual Box, Adobe Acrobat Professional, Photoshop Elements, Lightroom
- Web TYPO3 CMS (<http://imgw.univie.ac.at/en/research/tm>)
- Operating systems Linux, Windows, Mac OS X